



Universiteit
Leiden
The Netherlands

Chasing cosmic tau neutrinos in the abyss

Bormuth, R.; Bormuth R.

Citation

Bormuth, R. (2017, December 7). *Chasing cosmic tau neutrinos in the abyss*. *Casimir PhD Series*. Retrieved from <https://hdl.handle.net/1887/56023>

Version: Not Applicable (or Unknown)

License: [Licence agreement concerning inclusion of doctoral thesis in the Institutional Repository of the University of Leiden](#)

Downloaded from: <https://hdl.handle.net/1887/56023>

Note: To cite this publication please use the final published version (if applicable).

Cover Page



Universiteit Leiden



The handle <http://hdl.handle.net/1887/56023> holds various files of this Leiden University dissertation.

Author: Bormuth, R.

Title: Chasing cosmic tau neutrinos in the abyss

Issue Date: 2017-12-07

CHASING COSMIC TAU NEUTRINOS IN THE ABYSS

Proefschrift

ter verkrijging van
de graad van Doctor aan de Universiteit Leiden,
op gezag van Rector Magnificus prof. mr. C.J.J.M. Stolker,
volgens besluit van het College voor Promoties
te verdedigen op donderdag 7 december 2017
klokke 11:15 uur

door

ROBERT BORMUTH
geboren te Heppenheim, Duitsland
in 1986

Promotor: Prof. dr. M. de Jong
Co-promotor: Dr. D.F.E. Samtleben

Promotiecommissie: Prof. dr. E.N. Koffeman, University of Amsterdam
Dr. A. Heijboer, Nikhef
Dr. T. Eberl, University of Erlangen-Nürnberg
Prof. dr. E.R. Eliel
Prof. dr. A. Achúcarro

Casimir PhD series, Delft-Leiden 2017-42

ISBN 978-90-8593-326-7

published in print format 2017

An electronic version of this thesis can be found at <https://openaccess.leidenuniv.nl>

©Robert Bormuth 2017

This document was typeset using the typographical look-and-feel `classicthesis` developed by André Miede. The style was inspired by Robert Bringhurst's seminal book on typography "*The Elements of Typographic Style*". `classicthesis` is available for both \LaTeX and `LyX`:

<http://code.google.com/p/classicthesis>

Cover picture by Matthijs Damen

LOCATION:

Leiden University, Leiden

For my loved ones

CONTENTS

1	INTRODUCTION	7
1.1	Cosmic Rays	7
1.2	Neutrino astronomy	15
1.2.1	Neutrino history and properties	15
1.2.2	Neutrino interactions with matter	17
1.2.3	Neutrino sources	21
1.2.4	Neutrino telescopes	25
1.2.5	Cosmic neutrino observations: SN1987 and the IceCube flux	32
2	THE KM3NET DETECTOR	35
2.1	KM3Net ARCA	35
2.2	Detection unit	36
2.3	Detection module	39
2.4	Background sources	39
2.5	Data acquisition system	42
2.5.1	Trigger algorithm	42
3	SIMULATION	43
3.1	Event generation	43
3.1.1	Tau neutrino simulations	44
3.2	Light simulation and detector response	45
3.3	Tau Toy Monte Carlo	46
4	DETECTION UNIT PROTOTYPE	49
4.1	Introduction	49
4.2	Technical design	50
4.3	Data acquisition system	53
4.3.1	Trigger algorithm	53
4.3.2	Recorded data	54
4.4	PPM-DU Monte Carlo simulation	56
4.5	In-situ detector calibration	57
4.5.1	PMT calibration	58
4.5.2	PMT calibration stability studies	62
4.5.3	DOM beacon calibration	63
4.5.4	Calibrating DOM 3 using beacon 1 vs using beacon 2	66
4.5.5	Hit selection: Difference in using 2 nd hit vs using 1 st hit	68
4.5.6	DOM muon calibration	69
4.5.7	Data period calibration	70
4.6	PPM-DU data analysis	71
4.6.1	Time over threshold signal	71
4.6.2	Single rates	71
4.6.3	Recorded triggered events	72
4.6.4	Muon detection	74
4.7	Muon reconstruction	79

CONTENTS

4.7.1	Fitting procedure	79
4.7.2	Event selection	81
4.7.3	Zenith angle reconstruction	82
4.8	PPM-DU conclusion	86
5	BELLE STARR RECONSTRUCTION	87
5.1	Tau “Double Bang” event signature	88
5.2	Background signatures	93
5.3	Belle Starr Prefit	95
5.3.1	Position and time fit	95
5.3.2	Energy and direction fit	101
5.4	Belle Starr Scan	104
5.5	Belle Starr Peak	110
5.5.1	TSpectrum background estimation	110
5.5.2	TSpectrum peak identification	111
5.5.3	TSpectrum for likelihood scans	111
5.5.4	Improvement of reconstructed positions	114
5.5.5	Vertex position reconstruction performance	115
5.6	Belle Starr Refit	118
5.6.1	Full fit performance	118
6	TAU “DOUBLE BANG” SELECTION	121
6.1	Selection Criteria	121
6.1.1	Energy cut	123
6.1.2	Position cut	124
6.1.3	Peak cut	125
6.1.4	Background cut	127
6.1.5	Length cut	129
6.2	Selection criteria efficiency	131
6.3	Belle Starr resolution for selected events	134
6.4	Results of the tau “Double Bang” selection	136
6.5	Discussion	139
7	APPENDIX	141
	Summary	155
	Samenvatting	163
	About the Author	171
	Acknowledgements	173

INTRODUCTION

Good resolutions [...] are simply
cheques that men draw on a bank
where they have no account

Oscar Wild, *The Picture of Dorian
Gray*

In this chapter the motivation for observing the Universe with neutrinos is laid out. This process is called neutrino astronomy and offers a new window to the Universe which complements the traditional branches of astronomy. A brief historic overview as well as the current status of neutrino astronomy are presented.

Neutrino astronomy is especially relevant to the understanding of the origin of cosmic rays. Therefore, this chapter first focuses on the status of cosmic ray astronomy. This is followed by an introduction to neutrino astronomy and its link to cosmic ray astronomy.

1.1 COSMIC RAYS

Cosmic rays are sub-atomic particles which traverse the universe. They originate in outer space and were first observed over 100 years ago. Cosmic rays are believed to be accelerated in some astrophysical sources. For these particle accelerators, neutrinos can offer unique insights into their creation and evolution in time.

Since the discovery of cosmic rays, despite numerous efforts, some fundamental questions remain unanswered. The list of open questions includes the origin, propagation through the Universe and the acceleration mechanism of cosmic rays. This section will focus on the history and current status of cosmic ray research.

A brief history

Before the notion of cosmic rays existed, Charles-Augustin Coulomb in 1785 observed that a charged metal sphere will gradually lose its charge in air. From this observation, he and other scientists concluded that the air is ionized. At that time, the ionization was believed to be caused by radioactive elements in the Earth's crust.

If Earth's crust is the origin of the radiation it implies a gradual decrease of ionization in air with increasing distance from the crust. This prediction was tested by Victor Hess in the years of 1911-1913. After greatly improving the

measurement accuracies, Hess undertook several balloon flights in order to validate this theory. He found the radiation levels to increase with the distance from Earth, thereby falsifying the Earth crust theory. From his observations he concluded that there was radiation penetrating the atmosphere from outer space [1], today this radiation is commonly referred to as cosmic rays. This conclusion was confirmed by Werner Kolhörster in 1913 [2].

Clay in 1927 and Milikan in 1932 each undertook sea voyages to measure the dependence of the cosmic ray flux on Earth's latitude. Both found the flux to depend on the latitude which led to the conclusion that cosmic rays are affected by the Earth's magnetic field and therefore mainly composed of charged particles. Following up on this, other experiments showed an abundance of cosmic rays in cardinal direction from the west, proving them to be mainly positively charged.

In the early days of particle physics, cosmic rays led to important scientific discoveries in the field. Before the invention of particle accelerators, cosmic rays were the only way to study interactions of highly energetic particles. The positron was discovered by Carl D. Anderson in 1933 by observing interactions of cosmic rays in a cloud chamber in the presence of a magnetic field [3]. The magnetic field allowed to distinguish positively and negatively charged particles. Anderson also discovered the muon in 1936 in a similar experimental setup. In a different experimental setup, cosmic rays allowed for the discovery of the pion by Ochialini et.al. [4]. Today, particle accelerators have not reached the energies attainable with cosmic rays but the low flux of cosmic rays makes groundbreaking particle physics observations unfeasible.

Matter composition of Cosmic Rays

Following the early observations of cosmic rays, it could be concluded that most cosmic rays are nuclei, with protons being most common amongst them. Measuring the mass of the particle impinging on Earth's atmosphere is non trivial, especially as the energy of the cosmic ray particles increase. The current data agree on the most prevalent particles but vary in the exact composition. To give an idea, one example, Bluemer et al. estimate the composition to be: protons 85 %, helium 12 % and 1 % of nuclei with atomic number $Z \geq 3$. The remainder of the cosmic rays is composed of other particles such as electrons [5].

Anti-particles make up for a small fraction of the observed cosmic rays. At present, the bulk of the observed anti-particles are anti-protons and positrons [5]. Some neutral particles reaching Earth from outer space are believed to be neutrons. A different sample of high energetic particles in the Universe is composed of photons which are commonly referred to as Gamma Rays.

Energy spectrum

The cosmic ray energy spectrum for different primary particles is shown in Fig. 1. The energy spectrum of cosmic rays spans roughly 12 orders of magnitude. It is described reasonably well by a power law

$$\frac{dN}{dE} \approx E^{-\gamma} \quad , \quad (1)$$

where E is the energy of the primary particle and γ the so-called spectral index.

The energy spectrum is only depicted down to energies of one GeV because below those energies the modulation of the cosmic rays due to irregular solar wind magnetic field fluctuations is such that the energy spectrum is not well defined [6]. At energies below 0.1 GeV most cosmic rays originate from the sun. These are not considered in this work.

The best fit to the all particle energy spectrum has different spectral indices for different energy ranges. The two points where the spectral index significantly changes are the so-called knee at $E \simeq 5 \times 10^6$ GeV and the ankle at $E \simeq 5 \times 10^9$ GeV. From the lowest energies up to the knee the spectral index is approximately $\gamma \simeq 2.7$. At energies above the knee the spectral index changes to $\gamma \simeq 3$. At the ankle, the spectrum flattens to the original $\gamma \simeq 2.7$ and then steepens again [7].

The changes in spectral index indicate a change in origin, propagation or composition of the cosmic rays. Multiple theories for the cause of spectral index change exist. Most commonly, the knee is attributed to either a limit in the acceleration capability of galactic cosmic ray sources or galactic cosmic rays having sufficient energy to leave the galaxy or both. Whereas, the ankle is attributed to either a transition in origin from galactic to extra-galactic cosmic rays or to interactions of cosmic rays with other particles [8]. The reasoning for these assumptions and the mechanisms involved are discussed in the following.

Origin and propagation

To date, no sources of cosmic rays have been observed, but the origin of cosmic rays can be categorized into two types: galactic or extra galactic origin. The two possibilities can be distinguished due to the way cosmic rays interact with the galactic magnetic field. The galactic magnetic field is composed of two parts with a regular and random field which have different strengths in the disc and the halo of the galaxy, respectively [10, 11]. In the halo, the total magnetic field is weaker than in the disk but due to its larger size the halo magnetic field dominates the deflection of cosmic rays. The typical halo magnetic field has a strength of 0.3 nT and a height of around 1.4 pc.

A charged particle interacting with a magnetic field will follow a curved trajectory described by the Larmor radius:

$$r_L = \frac{p}{qB} = 1.08 \times 10^{-6} \text{pc} \times \frac{p \times c/\text{GeV}}{ZB/0.1 \text{nT}} \quad , \quad (2)$$

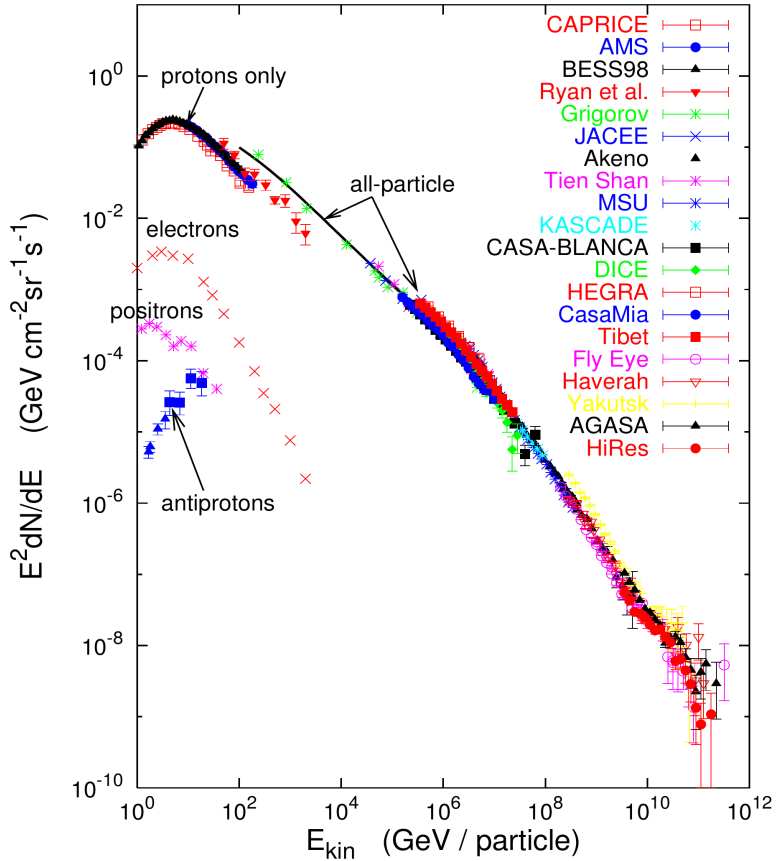


Figure 1: The energy spectrum of cosmic rays of different initial particles as measured by different experiments; The spectrum is reasonable well described by Eq. 1 with a varying spectral index γ , changing at the so-called knee ($E \simeq 5 \times 10^6 \text{ GeV}$) and the ankle ($E \simeq 5 \times 10^9 \text{ GeV}$); taken from [9].

where B is the magnetic field strength and p the particle momentum. For the typical halo magnetic field of 0.3 nT and a proton of energy 1×10^6 GeV the Larmor radius is 0.36 pc. A charged particle with a Larmor radius smaller than the galactic halo is confined to the galaxy. With energies above 1×10^9 GeV, the proton will leave the galaxy, making its detection at Earth less likely. Hence, cosmic rays with energies above the 1×10^9 GeV threshold are more likely to be of extra-galactic origin while cosmic rays of lower energies are assumed to be of galactic origin. This is one of the arguments associating the ankle in the cosmic ray energy distribution with a transition from cosmic rays of galactic to extra-galactic origin.

The discussed interaction of cosmic rays with the magnetic fields changes their direction and thereby making their origin untraceable. Only at the highest energies (around $E \simeq 1 \times 10^9$ GeV) the curvature of the particles is small enough so that the directions of the particles approximately point back to their origin. However, at these energies cosmic rays can interact with the cosmic microwave background (CMB) which causes them to lose energy. This effect is called the Greisen, Zatespin and Kuz'min cut-off [12] (GZK). It limits the distances cosmic rays can travel to around 200 Mpc. Protons with these energies can interact with the CMB via the Δ -resonance, causing the cosmic ray to lose energy (photo-disintegration) or produces a pion (pion-photo-production). Similarly, nuclei with these energies are also absorbed. As a result, the Universe becomes opaque to these cosmic rays. The interaction with the CMB produce photons and neutrinos at characteristic energies. Such photons and neutrinos have not yet been observed.

The energy threshold of the GZK cut-off is at the same energy as the ankle in the cosmic ray energy spectrum. Therefore, the drop-off at the ankle could also be explained by the GZK cut-off as cosmic rays of energies higher energies accumulate at lower energies.

The combination of the GZK cut-off and the galactic magnetic fields causes the identification of cosmic ray sources by the direct observations of cosmic rays to be unfeasible.

Cosmic Ray Sources

Identification of possible sources of cosmic rays is one of the main challenges of current research. In this section, a brief summary of the current knowledge is presented.

Source candidates for cosmic rays have to comply with the observed energy and intensity of the cosmic ray spectrum. It is generally agreed that the observed energies and fluxes can only be supplied by gravitational collapses of objects such as super nova remnants (SNR), often found in starburst galaxies, or by matter accreting objects such as active galactic nuclei (AGN). These sources are discussed below.

A SNR is the structure remaining after the implosion of a star that produced the supernova. On the outskirts, a SNR is confined by an expanding shock

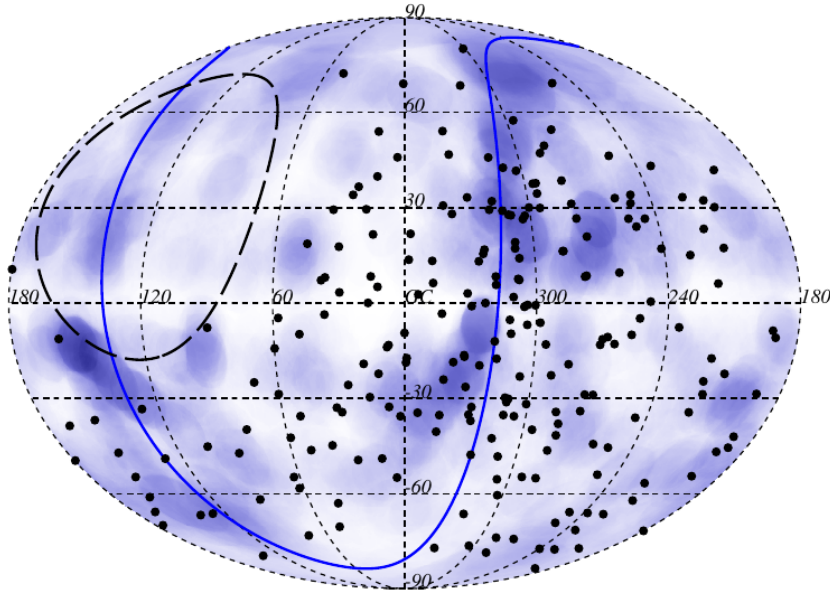


Figure 2: Skymap of the arrival directions (in galactic coordinates) of cosmic ray events with $E \geq 52 \text{ EeV}$ as detected by the Pierre Auger Observatory until the end of 2015 (black dots); the solid line depicts the field of view of the experiment for zenith angles smaller than 80° ; blue shapes represent the sources from the considered 2MRS catalog within a distance of 90 Mpc which are in the field of view of the experiment; taken from [15].

wave. This shell consists of material ejected during the explosion and material picked up during its expansion from the interstellar matter. In the cosmic ray composition, a small relative abundance of iron atoms is recorded, which can be linked to the supernovae explosions of evolved early-type stars [6]. The shock waves can be an efficient particle accelerator (see a discussion below). Furthermore, supernovae and their implosions can produce the energy needed to support the intensity of the observed cosmic ray flux [13]. Recently, the Fermi collaboration reported the observation of the characteristic photon signal produced by the pion-photo-production effect for two SNRs (IC 443 and W 44) [14]. This detection is the first experimental evidence that correlates supernovae remnants with cosmic rays and is a strong indication that SNRs are sources of cosmic rays. Therefore, SNRs are the most likely explanation for the observed cosmic ray energy spectra and matter composition up to energies of $\mathcal{O}(1 \times 10^6 \text{ GeV})$. It is not expected that SNRs produce cosmic rays beyond this energy, due to their limited size and magnetic field strength.

Starburst galaxies are galaxies which undergo a phase of unusually high star production. The high star production rate is caused by a relative large amount of gas present in these galaxies. These are ideal conditions to form high-mass stars which are very bright and therefore likely to implode into supernovae. This makes starburst galaxies natural candidates for extra-galactic cosmic ray sources.

An AGN is a region of dense matter located at the center of a galaxy with a high luminosity in emitted photons. An early observation by the Pierre Auger Observatory in 2010 showed evidence for anisotropy in the arrival direction of cosmic rays correlated with the locations of AGNs [16, 17]. Due to their large size and the presence of strong magnetic fields, AGNs could be the sources of cosmic rays with energies in excess of $\mathcal{O}(1 \times 10^6 \text{ GeV})$. An improved search on a larger data set in 2015 [15] could not reproduce this correlation for considered catalogs as shown in Fig. 2. If cosmic rays were still to originate from AGNs, limits on magnetic fields and cosmic ray fluxes from AGNs can be set [18].

Acceleration mechanism

The highest energies at which cosmic rays are observed at Earth are significantly higher than the temperature of the sources discussed before. Therefore, cosmic rays have to undergo further acceleration. A possible scenario for the acceleration is that the particles interact with moving magnetic fields. The mechanisms discussed here cover models for cosmic ray acceleration due to SNRs and AGNs.

The first mechanism for cosmic ray acceleration was proposed by Fermi in 1949 [19]. The mechanism involves the repeated scattering of charged particles on moving magnetic shock waves. Such shock waves exist in the Universe in form of magnetic gas clouds. A sketch of such a process is shown in Fig. 3a. Considering a particle moving at speed v with mass m scattering of a gas cloud moving at speed u , the energy gain per scattering is given by:

$$\Delta E_{\pm} = \frac{1}{2}m(v \pm u)^2 - \frac{1}{2}mv^2 \quad , \quad (3)$$

where the relative sign is linked to the alignment of the directions of v and u ; if they are parallel it is positive, if they are anti parallel it is negative. In general, a particle will scatter multiple times, causing an energy gain per pair of parallel and anti-parallel scattering of $\Delta E = mu^2$ and an average energy gain of:

$$\frac{\Delta E}{E} = 2 \frac{u^2}{v^2} \quad . \quad (4)$$

Equation. 4 also holds for relativistic calculations [20]. This process is called 2nd order Fermi acceleration due to the cloud velocity contributing quadratically in Eq. 4.

During the acceleration process, particles will also suffer energy losses due to interactions with the medium. For charged particles the most dominant energy loss is caused by synchrotron radiation and ionization. For a proton, the energy gain can become larger than the energy loss for energies greater than 200 MeV or so. The problem of particles achieving this initial energy is called the injection problem. It is currently not clear how particles achieve these initial energies.

The energy losses can explain the absence of electrons in the observed cosmic ray spectrum since they suffer more from radiation losses than heavier charged

particles. For electrons at initial energies higher than 300 MeV or so, energy loss due to radiation outweighs the energy gain by acceleration.

The 2nd order Fermi acceleration processes can in principle be repeated an infinite amount of times. The energy is then only limited by the size of the accelerator and the strength of the magnetic field.

The acceleration process proposed by Fermi in 1949 was extended in the 1970's by different groups [21, 22]. This work focused on the impact of shock fronts created by super nova explosions on particle accelerations. In this process a particle will gain energy by passing over a shock front multiple times. In Fig. 3b such a process is sketched for a particle of speed v hitting a shock front moving at speed u_1 . On both sides of the shock the particle can scatter off magnetic field irregularities which allows some particles to scatter from upstream to downstream multiple times. The gas behind the shock waves streams away from the shock front at a speed u_2 causing the gas to have a relative velocity of $u_1 - u_2$. The relative energy gain is then given by:

$$\frac{\Delta E}{E} = 2 \frac{(u_1 - u_2)}{v} . \quad (5)$$

A more sophisticated relativistic calculation taking into account different scattering angles as illustrated in [13] results in a similar linear dependence on the energy, namely:

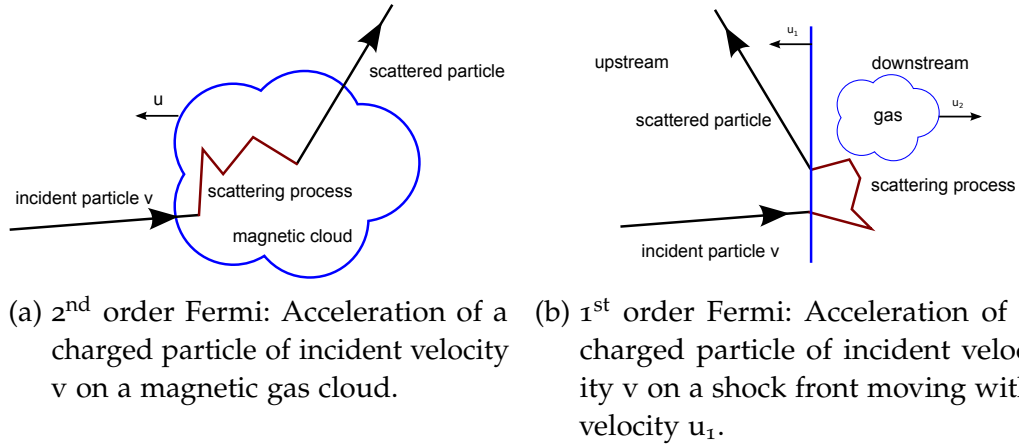
$$\frac{\Delta E}{E} = \frac{4}{3} \frac{(u_1 - u_2)}{c} . \quad (6)$$

Since this mechanism has a linear dependence on the velocity of the shock front it is commonly referred to as 1st order Fermi acceleration.

Both mechanisms result in a power law spectrum for the energy of the cosmic rays as observed in Eq. 1. Assuming a fixed escape probability, the power law nature of the spectrum is the result of combining the typical mean free path of a cosmic ray and the average energy gain per acceleration. In the case of the 1st order Fermi acceleration the two effects result in a spectral index of $\gamma = 2$ while for the 2nd order the spectral index cannot be uniquely determined [20].

It is generally believed that the two Fermi mechanisms together can accelerate particles starting from arbitrary initial energies to the highest energies observed for cosmic rays at Earth. Therefore, the injection problem of the 2nd order acceleration is overcome by accelerating particles to sufficient energies using the 1st order Fermi acceleration. However, evidence for this hypothesis has not yet been found.

Acceleration of cosmic ray in AGNs is believed to be a stochastic process connected to the 2nd order Fermi mechanism. Close to the center of an AGN highly turbulent magnetic fields can accelerate particles to energies above the injection problem. Once a particle reaches the injection energy, they scatter off time varying magnetic fields by means of the 2nd order Fermi mechanism. The existence of such fields was predicted in reference [23]. A calculation of this mechanism as performed in reference [24] shows that particles can be accelerated up to $\simeq 10 \times 10^{11}$ GeV within $\simeq 1 \times 10^6$ years in such environments.



(a) 2nd order Fermi: Acceleration of a charged particle of incident velocity v on a magnetic gas cloud. (b) 1st order Fermi: Acceleration of a charged particle of incident velocity v on a shock front moving with velocity u_1 .

Figure 3: Sketches of the two Fermi acceleration mechanisms (see text).

The spectral index can be reproduced depending on the assumed magnetic fields in these sources. The cut-off in the energy distribution of cosmic rays can thus be caused either due to an exhaustion of the source power or the GZK cut-off.

1.2 NEUTRINO ASTRONOMY

Neutrino astronomy is a branch of astronomy utilizing very large neutrino detectors. The neutrino's small cross section and zero charge allows them to escape dense areas and travel through the Universe without being deflected or absorbed. These unique characteristics enable unprecedented observation opportunities, most notably the identification of the sources of cosmic rays. If cosmic rays interact within the vicinity of their source, pions will be produced which inevitably decay into neutrinos. Detection of these neutrinos will reveal the origin of the cosmic rays.

In this chapter the properties of neutrinos important for neutrino astronomy are discussed followed by an introduction to the concepts of neutrino astronomy.

1.2.1 *Neutrino history and properties*

The existence of the neutrino was postulated by Wolfgang Pauli in 1930 [25] to explain the observed energy spectrum of the electron in radioactive decays of atomic nuclei. The first direct detection was achieved following a proposal by Ganchang in 1942 [26] by Cowan and Reines in 1956 [27]. The experiment was based on the capture of anti-electron neutrinos produced in a nuclear reactor.

In 1962, following the discovery of the muon and the development of a pion beam, Lederman, Schwartz and Steinberger made the first direct detection of the muon neutrino [28]. The existence of the tau neutrino was postulated as a result of the development of the Standard Model of particle physics and the discovery of the tau lepton. Direct detection of the tau neutrino was first achieved by the DONUT experiment in 2001 [29]. Also with the development

of the Standard Model, the force which describes neutrino interactions was unified with the electro-magnetic force. This force is called the weak interaction.

The weak interaction was found to be parity violating in a series of experiments in the years of 1956-58 [30]. This is formulated in the Standard Model as the left-handedness of neutrinos and the right-handedness of anti-neutrinos. To this day, no right-handed neutrino or left-handed anti-neutrino has been observed, suggesting they do not exist.

The Homestake experiment in 1962 [31] was the first in a series of experiments to detect neutrinos produced by the sun. The observed lack of solar neutrinos led to the discovery neutrino flavor oscillations (for more information see Section 1.2.1.1).

This discovery implied that neutrinos are massive particles. The current best global fit to all measurements can be found in reference [32]. Because two mass differences are measured via neutrino oscillations, the ordering of mass eigenstates is limited to two scenarios: referred to as the normal hierarchy ($m_{\nu_1} < m_{\nu_2} < m_{\nu_3}$, NH) and the inverted hierarchy ($m_{\nu_3} < m_{\nu_1} < m_{\nu_2}$, IH).

1.2.1.1 Neutrino oscillations

As discussed previously neutrinos change their flavors while travelling through space. This phenomenon is called neutrino oscillations. It is in analogy with the mixing between mass and weak eigenstates in the quark sector as described by the so-called CKM mixing matrix [33].

The first experimental evidence for neutrino oscillations was found by Ray Davis in the 1960s in the Homestake experiment [31]. A deficit of the predicted solar neutrino flux was found. This finding was originally called the solar neutrino problem and was only later understood as a consequence of neutrino oscillations. First proposed solutions to the solar neutrino problem suggested errors in the solar model. Doubts on the solar neutrino models were rebut by other experiments thereby confirming the solar model [34, 35]. Further progress in helioseismology and more precise measurements proved the solar model to be accurate.

One way of solving the solar neutrino problem is for the neutrinos to have mass allowing the mass eigenstates of the neutrinos to mix with the flavor eigenstates, giving rise to neutrino oscillations. The possibility of this mechanism was first proposed by Bruno Pontecorvo in 1957. After the discovery of the solar neutrino problem, Pontecorvo and Gribov utilized this mechanism to explain the observed deficit [36]. They proposed that the deficit in the observed electron neutrino rate was caused by oscillations of electron neutrinos into other flavors, which were not detected by the experiments.

Neutrino oscillations can be described by a unitary matrix which translates flavor and mass eigenstates into each other as shown in Eq. 7 and 8:

$$|\nu_\alpha\rangle = \sum_i U_{\alpha i}^* |\nu_i\rangle \quad (7)$$

$$|\nu_i\rangle = \sum_\alpha U_{\alpha i} |\nu_\alpha\rangle \quad (8)$$

where $|\nu_\alpha\rangle$ denotes a neutrino in a definite flavor state, $|\nu_i\rangle$ a neutrino mass state and $U_{\alpha i}$ the corresponding matrix element. The transition matrix U is referred to as the PMNS matrix after Pontecorvo, Maki, Nakagawa and Sakata and can be parameterized as follows:

$$\begin{aligned} & \begin{bmatrix} 1 & 0 & 0 \\ 0 & c_{23} & s_{23} \\ 0 & -s_{23} & c_{23} \end{bmatrix} \times \begin{bmatrix} c_{13} & 0 & s_{13}e^{-i\delta_{CP}} \\ 0 & 1 & 0 \\ -s_{13}e^{i\delta_{CP}} & 0 & c_{13} \end{bmatrix} \times \begin{bmatrix} c_{12} & s_{12} & 0 \\ -s_{12} & c_{12} & 0 \\ 0 & 0 & 1 \end{bmatrix} \\ & = \begin{bmatrix} c_{12}c_{13} & s_{12}c_{13} & s_{13}e^{-i\delta_{CP}} \\ -s_{12}c_{23} - c_{12}s_{23}s_{13}e^{i\delta_{CP}} & c_{12}c_{23} - s_{12}s_{23}s_{13}e^{i\delta_{CP}} & s_{23}c_{13} \\ s_{12}s_{23} - c_{12}c_{23}s_{13}e^{i\delta_{CP}} & -c_{12}s_{23} - s_{12}c_{23}s_{13}e^{i\delta_{CP}} & c_{23}c_{13} \end{bmatrix} \end{aligned} \quad (9)$$

where c_{ij} denotes the cosine of the mixing angle θ_{ij} between the mass eigenstates i and j , s_{ij} denotes the sine of θ_{ij} and δ_{CP} the CP violating phase. CP violation in the neutrino sector has not yet been observed. Current best estimates of θ_{ij} from global fits have a precision better than 15% with θ_{23} having the largest uncertainty. The current best values are summarized in reference [32].

A neutrino evolves in time by the wave function of the mass eigenstates:

$$|\nu_\alpha(t)\rangle = \sum_i U_{\alpha i} \exp^{-iE_{\nu_i}t/\hbar} |\nu_i\rangle \quad . \quad (10)$$

In a two flavor scenario the probability of finding back an electron neutrino after a given time t is [37]:

$$P_{\nu_e \rightarrow \nu_e}(t) = \langle \nu_e | \nu_e \rangle = |U_{e1}|^2 + |U_{e2}|^2 + 2|U_{e1}||U_{e2}|\cos\left(\frac{(m_{\nu_1}^2 - m_{\nu_2}^2)c^4}{\hbar pc^2}ct\right) \quad . \quad (11)$$

As can be seen from Eq. 11, the oscillation probability is proportional to the mass square difference $\Delta m_{21}^2 = (m_{\nu_1}^2 - m_{\nu_2}^2)$. As a consequence, only mass differences can be determined by observing neutrino oscillations. The distance traversed during one period is called oscillation length L and amounts to:

$$L = 2\pi \frac{\hbar p}{\Delta m_{21}^2 c^2} \quad . \quad (12)$$

The current estimates of the matrix elements of the PMNS matrix and the CKM matrix are shown in Fig. 4. As can be seen from Fig. 4, the off-diagonal matrix elements are much larger for the PMNS matrix, causing more mixing between the flavor eigenstates compared to the quark sector.

1.2.2 Neutrino interactions with matter

Neutrinos interact with matter via gravitation and the weak interaction. Weak interactions are mediated via one of two force carriers referred to as W and Z boson. The W boson is electrically charged while the Z boson is electrically

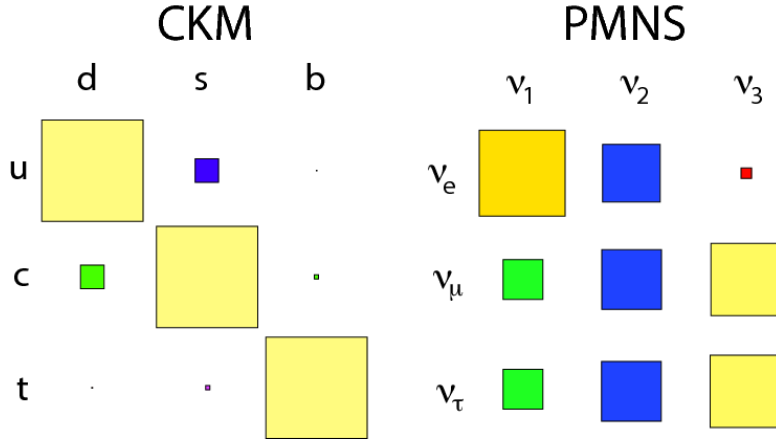


Figure 4: Visual representation of the size of the matrix elements in the two mixing matrices for quark (CKM) and neutrino (PMNS) flavors respectively; the size of the square represents the likeliness of mixing between two states; taken from [38].

neutral. Although the coupling strength of the weak force is comparable to that of the electromagnetic force, the mass of the mediator particles ($M_{W^\pm} \simeq 80 \text{ GeV}$ and $M_Z \simeq 91 \text{ GeV}$) causes the interaction cross sections to be much smaller than that of the electromagnetic force. Hence, the name weak interaction.

Depending on the energy of the neutrino, different interaction modes contribute to the cross section. Below 1 GeV quasi-elastic scattering (QES) dominates; around 1 GeV quasi-resonant scattering (QRS) has a significant contribution; and above 5 GeV deep inelastic scattering (DIS) dominates [39]. The measured cross sections are shown in Fig. 5. The three interaction modes can be differentiated by the state of the nucleus (nucleon) after the interaction. In QES, a single nucleon is kicked out of the nucleus. In QRS, the struck nucleon gets excited (typically Δ -resonance). In DIS, the momentum transfer is so large that the struck nucleon fragments into many particles (mainly light hadrons).

In addition to these different modes, weak interactions can be differentiated in charged current (CC) and neutral current (NC). The exchanged mediator boson is then a W^\pm or Z , respectively. While the NC interaction only transfers momentum and energy, the CC interaction also transfers charge. As a consequence, the neutrino is converted into its corresponding charged lepton. Hence, the outcome of CC interactions differs between neutrino flavors while outcome of the NC interactions does not.

When neutrinos interact with matter they either interact with a nucleon or an electron. With one exception discussed below, the neutrino-nucleon interaction is dominant for all flavors and energies considered in this work.

Measurements of the neutrino-nucleon cross section have been performed since high-luminosity neutrino sources became available and are still performed today [8]. Neutrino beams typically run up to energies of hundreds of GeV. The DIS cross sections can, however, accurately be extrapolated using the precise knowledge of the nucleon structure functions [40]. The main uncertainty in the neutrino-nucleon cross section is then caused by the uncertainties of the parton

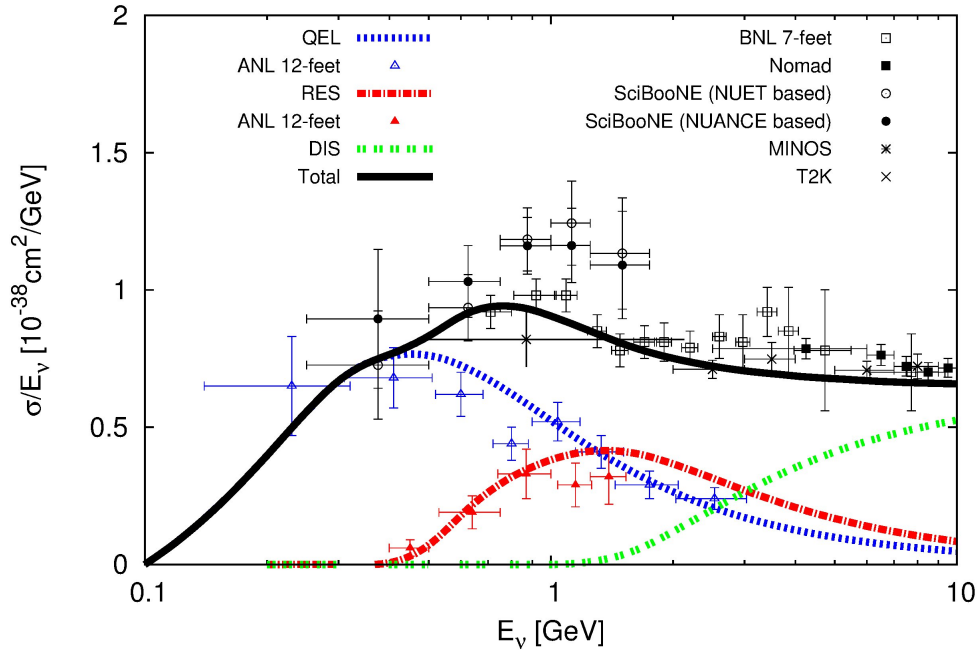


Figure 5: Measured muon neutrino-nucleus cross sections as a function of neutrino energy as taken from [39] (points); the curves correspond to fits of certain models to the data.

distributions. Currently, reliable estimations up to neutrino energies of 10^7 GeV can be made [41]. The resulting neutrino-nucleon cross sections for CC and NC muon neutrino interactions are shown in Fig. 6. As can be seen from Fig. 6, the cross section scales linear with the energy for energies up to 10^3 GeV and is proportional to $E^{0.4}$ at higher energies. This change in dependence is caused by the Z and W boson masses. Neutral current cross sections are about a factor five smaller than the CC cross sections. Anti-neutrino cross-sections are around a factor two lower than those of neutrinos for energies below 100 GeV or so, due to the contribution of valence quarks.

The cross section for a 100 TeV neutrino translates to an interaction length of $250 \times 10^3 \text{ kg cm}^{-2}$. For water this equals to a depth of $2.5 \times 10^6 \text{ km}$. Since the average density of Earth is about 5.5 times higher than that of water this translates to an interaction length significantly smaller than Earth's diameter ($7.9 \times 10^6 \text{ m}$) thereby making the Earth opaque for high energy neutrinos.

The Earth is not completely opaque for all neutrino flavors. Of the two neutrino interactions, the CC is the one which transforms the neutrino into a charged lepton. The CC interactions of the tau neutrino flavor, discussed in more detail below, produce a tau which rapidly decays into a tau neutrino and other particles. This effect is called "tau regeneration" and allows a certain fraction of tau neutrinos to traverse Earth. Since the cross-section increases with energy and every interaction reduces the energy of the daughter tau neutrino, the energy loss increases with initial neutrino energy. For more details see Chap. 3.1.1.

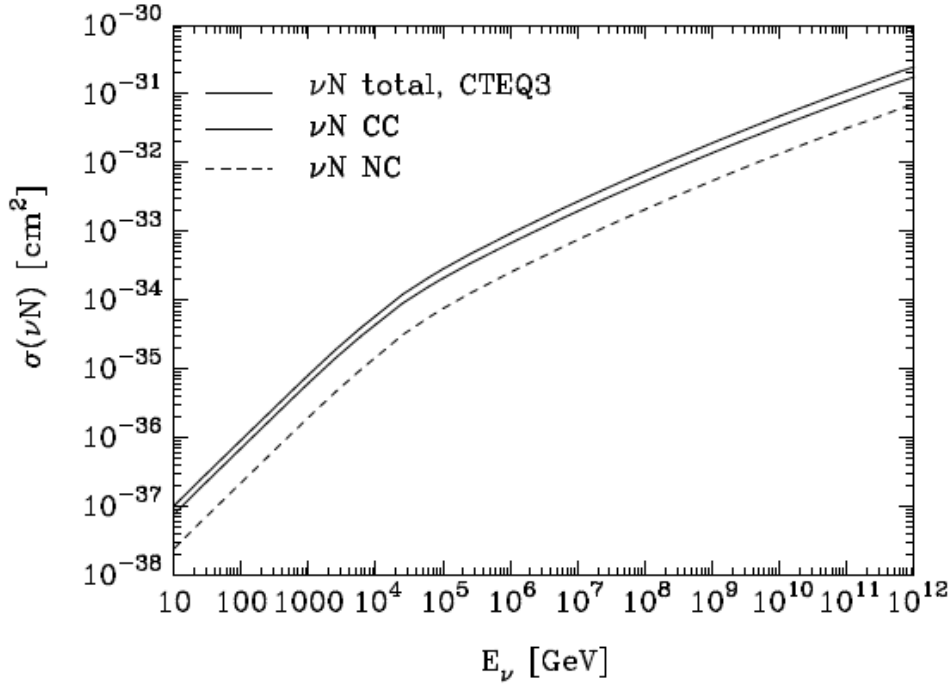


Figure 6: Calculated muon neutrino-nucleon cross section for DIS as taken from [41].

The Glashow Resonance

The neutrino-electron cross section gets much larger for anti-electron neutrinos around an energy of 6.3 PeV [42]. At that energy, the W boson can resonantly be produced: $\bar{\nu}_e + e^- \rightarrow W^-$. The effect was first studied by S. Glashow in 1960 and is consequently named the Glashow resonance.

The shape is well described by a Breit-Wigner function [43] with a width of around PeV. An illustration of the Glashow resonance is shown in Fig. 7. As can be seen from Fig. 7, the neutrino-electron cross sections is about 300 times larger than the neutrino-nucleon cross section at the resonance.

The produced W^- boson has a branching ratio to decay into hadrons of about 68% and roughly 11% per flavor to decay into leptons. In the case of a hadronic decay, essentially all energy is deposited in the medium. This mimics a NC interaction in which all energy is transferred to the target. In the case of a leptonic decay, the produced neutrino takes away a substantial amount of energy. This mimics a CC interaction in which some energy is transferred to the target. For example, in the case of the W decaying into an electron, the average deposited energy is 1.57 PeV [43].

Neutrino oscillations in matter: The MSW effect

So far, only neutrino oscillations in vacuum have been considered. Neutrino oscillations are changed when neutrinos propagate through matter, as a direct result of the interactions between neutrinos and matter. The abundance of electrons in normal matter allow for the electron neutrino to interact via CC

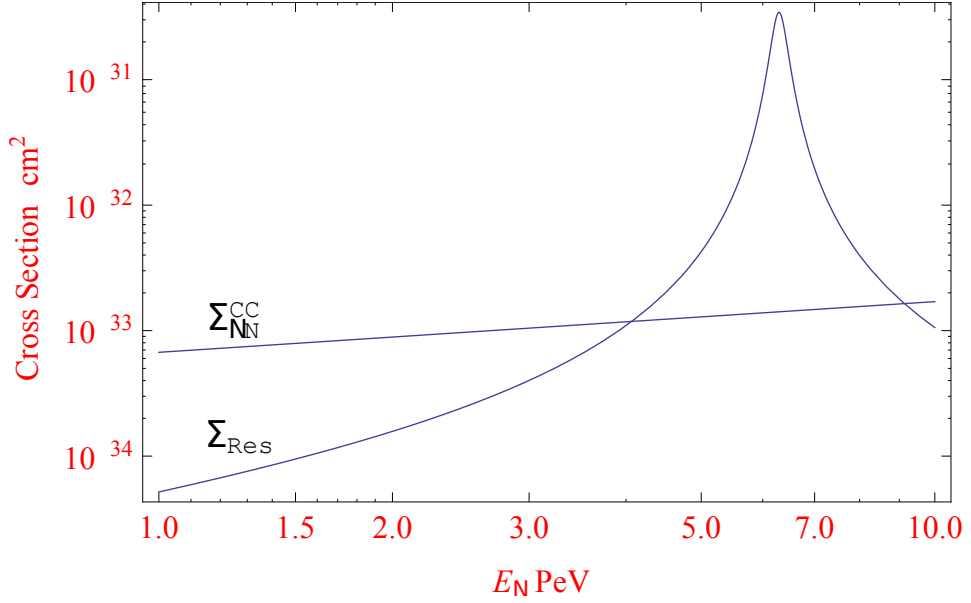


Figure 7: Theoretical predictions of the Glashow resonance cross section (Σ_{res}) and the CC neutrino-nucleon cross section ($\Sigma_{\text{NN}}^{\text{CC}}$) as taken from [43].

and NC while maintaining its initial state. This is not the case for muon and tau neutrinos or anti-neutrinos, which can only interact with the electrons via the NC while maintaining the initial state. This asymmetry was first pointed out by Mikhaev, Smirnov and Wolfenstein and was subsequently named the MSW effect [44, 45].

In a two flavor neutrino scenario the vacuum oscillation is described by the Hamiltonian:

$$H_V = \frac{\Delta m^2}{4E} \begin{bmatrix} -\cos(2\theta) & \sin(2\theta) \\ \sin(2\theta) & \cos(2\theta) \end{bmatrix}, \quad (13)$$

in analogy with Eq. 9. In matter, the MSW effect gives rise to an additional potential of $V = \pm\sqrt{2}G_F N_e$ where \pm corresponds to neutrino/anti-neutrino, G_F is the Fermi constant and N_e is the electron number density. This potential only effects the electron neutrinos. This causes the Hamiltonian in matter to change to:

$$H_M = \frac{\Delta m^2}{4E} \begin{bmatrix} -\cos(2\theta) + A & \sin(2\theta) \\ \sin(2\theta) & \cos(2\theta) - A \end{bmatrix}, \quad (14)$$

with $A = 2EV/\Delta m^2$. This effectively causes the apparent mixing angle of neutrinos in matter to change [46].

1.2.3 Neutrino sources

In this section the different sources and their relevance to neutrino astronomy are summarized. The discussion focuses on the most prominent sources.

Geoneutrinos: The term geoneutrino refers to all neutrinos produced in the Earth. Most of the geoneutrinos are produced in β^- decays of the nuclides ^{40}K , ^{232}Th and ^{238}U . These are anti-electron neutrinos with a maximum energy of a few MeV. These neutrinos are not considered in this work.

Reactor neutrinos: Neutrinos generated in nuclear fission reactors are the main source of man made neutrinos. The bulk of reactor neutrinos get produced in the β^- decay of the daughter nucleus resulting from the fission. These are anti-electron neutrinos. Reactor neutrinos have been used to study neutrino oscillations [47] but are not part of this thesis.

Atmospheric neutrinos: Interactions of cosmic rays in the Earth's atmosphere produce mainly charged pions and kaons. Both can decay into charged leptons and neutrinos. Their finite lifetime gives rise to a large flux of neutrinos which is commonly referred to as atmospheric neutrinos. The energy spectrum of the atmospheric neutrino flux is steeper than that of the cosmic rays because the pions and kaons can interact with the atmosphere before they decay. Depending on the energy involved, also muons produced by the decay of pions and kaons can decay before hitting the Earth, thereby producing neutrinos as well.

For initial cosmic ray energies in excess of 1 TeV, the production of charmed mesons becomes significant. These charmed mesons have much shorter lifetimes than pions and kaons. As a consequence, the neutrinos produced in the decays of charmed mesons maintain the cosmic ray energy spectrum to a large extent. Due to the rapid decay of the charmed mesons, these neutrinos are referred to as "prompt neutrinos".

The prompt neutrino flux is poorly constrained by experimental data. To date, the best measurement is performed by IceCube [48]. Although understanding of the prompt flux may be limited, it can safely be assumed that the fraction of tau neutrinos is at least one order of magnitude below that of the other flavors, as charmed mesons heavy enough to decay into tau leptons are produced at a significantly lower rate [49].

The flux of atmospheric muon and electron neutrinos was measured by Antares [50] and IceCube [51, 52]. See Fig. 8 for an overview. For neutrino astronomy, atmospheric neutrinos constitute an important background.

Solar neutrinos: The sun is known to be a powerful source of neutrinos. The model to describe the sun and the processes taking place inside it is called the Standard Solar Model (SSM) [53]. In the SSM, the various reaction chains that fuel the sun and produce neutrinos are included. The main reaction is the fusion of four protons into a helium nucleus. The different processes and their fluxes as a function of energy are shown in Fig. 9. Also, solar neutrinos are not a part of this work.

Cosmic neutrino background: Following Big Bang cosmology, a cosmic neutrino background should be present anywhere in the Universe. These are neutrinos which decoupled from matter about 1 second after the Big Bang [55]. The expansion of the Universe cooled the cosmic neutrino background to a temperature of about 1.95 K (or 16.81×10^{-5} eV). The expected density is about 340 neutrinos per cm^3 . The CNB is not part of this work.

Cosmic neutrino sources: Cosmic neutrinos originate somewhere in the cosmos, beyond our solar system. Due to the distinction of cosmic rays into galactic and extra-galactic, cosmic neutrinos are commonly distinguished the same way. To date, no sources of cosmic neutrinos have been discovered with the exception of Supernova SN1987A. Nonetheless, possible galactic sources have

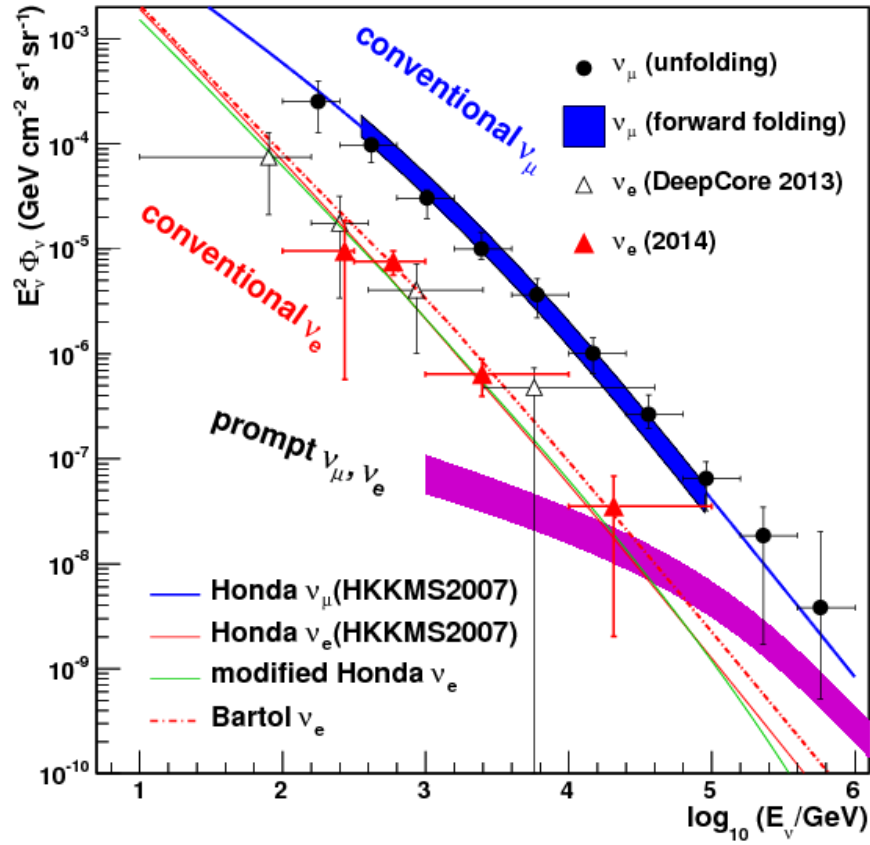


Figure 8: Atmospheric neutrino fluxes as measured by IceCube in [51] together with theoretical calculations.

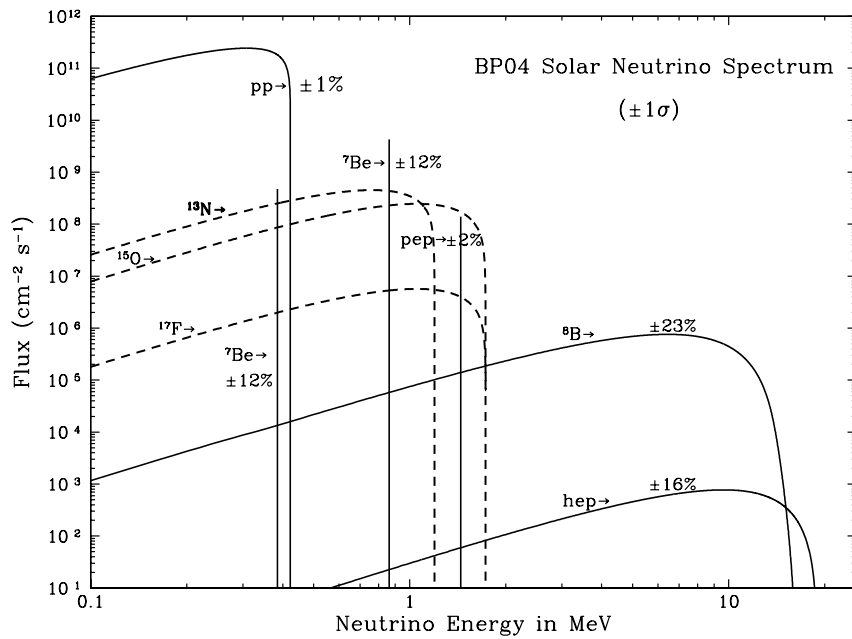


Figure 9: Flux of solar electron-neutrinos as predicted by the BBP04 solar model. Taken from [54].

been identified by gamma ray observations [56]. Based on these observations, three candidate galactic sources have been identified with a neutrino flux large enough to be detected, namely SNRs, RX J1713.7-3946 and RX J0852.0-4622, and one Pulsar Wind Nebula, Vela X. Uncertainties remain regarding the correlation between the observed gamma flux and the assumed neutrino flux of these sources, as different production mechanisms yield different results. Also, extragalactic sources could produce neutrinos. Since neutrinos are not deflected by magnetic fields, their detection could pinpoint the origin of cosmic rays. The majority of cosmic neutrinos are expected to originate from pion and kaon decays in the vicinity of the source, following the same reasoning as for atmospheric neutrinos. Since the matter density may be lower than that in the Earth's atmosphere, the energy spectrum of cosmic neutrinos is generally believed to follow that of cosmic rays.

For all cosmic neutrinos, different scenarios for the flavor composition at the source exist. The standard scenario assuming interactions in analogy to atmospheric neutrinos predict a flavor composition of $\nu_e : \nu_\mu : \nu_\tau = 1 : 2 : 0$ which results from decays of the charged pions, kaons and muons. The two most-important different scenarios are the so-called muon-damped and neutron-beam sources [57]. For the muon-damped scenario it is assumed that the muons from the pion decay lose most of their energy in the matter surrounding the source before they decay. As a result, the daughter neutrinos from these muon decays have such low energies that their flux can safely be neglected. Consequently, the flavor composition at the source is $\nu_e : \nu_\mu : \nu_\tau = 0 : 1 : 0$. For the neutron-beam, it is assumed the neutrinos then are produced from neutron decays leading to flavor composition at the source of $\nu_e : \nu_\mu : \nu_\tau = 1 : 0 : 0$ of purely anti-electron neutrinos. The neutrino flavor ratios at the source translate to a certain flavor ratio at Earth since the neutrinos oscillate during their propagation through the Universe. On average, the three discussed source models roughly oscillate into a flavor ratio at Earth of $\nu_e : \nu_\mu : \nu_\tau \simeq 1 : 1 : 1$. Using a full flavor oscillations calculation (assuming inverted mass hierarchy [58]), the different source flavor compositions translate to different compositions on Earth: $1 : 2 : 0 \rightarrow 0.93 : 1.05 : 1.02$ (pion-decay), $0 : 1 : 0 \rightarrow 0.19 : 0.43 : 0.38$ (muon-damped) and $1 : 0 : 0 \rightarrow 0.55 : 0.19 : 0.26$ (neutron-decay) [59]. It should be noted, that although no source scenario initially produces tau neutrinos, due to the neutrino oscillations, tau neutrinos are expected at Earth for any source composition.

In addition to the flavor composition, cosmic neutrinos also have a mixture of neutrinos and anti-neutrinos. A mechanism for an asymmetric mixture is the imbalance between matter and anti-matter present in the Universe and in the composition of cosmic rays. For a specific model, the resulting flavor compositions for neutrinos and anti-neutrinos at Earth are: 14:11:11 for neutrinos and 4:7:7 for anti-neutrinos [60].

1.2.4 *Neutrino telescopes*

The detection technique employed by cosmic neutrino telescopes to date was proposed by Moisey Markov in 1960 [61]: He suggested to detect Cherenkov radiation from the products of a neutrino interaction (see Sec. 1.2.4.1) in a suitable medium. As these reactions can produce large signatures, cosmic neutrino telescopes instrument up to cubic kilometers of a medium. Neutrino telescopes are usually located deep under ground (or water), in order to shield them from the background of atmospheric muons produced above the telescope. For the detection of the Cherenkov photons photomultiplier tubes are used (see Sec. 2.3).

The first experiment following this approach was the DUMAND experiment off the coast of Hawaii. Due to technical difficulties the project was cancelled in 1995 [62]. Following a series of pioneering projects, the world wide efforts now concentrate in the IceCube project at the South Pole [63], the GVD project in lake Baikal [64, 65] and the Antares [66] and KM₃NeT [67] projects in the Mediterranean Sea.

These projects are united in a umbrella organization called the Global Neutrino Network (GNN) [68]. The GNN aims at combining the efforts of all neutrino telescopes in order to develop a coherent strategy and promote an exchange of ideas among them.

Since this work is made for the KM₃NeT experiment, in the following the most important aspects of detecting neutrino interactions in water are discussed.

1.2.4.1 *Cherenkov Radiation*

Cherenkov radiation is named after the Russian scientist Pavel Cherenkov who was the first to study the process in 1933 [69]. Together with theoreticians Il'Ja Frank and Igor Tamm, Cherenkov was awarded the Nobel Prize in 1958 [70]. Cherenkov radiation occurs when a charged particle moves through a transparent medium with a speed exceeding the speed of light in that medium. This causes the medium to be asymmetrically polarized with respect to the particle trajectory which gives rise to a changing dipole moment causing the radiation. Properties of the Cherenkov radiation such as the speed threshold and the radiation angle are governed by the refractive index of the medium. The phase velocity of light v in a medium is given by:

$$v = c/n \quad , \quad (15)$$

where c is the speed of light in vacuum and n the refractive index of the medium. The angle of the emitted light with respect to the charged particle trajectory is given by:

$$\cos \theta_C = \frac{1}{n\beta} \quad ,$$

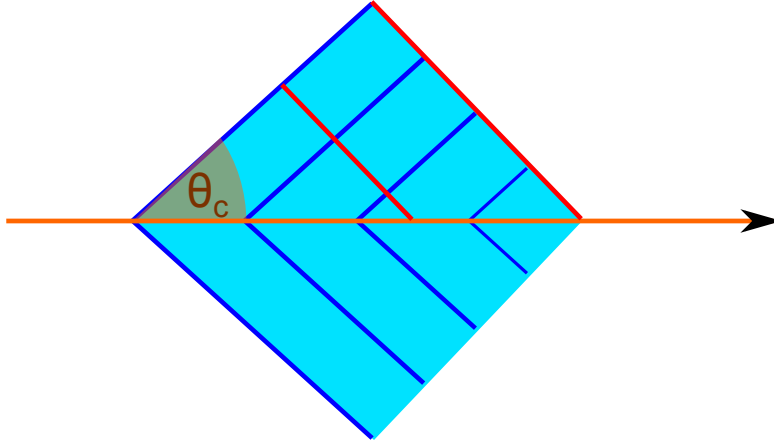


Figure 10: A sketch of a charged particle (orange line) traversing water. The resulting Cherenkov cone emitted at θ_c ; the dark blue lines indicate single photon trajectories and the red lines indicate the surface crossed by these photons at equal times.

where θ_c is the angle of emittance and β the speed of the charged particle (relative to the speed of light in vacuum). The frequency spectrum is described by the Frank-Tamm formula [71]:

$$\frac{d^2E}{d\omega dx} = \frac{q^2}{4\pi} \mu(\omega) \omega \left(1 - \frac{c^2}{v_p^2 n^2(\omega)} \right) ,$$

where ω is the frequency, q is the electric charge of the particle, $\mu(\omega)$ and $n(\omega)$ are the frequency dependent permeability and index of refraction of the medium. The number of emitted photons per unit track length x and wavelength λ are given by:

$$\frac{d^2N}{d\lambda dx} = \frac{2\pi q^2}{\lambda^2} \alpha \sin^2(\theta_c) ,$$

where $\alpha = 2\pi e^2/\hbar c$ and e is the unit electric charge.

For typical conditions found in the abyss of the Mediterranean Sea this results in a Cherenkov angle of $\theta_c = 42.2^\circ$ and a wavelength range from 350 nm to 550 nm. A sketch of a charged particle traveling through water and the resulting Cherenkov cone is depicted in Fig. 10.

1.2.4.2 Light propagation in water

While the photon phase velocity determines the Cherenkov angle, the photons actually propagates at a speed equal to the group velocity. The refraction indices of group and phase velocity n and n_g both depend on the wavelength. The values for KM₃NeT are shown in Fig. 11.

While propagating through water, light will undergo scattering and absorption. Scattering describes the process of a photon changing its direction whereas absorption describes the disappearance of a photon. Both effects depend on the

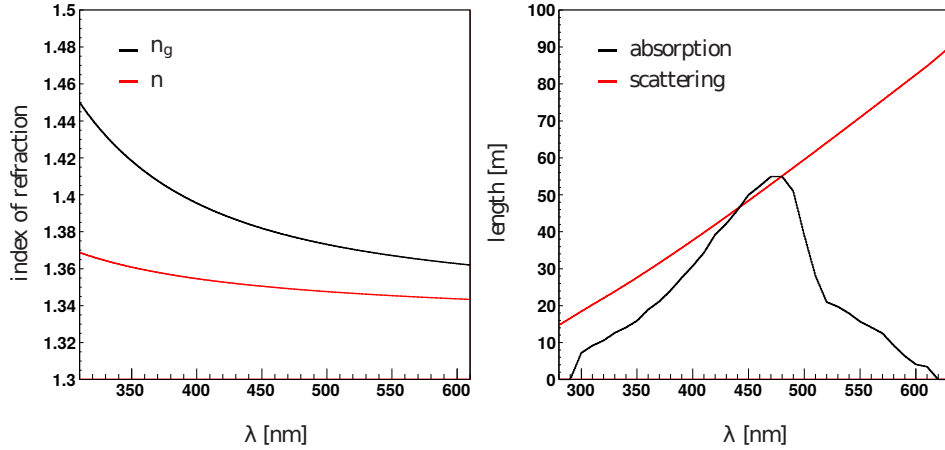


Figure 11: Indices of refraction (left), absorption length (right) and scattering length (right) as a function of the wavelength of the light for KM₃NeT water taken from [72].

wavelength of the light. The probability for such a process to happen can be expressed in form of a length. The typical scattering and absorption lengths of KM₃NeT are shown in Fig. 11.

In the deep waters of the Mediterranean Sea, the light scattering is very forward peaked. The average cosine of the scattering angle is around $\cos(\theta_c) = 0.9$. For KM₃NeT, recent simulations indicate that direct and single scattered light constitute the dominant signal [73].

1.2.4.3 Detection Signatures

The different neutrino flavors in combination with the different weak interaction modes lead to distinct signatures in the detector. All neutrino interactions are a combination of two signatures, namely: shower and track. In the following, first the shower and track signatures are discussed. This is followed by a description of the NC and CC interactions in terms of combinations of track and shower signatures.

Track Signature

A track signature corresponds to a single charged particle that traverses the medium producing Cherenkov light on its way. At the energies under consideration, the only particle with a sufficiently long lifetime and mean free path are muons. Therefore, the track signature usually refers to CC interactions of muon neutrinos. Muons with an energy of a TeV or higher have their lifetime significantly prolonged to travel for kilometers through water at the speed of light. During their flight, muons can lose energy due to Bremsstrahlung and other processes. Most of these processes will also lead to the production of Cherenkov light thereby contributing to the detectable signal. Due to momentum conservation, these photons are emitted at an angle close to the Cherenkov angle with respect to the muon direction. The total signal of a muon is there-

fore primarily observed at the Cherenkov angle with respect to its path with contributions at different angles.

Shower Signature

A shower signature corresponds to a multitude of charged particles which each produce Cherenkov light. A particle shower can be caused by an initial particle which via a decay or interaction produces other particles. In this process, energy is converted to mass. The particles produced can subsequently decay or interact, thereby producing even more particles. This avalanche comes to a halt once the energy of the particles is too low to produce new particles. The typical length of a shower is governed by the energy and type of the initial particle. The logarithm of the initial energy correlates with the number of steps, due to the iterative nature of the process. The typical length of each interaction step is governed by the different mean free paths of the particles.

One important characteristic of a shower is the shower maximum, which is defined as the point in the shower evolution where the largest amount of particles exist. For an initial electron, the position of the shower maximum and light emission profile for a given initial energy is shown in Fig. 12 [74]. The distribution for hadronic showers is similar, but typically 1 m shorter. This can be explained by the larger average mass of hadrons compared to that of an electron and the difference in interaction length. At a given energy, the amount of photons produced by a hadronic shower is typically 80 % of the amount of light produced by an electromagnetic shower. While the length and total amount of photons may be different, the emission profiles are very similar.

The distribution of emission angles for showers is well described by the distribution shown in Fig. 13 independent of the shower energy [75]. The figure shows a broad distribution of emission angles, which can be attributed to the spread in directions of the particles. Due to momentum conservation, a majority of photons is still emitted at the Cherenkov angle.

Neutral Current Interaction Signatures

In a NC interaction, a Z boson is exchanged between the neutrino and a nucleon. In the process, the neutrino transfers momentum and energy to the nucleon and continues thereafter. In the absence of interference terms, the NC interaction does not distinguish between neutrino flavors. At energies of interest, the interaction causes the nucleon to fragment (DIS), resulting in a hadronic shower. A diagram of the NC interaction is shown in Fig. 14a.

Charged Current Interaction Signatures

In a CC interaction a W^\pm boson is exchanged between the neutrino and the nucleon. Since the W boson is electrically charged, the conservation of charge and lepton number causes the neutrino to transform into its corresponding charged lepton. This causes the detector signatures of the electron, muon and tau neutrinos to differ. As for the NC interaction, the nucleon with which

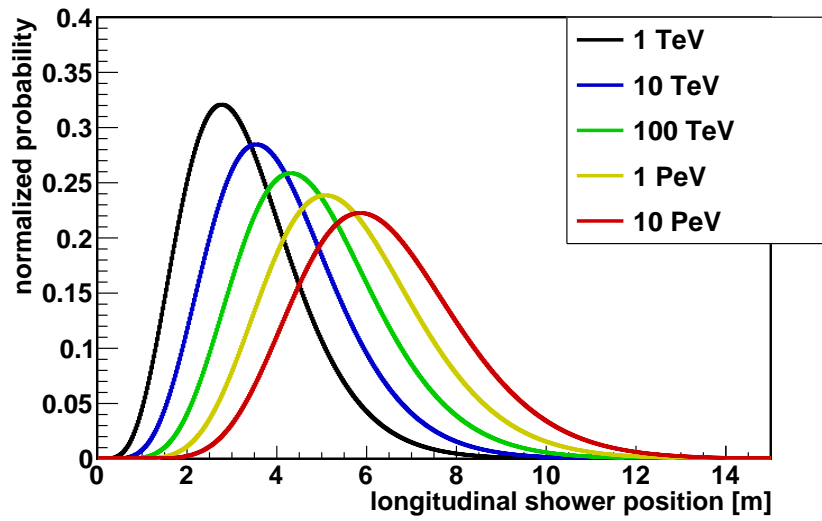


Figure 12: Longitudinal electromagnetic shower emission profiles for different initial electron energies; the shower maximum corresponds to the point with the maximal probability.

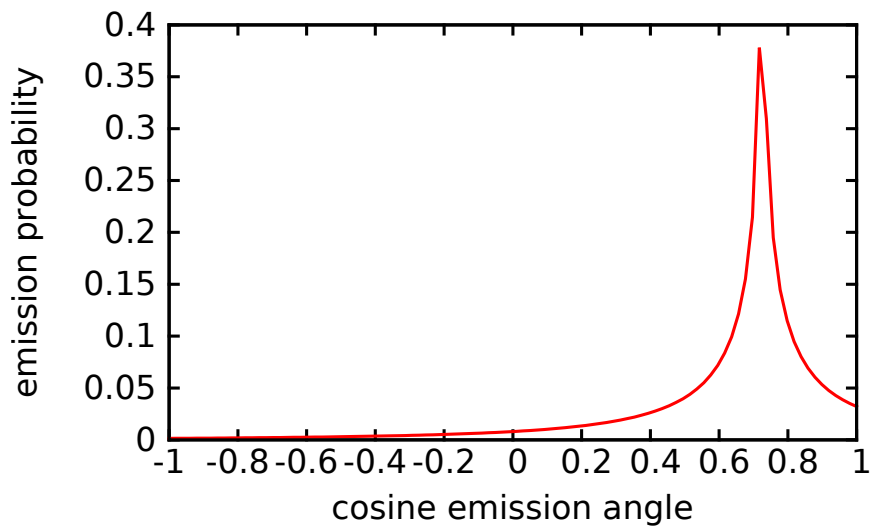


Figure 13: Photon angular emission profile independent of shower energy.

the neutrino interacts gets fragmented, producing a hadronic shower at the interaction vertex.

Electron neutrino: Electrons have a short mean free path length in water, which leads to an electromagnetic shower. As a result, the hadronic and electromagnetic shower overlap. Therefore, electron neutrino CC interactions have a signature of a single shower event similar to NC interactions. See Fig. 14b for a diagram.

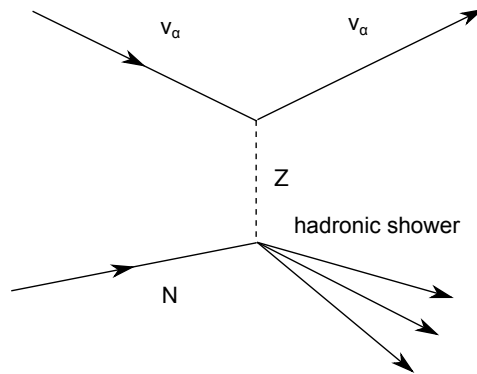
Muon neutrino: Muons have a much longer mean free path compared to electrons due to their larger mass ($\approx 200 \times m_e$), which suppresses electromagnetic interactions with the medium. This leads to a signature with a hadronic shower and a track. See Fig. 14c for a diagram.

Tau neutrino: Taus have an even larger mean free path due to their immense mass ($\approx 9 \times m_\mu$). However, their lifetime of 290.6×10^{-15} s is seven orders of magnitude smaller than the muon lifetime, causing them to rapidly decay. Only at high energies the tau lepton can travel visible distances thanks to relativistic time dilation (at $E_\tau = 1$ PeV the tau mean lifetime corresponds to a flight length of about 50 m). Tau neutrino CC interactions can lead to different signatures due to the various tau lepton decay modes: In 17.4 % of the cases the tau decays into a muon which appears as a track. This interaction is called the “Sugar Daddy” signature, see Fig. 14e for a diagram. The remaining tau decay modes (83.6 %) cause either an electromagnetic or hadronic shower at the tau decay position. These events have therefore two showers: the hadronic shower at the neutrino interaction vertex and a second shower at the tau decay position. Different from the electron neutrino interaction, these can be separated by visible distances. Therefore, the double shower nature gives rise to the name of “Double Bang” events. See Fig. 14d for a diagram.

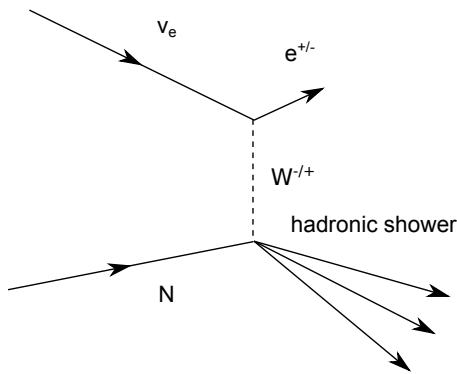
Neutrino flavor identification in a neutrino telescope

Identifying the neutrino flavor of a detected interaction with a neutrino telescope opens up new measurements opportunities and enhances background suppression. Currently, neutrino telescopes categorize events in two classes: tracks and showers. This does not yield an actual flavor reconstruction because NC interactions are classified as shower events for all flavors and tau CC interactions can fall into either category.

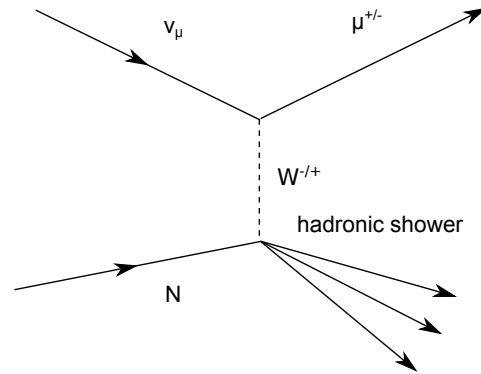
Certain CC interactions allow for a flavor identification. For example, the “Double Bang” interaction for tau flavors is unambiguous, allowing for a clean tau flavor identification. As stated earlier, tau neutrinos have low atmospheric backgrounds compared to the other flavors. An ideal full three flavor identification allows to determine the flavor composition at the source of cosmic neutrinos.



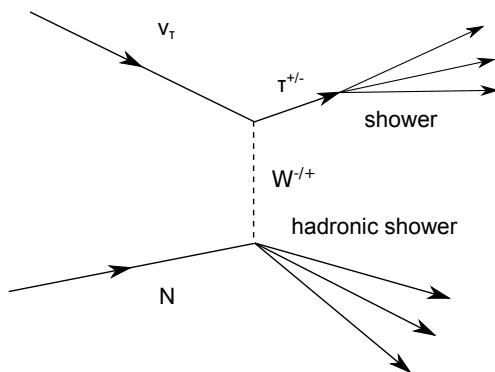
(a) Neutral current interaction for all three neutrino flavors.



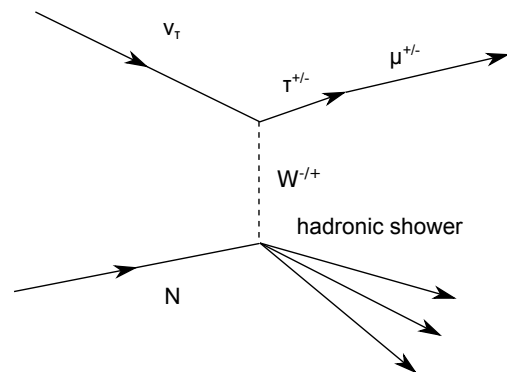
(b) Charged current interaction for electron neutrinos causing an electromagnetic shower.



(c) Charged current interaction for muon neutrinos lead to a muon track.



(d) Charged current interaction for tau neutrinos with the tau decaying to an electron or hadrons leading to a second shower.



(e) Charged current interaction for tau neutrinos with the tau decaying to a muon (neutrinos neglected).

Figure 14: Diagrams for the different neutrino interactions in water; no distinction made between neutrino and anti-neutrino (all denoted ν).

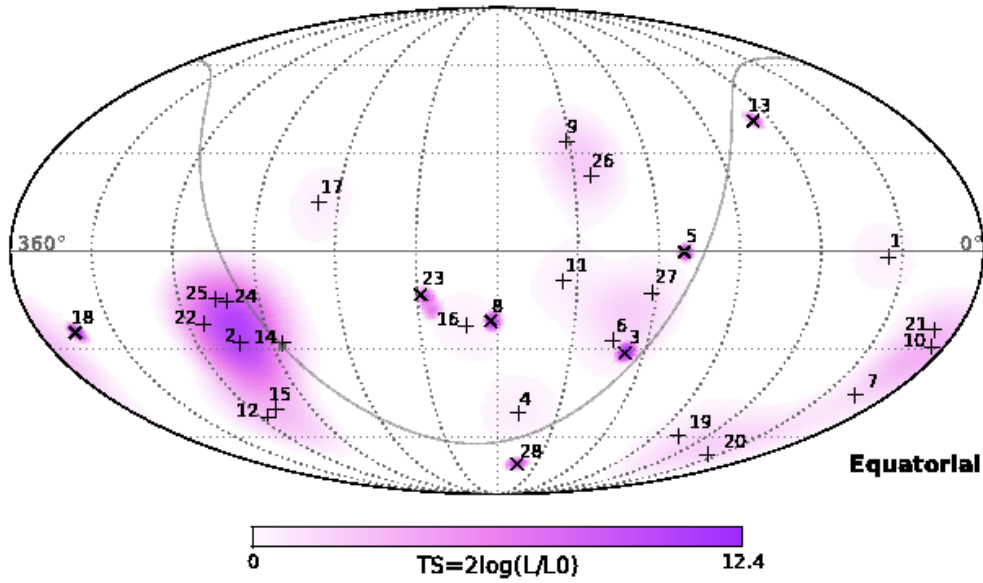


Figure 15: Skymaps of IceCube flux neutrinos; Vertical crosses (+) denote shower-like events and angled crosses (x) denote track-like events; As measured in 2013 [80].

1.2.5 Cosmic neutrino observations: SN1987 and the IceCube flux

So far, two observations of neutrinos of cosmic origins have been made, namely supernova SN1987A and the excess of high energetic neutrinos by IceCube in 2013.

In 1987 the star Sanduleak in the Large Magellanic Cloud core-collapsed into a supernova. The supernova was around 51 kpc away and visible by the naked eye. It was the closest observed supernova since 1604 and therefore the first opportunity for modern astronomy to study a supernova in detail. About a decade before SN1987A, the first large neutrino detectors Kamiokande-II and IMB were put into operation. Together these experiments detected 20 neutrino interactions within 13 s of SN1987 [76, 77]. These observations allowed further insights into the mechanisms of core-collapses and neutrino related alternative theories [78].

In November 2013 the IceCube collaboration announced the detection of two neutrino interactions of around 1 PeV energies [79]. Within the same year a follow up analysis of a two year data set yielded another 26 events between 30 TeV to 1200 TeV [80]. Together, these 28 neutrinos were inferred to be of cosmic origin as they were with 4σ significance incompatible with the atmospheric background. Of these initial 28 neutrino events, 21 are shower-like and 7 track-like events. The events are shown in Fig. 15. Today, no point-source(s) could be identified, possibly due to the poor angular resolution for shower events.

The latest results include an all sky search performed for so-called high energy starting events (HESE). These events are required to have their neutrino

vertex in the inner part of the detector volume and to have a deposited energy of at least 60 TeV in that volume. By limiting the volume to an inner part, the outer edge of the detector can be used for suppressing the atmospheric background, hence making an all sky search possible. The selection leaves 32 events in 4 years of IceCube data of which 8 are track-like and the rest shower-like, with 22 from the southern sky (4 tracks). The current best flavor fit of the IceCube results are in agreement with a $\nu_e : \nu_\mu : \nu_\tau$ flavor ratio of 1 : 1 : 1. Due to low statistics and the lack of a powerful tau neutrino identification, the flavor ratio fits are still unprecise.

The present observations do not yield in a definite result for the cosmic neutrino flux. Corresponding to the cosmic ray flux, the neutrino flux can be described by a normalization Φ and a spectral index Γ . The results of the different analysis assuming a constant spectral index and no cut-off are summarized in Fig. 16. The fit results prefer a scenario with a cut-off at 3 PeV. Also other groups analyzed the IceCube data considering various spectral indices and cut-off scenarios but no clear answer could be found [60].

For the found spectral indices between $\Gamma = 2-2.8$ the lack of signals from the Glashow resonance indicates that the spectrum either has an energy cut-off somewhere between 3 PeV and 4 PeV, an asymmetry between electron and anti-electron neutrino flavors or a changing spectral index.

The presence of such a cut-off energy is in conflict with the absence of such a cut-off in the cosmic ray spectrum. This tension could be mended, as a recent analysis by IceCube indicates a 1.1σ difference between North-South directions compared to an isotropic flux [59]. Thereby indicating a possibly larger galactic flux component than assumed. Since for the galactic component, a cut-off at these energies is not so unlikely. Future measurements will help to scrutinize this possible asymmetry.

An asymmetry between the flux of electron and anti-electron neutrinos could be explained by certain cosmic ray interactions such as proton-photon interactions. The low statistics of PeV neutrinos make it currently impossible to reliably quantify such an asymmetry. While some sources may have a suitable mechanism to produce such an asymmetry it is not clear why this should be the case for all sources [60].

A change in spectral index (“broken power law”) allows for a softer spectrum for neutrino energies above 3 PeV, thereby effectively reducing the flux of neutrinos present at the Glashow resonance. Currently, none of the performed fits to the IceCube data significantly improve using various broken power laws. Consequently, the data does not indicate the broken power law scenario to be more probable than a single power law [60].

Of the three discussed scenarios, the existence of a cut-off energy in the spectrum seems to be most likely, as it slightly improves fit results.

In summary, there is a strong case for another large scale neutrino telescope. The KM3NeT experiment will measure the IceCube flux with a different methodology, improved resolutions and complementary field of view.

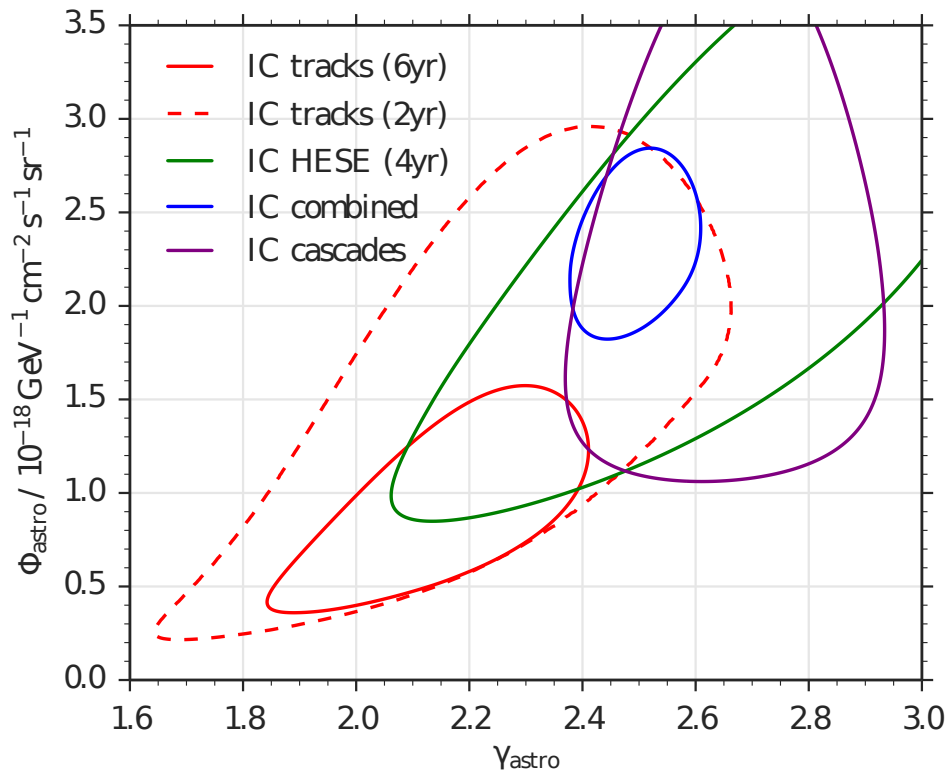


Figure 16: Results of different IceCube analysis measuring the astrophysical flux parameters Φ and Γ taken from [81]; lines show the 90% confidence areas intervals; γ_{astro} refers to the spectral index Γ and label cascades to shower signatures (see text).

THE KM₃NET DETECTOR

I know who I am. And after all
these years, there's a victory in
that

Rust Cohle, True Detective

In this chapter a brief description of the KM₃NeT detector is presented. For more details, the reader is referred to the KM₃NeT letter of intent [67].

The KM₃NeT detector consists of 2-dimensional arrays of detection units located in the Mediterranean Sea. Each detection unit holds the detection modules in place, which contain the photo-sensors and the electronics needed to detect the Cherenkov light from a neutrino interaction.

The main goals are to identify sources of cosmic neutrinos and to establish the neutrino mass hierarchy. To achieve these goals, the energy and direction of cosmic and atmospheric neutrinos should be measured. As these neutrinos have drastically different energies, different detector configurations are foreseen, namely: A high energy neutrino detector called ARCA and a low energy neutrino detector called ORCA. The distribution of modules in the ORCA detector will be much denser than in the ARCA detector.

A set of 115 detection units is called a building block. For KM₃NeT 2.0 three building blocks are planned: two ARCA blocks and one ORCA block. Currently KM₃NeT phase 1 is under construction, which will see 24 ARCA strings and 7 ORCA strings deployed. Since this work is dedicated to cosmic neutrino detection, this chapter will focus on the ARCA detector. In the following, an overview of the detection hardware and software will be given. In addition, the main background sources are discussed.

2.1 KM₃NET ARCA

The KM₃NeT ARCA telescope is designed to detect neutrinos with energies of TeV and beyond. Each ARCA block instruments a volume of around 0.5 km³ to efficiently detect the Cherenkov light produced by interactions of neutrinos with these energies. In order to instrument this volume, the horizontal distance between the detection units is set to about 90 m and the vertical distance between the modules is set to about 36 m. A top-view of detector is shown in Fig. 17. The location for the ARCA detector is at 36°16'0'' N and 16°6'0'' E at a depth of 3.5 km about 100 km southeast of the Sicilian coast.

The power and data transmission is provided via two electro-optical cables from a shore station at Capa Passero to the ARCA detector. The first cable was

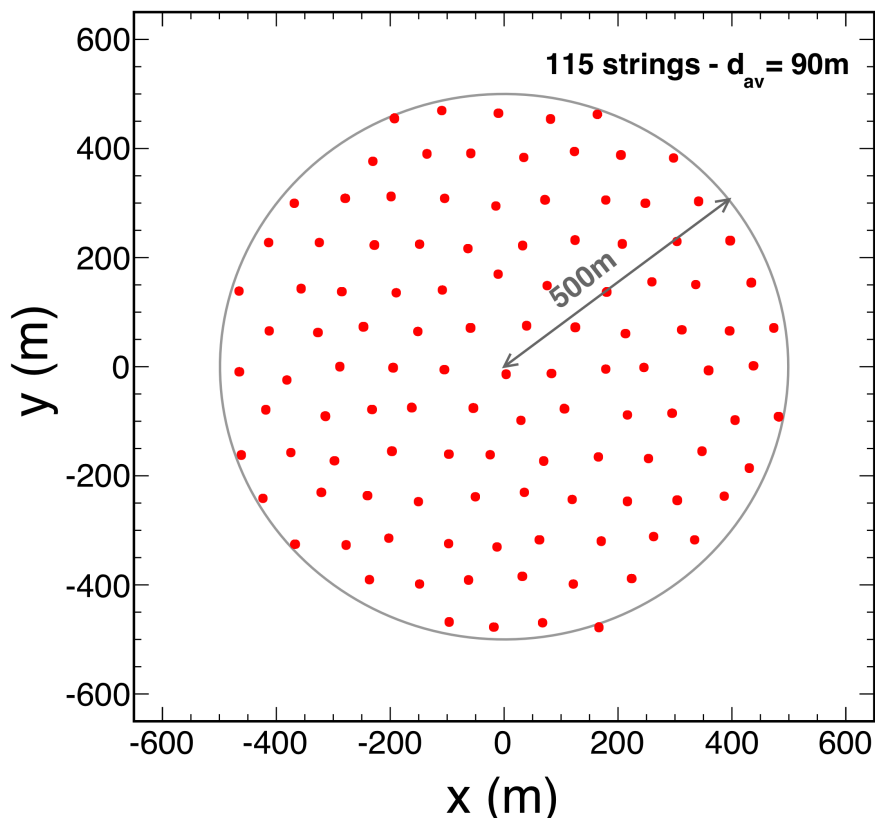


Figure 17: Top-view of an ARCA building block.

installed in December 2008, followed by a first junction box in the summer of 2015.

2.2 DETECTION UNIT

Each detection unit holds 18 modules. The lowest module is located at about 80 m above the sea floor. The modules are spaced 36 m in vertical direction, covering a total length of about 700 m. An additional buoy is mounted at the top. The mechanical backbone of the detection unit consists of two 4 mm thick ropes made out of Dyneema[®]. As these Dyneema ropes are flexible, the detection unit is commonly referred to as a “string” of modules. A drawing of a detection unit and a picture of a module are shown in Fig. 18.

The 18 optical fibers needed for the read-out and the two copper wires needed for the power supply are guided along the ropes in a pressure-balanced, oil-filled plastic tube. At each module, one optical fiber and two wires are branched out in a small box (black cylindrical shape on the photo in Fig. 18). They enter the glass spheres via a penetrator.

The string is anchored to the sea floor using a dead weight. The anchor contains an electronics container which interfaces each detection unit with the designated junction box.

For deployment, the strings are rolled up on a launcher vehicle as shown in Fig. 19. The launcher vehicle is a spherical metal frame which is temporarily



Figure 18: A drawing of KM₃Net detection units and a photo of a KM₃Net module attached to a string.

mounted onto the anchor. A picture of a string prototype on a launcher vehicle is shown in Fig. 19. The results obtained with this prototype are presented in Chap. 4. The string, launcher vehicle and anchor are lowered to the seabed using a mooring line from a surface vessel. Once in place, the launcher vehicle is released from the anchor. The string then unfurls while the launcher vehicle floats to the surface. The string stays upright thanks to the buoyancy of the modules and the additional buoy. The launcher vehicle rises all the way to the surface and is then recovered.

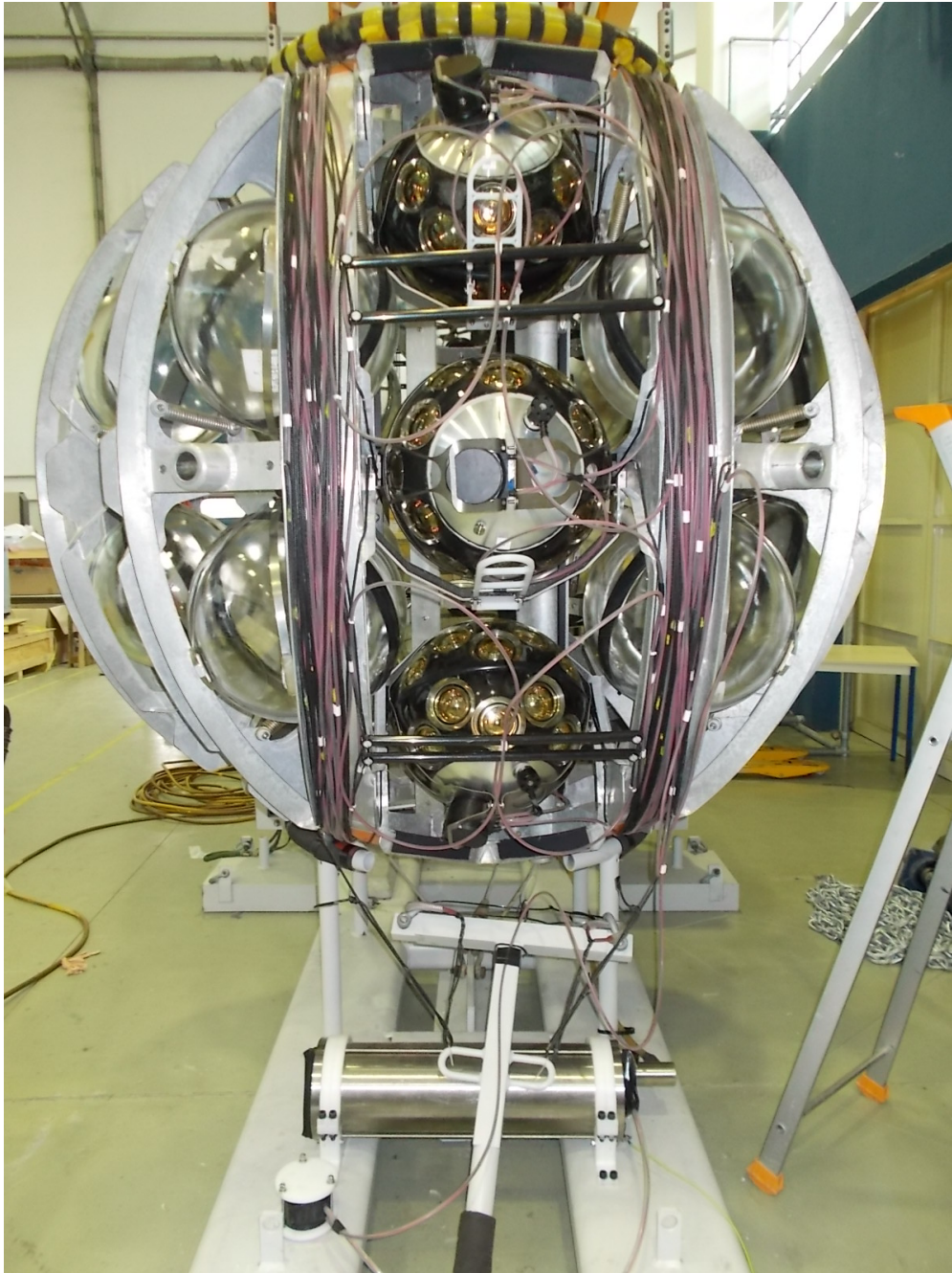


Figure 19: The string prototype (See Chap. 4) loaded on the launcher vehicle.

2.3 DETECTION MODULE

A detection module contains the photo-sensors to detect Cherenkov light. The photo-sensors are housed in a pressure-resistant 17 inch glass sphere which is attached to the string with a titanium collar. The glass sphere is punctuated at the entrance of a penetrator for power supply and data transmission. Each module has a total of 31 3-inch photo-multiplier tubes (PMTs) housed in a 3D-printed structure. The PMTs are arranged in five rings with six PMTs each and one ring with a single PMT looking downward. This design is known as “multi-PMT” and it allows for better signal discrimination compared to the traditional single 10 inch PMT designs used in IceCube and Antares. The space between the PMTs and the glass sphere is filled with an optical gel to avoid the reflection of photons. A reflector ring surrounds each PMT, increasing its detection area by 20 % to 40 % [82].

For KM₃NeT phase 1, Hamamatsu PMTs are used [83]. These PMTs have a minimum quantum efficiency of 20 % (28 %) at a wavelength of 470 nm (404 nm) and a maximal dark count of 1.5 kHz.

Each PMT is equipped with a base [84] which provides the photo-cathode and dynodes with the necessary voltages and digitizes the PMT signal. Digitization is done by processing the analog signal through a time-over-threshold (ToT) discriminator. At nominal operation, a PMT amplifies a single photo-electron to 3×10^6 electrons, which translates at a threshold of 0.3 photo-electron equivalent to a ToT of 27 ns. The leading edge and duration of each pulse are time stamped inside the modules by a so-called central logic board (CLB).

The CLB arranges the data of the 31 PMTs in data frames and sends these data frames to the shore via the optical-fiber network. The temperature of the CLB is kept low by a metal cooling structure. As the read-out of the photo-sensors is done inside the module, the system is commonly referred to as Digital Optical Module (DOM).

In addition to the PMTs, each DOM has an acoustic piezo sensor [85], an LED pointing to the DOM above [86] and a compass and tilt-meter. The piezo is used for acoustic position calibration, the compass and tilt-meter for orientation calibration and the LED for time calibration.

The reconstruction of cosmic neutrinos with sub-degree direction resolution requires a timing precision of about a nanosecond (ns). While the PMTs can supply a timing resolution of around 2 ns to 3 ns, the relative timing between PMTs requires an elaborate system, which is based on the so-called White Rabbit System [87]. It is based on the Ethernet protocol and allows to keep track of the relative timing of the CLBs in the whole detector.

2.4 BACKGROUND SOURCES

Neutrino telescopes suffer from two main sources of background, namely: Optical background and atmospheric background. Optical background encompasses all light producing effects from the detection medium, materials or

biomatter. Atmospheric background are due to particles which are produced in Earth's atmosphere and reach the neutrino telescope. The two different types of background are discussed in more detail below.

Optical background

The Optical background for KM₃NeT includes the PMT dark rates, bioluminescence and potassium decays from the sea salt.

PMT dark rates are property of the photo-sensor technology. The dark rates are primarily caused by the thermal noise from the photo-cathode materials and the non-perfect vacuum inside the PMTs. These dark rates are unavoidable, since PMTs are tuned to convert a single photon to a measurable electric signal. For KM₃NeT, typical dark rates are around 1 kHz.

The beta-decays of the radioactive potassium isotope ⁴⁰K present in the salt of the sea water causes counting rates on the PMTs of KM₃NeT of around 5 kHz. The light from ⁴⁰K decays actually is utilized for time calibration as discussed in Sec. 4.5.

Bioluminescence is caused by microscopic lifeforms such as bacteria living in the sea water. They typically emit light in localized bursts lasting a few seconds. These bursts can cause significant count rates in the PMTs. For KM₃NeT they may reach several MHz.

Atmospheric background

Atmospheric backgrounds are due to particles produced in Earth's atmosphere due to cosmic rays impinging on Earth. In these interactions a variety of mesons, leptons and neutrinos are produced. Of these particles, only the neutrinos and high energy muons can reach the neutrino telescope.

The atmospheric neutrinos constitute, in first order, an irreducible background for cosmic neutrino observations. Nevertheless, the signal-to-noise ratio can be improved by taking the energy and flavor of the neutrinos into account. It is generally believed that the energy spectrum of cosmic neutrinos is harder than that of atmospheric neutrinos. Furthermore, the much larger distance traveled by cosmic neutrinos increase the relative abundance of electron and tau flavors.

The atmospheric muons make up most of the recorded events. For KM₃NeT the rate of recorded atmospheric muons is about 100 000 more than that of neutrinos. An atmospheric muon traveling through the detector can mimic a neutrino interaction. As the production and propagation of atmospheric muons cause a specific zenith distribution as shown in Fig. 20, the best handle to distinguish them is limiting oneself to events which originate in the detector volume or move upwards.

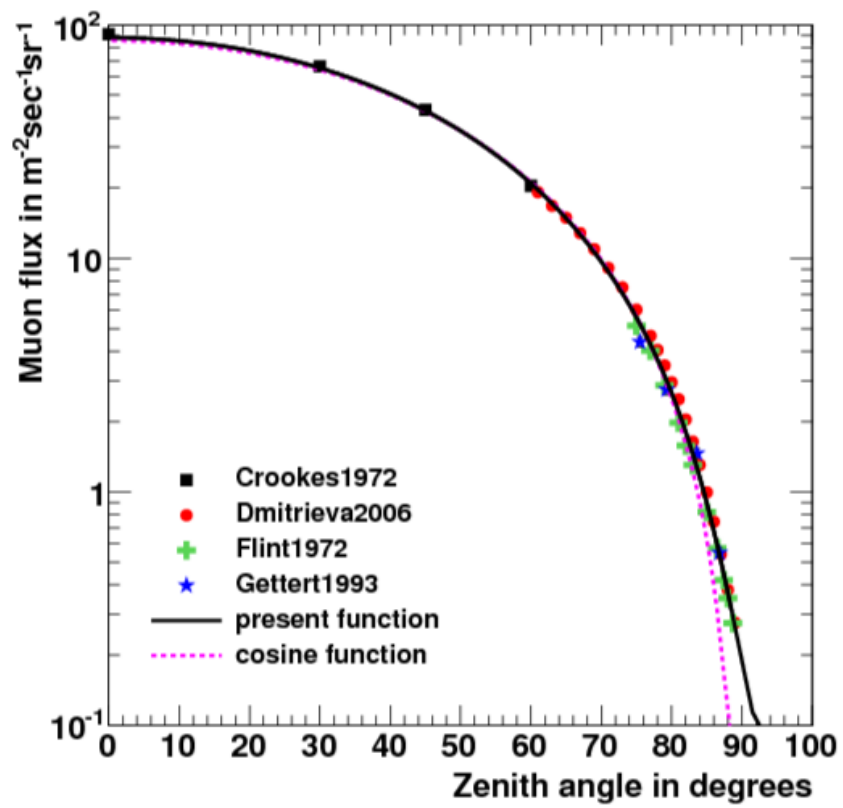


Figure 20: Atmospheric muon flux as a function of zenith angle at sea level [88].

2.5 DATA ACQUISITION SYSTEM

The data acquisition system (DAQ) of the KM3NeT detector handles the incoming data such that the interesting events can be written to disk. As all data from the detector are sent to the shore, about 25 GB of data per second needs processing. Thus, a reduction of the data rate of factor 1×10^5 is required to write the events to disk. This reduction is performed in real-time by software using a designated trigger algorithm.

The trigger selects interesting events based on certain criteria and writes them to disk. In this, all data in a certain time window around the triggered event are written to disk, so that all information is kept for further analysis.

In addition, other selections of the incoming data are written to disk for monitoring of the sea conditions and studies of the optical background.

2.5.1 *Trigger algorithm*

The trigger algorithm is the main tool to select events from the incoming data. In general, neutrino interactions are composed of a combination of shower and track signatures. Therefore, there are different triggers which search for events corresponding to these signatures. The trigger algorithm works in two stages: First a general hit selection which is then followed by a signature specific causality selection.

The hit selection is performed on all hits of all PMTs, inside the same module. By requiring at least two time coincident hits, the optical background is reduced to an acceptable level while most of the signal is maintained. The typical time window length for such a selection is 10 ns. Additionally, the angle between the PMT axes can be used to suppress the background even further.

Following the general hit selection, the trigger is used to select either of the two main event types: shower and track events. For track events, the sky is scanned using a set of directions with a relative angular distance of about 10° . For each direction, only hits inside a cylinder oriented in that direction with a typical radius of 120 m are considered. By requiring a minimum of 5 hits that are causally related, the track trigger improves the signal-to-noise ratio by at least a factor 1×10^4 compared to a standard trigger.

For the shower events, no scanning of direction is needed due to limited size of the object. By requiring a maximal distance of 250 m between PMTs and a minimum of 5 causally related hits the background is reduced to an acceptable level.

The achieved event rate due to random background is below 10 Hz and the overall event rate is about 200 Hz.

Although the trigger only targets a track or shower event signature, other signatures, such as a “Double Bang” signature is triggered equally well.

SIMULATION

We don't want to conquer the
cosmos, we simply want to extend
the boundaries of Earth to the
frontiers of the cosmos

Stanislaw Lem, *Solaris*

In order to determine the detection efficiency of the signal of interest and the backgrounds, a complete simulation of the envisaged measurement is made. In this chapter, a brief summary of the various simulation steps is presented. It is adapted from the KM₃NeT letter of intent [67]. Due to the complexity of the problem, the Monte Carlo technique is used. A comparison of the simulation with data from the first string prototype (PPM-DU) is discussed in Chap. 4.

3.1 EVENT GENERATION

In the event generation, the interaction of a neutrino or the passage of a particle through the detector is simulated. To save computing time, a region containing the instrumented volume at its center is defined (the so-called “can”). The can typically extends three times the absorption length of light in water around the instrumented volume.

The first step of the simulation chain is the generation of particle fluxes in the can. Since some particles can travel distances larger than the can, events are generated in a volume significantly larger than the can (called the generation volume). For each generated event, the produced particles are propagated and if at least one reaches the can, the event is recorded.

Each neutrino interaction is simulated using the GENHEN code [89]. In this, an energy spectrum according to a power law with a given index is assumed. The events can then be reweighted according to a specific neutrino flux to, for instance, represent the IceCube flux or an atmospheric neutrino flux. The simulation includes propagation through Earth, deep-inelastic scattering, quasi-elastic scattering and resonant interactions. For the propagation of the produced muons and taus, the MUSIC code [90] and TAUOLA code [91] are used, respectively.

The atmospheric muons are simulated using the MUPAGE code [92]. MUPAGE uses a parameterization of the atmospheric muon flux at different energies and zenith angles. As a result, events can be generated with sufficient statistics, to match the actual detection rate of atmospheric muons. In addition to single atmospheric muons, atmospheric muon bundles are simulated. Muon bundles are especially important at high energies. The results of MUPAGE

have been compared to results from a full air-shower simulation using CORSIKA [93] and are found to be in good agreement. Since the energy spectrum of atmospheric muons is steep, MUPAGE simulations have been performed for different muon threshold energies. This allows to simulate adequate statistics at energy regions of interest for cosmic neutrino detection.

3.1.1 *Tau neutrino simulations*

The tau neutrino CC interaction has some distinct features compared to the other neutrino flavors. Currently, the MC simulations lack an implementation for two of them: Regeneration of the tau neutrino when propagating through Earth and the light production during the propagation of the tau lepton through the can.

The Earth becomes opaque for neutrinos with energies in excess of 100 TeV (see Sec. 1.2.2). When a neutrino interacts via the CC, it is transformed into a charged lepton. Since electrons and muons are stopped in the Earth's matter, the neutrinos are effectively absorbed. This is not the case for tau leptons, because the tau leptons will decay into a tau neutrino before being stopped. The so produced tau neutrino will carry a substantial amount of the initial neutrino energy. This process is called "tau regeneration". It is energy dependent, as the tau neutrino interaction probability increases with the neutrino energy and energy is lost each interaction. Hence, the energy lost by a tau neutrino as it travels through Earth increases with its initial energy as shown in Fig. 21. For example, a tau neutrino of 1 PeV initial energy traversing Earth's full diameter will on average lose 90 % of its energy, while a tau neutrino of 10 PeV initial energy will on average lose 98 % of its energy [94]. This energy dependent effect causes tau neutrinos from below the horizon to reach the can, even if their energy is above 100 TeV. However, the rate of tau neutrinos from below the horizon is significantly lower than that from above the horizon. A rough estimate expects a 20 % increase in expected event rates due to this effect.

The light produced by the tau lepton during propagation is currently not simulated. This is a reasonable approximation, since the tau lepton acts as a minimal ionizing particle at the energies under consideration. Considering its typically short flight path [94], it will only produce a relative small amount of Cherenkov photons.

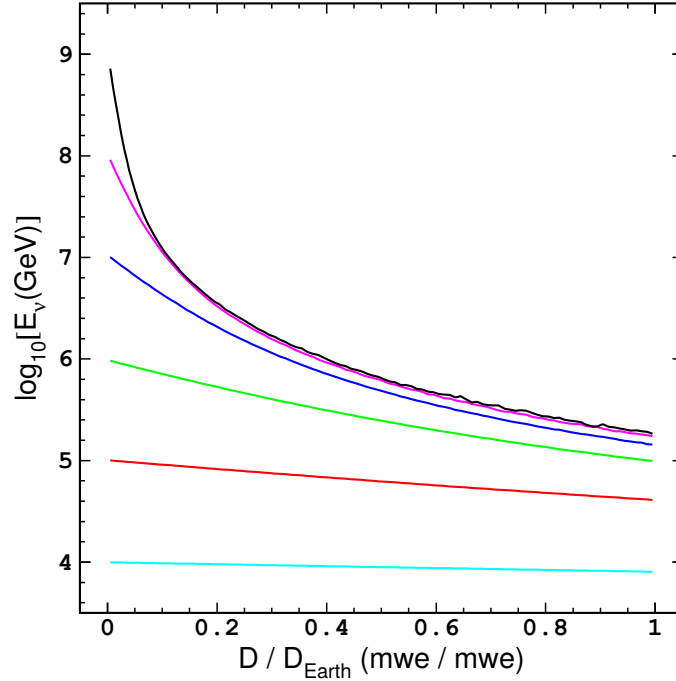


Figure 21: Mean remaining energy of ν_τ as a function of traversed fraction of Earth diameter for starting energies of 10^4 , 10^5 , 10^6 to 10^9 GeV (bottom to top) [94].

3.2 LIGHT SIMULATION AND DETECTOR RESPONSE

The light production of particles in the can is simulated using tabulated results from a GEANT 3.21 simulation. This approach is used as tracking of single photons is too time consuming. The code used for this is called KM3 and for this work KM3 v5r3 is used [95].

The light production for showers is simulated using a so-called “multi-particle” approximation. Except for muons and taus, the light production of particles is simulated by treating them like an electron shower with a scaled equivalent energy and distance to the vertex. This simulation technique results in shower maxima positions in agreement with calculated values as shown in Fig. 22. The light production of hadronic shower is scaled to be one third of that of an electron shower.

For the light produced, KM3 projects it to the PMTs in the detector taking into account the scattering and absorption of the light in the sea water. In the next step the light detection is modeled including absorption in the glass sphere and the gel, as well as the PMT efficiency and PMT angular acceptance.

Light from ^{40}K decays and dark rates from the PMTs are simulated by adding 5 kHz of random noise to the PMTs. Light from bioluminescence bursts is not simulated. The PMT response is simulated using the Jpp software package [96]. It includes the transition time and the amplification of the PMT as well as the effects of the readout electronics. After the PMT response is simulated, the events are then triggered with the algorithms described in Sec. 2.5.1.

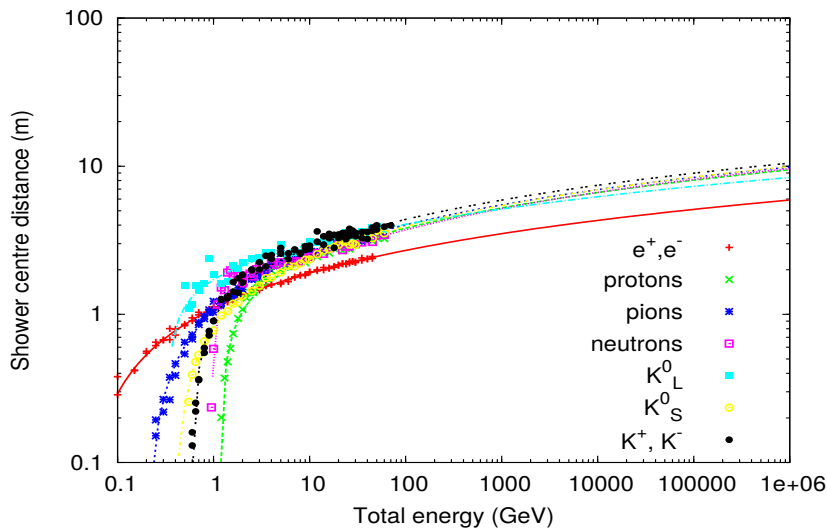


Figure 22: Shower maxima (points) compared to calculations (lines) for a given initial energy for different particles; pions denote charged pions (neutral pions are treated as electrons).

3.3 TAU TOY MONTE CARLO

The tau toy Monte Carlo (MC) simulation is a simplified approach to emulating the signature of tau events. Within the tau toy MC each parameter can be tuned independently, therefore allowing controlled studies of the influence of quantities such as Bjorken Y and tau travel distance on the reconstructions. In addition, the toy MC allows for the simulation of a large amount of contained events at interesting energies and flight length in a short time compared to a normal MC production. In the following all results produced using the toy MC are named as such.

The increase in speed to a normal MC simulation is achieved by approximating each shower with a single particle and using arbitrary positions and directions for the neutrino. The tau flight direction is aligned with the neutrino direction. The energy of the neutrino is set to a desired value and the tau energy fraction can also be freely chosen. The tau flight length is then calculated according to Eq. 22, fixing the lifetime for a given energy to the corresponding mean lifetime.

Events are only written if the tau decay position and the neutrino position are contained in the detector. At both positions a particle is placed which will cause the shower signature: At the neutrino position a π^+ with energy equal to the difference between neutrino and tau energy; at the tau decay position a π^+ or electron with energy equal to 75% of the tau energy. The choice of particle type for the tau shower allows to simulate the hadronic or e.m. decay modes of the tau. The reduction is approximately the average energy loss caused by the neutrinos created in a real tau decay. Consequently, each event contains the following particles:

- Neutrino of chosen energy
- Tau
 - Energy is a fraction of neutrino energy
 - Direction is neutrino direction
- Neutrino hadronic shower
 - Approximated with a π^+
 - Position: neutrino position
 - Direction: neutrino direction
 - Energy: neutrino energy with tau energy subtracted
- Tau decay shower
 - Approximated with a π^+ or electron
 - Position: offset a distance as given by Eq. 22 in tau direction from neutrino position
 - Direction: is neutrino direction
 - Energy: 75 % of tau energy

The files are then processed using KM3 for the light simulation. Afterwards they are triggered using standard trigger software. During the trigger process random background hits simulating the potassium decays are added for an assumed potassium singles rate of 5 kHz.

DETECTION UNIT PROTOTYPE

The future can ever promise but
one thing and one thing only:
surprises

Steven Erikson, House of Chains

4.1 INTRODUCTION

The preproduction model of a detection unit (PPM-DU) is a small scale string prototype made of 3 digital optical modules (DOMs). It was installed in May 2014 just 80 km off the Sicilian coast at a depth of 3500 m. The deployment was performed using a launcher optical module (LOM [97]), the procedure being equivalent to a final configured string. The total data taking period lasted from May 2014 to July 2015 with longer pauses inbetween due to maintenance or improvements on the deep sea infrastructure. Together with the previously deployed (April 2013) DOM prototype (PPM-DOM [98], for more details see below) at the ANTARES site in France the PPM-DU is the first DOM and string prototype installed by the KM₃NeT collaboration. A picture of the three DOMs of the PPM-DU installed on the launcher module is shown in Fig. 19.

The expected observations for the prototype are potassium decays, bioluminescence events and atmospheric muon events. Due to the small instrumented volume and statistics discussed below neutrino observations are not expected. In addition, the distinction between muon and neutrino signals is not possible due to the large probability of misreconstructed track parameters.

In this chapter the technical design, data taking methods, detector calibration and data analysis of the data from the PPM-DU will be discussed.

The DOM prototype

The first DOM prototype was deployed at the ANTARES site in April in 2013. It was installed on the ANTARES instrumentation line (IL [66]) at a depth of 2375 m about 100 m above the sea floor. The IL provides the PPM-DOM with the power supply and read-out to shore, making the PPM-DOM an autonomous detector within the ANTARES observatory. In Fig. 23 the PPM-DOM is shown attached to the instrumentation line with an ANTARES holding structure. The PPM-DOM holds ETEL PMTs of the type D783KFLA [99] as described in Sec. 4.2.

Operation covered about one year. In total 41.5 hours of data, which are feasible for analysis, have been recorded. The PPM-DOM analysis established



Figure 23: The PPM-DOM attached to the ANTARES instrumentation line before deployment.

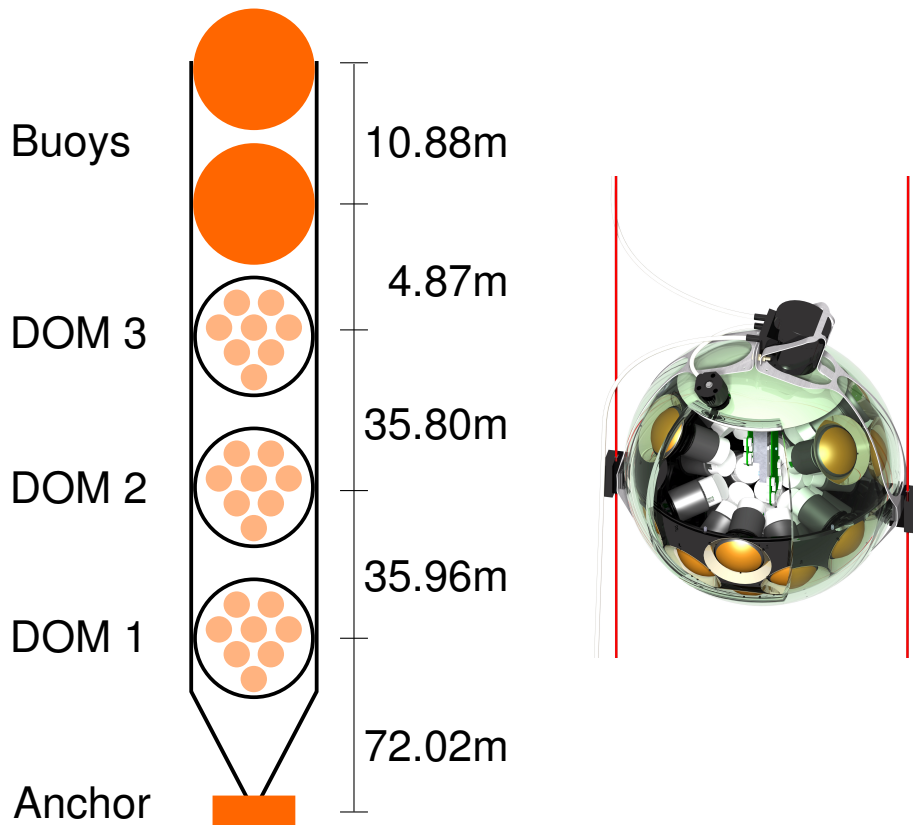
the PMT time calibration by observing potassium decays. Together with the PMT calibration the analysis of the PMT properties such as the single rate and angular dependence of coincident light allowed for a characterization of the small PMTs in the deep sea. The first observations of muons based on a single DOM with the multi-PMT design have been accomplished.

4.2 TECHNICAL DESIGN

The PPM-DU is a shortened string of a total length of about 160 m. It is attached to the ground via an anchor structure and holds three DOMs and two empty glass spheres is shown in Fig. 24a. On the anchor platform a base module [100] is situated. The base module functions as an interface between the detection unit and the sea floor network. The string is held upright by the buoyancy of the DOMs and the empty glass spheres.

Each DOM holds 31 PMTs, the corresponding read-out electronics, power supply as well as other supplementary sensors and devices. The supplementary installations include a LED light source (nano beacon [86]), an acoustic sensor [85], a compass and a tilt meter for time, position and orientation calibration, respectively.

The DOMs attached to the string differ from standard KM₃NeT DOMs. The main differences are the central logic boards (CLBs), compass and PMTs. A technical drawing of a DOM and many components it holds is shown in Fig. 24b.



(a) A sketch of the PPM-DU; DOM 1 and 2 contain ETEL PMTs while DOM 3 contains Hamamatsu PMTs. (b) A sketch of a DOM attached to a string.

Figure 24: Sketches of the PPM-DU and the DOMs.

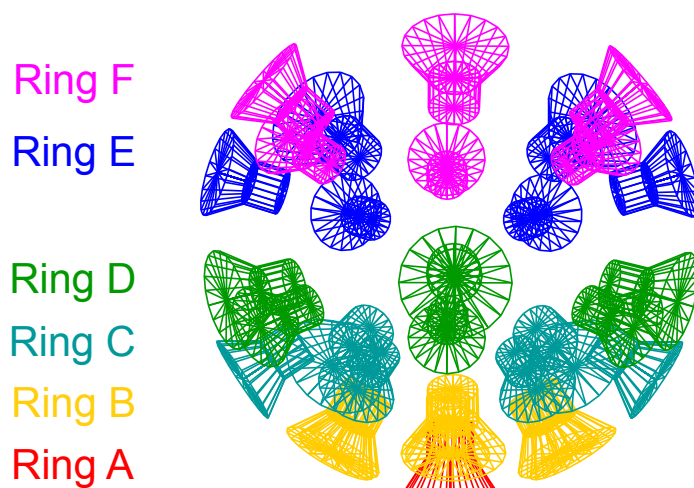


Figure 25: Sketch of the PMTs within a DOM; color indicates the ring; within the rings the PMTs are numbered from 1 to 6 depending on their zenith and phi angle.

The CLBs are prototype productions and hence lack some functionality. Among the missing features are the absence of a functioning positioning system and the loss of timing information on the installed LEDs.

The compass inside the PPM-DU DOMs is non functional. A measurement of the orientation of the DOMs was therefore not possible.

The PMTs are numbered and named according to their position in ring and angle is shown in Fig. 25 (see also Tab.4). The three DOMs have different installed PMT types. In DOM 1 and DOM 2 PMTs of the manufacturer ETEL of the type D783KFLA [99] are installed. DOM 3 holds PMTs produced by Hamamatsu of the type R12199-02 [83]. The main difference between the PMTs is the diameter of the photo-cathode area of 77 mm (ETEL) and 80 mm (Hamamatsu), respectively. Each PMT inside the DOM is surrounded by a reflecting aluminum ring at an angle of about 45° [82]. The reflector rings have a width of 17 mm (ETEL) and 18 mm (Hamamatsu).

Each PMT has its own power supply and electronics called PMT base [84]. The base is attached to each dynode and cathode of a PMT and provides them with the necessary high voltages. In addition, it converts the analog signal into a digital signal by a time over threshold method. For this, a threshold value equivalent to 30% of the charge produced by a single photo electron is used. The time the signal is above the threshold is then passed on to the CLB. The so produced digital signal is referred to as the time over threshold signal (ToT).

The PMTs are operated at an amplification of about 5×10^6 which yields an average ToT of about 30 ns for a single photo electron. The discrimination and digitization of the analog signal are performed by custom ASICs on the PMT base. The recorded ToT is limited to a maximum value of 256 ns. A signal extending beyond this value will be split in separate data. The original signal can be recovered by combining these data.

4.3 DATA ACQUISITION SYSTEM

The PPM-DU data acquisition system (DAQ) transfers the complete detector data to shore. The raw data packages are organized in segments called time slices of 134 ms duration. Each time slice contains a frame per DOM in which the hit information (hit time and ToT) of that DOM is stored. The hit time is determined relative to the internal clock of every DOM. The clock and data transfer per DOM is managed within the CLBs.

On shore the data is further processed by applying selection criteria to minimize the amount of background events recorded, this process is called triggering (see Sec. 4.3.1). During nominal data taking a total of 24 runs of 30 min length are recorded per day. The length of a run is limited by the file size of the raw data files. During the night these runs are processed with the standard trigger and the processed data is copied to the computing center. Per day one raw data file is recorded for minimum bias studies. This corresponds to a total data taking of 18 h. The fact that simultaneous data taking and triggering are not possible is caused by the prototype nature of the PPM-DU and the corresponding on shore facilities.

4.3.1 Trigger algorithm

The applied trigger algorithm selects from the raw data streams triggered events based on time correlations of the recorded hits. In order to be able to make statements about timing correlations the data is time calibrated (for more information on the time calibration see Sec. 4.5). After applying the time calibration the trigger algorithm scans raw hits (Lo) on the same DOM with a time difference smaller than 25 ns. Such a pair of hits is called L1 hit. The time of a L1 hit pair is set to the time of the earlier hit that constitutes the L1 hit. Once at least one L1 hit on a DOM is found a so called triggered event is recorded. A triggered event contains all Lo hits that form a L1 hit within a time window as given in Eq. 16 after the first recorded L1 hit.

$$t_{\text{first L1}} - t_{\text{last L1}} = \text{dst}(\text{DOM}_1, \text{DOM}_3) / c_{\text{water}} + T_{\text{extra}} (\equiv 20 \text{ ns}) \approx 330 \text{ ns} \quad , \quad (16)$$

where $\text{dst}(\text{DOM}_1, \text{DOM}_3)$ is the distance between top and bottom DOM and c_{water} is the speed of light in water for an average refraction index of $n \approx 1.38$. The time window corresponds to the maximum travel time difference between unscattered light emitted from a point. In addition to the Lo hits forming a L1 all Lo hits are stored in an extra ± 20 ns around the triggered event. All Lo hits within 20 ns on one DOM form a so called coincidence. The size of a coincidence corresponds to the number of hits that constitute it.

The parameters that govern the trigger behavior that are tunable are therefore the used distance $\text{dst}(\text{DOM}_1, \text{DOM}_3)$, the additional time T_{extra} , number of triggered L1 hits and the L1 hit time window. The used values in the PPM-DU trigger are chosen in order to record as much data as possible, since with only three DOMs the data size is small enough to allow for this approach. With

more strings and DOMs in the future KM₃NeT detector the trigger parameters need to be more restrictive to cope with the large amount of data produced by the detector.

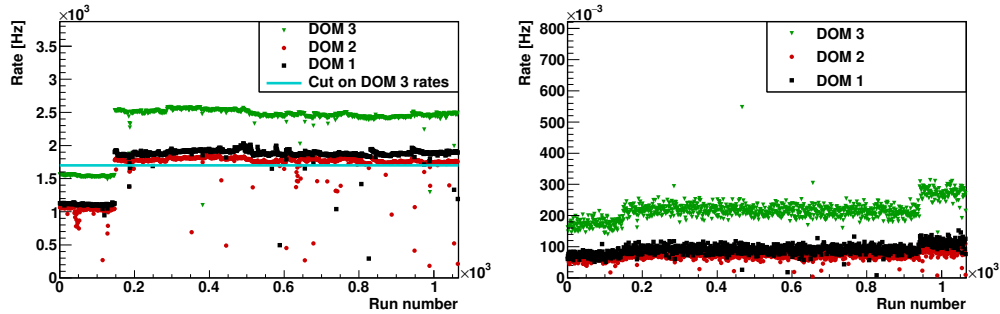
The triggered events, together with time slices of all L1 hits and some auxiliary information (PMT rates) are stored in a ROOT formatted file [101]. A triggered ROOT file contains three main branches: the triggered event, the L1 time slices and the summary slices. The L1 time slices are all L1 hits time sorted within a run and the summary slices contain the rates of each PMT per slice.

4.3.2 Recorded data

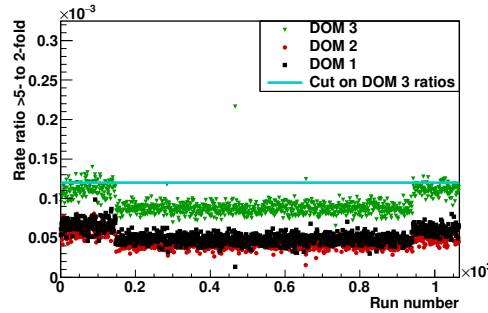
The data taking of the PPM-DU can be separated into three distinct periods by long breaks in data taking and changes in detector operation. The exact duration and data available in the different periods are summarized in Tab. 1. The first period differs most noticeably from the others due to manual data recording and early data taking variations (single DOM runs, problematic PMTs and different trigger setups) which causes a small amount of usable data. The second and third phase both have automatic data taking and a small amount of special runs. Period two and three are distinguished by a long break in data taking of 6 weeks and the use different of software versions for triggering.

The total amount of recorded data does not necessarily correspond to the amount of data available for data analysis. Runs are only suitable for general data analysis if they fulfill a range of criteria. The quality criteria are linked to the detector performance and detector operation mode.

The detector performance requirements are based on the rates of different coincidence sizes during data taking. Shown in Fig 26 are the rates as a function of coincidence size and the ratios between coincidences of different size. For the rates we observe shown in Fig. 26a groups of runs for which the 2-fold rate drops by a significant margin from the baseline for all three DOMs simultaneously. The cause for this drop is not identified, but could be linked to data transfer issues. In order to remove these runs from standard data analysis all runs in which DOM 3 has a 2-fold rate ≤ 1200 Hz are excluded. In addition to the drop in rates a scatter from the baseline for high coincidence sizes is visible as shown in Fig. 26b. Since the scatter could correspond to a variation in the singles rates indicating non-optimal data taking conditions we cut on the ratio between the 2-fold and rate and the 6-fold or higher rates of $>5\text{-fold}/2\text{-fold} \leq 0.12 \times 10^{-3}$ as shown in Fig. 26c. All three Figures shown in Fig. 26 show steps in the respective rates at the same time. The first step around run number 180 is related to a major upgrade in the triggering software. The update was needed after the triggering of the early runs in phase 2 was found defective for yet unknown reasons. The early runs were retriggered with the new software, but some defective effects remained. The second step to higher rates for coincidence sizes larger 2 at around run number 950 is also correlated with a change in the trigger algorithms. The cluster algorithm was updated, triggering more coincidences of higher size.



(a) Rate of 2-fold coincidences and cut value (see text). (b) Added rates of 6-fold and higher coincidences.



(c) Rate ratios of the added 6-fold and higher coincidences to 2-fold and cut value (see text).

Figure 26: Quality plots for the runs of phase 2 based on rate information.

The detector operation mode used for runs which enter the standard analysis is three DOMs taking data operating all functional PMTs at nominal HV. This data taking mode is considered standard operation mode and is the most frequent way the detector is operated. There are two PMTs which are non functional and turned off during standard operations (DOM 2: B1 and DOM 3: D5). PMT B1 in DOM 2 was not addressable since deployment while PMT D5 in DOM 3 was functional at first. But, after 3 months of operation, rates above 300 kHz have been observed and it was turned off since.

Other detector operation modes are excluded from this analysis. These modes include the flashing of the LED nano beacons, single DOM data runs and operating PMTs at non-nominal voltages.

Table 1: Summary of the data taking periods of the PPM-DU.

	first run taken	last run taken	usable data [h]
phase 1	07-05-2014	03-08-2014	65 h ^a
phase 2	25-08-2014	15-12-2014	456 h ^b
phase 3	22-01-2015	09-07-2015	565 h ^c

a data quality analyzed

b see footnote a

c total recorded runtime

4.4 PPM-DU MONTE CARLO SIMULATION

Monte Carlo simulations (MC) are an essential tool to understand, quantify and verify the collected data. By comparing distributions between data and MC inconsistencies can be identified.

Two kind of simulations have been performed for the PPM-DU. One contains atmospheric muon events with an added potassium background and the other a small sample contains of potassium background only.

The muon MC production simulates the expected signals from muons which are produced in the atmosphere by air showers. These are caused by high energetic cosmic rays impinging on Earth's atmosphere. The interaction with atoms in the atmosphere cause a cascade of energetic particles. Among these are muons which at relativistic energies have a lifetime long enough to reach the detector at the sea floor. The number of expected muons at a given sea level and data taking duration is determined using the MUPAGE code [102]. For this purpose the complex simulations of full air showers are substituted by a set of simple formulas [103]. The number of expected muons per shower (muon multiplicity) is taken from a complete air shower simulation. For the purpose of the PPM-DU simulations muons with energies of $E_{\mu} \geq 10$ GeV and a zenith angle range of 0° to 85° are produced. An equivalent of 15.3 d of statistics have been simulated.

The MUPAGE code only generates muon tracks in a certain volume around the detector and calculates the corresponding lifetime of the MC file. If a muon track reaches a certain area around the DU (the can) its light production is simulated using the KM3 program [104]. The considered light production mechanisms are cherenkov light and Bremsstrahlung (causing showers). The light production is simulated using look up tables produced by a designated application based on GEANT for fast processing. The light is then propagated through the water, taking into account the processes of light scattering and absorption in the sea water. In this, the measured water properties of the PPM-DU site have been used [105]. The simulation also takes into account the interaction of the light with the glass spheres of the DOMs, the reflector rings and the angular acceptance of the PMT cathodes.

The response of the detection unit including hit time smearing caused by the PMT transit time and converting photo electrons to ToT signals is simulated

using JPP software package [96]. The determined PMT efficiencies (see Sec. 4.5.1) are taken into account when simulating the response of a PMT to an incident photon. Depending on the efficiency of each PMT the corresponding percentage of the incident photo electrons are discarded. To counteract limitations caused by this rejection, the complete light production is scaled up by a factor 1.1.

The pure potassium MC is based on the single rates recorded with the PMTs. From the observation of the single rates the corresponding expected rates for observing coincidences of size 2, 3 and 4 have been calculated using a designated GEANT 4 simulation. For the single rates a rate of 5.5 kHz was assumed corresponding to correlated rate of 697 Hz (size 2), 57 Hz (size 3) and 7 Hz (size 4). The expected number of potassium hits is added to the muon MC.

In order to have a pure background sample which can be matched to data a dedicated potassium MC is created which consists of time slices filled with potassium hits only.

4.5 IN-SITU DETECTOR CALIBRATION

In this section, the possibilities of in-situ time calibration methods for a string like detection unit are presented, which are discussed in more detail in a KM₃NeT internal note [106]. The main task of the in-situ calibration is an exact understanding of the detector properties in a fully assembled state. The PMT characterization in the lab does not include the time calibration of all 31 PMTs in a DOM (intra DOM time calibration) in an assembled state. Many parameters established pre-deployment could be influenced by the surrounding conditions such as temperature or stress during deployment and therefore need to be re-established. The DOM time calibration (inter DOM time calibration) needs to be determined since it was lacking. Especially the time calibration is essential for any measurement performed with the detector. The trigger and reconstruction algorithms are based on timing information with a precision at the ns level. The time calibration of the detector has to achieve a precision of the order of ns or ideally sub-ns to allow for an optimal performance of the algorithms. Just as important as the precision is the long term stability and monitoring of the time calibration. The time offsets are stored in a data base for later use during data analysis. In addition to the time offsets other properties of the PMTs need an in-situ calibration method. These are discussed in detail in Sec. 4.5.1.

The prototype nature of the PPM-DU has an impact on the time calibration for two reasons: The lack of a functional pre-deployment time calibration and the lack of a white rabbit system on the CLBs.

The white rabbit system guarantees that after a reboot of the detector each DOM clock is synchronized with the rest of the detector timing system. The exact knowledge of the DOM clocks is crucial since the time of hits are determined with respect to that clock. The consequences of the absence of the white rabbit system will be discussed in the inter DOM time calibration section.

The lack of a pre-deployment calibration makes an in-situ calibration crucial. In addition, the lack of starting parameters causes the in-situ calibration execution difficult. That being the case, the best guess for inter DOM time offsets is based on the light travel time and the estimated lengths of the read-out cables.

Due to the absence of a white rabbit system and a pre-deployment calibrations a muon reconstruction is only feasible after inter and intra DOM time calibration have been established using in-situ methods.

4.5.1 PMT calibration

The PMT calibration procedure was developed within the JPP software package [96]. In this section, the method and results are presented. The PMT characteristics that can be in-situ calibrated are the PMT transit time (corresponds to time offset), the relative detection efficiency and the transit time spread.

The PMT transit time denotes the time it takes for a signal to travel from the cathode to the PMT base read-out. The transit time therefore corresponds to the time offset of each PMT since variations in read-out hardware are negligible. Variations in the transit time between PMTs are caused by internal production differences and are typically in the order of 10 ns.

The relative detection efficiency of the PMT system denotes the likeliness of a PMT detecting an impinging photon relative to a standard PMT. The detection efficiency is a composition of different causes such as the PMT cathode coating, the reflector rings or the homogeneity of the gel in front of the PMTs. It can change as a result of the tuning of the supplied voltage or aging. Exact knowledge of the total detection efficiency is needed in order to allow for precise data to MC comparisons.

The PMT calibration is based on the observation of light from radioactive decays. These decays originate from the natural abundant potassium isotopes (^{40}K) in the sea salt and cause a single rate per PMT of around 5.5 kHz. Since the ^{40}K isotopes decay mainly (89 %) via β decay at an energy of 1.3 MeV the subsequent light production is small. The other decay mode is via electron capture, emitting a γ ray of 1.46 MeV with comparable light production to the β decay. Due to the small light yield correlated observations are limited to a short distance. For a pair of PMTs the observed correlated ^{40}K rate depends on the detection efficiencies of the PMTs and the relative angular distance of the pair. Figure 27c shows the distribution of hit time differences (ΔT) for one PMT pair. The distribution shows an approximately Gaussian peak on top of a constant background. The peak corresponds to the observation of correlated light from ^{40}K decays. Its mean is offset from zero due to the time offsets of the two PMTs forming the pair. The constant background is caused by uncorrelated photons. The hit time difference distribution for all possible combination of PMT pairs on a DOM is shown in Fig. 27a, where the pair ID increases with lower angular distance (pair ID 0 has the largest possible angular distance, pair ID 465 lowest possible angular distance). For each DOM a total of 465 independent combinations between PMTs are possible, with $N_{\text{combinations}} = N(N - 1)/2$ with

$N = 31$ PMTs. Since the observation of correlated ^{40}K signals depends on the angular distance between PMTs, a steady increase in peak area is shown in Fig. 27a.

A χ^2 minimization procedure is applied simultaneously to all distributions evaluating the PMT properties of all PMTs in a DOM. The constant background is subtracted and a Gaussian fitted to each PMT pair distribution. The constant background due to random coincidences is estimated using the recorded PMT rates. The mean values, heights and widths of the Gaussian peaks are related to the time offsets, efficiencies and intrinsic transit time-spreads of the PMTs. In order to translate the area of the Gaussian to a PMT efficiencies a model for the decrease of the coincidence rates due to ^{40}K depending on the angular distance between the PMT pair is assumed (See Eq. 17). A graphical representation of the function (PMT angles on DOM from 33° to 165°) is shown in Fig. 28, the region of interest is indicated by the blue lines.

$${}^{40}\text{K}_{\text{rate}}(\theta) = \exp(p1 + \cos(\theta) * (p2 + \cos(\theta) * (p3 + \cos(\theta) * p4)))[\text{Hz}] \quad , \quad (17)$$

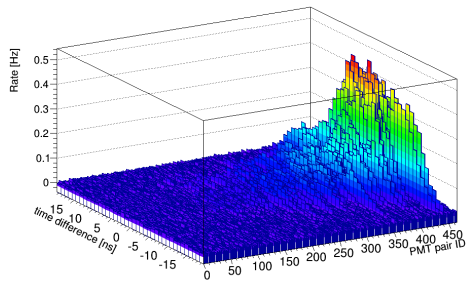
where $\cos(\theta)$ is the angle between the corresponding PMT pair and $p1$, $p2$, $p3$ and $p4$ are taken from a dedicated ^{40}K simulation [107] (for the used values see Appendix Tab. 5).

The results of the PMT calibration for the estimated time offsets, time spread and efficiency are shown in Fig. 29. Here a set of 320 quasi consecutively taken runs at the start of phase 3 data taking have been analyzed (from run number 1544 to run number 1900). A small sub sample of runs have been excluded because a nano beacon was flashing.

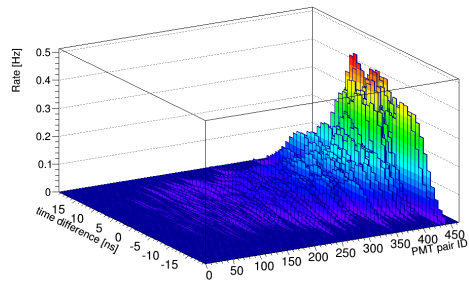
The results for the time offsets shown in Fig. 29a indicate the PMT time offsets to be in the order of ± 10 ns. The obtained calibration values are shifted such that the total offset value is as small as possible. The time spreads shown in Fig. 29b are mainly between 2 ns to 2.5 ns which agrees with the measured average time spread value of 2.3 ns in the pre-deployment PMT testing.

The results for the PMT efficiency are given relative to a reference PMT. Hence, the results shown in Fig. 29c show values larger than one. In phase 3 a second PMT in DOM 2 was taken offline, causing the empty bin in efficiency at PMT ID 20. In order to study the determined efficiencies the correlation between the singles rate and efficiency of a PMT is studied [108]. The single rate of and efficiency of a DOM are found to be well correlated. A correlation between the measured PMT quantum efficiencies pre-deployment and the total efficiency cannot be established as shown in Fig. 30. The lack of a correlation between these is puzzling and at the moment not understood.

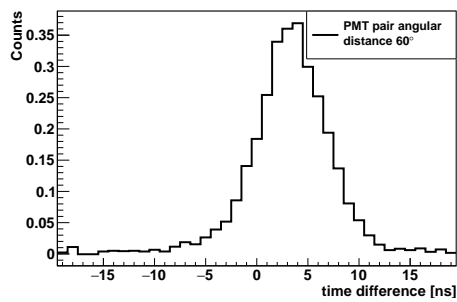
As shown in Fig. 29a and Fig. 29b the parameters of the PMTs in DOM 3 (Hamamatsu) show a lower scatter than the PMTs in DOM 1 and 2 (ETEL). Also for the efficiencies shown in Fig. 29c the results for DOM 3 are different, showing a higher total efficiency. The reason for the higher efficiencies in DOM 3 is expected due to a larger surface of the installed reflector rings and the larger cathode area of the Hamamatsu PMTs. For the stability of the obtained PMT calibration during this time see Sec. 4.5.2.



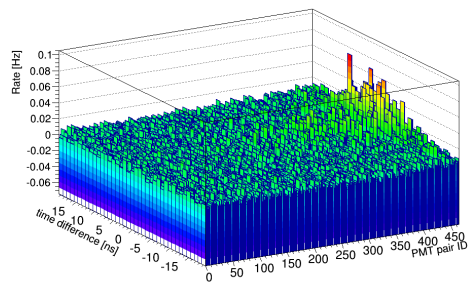
(a) ΔT distributions for all PMT pairs; y-axis sorted by angular distance.



(b) Fit to all ΔT distributions for all PMT pairs; y-axis sorted by angular distance.



(c) ΔT distribution for one PMT pair (channels F1 and F6).



(d) Z-axis shows Fig. 27a - Fig. 27b; y-axis sorted by angular distance.

Figure 27: PMT time calibration performance for DOM 1 in run 1547.

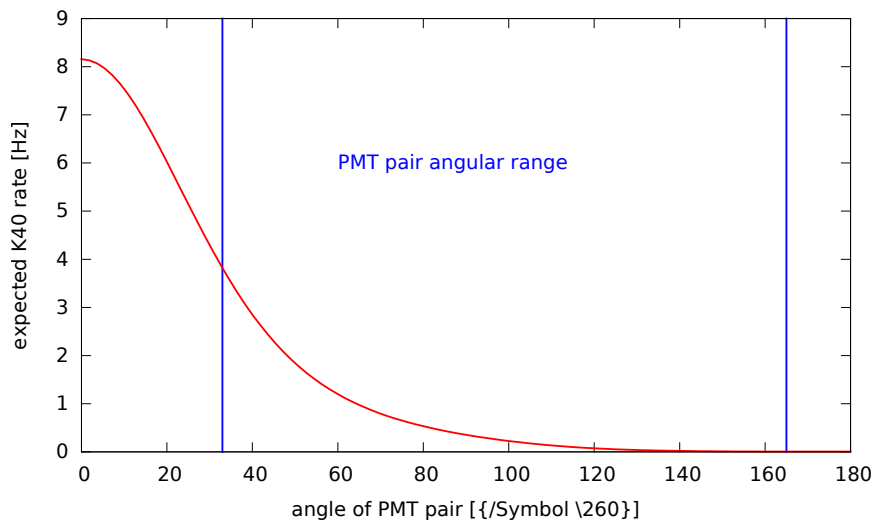


Figure 28: Estimated ^{40}K rates for a certain PMT pair angular distance.

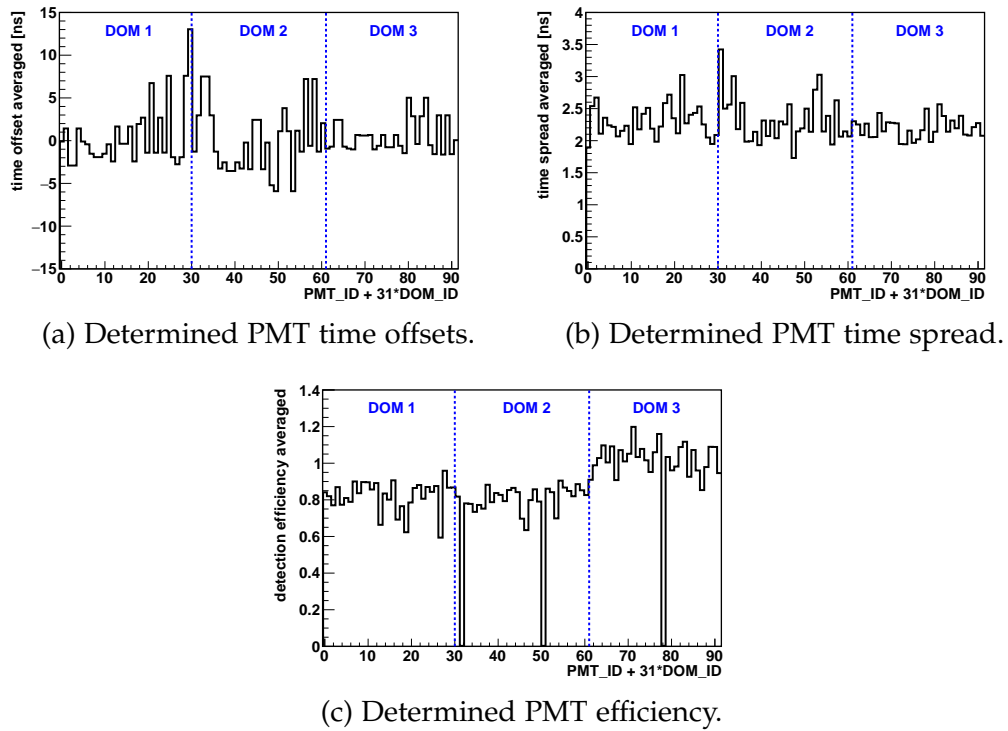


Figure 29: PMT time calibration results for 320 runs taken consecutively at the end of phase 2 and the beginning of phase 3.

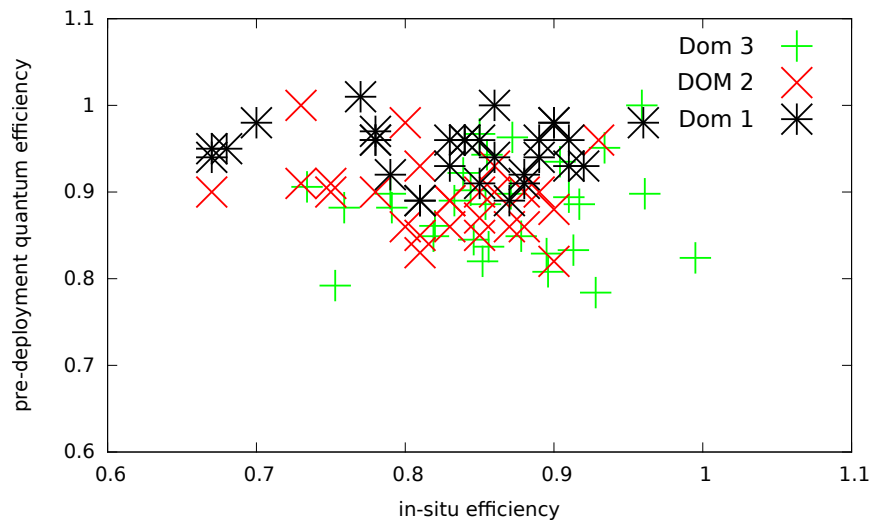


Figure 30: The pre-deployment PMT quantum efficiency plotted against that determined in-situ PMT efficiency; in-situ PMT efficiency value is scaled for a better comparison.

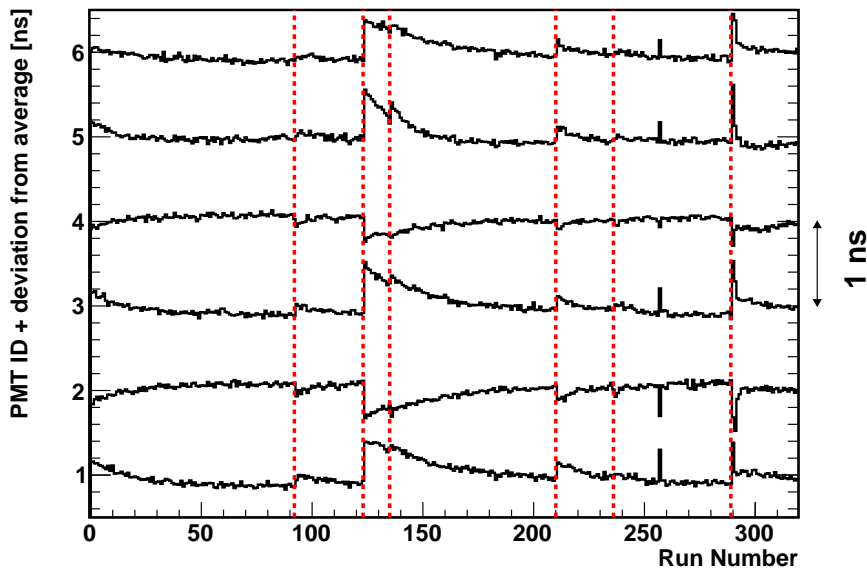


Figure 31: Long term behavior of PMT time offsets for DOM 1 Ring B; y-Axis shows the deviation from the average time offset for the corresponding PMT offset by the PMT ID, the difference in ns between y-Axis for two PMTs corresponds to exactly 1 ns; red lines indicate breaks in the data taking lasting between hours and months; runs taken between December 11, 2014 and July 9, 2015.

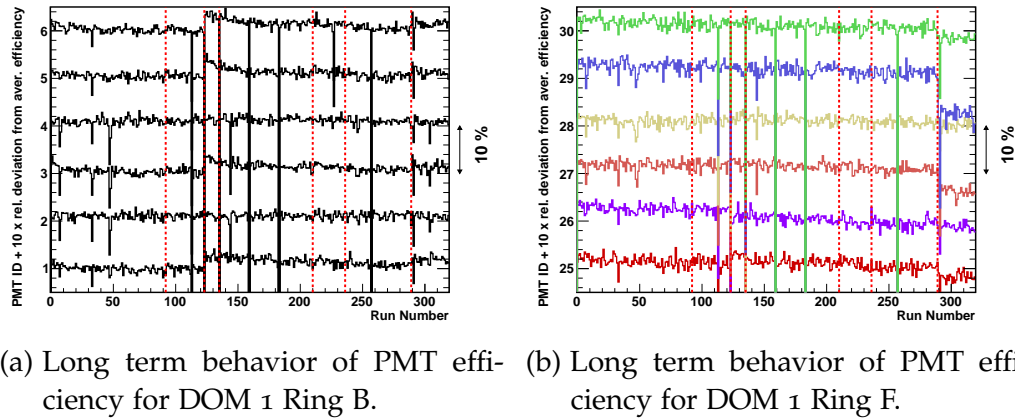
4.5.2 PMT calibration stability studies

The study of the long time behavior of the PMT calibration parameters is briefly discussed here and in more detail in [108]. The parameters are monitored for every run taken from December 11, 2014 to July 9, 2015 which includes runs from the end of data taking period 2 and the start of data taking phase 3. The values of parameters have been obtained for every third run. The results on PMT time-offsets, time transition and efficiencies vary and are discussed below.

In order to study the stability of the calibration parameters the deviation of the mean value is plotted over the data taking period for every PMT on each DOM. One such plot for Ring B of DOM 1 is shown in Fig. 31. The calibrated PMT time offsets are stable within the sub nano second range. The PMT time offsets are found to occasionally change up to a nano second and relax back to the original offset within a day. These seemingly spontaneous deviations correlate with breaks in the data taking that lasted between hours and months indicated by the dashed red lines. These changes in time offsets are linked to hardware effects on the PMTs such as temperature change or charge built up.

The PMT time spread calibration parameters behave like the PMT time calibration showing a sub nano second spread and spontaneous deviations up to a nano second correlated with breaks in data taking.

The PMT efficiencies are found to show the largest variations. The efficiencies of the PMTs looking upward (top two rings) are degrading with time and some



(a) Long term behavior of PMT efficiency for DOM 1 Ring B. (b) Long term behavior of PMT efficiency for DOM 1 Ring F.

Figure 32: Long term behavior of PMT efficiency for DOM 1; y-Axis shows the relative deviation from the average efficiency for the corresponding PMT offset by the PMT ID, the difference in relative efficiency between y-Axis for two PMTs corresponds to exactly 10%; red lines indicate breaks in the data taking lasting between hours and months; runs taken between December 11, 2014 and July 9, 2015.

PMTs show a spontaneous recovery of the efficiencies. Two histograms showing the relative deviation of the average PMT efficiency for Ring B and F of DOM 2 are shown in Fig. 32.

The degradation in efficiency of the two upper rings can be up to 20% from the original efficiencies as measured at the start of the PPM-DU data taking. The recovery is not correlated to any quantifiable hardware or software changes. The two effects together lead to the conclusion that the top of the DOMs accumulate dust at the glass of the spheres. This assumption is supported by the fact that the lower ring PMTs do not undergo any efficiencies changes. The spontaneous recovery also supports this assumption since it seems to indicate the material can slide off the glass sphere due to movement of the DOMs or the sea current.

The assumption of efficiency losses being linked to material on the glass sphere is further supported by a visual inspection of the PPM-DU during a sea operation. The pictures shown in Fig. 33 clearly show that all three DOMs of the PPM-DU accumulated dust on the top which was not observed right after deployment and could cause the previously discussed decrease in efficiency.

4.5.3 DOM beacon calibration

The nano beacons installed in every DOM are a flashable LED light source that allows for an inter DOM time calibration [86]. They are positioned between PMTs F3 and F4 in the PMT support structure pointing upwards. The beacons emit light at a wavelength of 470 nm with variable frequency and intensity. The frequency can be varied between 250 Hz to 8192 Hz and the intensity is controlled by the supply voltage which can be varied between 0 V to 24 V. A calibration for the intensity of the light flux is not known, therefore the



(a) DOM 1.

(b) DOM 2.



(c) DOM 3.

Figure 33: Pictures taken during sea operation in December 2015 of the DOMs of the PPM-DU showing accumulation of dust at the top of the DOMs.

ideal intensity was calibrated by taking beacon runs at different intensities and measuring the light on the neighboring DOM. The rise time of the light flash is between 5 ns to 10 ns.

The DOMs in the PPM-DU are time calibrated with respect to the lowest DOM (DOM 1). The original method foresaw to calibrate each DOM with the nano beacon on the DOM directly beneath it. Due to a lack of runs in which the beacon of DOM 2 was operated this approach was not feasible. Hence, DOM 2 and 3 are calibrated using runs in which the beacon of DOM 1 is flashing. The difference in time offsets for using beacon 1 (beacon in DOM 1) or beacon 2 (beacon in DOM 2) to calibrate DOM 3 has been studied and is discussed in Sec. 4.5.4.

During the phase 2 and phase 3 data taking no beacon data has been recorded. In order to translate the results from the beacon calibration to these data taking periods an extra calibration has to be performed based on the muon data, see Sec. 4.5.6.

All triggered events with at least one L1 hit (two hits within 25 ns) in DOM 1 and the to be calibrated DOM are used. For every triggered event the time difference between the 2nd hit on each DOM and the assumed light travel time is used. The reason for using the 2nd hit time instead of the 1st is due to the correlation between the nano beacon light profile and the different travel distances between beacon 1 and DOM 2 or DOM 3 (see Sec. 4.5.5). From these time differences the expected travel time of the nano beacon light is subtracted. The travel distance of the light is assumed to be a straight line between beacon and PMT position on the other DOM. The light speed is corrected by the refractive index of the sea water which is measured to be $n_{\text{light}} = 1.39$ for a wavelength of 470 nm (as taken from [109]). The time difference between the DOMs is therefore given by

$$\Delta T_{2/3} = [t(\text{hit}_{2\text{nd}}(\text{DOM}_{2/3})) - t(\text{hit}_{2\text{nd}}(\text{DOM}_1))] - \text{dst}(\text{beacon}, \text{PMT}(\text{DOM}_{2/3})) * (n_{\text{light}}/c)[\text{ns}] \quad , \quad (18)$$

where $t(\text{hit}_{2\text{nd}}(\text{DOM}_{2/3}))$ is the hit time of the 2nd on any DOM and $\text{dst}()$ is the distance between the beacon and the hit PMT on the to be calibrated DOM. The resulting histogram is fitted with a Gaussian function where the mean of the Gaussian denotes the time offset of the DOM. One such histogram for calibrating DOM 2 and DOM 3 using beacon 1 is shown in Fig. 34.

The resulting time offsets for each beacon 1 run in phase 1 are shown in Fig. 35. The DOM 2 offsets show a stable behavior with a variation of around 2 ns while the offsets of DOM 3 are grouped in periods with different mean offsets. Every single period of DOM 3 shows the same stable behavior as for DOM 2. The two changes in mean time offset for DOM 3 coincides with a power outage (first change in mean) of the DU and a repowering of the on-shore system of DOM 3 (second change in mean). These shifts in means are caused by a shift in one of the clocks in the system due to the lack of a reproducible calibration. The repowering of the system can cause the internal clock to come up with a different time offset. The calibration of DOM 3 therefore requires different detector settings for the corresponding periods.

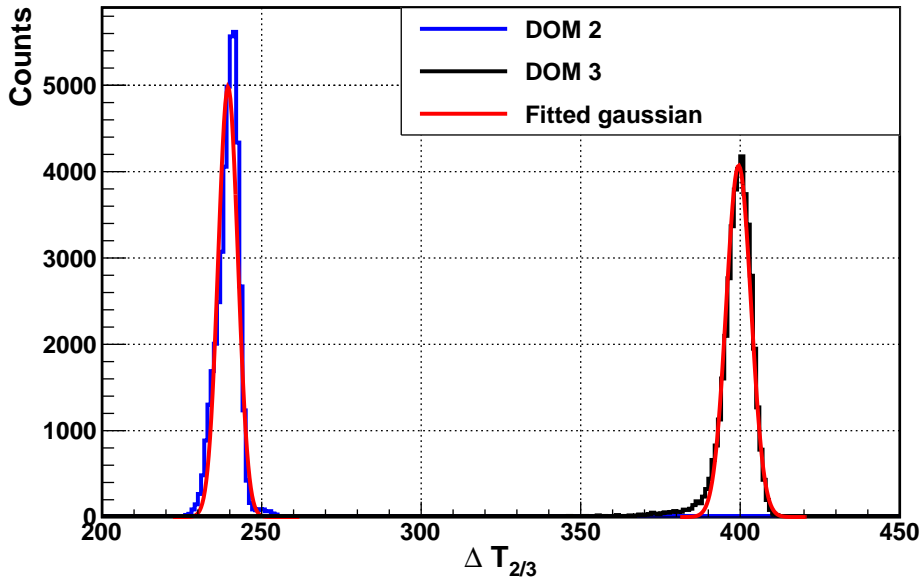


Figure 34: ΔT distributions with Gaussian fit for DOM 2 and DOM 3 relative to DOM 1 with beacon 1 flashing for run 212, DOM 3 data is scaled by the number of entries.

A cross check for the time calibration has been performed by comparing the time differences in the DOMs for muon signals in data and simulation see Sec. 4.5.6 for the results. The time difference distributions in the different DOMs for muon signals are shown in a comparison of data and simulation in Fig. 36 for phase 1 data which have been calibrated according to the nano beacon time offsets. The difference between beacon and muon calibration as determined from these distributions are found to be consistent.

4.5.4 Calibrating DOM 3 using beacon 1 vs using beacon 2

Calibrating DOM 3 with beacon 1 as discussed in Sec. 4.5.3 can cause different systematics of the time calibration. Possible effects could be a relatively larger fraction of scattered light due to the larger distance between DOM 3 and beacon 1 or effects connected to the pulse shape of the beacon. In order to check possible changes in the time calibration the results have been compared with those obtained from the available beacon 2 runs (for the results see Appendix Tab. 6). A histogram depicting the fitted time difference distributions for DOM 3 in two runs using beacon 1 or 2 is shown in Fig. 37. One finds that the average time offsets determined from beacon 2 runs is 8.5 ns larger and the fitted σ is 1.9 ns larger than determined by beacon 1 runs (5.2 ns for beacon 1).

The difference in fitted Gaussian σ is attributed to the difference in light travel distance (beacon 2 35.80 m, beacon 1 72.02 m), causing more scattering and absorption of the LED light. The larger time offset cannot be caused by shadowing of DOM 2 one would expect an increased pathway of the light is about 10 cm or so which corresponds to less than 1 ns. A source of the shift in

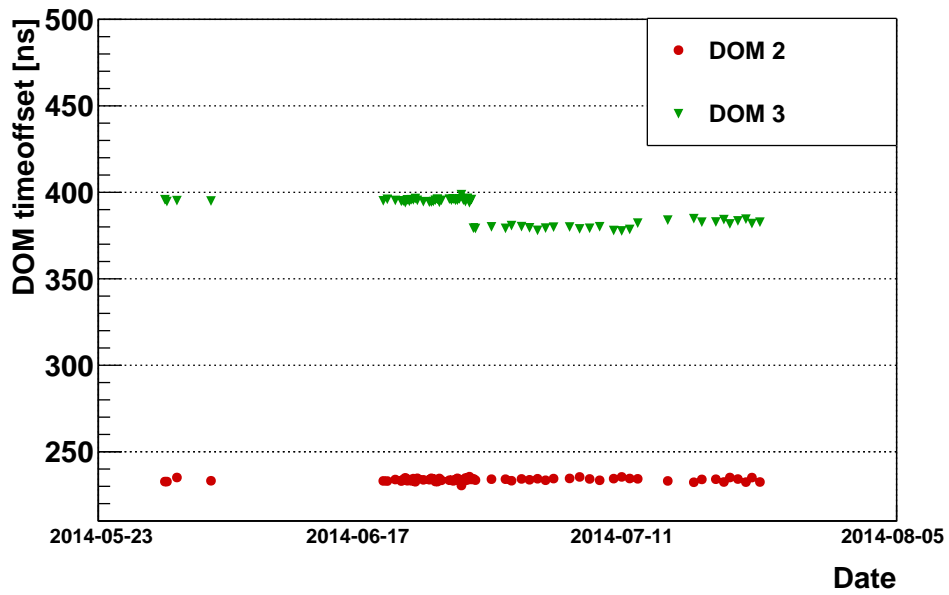


Figure 35: Obtained time offsets for DOM 2 and 3 with beacon 1 in phase 1.

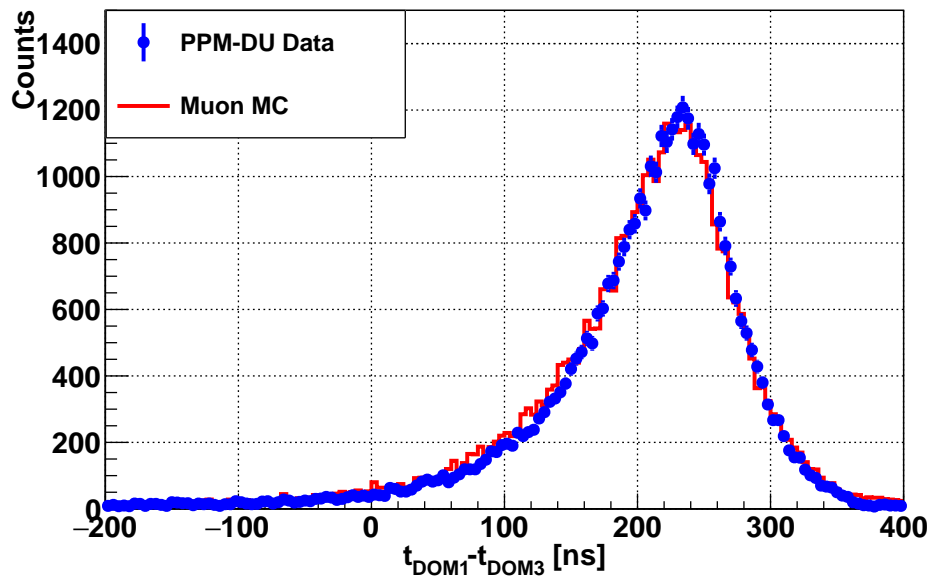


Figure 36: Time difference between DOM 1 and 3 for at least one L1 in every DOM, MC scaled by the number of entries.

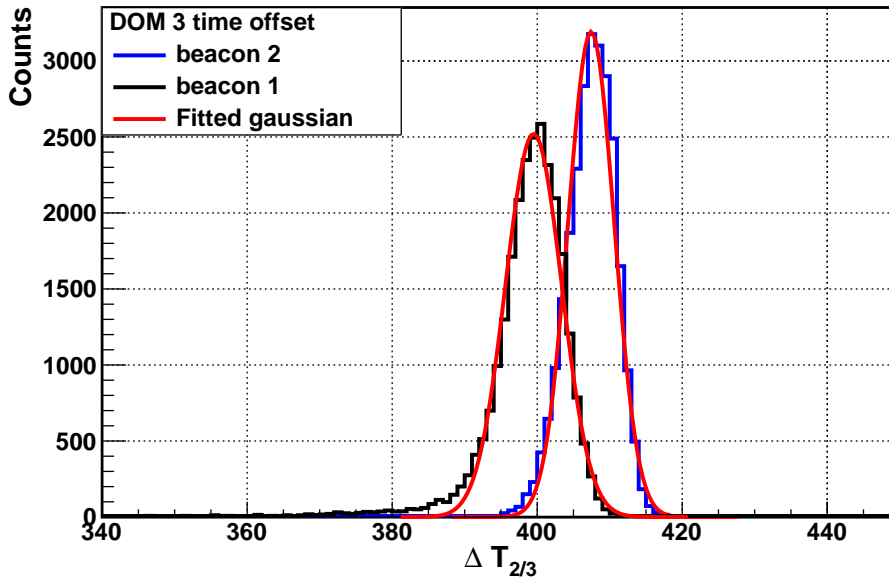


Figure 37: Obtained time offsets for DOM 3 using beacon 1 (run 212) or beacon 2 (run 196); lines show Gaussian fits to the distributions; beacon 1 data scaled by entries.

time offsets could be the rise time of the LED which is around 5 ns to 10 ns. Since DOM 3 is far away from the beacon 1 the arriving light is more likely to be in the main peak of the light burst than in the rising flank. While when the beacon 2 is used to calibrate DOM 3 the distance is much closer and light from the rising flank reaches DOM 3. The determined DOM 3 time offsets with beacon 1 are corrected for this extra offset.

4.5.5 Hit selection: Difference in using 2nd hit vs using 1st hit

A first order approach would suggest to use the time of the 1st hit on a DOM, since the earliest hit is most likely caused by direct light. In the case of the beacon calibration this effect is outdone by effects linked to the nano beacon properties as described below.

The difference between using the first and second hit on the beacon DOM and the to be calibrated DOM (calibrate DOM) has been studied. In the case of using the first hit the ΔT distributions show tails towards early values and the mean of the distribution is shifted to larger time differences (by 5 ns). In order to suppress these tails the effect of using the second hit on the DOMs has been studied. It is found that the distortion of the distribution is mainly caused by the use of the first hit on the DOM. An explanation is that the earliest detected hits are emitted during the rise time of the nano beacon. As shown in Fig. 38a the three DOMs see distinctly different amounts of light from the beacon. The best measure for the number of photo electrons is the recorded ToT, on average a large ToT indicates many incident photo electrons. Looking at the ToT for events recorded during beacon runs shown in Fig. 38b, 38c and 38d we find

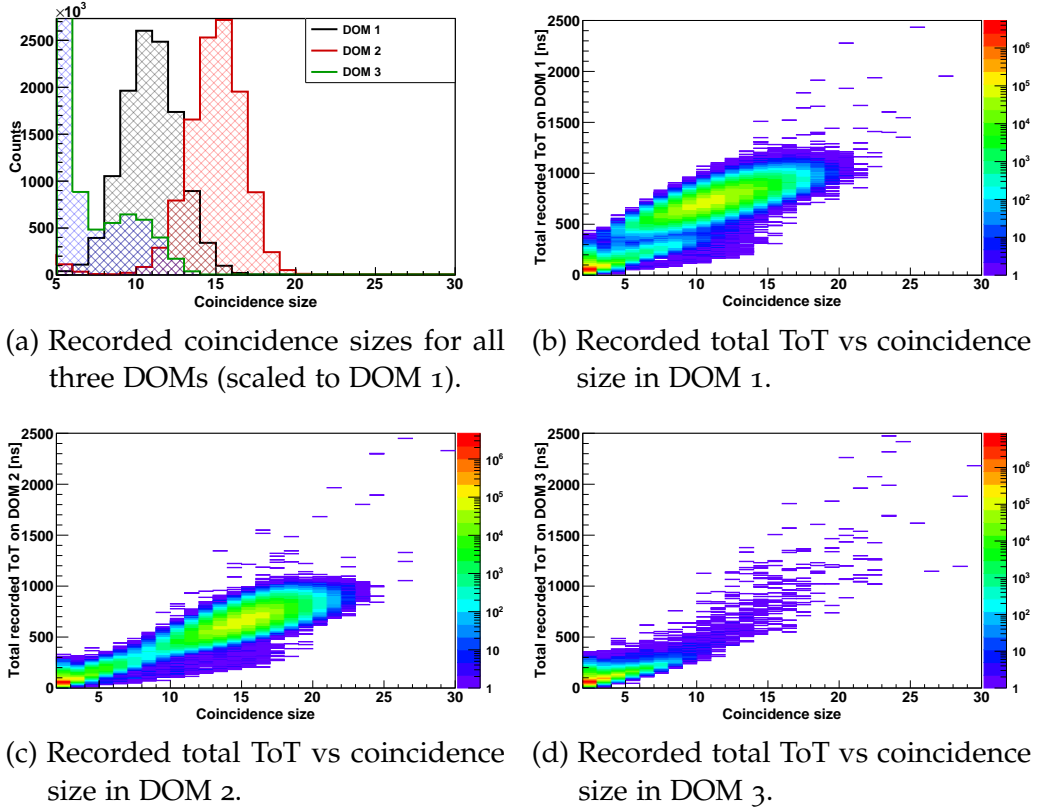


Figure 38: Intensity studies for all beacon 1 runs in phase 1 data taking.

DOM 2 to be the DOM with the largest recorded ToT. Therefore DOM 2 is the DOM which sees the highest light intensity from the beacon. It is more likely for DOM 2 to pick up photons emitted during the rise time of the LED. The effect of using the second hit on the beacon DOM is much more subtle and results in a 1.5 ns shift in the mean of the distribution and reducing the σ from 2.1 ns to 1.8 ns. Due to these findings the second hit was used for the calibration in both DOMs.

4.5.6 DOM muon calibration

As mentioned in Sec. 4.5.3 and shown in Fig. 35 a shift in DOM time offsets has been observed for DOM 3 in data taking phase 1. Such a shift in DOM time offsets is caused by the lack of a White Rabbit system as discussed previously. Therefore, any inter DOM time calibration established in phase 1 is not applicable in other data taking phases. During data taking phase 2 no beacon runs have been recorded and therefore a method was devised to translate the DOM time offsets as established from beacon runs in phase 1 to phase 2. The method used for this purpose is based on the observation of muons and will be referred to as the muon calibration [106]. In order for the muon calibration to be performed, the DOM time offsets have to be known with a precision of around 50 ns in order to be able to trigger the muon events. The observed shifts

in the DOM time offsets are of the order of 10 ns to 20 ns and therefore the beacon offsets from phase 1 are a sufficient starting point.

By comparing the time differences for muon signals in the DOMs between data and simulation the DOM time calibration can be validated. The comparison is done using three time difference histograms: Time difference between DOM 1 and 2 (ΔT_{12}), DOM 2 and 3 (ΔT_{23}) and between DOM 1 and 3 (ΔT_{13}). For the first two combinations events with a L1 hit in two DOMs is required and for the last events with a L1 hit per DOM (causing a higher muon purity in this histogram see Chap. 4.6.3). The event selection for the histograms is exclusive (a ΔT_{13} event is not entered in the ΔT_{12} or ΔT_{23} histogram) and the three histograms are therefore independent. In order to reduce the background further a coincidence size selection of events with coincidences ≥ 6 per DOM has been performed which relates to an expected muon rate of about 70 mHz. For each event the time difference between the 1st hit on each DOM pair is filled into the histogram. The histogram for time differences between DOM 1 and 3 is shown in Fig. 36.

The simulation and data histogram for each DOM time difference is then compared with a bin by bin χ^2 method. The resulting χ^2 distributions are fitted with a paraboloid finding the corresponding best matching time offset. The determined time offsets are correlated since $\Delta T_{12} + \Delta T_{23}$ should equal ΔT_{13} . A consistency check is performed and they are found to be within 1 ns agreement. All three established time offsets are then used for the calibration.

The procedure is limited by statistics in the ΔT histograms. It was found to perform with sub nano second precision for data period lengths down to 5 h.

The muon calibration was cross checked with the beacon calibration for data taken in phase 1. For data taking periods of sufficient length the two calibration procedures are found to be within 2 ns agreement.

4.5.7 Data period calibration

Calibration for the three different data taking periods of the PPM-DU varies because of the availability of nano beacon runs. In phase 1 runs with the nano beacon in DOM 1 flashing have been taken throughout it's duration and it can therefore be calibrated with the beacon method.

In phase 2 and 3 no beacon runs have been recorded. Due to the shifts in time offsets as discussed in Sec. 4.5.3 the time calibration is performed as follows. The time offsets estimated in phase 1 from the beacons are used as a basis for the muon time calibration. The data taking periods are subdivided into phases of data taking uninterrupted by a power cycle in the on- or off-shore hardware system. Each subperiod is then fitted with the muon calibration procedure to obtain the relative shifts from the phase 1 time offset shown in Tab. ??.

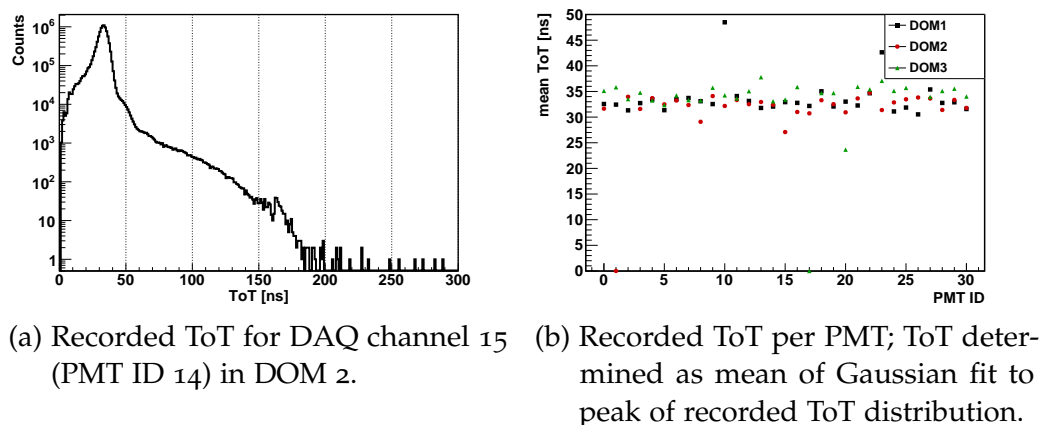


Figure 39: ToT study plots for run 311.

4.6 PPM-DU DATA ANALYSIS

4.6.1 *Time over threshold signal*

The time over threshold (ToT) as discussed in Sec. 4.3 is a quantity extracted from the analog PMT signal at the PMT base.

The ToT of a signal does not allow for an exact reconstruction of the number of incident photons. Two incident photons at the same time cause for instance a larger ToT than a single photon due to the larger amplitude of the resulting analog signal which roughly corresponds to 40 ns compared to the 30 ns for one photon [110]. But a second photo electron arriving during the falling flank of the first can cause a ToT of up to 60 ns.

A plot of the recorded ToT for a single PMT is shown in Fig. 39a. The distribution peaks around 30 ns since most of the recorded light is caused by single photo electrons created by potassium decays. The ToT is determined as the mean of a Gaussian fit to in a range of ± 4 ns around the mean of the ToT distribution. The resulting ToT for all PMTs in run 311 is shown in Fig. 39b. Most PMTs show a ToT around 33 ns, with the two turned off PMTs having no signals and therefore no recorded ToT. During the data taking the ToT was monitored by looking at the mean of the ToT distribution per PMT which yields an average ToT of 30 ns per PMT and therefore no HV retuning was performed. Two channels in DOM 1 show a significantly higher ToT and were re-tuned accordingly in later data taking.

4.6.2 *Single rates*

The single counting rate is the most rudimentary detector measurement and gives insight into the functionality of the PMTs. On each DOM a group of six PMTs share a high rate veto criteria. The veto is triggered when the six PMTs have an accumulated joined counting rate greater than 250 kHz in a time slice. Data is written until the count rate surpasses the veto value, once the veto value

is exceeded no more data is written for these PMTs. Due to the grouping of 6 PMTs per high rate veto one channel per DOM is left with a single high rate veto, DAQ channel 15. Hence the rate studies are performed with channel 15 to avoid high rate veto influence.

Two PMTs out of the 93 have been found faulty and are not used. DAQ channel 27 (PMT ID 17) in DOM 3 was found to saturate the high rate veto continuously and was therefore turned off. DAQ channel 14 (PMT ID 1) in DOM 2 was not reachable after DOM assembly. The remaining 91 PMTs are fully operational.

For triggered data files the singles rate per slice is stored in the so-called summary slices data structure. The recorded rates for one PMT and run are shown in Fig. 40a. The rate is stored in a 8 bit compressed datum with a higher resolution in the region of interest from 5.5 kHz to 7.5 kHz. The rate shows a Gaussian distribution around the mean of 6.5 kHz with a tail towards higher values. These two parts of the distribution correspond to different physical sources. The Gaussian distribution is caused by potassium decays and PMT dark rate while the tail is caused by bursting bioluminescence events.

In order to check the data recorded in the summary slices a second method was used to determine the singles rates. For this purpose untriggered data files are used. By recording the time difference of consecutive hits on the same PMT the single rate can be determined. A histogram of such a distribution for DAQ channel 15 (PMT ID 14) in DOM 2 for run 311 is shown in Fig. 40b. The histogram shows structure around at time differences around 3 μ s. At late time differences an exponential decay of the single rate is observed. The structure around 3 μ s is caused by so called afterpulses in the PMTs. These originate due to rest gas atoms inside the PMT vacuum tube which can be ionized and due to their higher mass arrive later. The time difference is typical for the expected rest gas ions from PMT production. By fitting the exponential decay part the single rate of each PMT can be obtained. The used fit function is

$$f(x) = p_0 \times \exp(-p_1 \times x) \quad ,$$

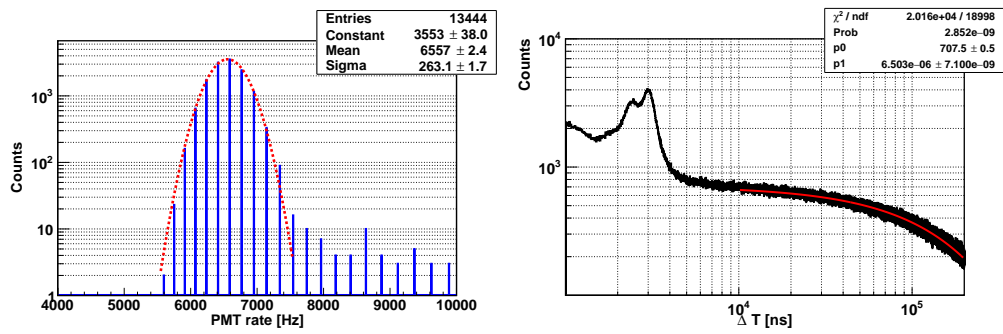
where p_1 is the rate and p_0 is a scaling factor.

Comparing both methods the results are found to be summary 6557 Hz and exponential 6503 Hz which agree reasonably well. The resulting rates from the exponential fits for run 311 are shown in Fig. 40c. The PMTs in DOM3 show a systematically higher rate, this is caused by the higher PMT efficiency as discussed in Sec. 4.2.

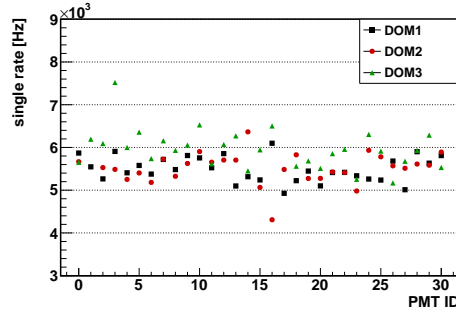
The counting rate of the PMTs are well understood. Two different methods are established to monitor them which are in good agreement. This knowledge of the single rates is needed as input to the background simulations and the time calibration as discussed previously.

4.6.3 Recorded triggered events

The trigger algorithms are discussed in Sec. 4.3.1. A comparison of the trigger rates between data and MC helps to identify trigger settings which separate



(a) Rate per summary slice for DAQ channel 15 (PMT ID 17) in DOM 2; red line shows Gaussian fit. (b) Consecutive hits on same PMT for DAQ channel 15 in DOM 2; red line shows exponential fit.



(c) Obtained single rates from exponential fit.

Figure 40: Single rate study plots for run 311.

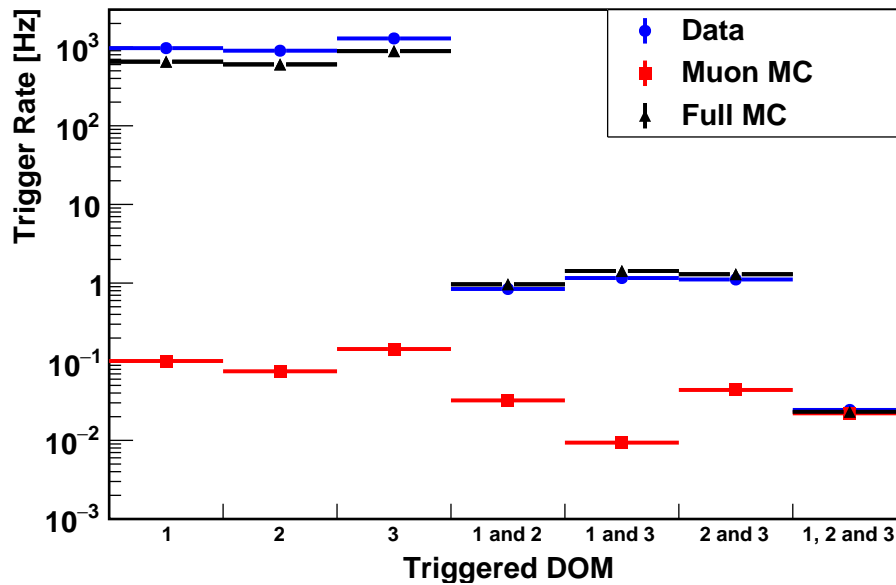


Figure 41: Rate of the different triggered events by DOMs with at least one L1 hit of all triggered events in phase 2, Full MC is the muon MC plus potassium MC.

muon and background events. Shown in Fig. 41 are the rates of the different types of triggered events. The triggered events either have a single DOM, two DOMs or three DOMs with L1 hits within the trigger time window. The different number of DOM triggers are plotted in an exclusive manner. For example a 3 DOM trigger event is not counted as a 2 DOM trigger events as well. As can be seen the single DOM and two DOM triggered events are dominated by random potassium background, while the three DOM triggers are dominated by muon signals. The over estimation of the data in the MC for single DOM triggers of around 30 % and the underestimation of 2 DOM triggers of around 30 % is significant and points to a flaw in the corresponding calculations of the expected random coincidences by potassium decays (see Sec. 4.4).

4.6.4 Muon detection

The detection of muon signals with the PPM-DU illustrates the advantages of multiple PMTs in the same DOM. Already a single multi-PMT DOM allows a discrimination between potassium and muon signals.

A method to distinguish random background and physical events is made possible by observing correlated signals in different PMTs on a DOM. A plot of the recorded coincidences in phase 2 is shown in Fig. 42a. The distribution in data and full MC (muon and potassium MC added together) both show two regimes of different slope. The larger slope from coincidence size 2 to 6 is dominated by coincidences from potassium decays. The higher rate of DOM 3 in this area is caused by the higher total detection efficiency of the Hamamatsu PMTs. The region of with a smaller slope from coincidence size 7 and upwards

matches that of the muon data shown in the filled histograms. Coincidences of size 7 and greater are therefore dominated by muon events.

A plot of the ratios between data and MC is shown in Fig. 42b. The data and MC show good agreement for coincidences of size three while deviating for size two and in the region of coincidence size 4 to 6. For these coincidence sizes the MC underestimates the MC and for coincidence sizes 4 to 6 the underestimation gets more drastic with increasing coincidence size. This deviation is caused by two different effects, namely: The simulation of random coincidences and the PMT efficiency.

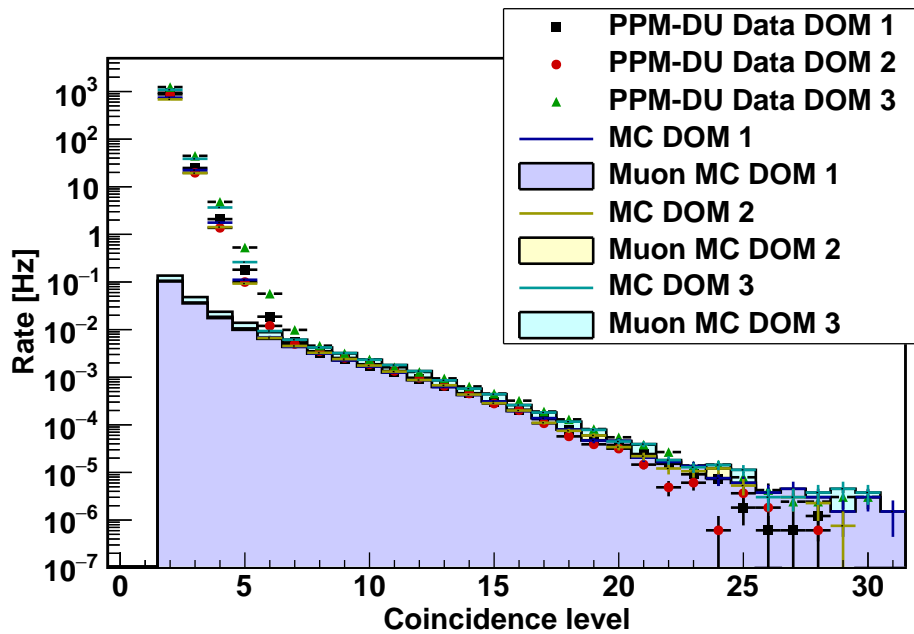
For coincidence size two the dominant contribution is due to random coincidences and spurious pulses may have a significant influence. These effects are not taken into account in the simulation. Therefore, the data is underestimated, especially for the two ETEL DOMs. For coincidence sizes larger than two the random background contribution is negligible causing the MC to match the data well for coincidences of size three. With increasing coincidence size the deviation of the MC starts to grow exponentially. This effect is most likely caused by an underestimation of the efficiencies which indeed affects the rate exponentially with increasing coincidence size. This effect is most likely caused by the angular acceptance of the PMTs on potassium decays. The larger the coincidence the more likely it is to observe light at large incident angles on the PMT cathode. The MC simulation therefore seems to underestimate the angular acceptance of the PMTs, causing the agreement between data and MC to worsen in that regime. From coincidence 7 to 18 data and MC are in good agreement. At coincidence sizes 19 and upward MC starts to overestimate the number of events. The cause for this is not identified yet but could be correlated with the assumed water parameters. The difference in data between DOM 1 and the other two at the largest coincidence sizes is caused by the fact that only DOM 1 has 31 PMTs operating. Therefore DOM 1 has a higher chance of detecting large coincidences and is the only DOM that can record coincidences of size 31. The illumination of a DOM is not strongly correlated with the energy of the muons but rather with the distance between the muon and the DOM. Coincidence sizes of 25 and larger are mainly caused by muons which are within 10 m distance of closest approach to the PPM-DU.

In order to confirm the observation that coincidences of size 6 and larger are muon events the zenith pattern of the hit PMTs gives further insight. For an atmospheric muon to reach the detector it has to traverse about 3.5 km sea water. Due to the energy loss most muons are down-going (zenith angle close to 0°). The expected angular distribution of the atmospheric muons would cause a characteristic signature in the multi-PMT DOMs. Since PMTs which point towards the muon track have a higher possibility to be hit by Cherenkov light, it is expected that the upward looking PMT rings E and F to record more hits than the downward looking PMT rings.

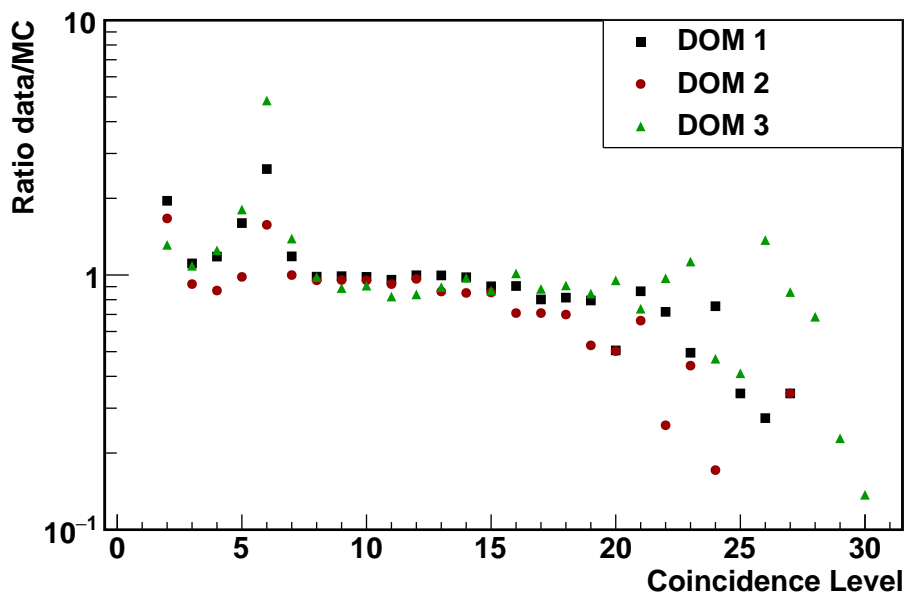
A histogram of the hit PMTs for coincidence sizes 6 and greater is shown in Fig. 43. As can be seen, all three DOMs show significantly more hits in the upward pointing rings. This confirms the conclusion drawn from Fig. 42a that coincidence of sizes 6 and larger are dominated by muon events. Comparing

the data and MC in this plot shows a difference in the expected rates in the individual PMTs although the MC is adjusted with the estimated efficiencies. This could be caused by the fact that the efficiencies are estimated using potassium decays. The light observed by the PMTs for muon events is mainly produced via the Cherenkov effect. The PMT efficiencies for these two light sources could be different. For instance the wavelengths or the angle of the incident photons could be different, causing the effective efficiencies to vary. The difference in the overall scale per DOM is caused by the fact that DOM 3 and 2 are more likely to be hit by muon light than DOM 1 since they are higher up and therefore more muons can reach them and the higher efficiency of PMTs in DOM3.

For a muon event the light arrival time on the DOMs is correlated with the travel time of the muon along the string. The travel time of the muons depends on the zenith angle of the muons, with straight down-going muons having the shortest travel time. The energy of a muon does not affect the travel time since at the typical energies of 1 GeV or higher all muons travel at the speed of light. For the purposes of studying the muon travel time the time difference between the first L1 hits on each DOM are an ideal measurement. The histograms of DOM time differences for two and three triggered DOM events are shown in Fig. 44. Both histograms show a distinct peak in the distribution that corresponds to muons traveling down along the PPM-DU. The shapes of the peaks are correlated with the zenith distribution of the muons, the detection efficiency of the PMTs and the scattering length of light in water. The two DOM trigger histogram shows the peak above a constant background of random coincidences while the three DOM histogram is almost background free. The difference in random background between different DOM triggers was already shown and discussed in Sec. 4.6.3. The shapes of the data is reproduced by the MC scaled by entries showing that the simulated muon fluxes per angle is in good agreement with what is measured in the deep sea. For difference scaled by lifetime see the corresponding entries shown in Fig. 41.



(a) Rate as function of size of recorded coincidences in phase 2 data taking period; Filled histograms show the muon MC, lines without markers muon and potassium MC added and lines with markers the data; MC scaled by lifetime to the data.



(b) Ratio between lifetime scaled data and MC for different recorded coincidence sizes as shown in Fig. 42a in phase 2 data taking period.

Figure 42: Coincidence size studies for phase 2 data taking.

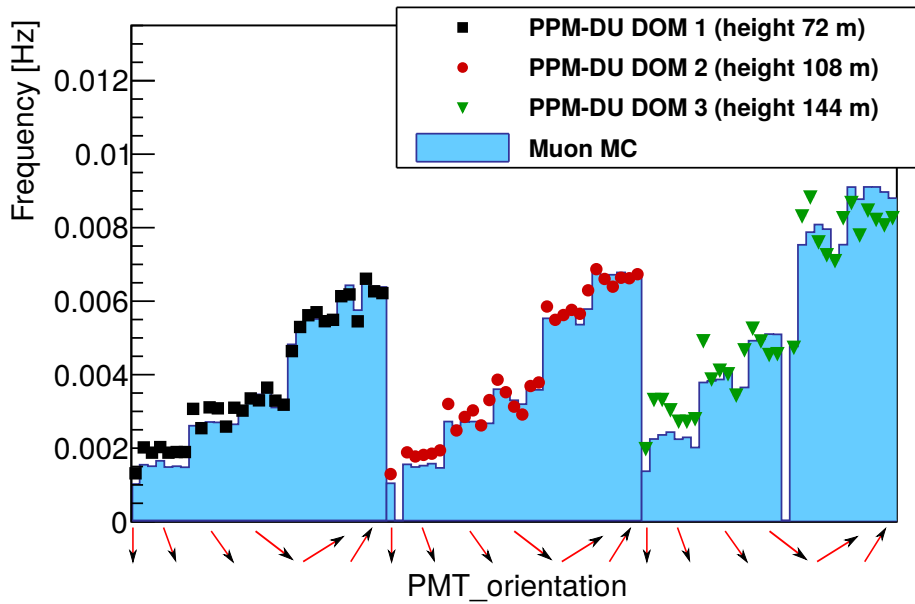
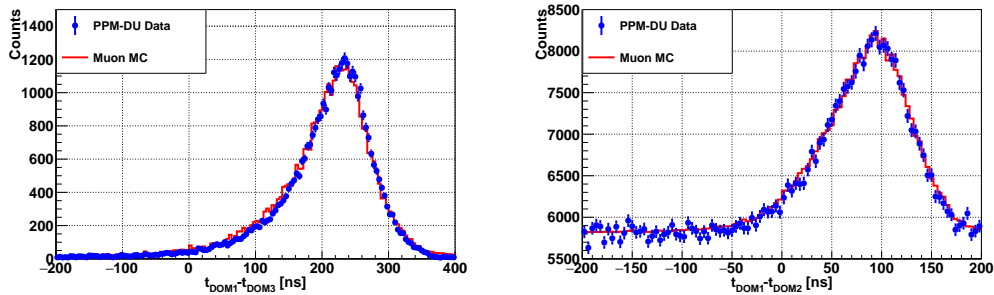


Figure 43: Rate of PMTs for events of coincidence size 6 and greater; Filled histograms show the muon MC, markers the data; MC scaled by lifetime to the data per DOM.



(a) Time difference between first L1 on DOM 1 and DOM 3 in case of a three DOM trigger (at least one L1 on each DOM).

(b) Time difference between first L1 on DOM 2 and DOM 3 in case of a two DOM trigger (at least one L1 on DOM 2 and 3, no L1 on DOM 1).

Figure 44: DOM ΔT distributions for the first L1 on each DOM; event selection is exclusive (no double counting of three DOM triggers); MC scaled to data by entries.

4.7 MUON RECONSTRUCTION

The reconstruction of the muon tracks with the PPM-DU is a first step towards the analysis needed for a fully operational KM₃NeT detector. The final goal of a neutrino telescope is the detection and reconstruction of neutrino events. For the reconstruction of neutrino events two different channels have to be distinguished, the shower and the track events. Of these two types the track reconstruction is attempted with the available number of DOMs.

A charged particle traveling through the water at the speed of light continuously radiates Cherenkov photons in a characteristic angle of about 42°. This so called Cherenkov cone allows for a reconstruction of a straight trajectory due to a muon passing by the PPM-DU.

The track reconstruction algorithm used is based on the Antares single line fit [111]. A track can be parameterized as a function of arrival time of the Cherenkov photons on the DOMs as given by

$$t = \left[(z - z_0) * \cos \theta + \sqrt{n^2 - 1} * \sqrt{d_0^2 + (z - z_0)^2 * (\sin^2 \theta)} \right] / c + t_0 \quad , \quad (19)$$

where t_0 , z_0 , d_0 are the time, height and distance of the point of closest approach between DOM and track, n is the refractive index of light in water, θ is the zenith angle of the track and t is the expected hit time on the DOM. An example sketch of a muon event and the parameters are shown in Fig. 45.

In order to select a clean muon sample only events with three triggered DOMs are considered. As discussed in Sec. 4.6.3 this selects an almost background free muon sample.

This single line track fit suffers from symmetric solutions in the ϕ angle of the track. These are caused by the fact that a single string without taking into account the position of the hit PMTs can not distinguish between rotation symmetric solutions around the z -axis. The fact that the PPM-DU only includes three DOMs introduces further degeneracies in the track fit. A track that neglects the ϕ reconstruction as shown in Eq. 19 has four degrees of freedom. Therefore by using one hit time per DOM degeneracies in the solution phase space are caused. By a proper selection of the phase space these degeneracies can be reduced.

4.7.1 Fitting procedure

All events with three triggered DOMs are processed in the reconstruction. From the triggered hits the start values of the fit are deducted. The mean z height (z_{mean}) and mean time (t_{mean}) of all hits that compose a L1 hit on the three DOMs is calculated. The starting values of the fit are then set as $t_0 = t_{\text{mean}}$, $z_0 = z_{\text{mean}}$, $d_0 = 0$ and $\cos \theta$ is varied between 1 to 0.505 in steps of 0.005. For every value of $\cos \theta$ Eq. 19 is minimized using the ROOT Migrad

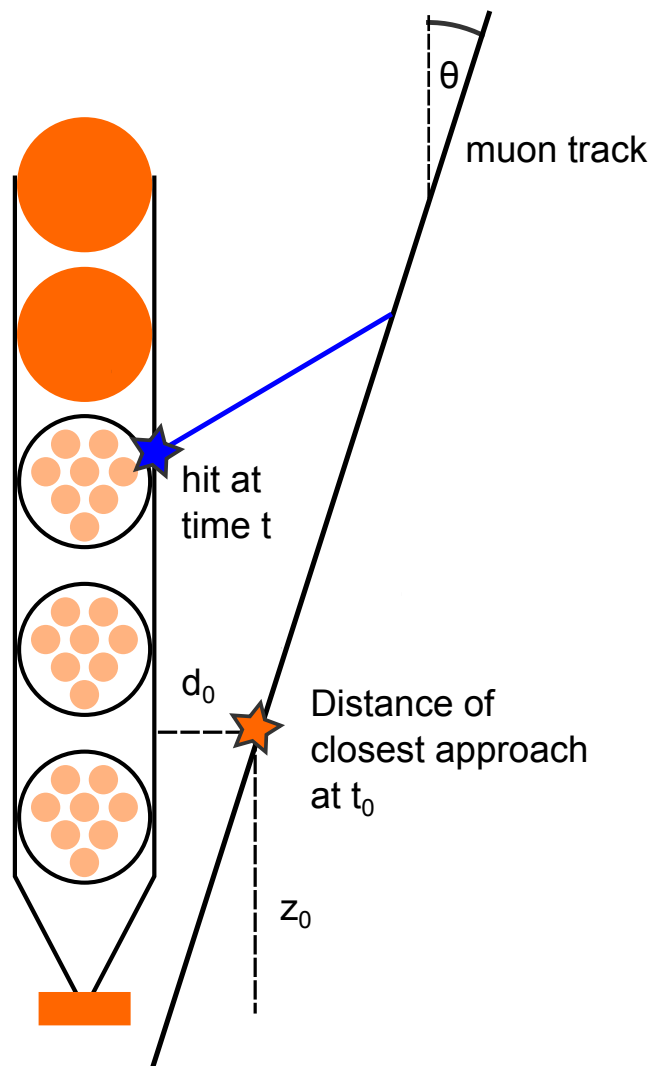


Figure 45: Sketch of a muon event passing the PPM-DU with the parameters of a parametrization discussed in Eq. 19.

minimizer [101]. The χ^2 of each fit is calculated based on the hit time residuals of all triggered hits to the fitted track as shown in Eq. 20

$$\chi^2 = \sum_i \left(t_{\text{hit}}^i - \text{expected } t_{\text{hit}}^i \right)^2, \quad (20)$$

where t_{hit}^i is the hit time of all Lo hits composing the L1 hits and the expected hit time is based on the reconstructed track. The best fit is selected as the fit with the lowest χ^2 . Every reconstructed event is then discriminated based on selection criteria discussed in Sec. 4.7.2.

4.7.2 Event selection

The event selection is an essential part of the reconstruction in order to limit the influence of the degeneracies in the solution phase space. A way to identify regions with degeneracies is by calculating the expected DOM time differences from Eq. 19 for a set of values. Therefore the parameters of Eq. 19 are varied as follows: $\cos \theta$ from 0.98 to 0.5 in different step sizes (see legend of Fig. 46a), d_0 from 0 m to 10 m in steps of 1 m and z_0 from $\text{DOM}_1.z - 30$ m to $\text{DOM}_3.z + 30$ m in steps of 1 m. The resulting DOM time differences are shown in Fig. 46a. The different solutions show specific characteristics that can be exploited to select regions with minimum degeneracies and reject unphysical events. The regions with most overlays in different $\cos \theta$ distributions are at $t_{\text{DOM}_1} - t_{\text{DOM}_2} \geq 150$ ns ($\Delta T_{12} \geq 150$ ns) and tracks approaching horizontal directions. Since tracks that approach horizontal directions are suppressed naturally by the small amount of muons reaching the detector at these angles the corresponding regions is not excluded by a specific selection. Three other selections on the DOM time differences have been performed in order further limit the selection of tracks with reasonable phase space: $-50 \text{ ns} \leq \Delta T_{12} \leq 150 \text{ ns}$, $-50 \text{ ns} \leq \Delta T_{23} \leq 165 \text{ ns}$ and $\Delta T_{23} - \Delta T_{12} \leq 10 \text{ ns}$. The selections on the DOM time differences cuts out a triangle as indicated by the black lines shown in Fig. 46a.

The distribution of data events in the DOM time differences is shown in Fig. 46b together with the selections. As can be seen a low amount of the events lies outside of the selection. These are mainly events caused from random coincidences. The main part of the data is in the region of down-ward going muons which we expect from the survival probability of the muons. The area at ΔT_{12} between 150 ns to 160 ns shows a significant number of events and is excluded, but since the highest degeneracies are expected in this region no well reconstructed tracks are lost

A selection on the distance of closest approach between the PPM-DU and the muon track was performed. The effect of the distance on the degeneracies is shown in Fig. 47, here the variables are the same as shown in Fig. 46a except for d_0 was varied from 10 m to 20 m (instead of 0 m to 10 m). The tracks with larger distances cause high degeneracies, even at highly down-ward going angles. The distance of closest approach was therefore selected to be $d_0 \leq 10$ m.

The rate of selected events for the selection criteria in data and MC are shown in Fig. 48. The rates are inclusive and the selection criteria are applied from

left to right as shown in the figure. An event that is rejected by one criterion is therefore not passed on to the next. It can be seen that the MC is underestimating the data by roughly 10%. This factor is observed in all comparisons. Except for the offset the MC and data match nicely for all selection criteria. We can also observe that after cutting on $d_0 \leq 10$ m the last cut on unphysical events $\Delta T_{23} - \Delta T_{12} \leq 10$ ns rejects no further events, proving the distance of closest approach cut to be effective in rejecting unphysical events.

The performance of the cuts on the reconstructed zenith angle resolution is shown in Fig. 49. Although well reconstructed events are lost during the selection, the tails towards badly reconstructed events are highly suppressed. This shows that the sample of select tracks is of high quality.

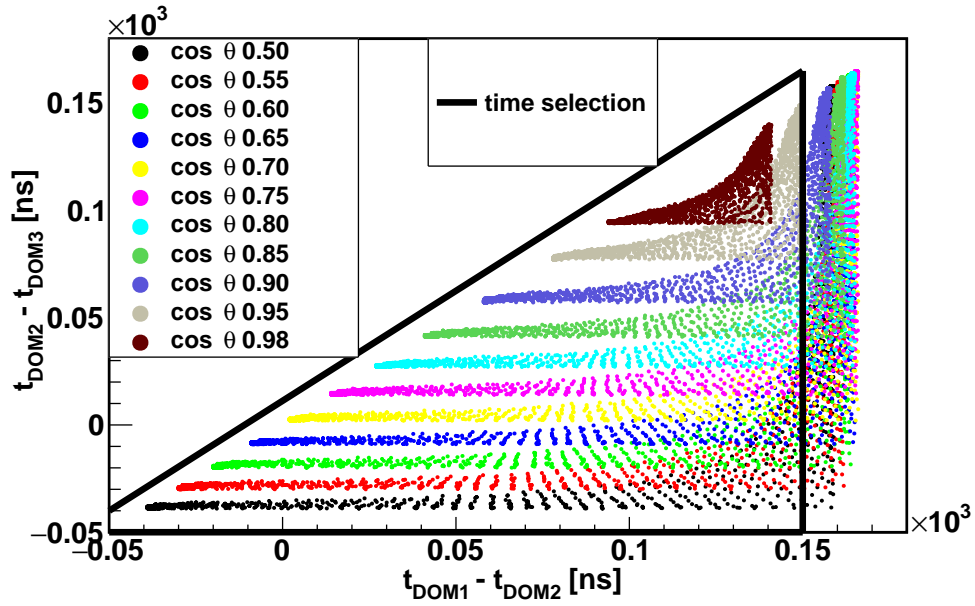
4.7.3 Zenith angle reconstruction

The goal of the track reconstruction is the identification of muons passing the PPM-DU. Since the Φ angle is neglected, the zenith angle θ is the only parameter that can be sensibly reconstructed. The distance of closest approach between line and track is needed for the track reconstruction, but the parameter itself holds little physical interest.

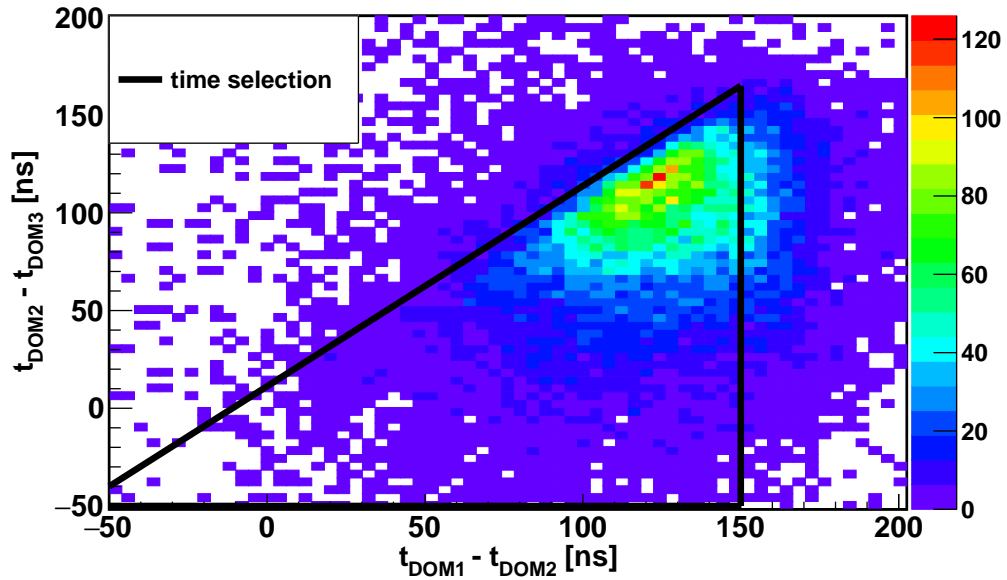
The θ angle is of high interest for MC studies. It can probe if the production of the muons in the atmosphere and the propagation through the sea water is performed correctly.

The resolution of the zenith angle reconstruction is determined using the MC production. By comparing event by event the reconstructed angle with the simulated angle the resolution can be determined. In Fig. 49 the resulting resolution is shown. The reconstruction after selection criteria achieves in angular resolution of 8.3° RMS.

The reconstructed $\cos\theta$ distribution is shown in Fig. 50. As discussed previously the MC underestimates the data by roughly 10%. Except for that offset, data and MC are in excellent agreement.



(a) Possible DOM time differences for Eq. 19 and different $\cos \theta$; varying d_0 from 0 m to 10 m in steps of 1 m and z_0 from 30 m below DOM_1 to 30 m above DOM_3 in steps of 1 m.



(b) DOM time differences of all three DOM trigger events in phase 2.

Figure 46: Solution phase space studies in DOM time difference distributions; the black lines indicate the performed selection for DOM time differences.

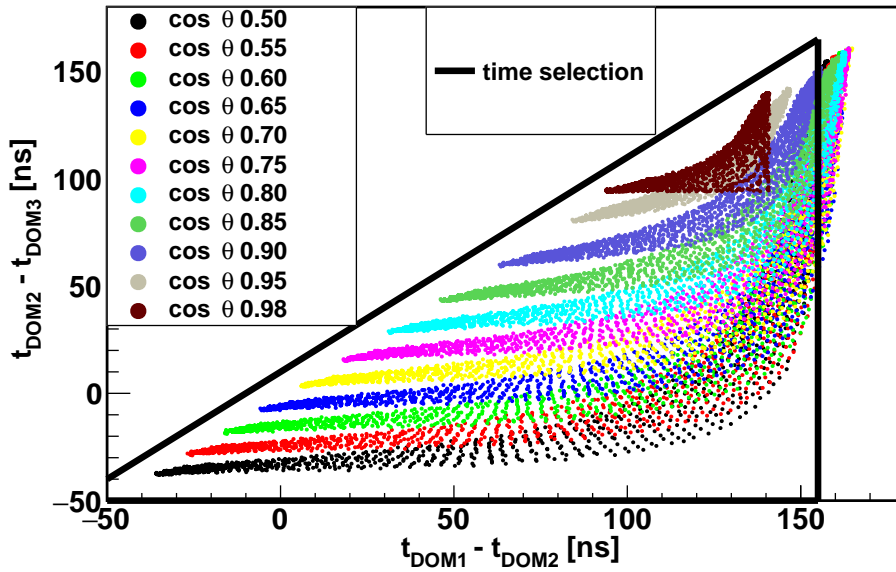


Figure 47: Possible DOM time differences for Eq. 19 and different $\cos \theta$; varying d_0 from 10 m to 20 m in steps of 1 m and z_0 from 30 m below DOM_1 to 30 m above DOM_3 in steps of 1 m.

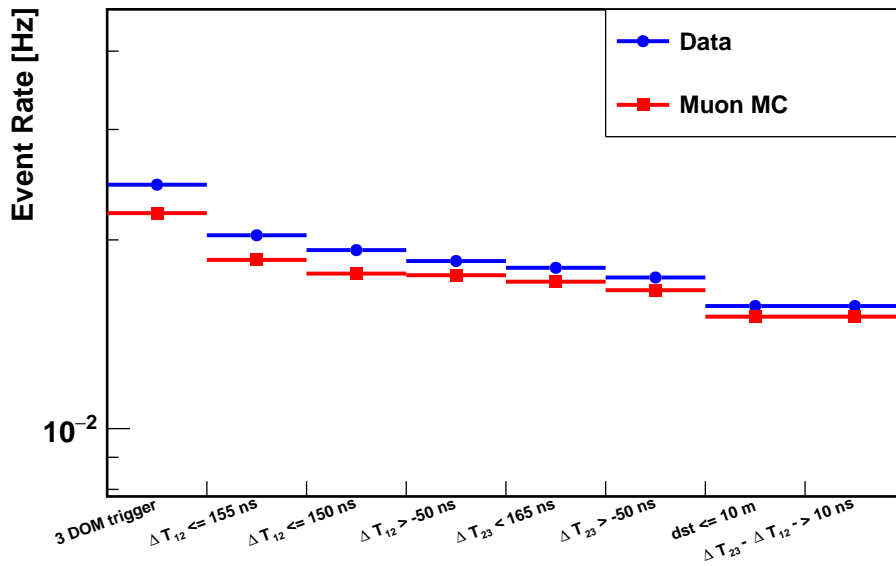


Figure 48: Event rate of all performed selection criteria of the muon reconstruction; event rates are inclusive and selections are performed from left to right.

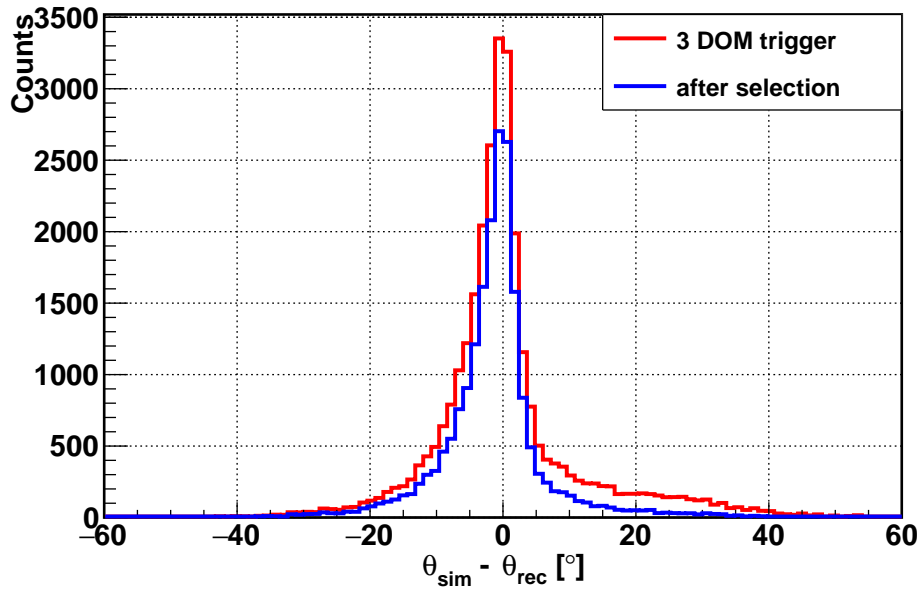


Figure 49: Zenith resolution of the reconstructed tracks for all three DOM trigger events and events that pass the selection respectively.

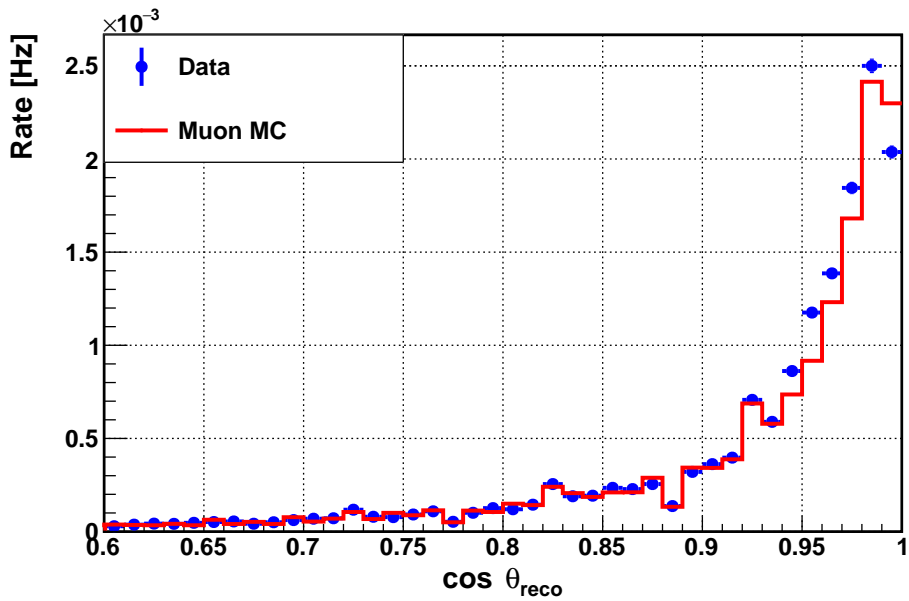


Figure 50: Reconstructed cosine of the zenith angle in data and MC.

4.8 PPM-DU CONCLUSION

The deployment of the string prototype proved a great success for the KM₃NeT collaboration. Especially regarding the calibration procedures and technical design.

The successful deployment and installation of the prototype was the first of a string with operational DOMs proving the procedures to be working. The use of different PMTs allowed for a direct in-situ comparison showing the advantages of the Hamamatsu PMTs.

The in-situ calibration of the PMTs utilizing the light from potassium decays proved to be working, thereby laying the ground for the in-situ PMT calibration of future detection units.

The time calibration between DOMs using the atmospheric muons and/or the LEDs showed to be working but needs further improvement in the future in order to achieve the 1 ns timing accuracy needed for the KM₃NeT detector.

The studies of the basic detector operations such as single rates and ToTs proved the basic understanding of the detection unit. Building on that and the results from the previous DOM prototype the identification of the atmospheric muons was performed utilizing the multi-PMT design.

The follow up muon reconstruction was based on a basic algorithm. Therefore, only a zenith angle reconstruction was possible. Different approaches utilizing the multi-PMT design in order to achieve azimuth sensitivity were performed but did not lead to a firm conclusion.

In total, the string prototype laid many important ground work for the first full strings to build upon. Allowing to prepare detector operation and data analysis for the KM₃NeT detector.

Light thinks it travels faster than anything but it is wrong. No matter how fast light travels, it finds the darkness has always got there first, and is waiting for it

Terry Pratchett, Reaper Man

The Belle Starr reconstruction is a set of algorithms developed to reconstruct a two shower signature caused by tau neutrino interactions. Additionally, it provides discriminators to distinguish two shower signatures from other signatures in the KM₃NeT detector. To achieve this goal the reconstruction is divided into four steps, namely:

- *Prefit*: Reconstruct position, direction and energy based on single shower hypothesis
- *Scan*: Evaluate two shower likelihood along the trajectory established by Prefit
- *Peak*: Apply a peak finding algorithm on the likelihood scan
- *Refit*: Perform a two shower likelihood fit starting at the two positions established by Peak

The Refit step uses all the information present in the event by applying the two shower likelihood. Ideally, one would evaluate the likelihood in each point in space and time, but such a complete scan over the whole volume of the KM₃NeT detector is computationally too demanding. Therefore, Refit uses a minimizer to evaluate the two shower likelihood. The performance of such a minimizer in finding the correct minimum is strongly dependent on the starting values of the parameters. Hence, such starting parameters are provided by employing the algorithms Prefit, Scan and Peak.

Dividing the reconstruction into consecutive steps provides practical advantages in the application of the reconstruction, for instance, by allowing optimal CPU usage.

In this chapter the signal and background signatures for the Belle Starr reconstruction are discussed, followed by a description of the different reconstruction steps and their performances. The results presented are based on an isotropic astrophysical neutrino flux of

$$E^{2.46} \Phi_{\nu}(E) = 4.11 \times 10^{-6} \left(E/\text{GeV}^{-.46} \right) \text{GeV cm}^{-2} \text{s}^{-1} \text{sr}^{-1}$$

with a 3 PeV cut-off (see Chap 6), unless stated otherwise. Only neutrino events are considered, since at energies exceeding 10 TeV no differences between neutrino and anti-neutrinos are expected.

5.1 TAU “DOUBLE BANG” EVENT SIGNATURE

“Double Bang” events are one possible outcome of the CC interactions of tau neutrinos with a nucleon. In the “Double Bang” case, two showers are present, namely: One at the tau neutrino interaction vertex and another at the tau decay vertex for 82.4 % of the tau decays (see Sec. 1.2.4.3). The “Double Bang” events are also referred to as “tauCCshow” events in this work. Henceforth, the shower at the neutrino interaction is referred to as the neutrino shower and the shower at the tau decay as the tau decay shower.

While most “Double Bang” events look similar to electron neutrino CC interactions, for tau lepton energies in excess of $\mathcal{O}(100 \text{ TeV})$ the tau can fly visible distances before its decay. In this case, the two showers of “Double Bang” events can be independently identified. The likeliness of identifying these events mainly depends on the energy distribution between the two showers and the length of the tau flight path.

The energy distribution between the two showers is expressed in the Bjorken y variable which, in the detector frame, is given by:

$$y = \frac{E_\tau}{E_\nu} \quad , \quad (21)$$

where E_τ is the energy of the tau lepton and E_ν the energy of the neutrino that produced it. By definition, Bjorken y gives the energy distribution between the two showers of a “Double Bang” event not accounting for energy carried away by neutrinos. Since the energy of a shower approximately scales with the number of photons produced, Bjorken y is a measure for the relative luminosity of the showers. For “Double Bang” events with values of Bjorken y close to one or zero either of the showers can be so luminous as to make the other shower indistinguishable, causing the event to resemble a single shower signature. This effect is shown in Fig. 51, for event displays of the same event with different Bjorken y values. As can be seen, with Bjorken y approaching one the neutrino shower produces less light, to such a degree that it is not identifiable anymore by eye for Bjorken $y= 0.99$. Although these event displays cannot portray the full event information (e.g. they lack the time of all hits) they give a good indication on the likeliness of reconstructing two showers.

The second important characteristic is the spatial separation between the two showers, which is given by the tau flight length. In order to distinguish “Double Bang” events from single shower events, they have to be separated by visible distances. For most “Double Bang” events the two showers are mainly overlapping due to the short lifetime of the tau lepton. However, at relativistic

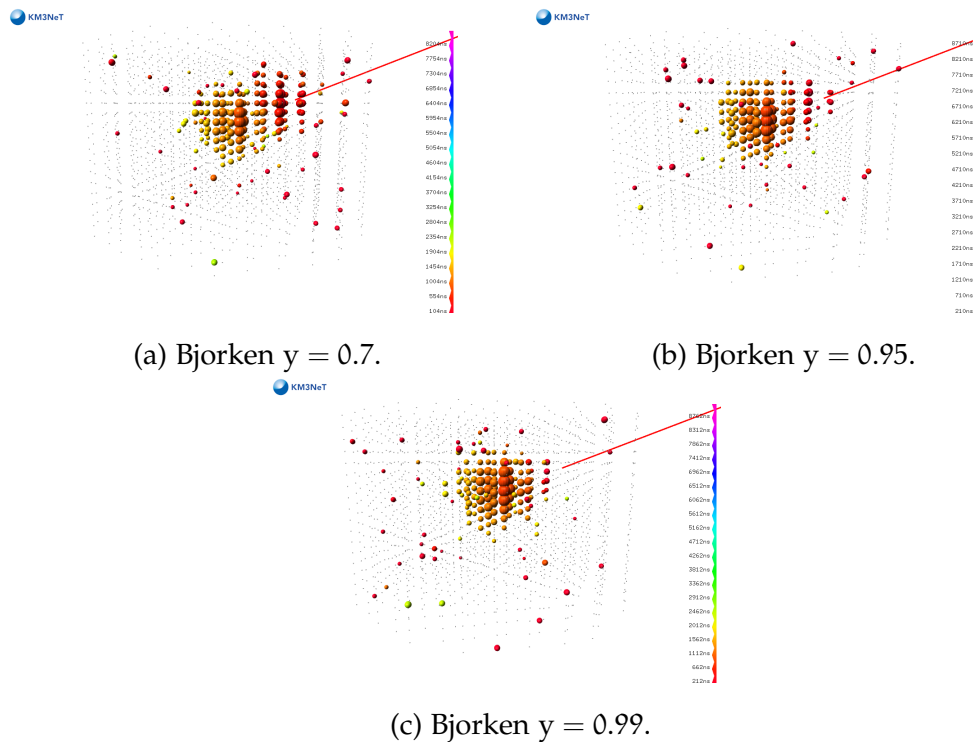


Figure 51: Event displays for a toy MC simulation of a “Double Bang” event with different Bjorken y values but otherwise identical kinematics; initial neutrino energy of 500 TeV and a tau flight length of 200 m; the red line indicates neutrino flight path; colored spheres show hit DOMs, the size of the spheres indicates the number of hits and the color indicates the time of the first hit.

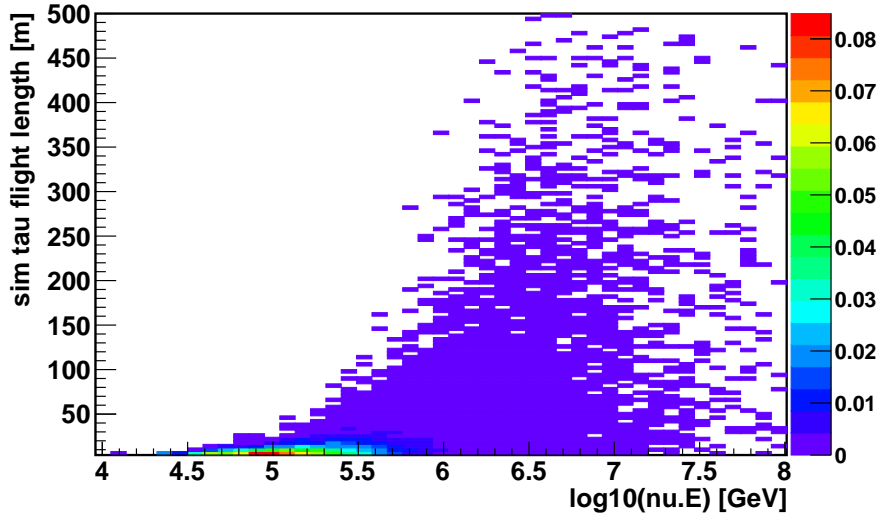


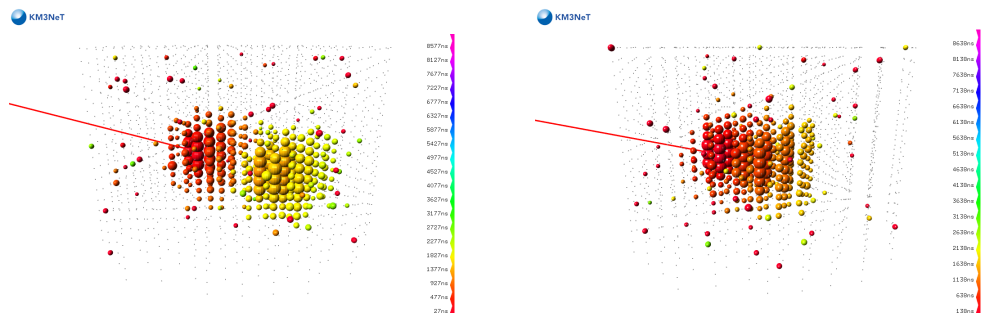
Figure 52: Simulated tau flight length versus neutrino energy for “Double Bang” events for which the tau flies at least 5 m and both shower vertices are contained in the instrumented volume; Z-axis: rate per year per block.

energies, the tau lepton can fly visible distances. The relation between tau flight length L_τ and tau energy at mean lifetime is given by:

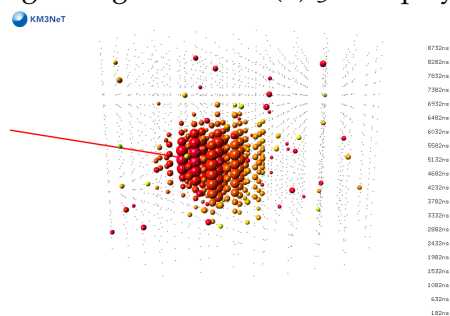
$$L_\tau = 4.9 \text{ m} \times \frac{E_\tau}{100 \text{ TeV}} \quad . \quad (22)$$

The distribution of the tau flight lengths as a function of the neutrino energy is shown in Fig. 52. As anticipated, the tau flight length increases with simulated energy. The Belle Starr reconstruction is expected to resolve the two showers if they are separated by a distance larger than its position resolution. Typical position resolutions for shower events in KM₃NeT are around one meter, corresponding to a tau lepton energy of around 100 TeV and higher. Tau events with shorter flight length cannot be distinguished from single shower events using a position reconstruction. An example of the apparent distance between showers is shown in Fig. 53. In the figure, the same “Double Bang” event is shown for varying tau flight length. As can readably be seen, the two showers are easily identified at a flight length of 300 m, while they are hard to be identified at 150 m and at 70 m the signature looks like a single shower by eye.

The requirements for Bjorken y and tau flight length for a “Double Bang” event to be identifiable are contradictory. While large Bjorken y enhances the energy of the tau lepton and thereby the tau flight length, it can cause the tau decay shower to be too luminous to identify the neutrino shower. This conflict is especially significant at neutrino energies of $\mathcal{O}(100 \text{ TeV})$, since the tau lepton needs a significant fraction of the energy to achieve visible flight length. The energy dependence is shown in Fig. 54, by requiring a minimum flight length of 5 m and looking at the tau decay shower energy versus the neutrino shower energy. As can be seen, the distribution at energies below $\mathcal{O}(100 \text{ TeV})$ favors



(a) 3D display; tau flight length 300 m. (b) 3D display; tau flight length 150 m.



(c) 3D display; tau flight length 70 m.

Figure 53: Event displays for a toy MC simulation of a “Double Bang” event with different simulated tau flight length but otherwise identical kinematics; initial neutrino energy of 2 PeV and a Bjorken y of 0.7; the red line indicates the neutrino flight path; colored spheres show hit DOMs, the size of the spheres indicates the number of hits and the color indicates the time of the first hit.

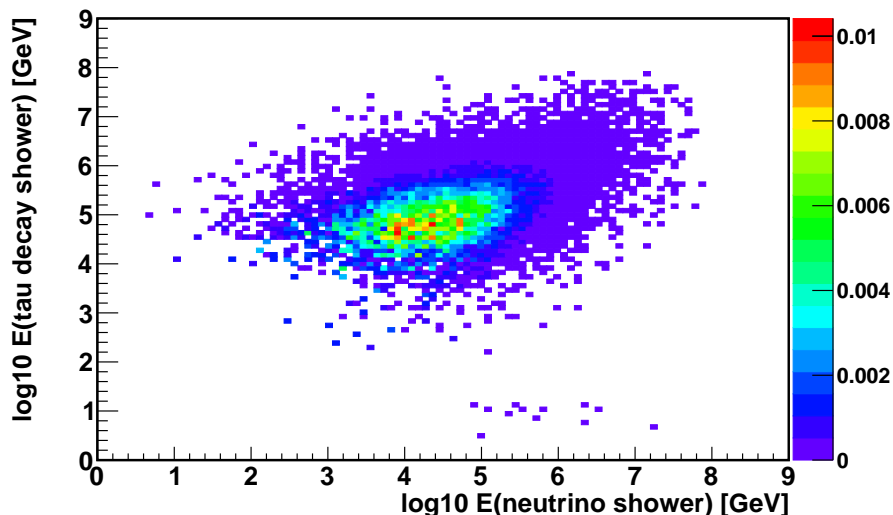


Figure 54: Visible energy of the tau decay shower plotted against the visible energy of the neutrino shower for “Double Bang” events which fly at least 5 m and have both vertices contained in the detector; Z-axis: the rate per year per block.

the tau decay shower to have more energy than the neutrino shower while no such effect is visible for larger energies. If one would require a larger tau flight length, the asymmetry would increase and extend to higher energies. Due to this conflict, identifying a clear threshold value of Bjorken y at which “Double Bang” events are identifiable is not straightforward. One should keep in mind, that large Bjorken y values benefit the tau flight length and thereby tau identification, but extremely large y values can be detrimental to the “Double Bang” identification.

In addition to the Bjorken y and tau flight length, it is more practical for both vertices to be located within the instrumented detector volume. A “Double Bang” event is considered contained, if both the neutrino interaction vertex and the tau decay vertex are located within the instrumented detector volume.

For the above reasons, a subclass of ideal “Double Bang” events is selected. These events are required to have a minimum tau flight length of 5 m and to be contained. They are referred to as “tau signal events” in this work. This selection causes the overall Bjorken y distribution to be peaked at one as shown in Fig. 55, which is dominated by events at $\mathcal{O}(100 \text{ TeV})$.

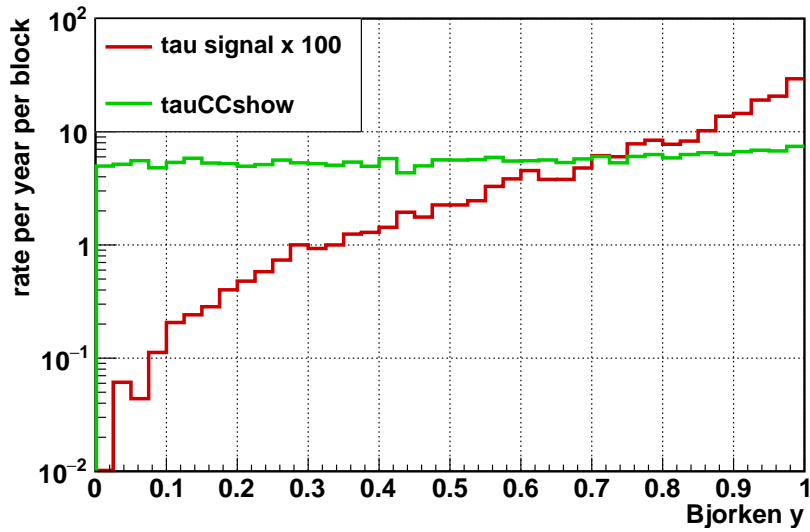


Figure 55: Bjorken y distribution for tau signal and all tauCCshow events; tau signal scaled by a factor 100.

5.2 BACKGROUND SIGNATURES

This section addresses how the track and single shower events can mimic a “Double Bang” signature. In the following, the most likely scenarios leading to “Double Bang” like signatures are illustrated.

Tracks: The muons can lose a significant fraction of their energy due to Bremsstrahlung. This will create showers along the track. These showers can cause “Double Bang” like signatures, since they are separated in time and space by the propagation of a relativistic particle. For neutrino induced track events, one shower is produced at the neutrino interaction vertex, requiring a single Bremsstrahlung shower to mimic a “Double Bang” signature. For atmospheric muons, two Bremsstrahlung showers or multiple muons are required.

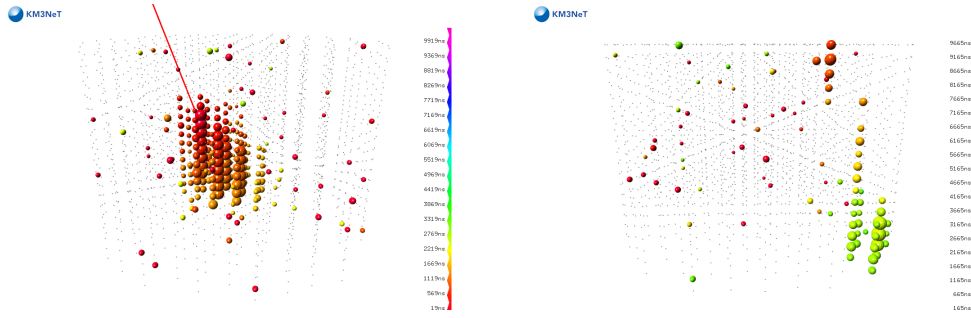
Some event displays of track events which produce a signature that can mimic “Double Bang” events are shown in Fig. 56.

Showers: There are three scenarios which can result in a “Double Bang” like signature: High energetic single showers, production of muons in the showers or different shower evolutions for showers with the same origin.

In the case of highly energetic showers, a single such shower can emit $\mathcal{O}(10^6)$ or more photons. This causes PMTs up to hundreds of meters away to be illuminated. In addition, a large amount of photons may scatter. Since scattered light arrives later at the PMTs, they can produce signals that mimic the presence of a second shower. An event display of such an event is shown in Fig. 57a.

In the rare case of a high energy secondary muon, the muon will propagate through the detector. It can then cause shower signatures by Bremsstrahlung leading to “Double Bang” like signals as discussed for track events. An event display of such an event is shown in Fig. 57b.

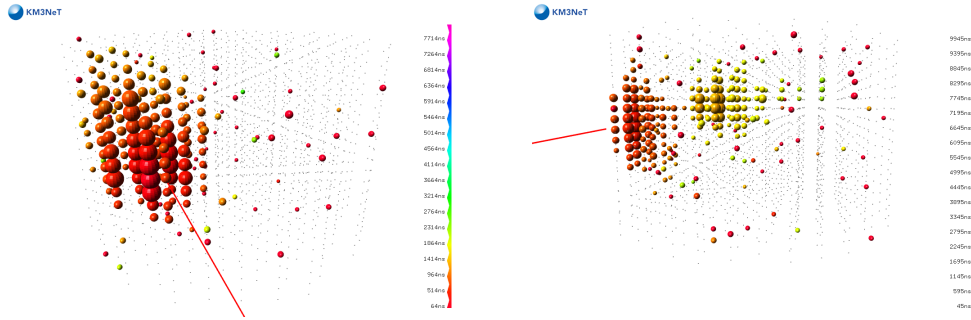
For two showers originating at the same vertex, different shower evolutions can be caused by a difference in particle content or energy. The effect can



(a) A numuCC with 7.2 PeV and 3.5 TeV muon energy. (b) An atmospheric muon event with a single muon of 0.88 PeV at can level.

Figure 56: Event displays for track events; the red line indicates neutrino flight path; colored spheres show hit DOMs, the size of the spheres indicates the number of hits and the color indicates the time of the first hit.

cause variations between shower maxima positions of up to $\mathcal{O}(10\text{ m})$, thereby mimicking a “Double Bang” signal.



(a) A nueCC event with a neutrino energy of 3.6 PeV and an electron energy of 0.36 PeV.

(b) A nueCC event with a secondary muon, initial neutrino energy of 0.59 PeV, an electron energy of 0.36 PeV and a muon energy of 0.05 PeV.

Figure 57: Event displays for nueCC events; the red line indicates neutrino flight path; colored spheres show hit DOMs, the size of the spheres indicates the number of hits and the color indicates the time of the first hit.

5.3 BELLE STARR PREFIT

The Prefit performs a fit of the position followed by a simultaneous fit of the direction and energy of a single shower to the data. The routine is adapted from the AAShowerFit package developed by A. Heijboer [112] by changing the hit selection for the position fit.

5.3.1 Position and time fit

The position and time fit is performed using an M-estimator fit method. M-estimators are generalized least-squares estimators which allow for a modification of the normal distribution [113]. These modifications can have multiple purposes. In this case they are used to reduce the effect of outliers on the results of the fit, thereby making the fit more robust. Robustness in a statistical sense was coined in 1953 as: “insensitive to small departures from the idealized assumptions for which the estimator is optimized” [114]. Such a reduction is needed due to the optical background present.

The M-estimator is used to fit the position and time (4 parameters) assuming a single shower vertex. As a starting point of the minimization, the position and time of the earliest hit on the DOM with the most hits is used. The minimization is based on the score-function m , given by

$$m = A_h \times \sqrt{0.5 + \Delta T_h^2} \quad , \quad (23)$$

where A_h denotes the number of hits and ΔT_h the difference between the hit time and the expected arrival time (so-called hit time residual) for a shower assumption. By minimizing m , the reconstructed position and time correspond

to that of the shower maximum position. The hit time residual for the shower assumption is given by:

$$\Delta T_h = \text{dst}(\text{pos}_h, \text{pos}_{\text{vertex}}) / c_{\text{water}} + T_{\text{vertex}} - T_h \quad , \quad (24)$$

where $\text{dst}(\text{pos}_h, \text{pos}_{\text{vertex}})$ is the distance between the assumed shower vertex and the hit PMT, c_{water} is the speed of light in water, T_{vertex} is the assumed time of the shower vertex and T_h is the time of the hit. The speed of light in water is defined as $c_{\text{light}}/n_{\text{water}}$ with $n_{\text{water}} = 1.35$ the refractive index corresponding to KM₃NeT like sea water.

If multiple shower vertices are contained within the detector, the fit is biased towards the shower with the most hits. As the number of hits a shower produces approximately scales with the shower energy, the prefit is biased to reconstruct the position of the most energetic shower. This bias can be adjusted by employing a hit selection. For ‘‘Double Bang’’ events, biasing the hit selection towards the neutrino shower is found to be beneficial for the reconstruction performance: The direction reconstruction gets improved if the tau decay shower is downstream because it causes the maximal amount of hits point in the tau flight direction.

In order to create a sample of hits which are dominated by the neutrino shower the relative timing of the two showers is used. Since the neutrino interaction is always earlier in time, one would intuitively expect the neutrino shower hits to arrive first on a PMT. However, the assumption does not hold for the arrival time of the hits on all PMTs. While light travels at the speed of light in water, the tau lepton travels at the speed of light in vacuum which is a factor n_{water} faster. This enables the tau to ‘‘overtake’’ the light emitted by the first shower. Some light from the tau decay can actually arrive earlier than the light from the first shower. However, this effect only applies to a relatively small subset of the hits. Therefore, selecting the first hits on DOMs and PMTs produces a selection biased towards the neutrino vertex. For the prefit all hits on the same PMT within 500 ns are merged into the first hit. The effect of the hit merging is shown in Fig. 58. As can be seen, without a hit selection, the prefit typically yields the position of the tau decay vertex. Once the hit selection is applied, the prefit reconstructs a position on the tau flight path which is most likely inbetween the two showers. Such a position on the axis between the two showers is beneficial for the later steps of the reconstruction compared to the large spread of positions without the hit selection.

While this hit selection, on average, leads to reconstructing the neutrino vertex, one problematic case remains, namely: A selection of approximately equal number of hits from both showers. In such cases, the M-estimator score function does not have a global minimum at either shower position, but rather at a position somewhere else. This position is typically far outside of the detector, resulting in a low efficiency reconstruction.

This unwanted feature can be counteracted by adding another step to the hit selection, namely clusterizing. Clusterizing uses the correlation between hits given a certain hypothesis and finds the largest sub sample of correlated hits.

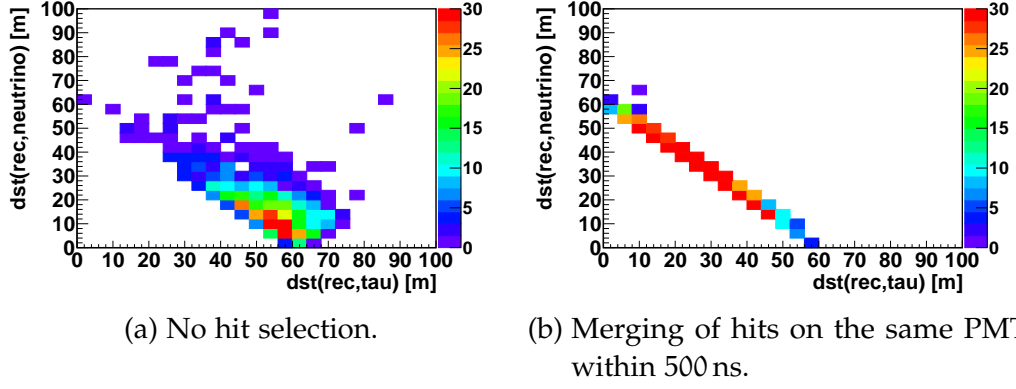


Figure 58: Toy MC simulation of events with a total energy of 1.5 PeV, a Bjorken y of 0.95 and a tau flight length of 60 m; X-axis: distance between prefit position and tau decay shower maximum; Y-axis: distance between prefit position and neutrino shower maximum; Z-axis: counts.

Given a shower hypothesis, hits are matched as follows: Per hit the number of hits with which this hit is correlated is determined and then the hit with the smallest number of correlated hits is discarded. This process is repeated until the hit with the lowest number of correlated hits has as many correlated hits as there are hits left in the selection. For showers, hits are correlated using the hit time differences assuming maximal spatial distance D_{\max} . For the “Double Bang” events $D_{\max} = 500$ m is chosen in order to select all hits. The maximal allowed time difference for two correlated hits from the same shower vertex depends on the distance between the two hits d in relation to the maximal distance D_{\max} as given by:

$$\begin{aligned} d \leq 0.5 \times D_{\max} : \\ \Delta T(\text{hit}_i, \text{hit}_j) - T_{\text{extra}} \leq d/c_{\text{water}} \end{aligned} \quad (25)$$

$$\begin{aligned} 0.5 \times D_{\max} \leq d \leq D_{\max} : \\ \Delta T(\text{hit}_i, \text{hit}_j) - T_{\text{extra}} \leq (D_{\max} - d)/v_{\text{water}} \end{aligned} \quad (26)$$

Considering that D_{\max} represents the typical distances between hits from a single shower, the reason for the two different cases is given by geometrical limitations: If the two hits are separated by more than half of the specified D_{\max} , the shower vertex has to be inbetween the two hits, thereby limiting the maximal time difference the hits can have. The quantity T_{extra} ensures that hits with extremely small distances are correlated independent of their distance. It is set to be 30 ns.

In the case of multiple showers, the algorithm starts by discarding the hit with the smallest number of correlated hits. If there is more than one such hit, one of them will randomly be discarded. As a consequence, the number of correlated hits will be reduced for the cluster to which the discarded hit belongs, causing clusterize to continually discard hits from that cluster. This results in a sub-sample of hits from one shower with a high purity. This effect

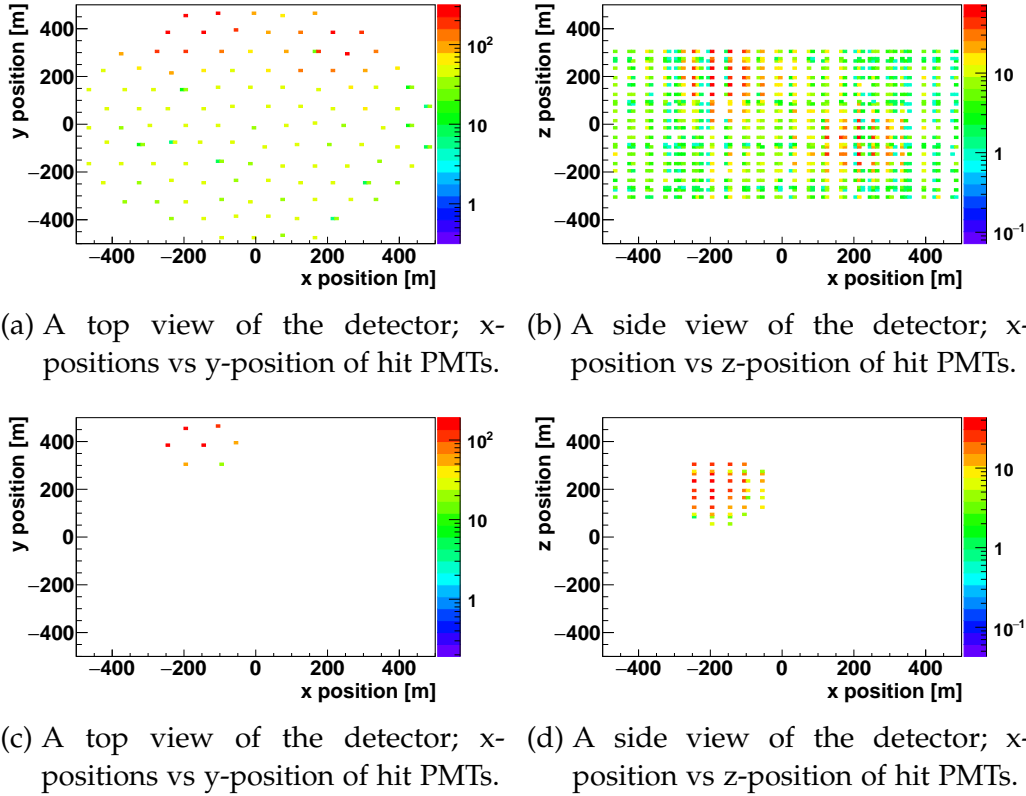


Figure 59: Event display of a contained “Double Bang” event with a tau flight length of 300 m and a neutrino energy of 2.54 PeV; top row shows the hits after merging, bottom row shows the hits after clusterize is applied.

is shown for a single “Double Bang” event with approximately equal hits from both showers in Fig. 59. In the top row, the distribution of hits for the event is shown before clusterize is applied. As can be seen, two clusters of similar sizes are present above a constant background of noise hits. These clusters correspond to the neutrino interaction and the tau decay vertices, respectively. In the bottom row, the same event is shown after applying clusterize. As can be seen, only one cluster of hits remains.

For the other “Double Bang” events the hit selection already selected a sample of hits biased towards one of the vertices. Starting on such a sample, the cluster algorithm will enhance the purity of that selection.

The added effect of applying the cluster algorithm to all “Double Bang” events is shown in Fig. 60. As can be seen, applying the cluster algorithm improves the performance of the prefit to find either of the two vertex positions at all simulated tau flight lengths. Therefore it is used as a final step of the prefit hit selection.

In addition to the hits, the used starting values could influence the prefit performance. Therefore, the prefit was tested by using either the simulated neutrino interaction or the simulated tau decay vertex as a starting point. It was found that the reconstructed prefit position is independent of the used starting

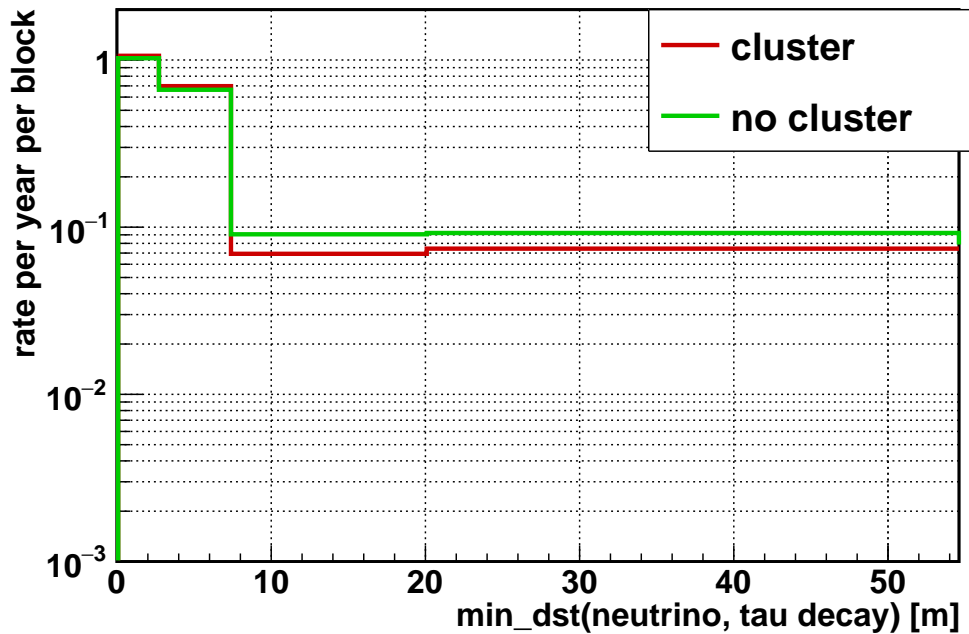


Figure 60: Minimal distance between the reconstructed prefit position and the shower position of the neutrino interaction or tau decay ($\text{min_dst}(\text{neutrino}, \text{tau decay})$) for the hit selection with and without clusterize; shown are tau signal events.

position, proving the position fit result to be independent of the starting values as long as they are within reasonable limits (e.g. the instrumented detector volume). Therefore, the position of the DOM with the most hits and the time of the first hit on that DOM are used as starting values (as done in AAshowerfit).

Position reconstruction

The achieved precision of the single shower position reconstruction is around 1 m for KM₃NeT [67]. The performance for single showers can be considered as a benchmark for events with multiple showers.

For multiple showers events the determination of the precision of the position reconstruction is ambiguous, as multiple true shower positions exist. A solution is to scrutinize the position resolution by using the minimal distance between the reconstructed position and all shower maxima positions as shown in Fig. 61. As can be seen, the minimal median distance achieved by the Prefit in the “Double Bang” case is around 3 m. The performance is worse than for single showers due to the presence of two showers. This also causes the long tails in the distribution. The distance between the reconstructed positions and either shower being larger than 10 m for approximately 10% of the events.

For a better understanding of the position reconstruction performance for “Double Bang” events, the dependence of the position resolution on the tau flight length is helpful. In Fig. 62 the distance between the reconstructed position

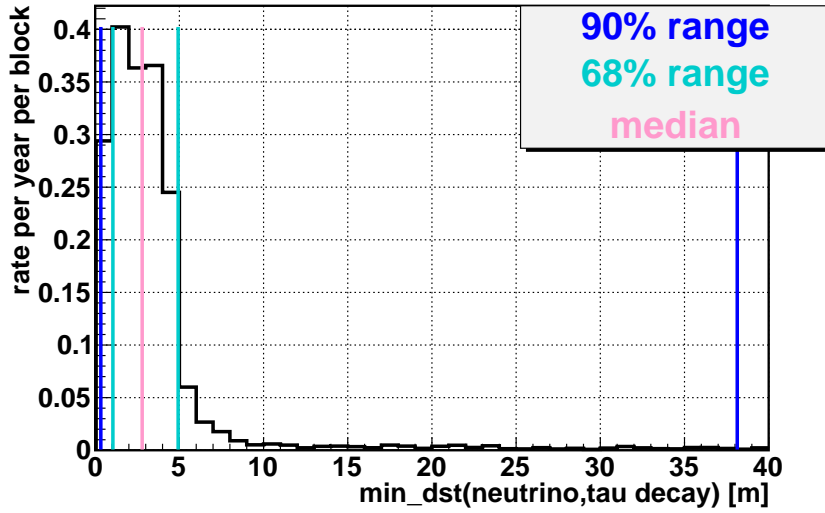


Figure 61: Minimal distance between the reconstructed Prefit position and the positions of the shower maxima of the neutrino vertex or tau decay ($\text{min_dst}(\text{neutrino}, \text{tau decay})$) for tau signal events.

and the neutrino shower maximum is shown as a function of the tau flight length. There are two populations: one at distances close to zero and another at distances equal to the tau flight distance. The population at distances smaller than 5 m corresponds to the Prefit reconstructing the neutrino interaction vertex and the population at distances equal to tau flight length corresponds to the Prefit reconstructing the tau decay vertex. Only a small number of events is not found within the two populations. These are the events in which the Prefit did not reconstruct either of the two vertices.

Given the median resolution and the robustness of the starting values, the prefit position is used as input to the subsequent reconstruction steps.

Time reconstruction

Minimizing the score function recovers also the time of the interaction. In order to check the performance of the time reconstruction, the reconstructed time is compared to the simulated time of that position as given by:

$$T_{\text{res}} = T_{\text{MC}_\nu} + \text{dst}(\text{pos}_{\nu}, \text{pos}_{\text{rec}}) / c_{\text{light}} - T_{\text{rec}} \quad , \quad (27)$$

where T_{MC_ν} is the simulated neutrino interaction time, $\text{dst}(\text{pos}_{\nu}, \text{pos}_{\text{rec}})$ is the distance between the neutrino interaction and the reconstructed position. Therefore, $T_{\text{MC}_\nu} + \text{dst}(\text{pos}_{\nu}, \text{pos}_{\text{rec}}) / c_{\text{light}}$ is the simulated time of the reconstructed position, assuming the shower propagates with c_{light} . In most cases, this position will correspond to the shower maximum. A plot of the time resolution T_{res} for the different neutrino channels is shown in Fig. 63a. As can be seen, all neutrino channels have an positive offset corresponding to the reconstructed

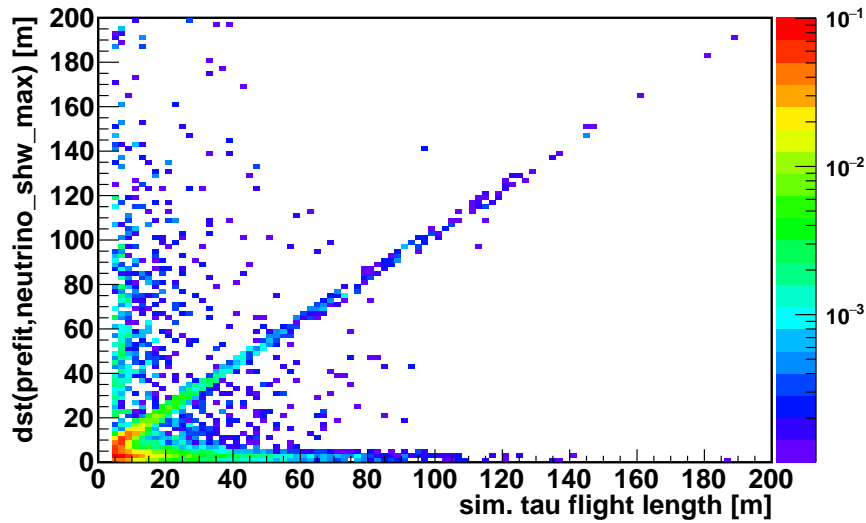


Figure 62: Distance between Prefit position and neutrino shower maximum vs the simulated tau flight length for tau signal events; z-Axis: rate per block per year.

time being too early. The offset is especially pronounced for the tau signal events.

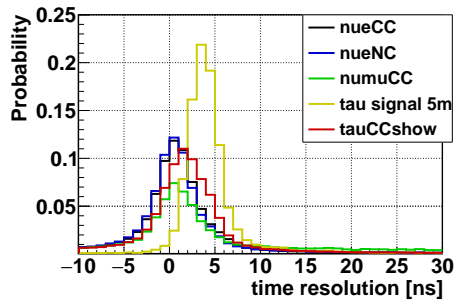
This offset is found to be increasing with simulated neutrino energy as shown in Fig. 63b for single showers and the effect is even larger for “Double Bang” events as shown in Fig. 63c. This causes the larger offset of approximately 5 ns for the tau signal events as shown in Fig. 63a, as they are events with high energies. As a more refined fit will be made afterwards, this offset is simply corrected for by adding 5 ns to the reconstructed time after the Prefit step.

5.3.2 Energy and direction fit

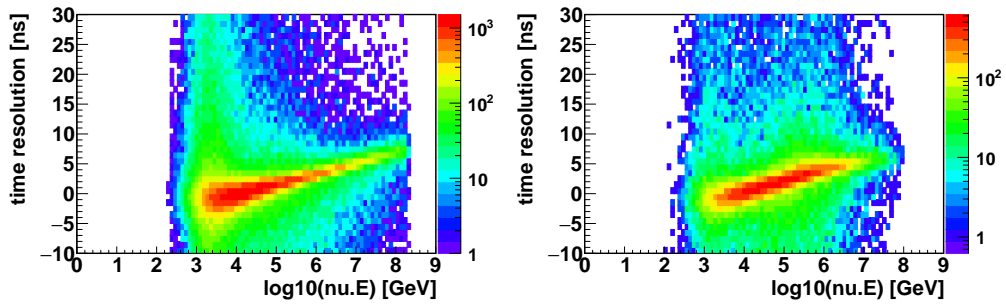
The energy and direction fit is adopted from the AAShowerfit reconstruction. It is a likelihood minimization based on the probability of a PMT being not hit or hit given a shower energy and direction. This section will illustrate the reconstruction procedure and the performance for “Double Bang” events.

The energy and direction fit takes the result of the position Prefit as a starting point to reconstruct the direction and energy (4 parameters). In order to evaluate the 4π phase space evenly, the likelihood is minimized for different starting directions. These are chosen as the 12 corners of an icosahedron around the prefit position. For the energy the start parameter is arbitrarily set to 10 TeV.

For each starting direction a likelihood minimization is performed based on a multidimensional probability density function (PDF). The PDF describes the probability of a PMT being not hit or hit with one or more photons from a shower given the PMT alignment, shower direction and shower energy. The likelihood is evaluated for all hits with $|\Delta T_h| \leq 800$ ns given the reconstructed



(a) Distribution of time difference between simulated neutrino interaction time and reconstructed time.



(b) Time resolution as function of simulated neutrino energy for nueCC single shower events. (c) Time resolution as function of simulated neutrino energy for tauCCshow events.

Figure 63: Time resolution performance studies.

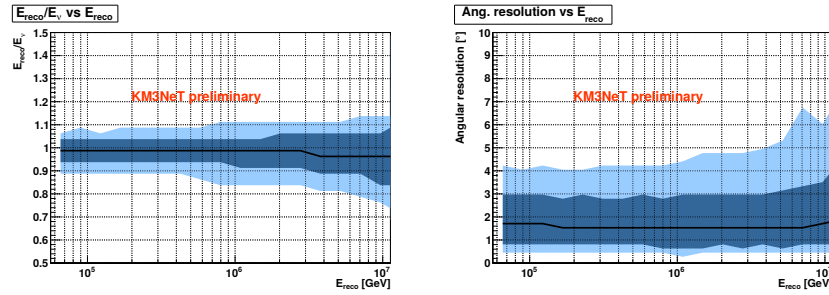


Figure 64: AAShowerfit energy and direction resolution for contained nueCC events; black line shows the median, dark blue the 68% quantiles and light blue the 90% quantiles; as taken from [67].

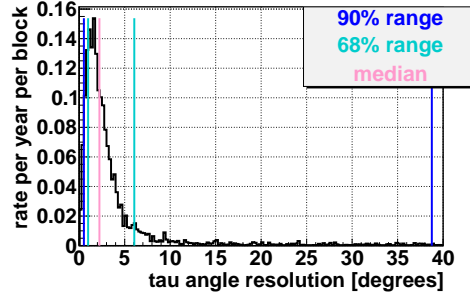
position. From the 12 fit results, the one with the best likelihood value is selected as the result of the minimization.

The performance of the direction fit depends on the energy of an event. A minimal energy of 10 TeV is required for the shower to produce sufficient hits in the ARCA detector to be properly reconstructed. Above this energy, the direction reconstruction performance for single showers changes with energy as shown in Fig. 64 on the right. The median angular resolution varies between 1.5° to 2° and is worst at low and high energies.

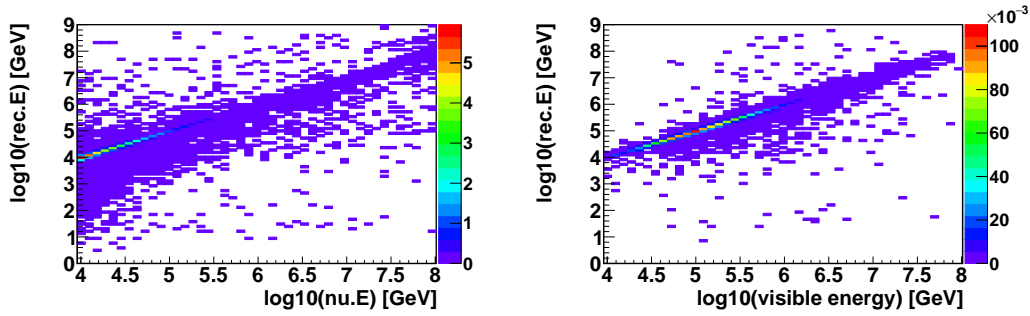
A similar performance is to be expected for “Double Bang” events because the two showers give comparable photon distributions to a single shower event. The resulting angular resolution of the tau lepton (which closely matches that of the neutrino) and the reconstructed energy resolution are shown in Fig. 65 for tau signal events. As can be seen in Fig. 65a a median angular resolution of around 2° is achieved which is indeed comparable to the resolution for nueCC events.

Figure 65b and Fig. 65c show the reconstructed energy as a function of the simulated visible energy for contained nueCC and tau signal events respectively. The distributions show the same correlation between simulated and reconstructed energy, demonstrating a successful energy reconstruction for contained “Double Bang” events. The underestimation of energies in the region below $\mathcal{O}(100 \text{ TeV})$ is a known bias which can be correct. This effect is negligible for a “Double Bang” reconstruction, due to the characteristic energies of the tau signal events.

Directly inferring the neutrino energy from the reconstructed energy in the “Double Bang” case is not possible, since the tau decays produce at least one neutrino. The neutrino, on average, carries away around one third of the tau energy for three body decays. Since the tau lepton decays into three particles about 60% of the time, the neutrino can be estimated to have about 25% of the tau energy for all tau decays. Therefore, the reconstructed energy can be considered a lower bound of the true tau energy in the “Double Bang” case.



(a) Tau angular resolution of the tau lepton for tau signal events.



(b) Reconstructed energy vs neutrino energy for nueCC events.

(c) Reconstructed energy vs neutrino energy for tau signal events.

Figure 65: Direction and energy reconstruction performance; z-Axis shows rate per year per block.

5.4 BELLE STARR SCAN

The Scan algorithm utilizes the results of the Pfit to scan a sub-region of the detector volume for a second shower vertex. For this purpose, a two shower position likelihood is evaluated along the Pfit trajectory. In theory, the evaluation of such a likelihood for the whole detector volume could optimally reconstruct the two shower parameters. But, as discussed before, such a scan requires significant computational resources. Restricting the evaluation of the likelihood to a trajectory results in a statistically robust and computationally less demanding procedure. As discussed in Sec. 5.3, the Pfit yields a good position resolution for one of the showers and good tau lepton direction resolution. Therefore, the search for the second shower position can be limited to points along the Pfit trajectory.

In the following, first the characterization of the “Double Bang” likelihood is discussed and then the scan procedure is elaborated upon.

“Double Bang” likelihood

A two shower position likelihood for “Double Bang” events has a total of seven free parameters, namely: Six position parameters and one interaction time. The

second time can be concluded from the distance between the positions, as the two vertices are connected by the tau flight duration.

The ‘‘Double Bang’’ likelihood for a given hit_i is defined as the sum of the probabilities of the hit originating from either shower vertex and the probability of the hit being background:

$$\mathcal{L}_i = c_1 * P(\Delta T_{1;i}) + c_2 * P(\Delta T_{2;i}) + c_3 * P(\text{hit}_i | \text{bkg}) \quad , \quad (28)$$

where $\Delta T_{1/2;i}$ is the hit time residual given shower 1/2, $P(\Delta T_{1/2;i})$ is the probability that hit_i is a hit originating from shower vertex $_{1/2}$, $P(\text{hit}_i | \text{bkg})$ is the probability of the hit being a background hit and c_i are weighting parameters. The different probabilities are added in the likelihood since they are independent hypotheses: a hit can only be caused by one of the shower vertices or background. In theory, a fourth probability should be added for the hit to be caused by the tau lepton. the tau lepton is minimum ionizing and hence the amount of light produced by the tau lepton as it traverses the medium is negligible. The total likelihood is given by the product of the likelihood of all hits. The characterization of the different hit probabilities and weighting parameters is discussed in the following paragraphs.

The probability of a hit being produced by a shower (signal hit) is parameterized by a one-dimensional probability distribution function (PDF) of the hit time residuals given a single shower. In general, the PDF is a multi-dimensional function depending on other parameters such as shower energy, shower direction and the relative position and orientation of the PMTs and shower. In order to simplify the reconstruction, only a one-dimensional PDF of the hit time residuals is used.

The PDF is obtained by averaging the hit time residual distribution of 100 nueCC single shower events obtained from MC truth. These events are simulated with a shower energy of 1 PeV and contain no optical background. The resulting distribution is stored in a histogram and normalized such that its integral is one in order to represent a probability. Since the histogram is binned in hit time residuals, the PDF can suffer from binning effects. To avoid these, the cumulative histogram is fitted with a monotonously increasing spline function to achieve a continuous function. The spline fit is developed by A. Heijboer [112] in order to avoid irregularities which may be caused by empty bins in the residual histogram.

For the used hit selection a binned representation of the used spline function is shown in Fig. 66. Considering that the shape of the PDF depends on the used hit selection, this representation is only applicable to the specific hit selection of the scan procedure. The distribution shows a peak at zero with a FWHM of around 20 ns and a tail towards higher residuals. The peak and tail are caused by direct and scattered light respectively. Between them is a slight dip around hit time residuals of 30 ns which is caused by the merging of hits on the same PMT as discussed in Sec. 4.3.

Also shown in Fig. 66 are the PDF for different shower energies. As can be seen, the PDFs have different peak to tail ratios. With increasing shower energy, the tail of the distribution increases since the amount of scattered light

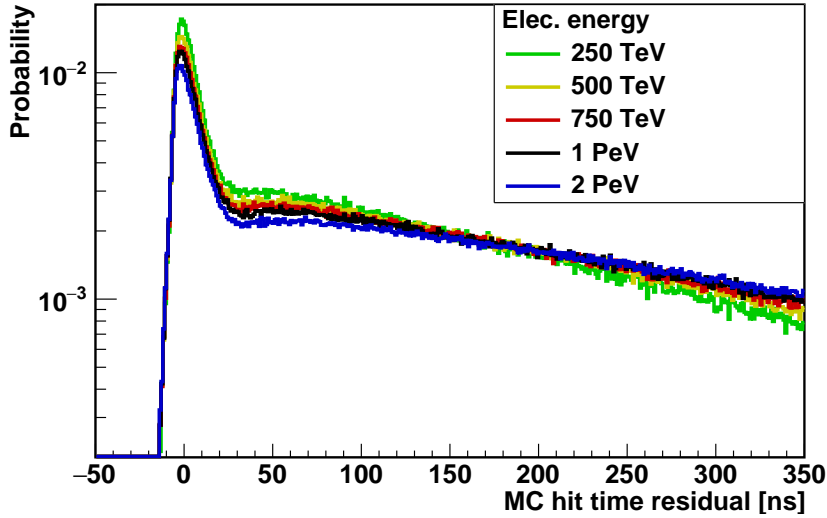


Figure 66: Binned representation of the spline function for the photon distribution function (PDF). The function histograms are normalized to an integral of one.

increases. Since the distributions are scaled to have an integral of one, this causes a decrease in peak height. Except for this shift in the peak to tail ratio the histograms show little variation with energy in the region of interest for “Double Bang” events. This supports the simplification to ignore the dependence of the PDF on shower energy. Otherwise, a much more complex reconstruction would be necessary. For the likelihood the PDF obtained for an electron energy of 1 PeV is used.

The probability of a hit being an optical background hit is given by the hit selection and the expected ^{40}K rate. For the used trigger time window of approximately $5\ \mu\text{s}$, hit merging within 500 ns on a PMT and an assumed ^{40}K rate of 5 kHz per PMT, the relative probability of a hit being background is around 0.008%. This probability depends to some degree on the energy of the showers event, since more energetic showers produce more hits and thereby decrease the probability of a background hit. But the change in probability is small and hence neglected.

The weighting constants c_i are then determined such that $\mathcal{L}_i = 1$ using $c_1 = c_2$ and $c_3 * P(\text{hit}^1|\text{bkg}) = 0.008\%$. In general, the assumption of $c_1 = c_2$ is only true for both showers producing an equal amount of light. But since a study in which the ratio c_1/c_2 has been adjusted according to Monte Carlo true information has shown no improvement in reconstruction performance and obtaining an estimate of the single shower energy distributions is not simple. Therefore, the assumption of $c_1 = c_2$ is used.

Instead of maximizing the likelihood, the negative log likelihood is minimized in order to simplify the computation. Therefore, the position of the second

shower is given by the minimal value of $-\log \mathcal{L}$. The negative logarithmic two shower likelihood is given by

$$-\log \mathcal{L} = - \sum_i \left[\log \mathcal{L}_i \right] . \quad (29)$$

Scan procedure

In the Scan, “Double Bang” likelihood from Eq. 29 is evaluated for each step of one meter in an interval of ± 800 m along the Prefit direction, resulting in 1601 scan points. While one shower vertex is set to the Prefit position, the other shower vertex position is set to the scan point. The time of a given scan point is given by the tau lepton propagation time between that point and the Prefit position. For each point, the likelihood is evaluated for all hits present in the event.

The interval range is chosen such that all positions within the detector volume are included. In order to avoid edge effects and limit computational time the likelihood is simply set to the maximum value of $\sum_i -c_3 * P(\text{hit}^i | \text{bkg})$ for scan points outside the detector volume.

The resulting likelihood scans for “Double Bang” events fall into different categories depending on the Prefit performance and event topology. The two main types for “Double Bang” events are likelihood scans with either one or two minima. The two scenarios are discussed in detail in the following.

Once the likelihood is scanned, the second reconstructed position is set to the position of the minimal bin in the likelihood scan while the first vertex position remains at the reconstructed Prefit position. If the likelihood scan has no minimum bin (e.g. is constant) the second vertex position is also set to the Prefit position. This can happen if neither reconstructed vertex is contained and the likelihood is set to the background probability as discussed earlier.

Single minimum in likelihood

Scans with one significant minimum are typically caused by events with a very asymmetric energy distribution between the two showers, resulting in one shower which produces most of the hits and the other shower to be basically invisible. This event topology is most likely for events with Bjorken y approaching one or zero (as discussed in Sec. 5.1).

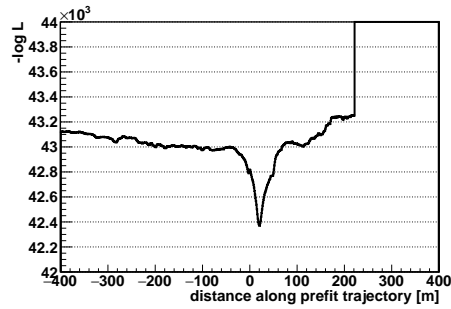
Bjorken $y \rightarrow 1$: For such events the tau decay shower has most of the initial neutrino energy. In that case, the neutrino vertex can often be recovered during the Prefit by a hit selection focusing on early hits as discussed in Sec. 5.3.1. A scan of an event with a very asymmetric energy distribution towards the tau decay shower in which the Prefit still selected the neutrino interaction vertex is shown in Fig. 67a. The Prefit position is given at distance zero, where the likelihood shows a little dip. The likelihood has a global minimum at 20 m which corresponds to the simulated tau decay shower maximum position. A scan of an event in which the Prefit failed to reconstruct the neutrino interaction

vertex because the energy distribution is even more asymmetric is shown in Fig. 67b. In this case the zero position is at the tau decay position together with the only significant minimum in the likelihood. At -20 m a small dip is visible where the neutrino vertex is located.

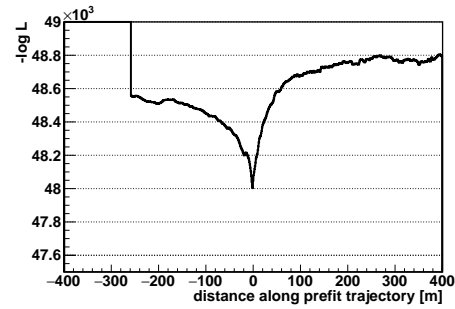
Bjorken $y \rightarrow 0$: Such events are only of relevance at the highest energies, since at low energies the tau flight length is typically too short to distinguish “Double Bang” and single shower events. For Bjorken y approaching zero the tau shower can already be difficult to detect at y values of 0.3. The reason being that the neutrino shower hits are earlier than the tau decay shower hits and therefore hit merging has a larger impact. An example of a scan of such an event is shown in Fig. 67c. There is only one significant minimum at zero distance which corresponds to the simulated neutrino interaction vertex.

Two minima in likelihood

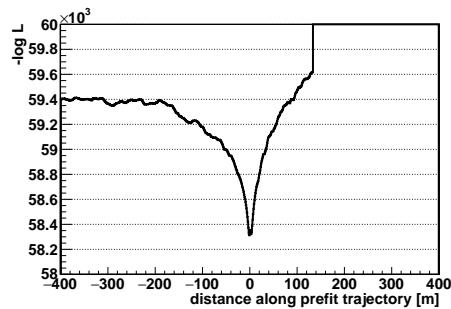
The scans which result in two minima are events in which the energy distribution between the two showers is reasonably balanced (Bjorken y between 0.3 to 0.9). For such energy distributions both showers produce a significant amount of hits. As a result, both are visible in the likelihood scan as a significant minima. In the case of a successful Prefit, one of the minima is at the Prefit position while the other is either at positive distances (the prefit reconstructed the neutrino hadronic shower position) or at negative distances (the prefit reconstructed the tau decay shower position). The global minimum is typically located at the shower which produced most hits. An example of a scan of such an event is shown in Fig. 67d.



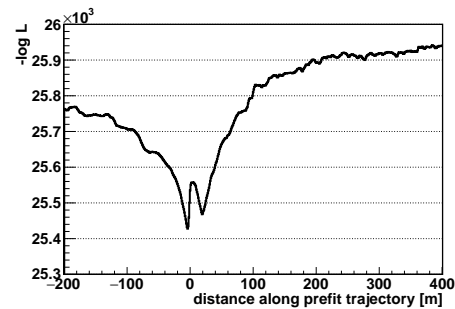
(a) Event with tau flight length 19.8 m, total energy of 205.2 TeV and Bjorken y of 0.87.



(b) Event with tau flight length 17.3 m, total energy of 247.2 TeV and Bjorken y of 0.998.



(c) Event with tau flight length 17.3 m, total energy of 1241.1 TeV and Bjorken y of 0.07.



(d) Event with tau flight length 37.2 m, total energy of 328.6 TeV and Bjorken y of 0.54.

Figure 67: Likelihood scans for different contained “Double Bang” events; zero on the X-axis marks the reconstructed Prefit position; the scan is performed along the Prefit direction; the discrete steps in the likelihood are scan positions outside of the detector volume at which the likelihood is set to be the pure background hypothesis.

5.5 BELLE STARR PEAK

The Belle Starr Peak algorithm evaluates the likelihood scans produced by the Scan. The main goals are to identify the significant minima and establish characteristics which help to suppress background events. In order to achieve this, the program utilizes a peak finder algorithm called TSpectrum which is part of the ROOT package [115, 116].

The algorithm was originally developed to determine the peaks and the continuous background for gamma ray spectra. Since the algorithm searches for peaks, the likelihood scans are inverted to turn the minima in the negative log likelihood into maxima. In the following, the background and peak identification of the algorithm and its use in the reconstruction chain are discussed.

5.5.1 *TSpectrum background estimation*

The background estimation is performed by the statistics-sensitive non-linear iterative peak-clipping algorithm (SNIP) developed in 1988 by C.G. Ryan et al. [117]. The algorithm depends on one parameter which is the typical width σ of peaks present in the spectrum. Peaks with widths differing from σ will generally be included in the continuous background although very significant ones can remain. For the likelihood scans a peak width of $\sigma = 4$ m is used (see Sec. 5.5.3). The background estimation is performed in three consecutive steps.

In the first step the values $y(x)$ of the scan histograms are internally compressed in order to reduce the dynamic range for a robust background estimation. This compression is needed in gamma ray spectra since the y -values span six orders of magnitude. Although this is not the case for the likelihood scans, the compression is incorporated in the algorithm package anyway. Nonetheless, the SNIP algorithm is appropriate for estimating the continuous background in the likelihood scans. The compression is performed according to Eq. 30, resulting in the values $C(x)$ and is reverted later.

$$C(x) = \log(\log(y(x) + 1) + 1) \quad . \quad (30)$$

In the second step the actual background estimation takes place. Here, the compressed likelihood scan histograms are iterated with a so-called peak clipping loop (for 20 iterations a sufficiently good background estimate could be achieved). The peak clipping loop estimates the background in each bin i of the scan histograms as given by

$$\text{bkg}(\text{bin}_i) = \min[C(x), C(x, \sigma)] \quad (31)$$

$$C(x, \sigma) = [C(x + \sigma) + C(x - \sigma)] / 2 \quad . \quad (32)$$

In the third step, the obtained continuous background is decompressed and subtracted from the scan histogram.

Examples of the SNIP procedure applied to inverted likelihood histograms are shown in Fig. 68.

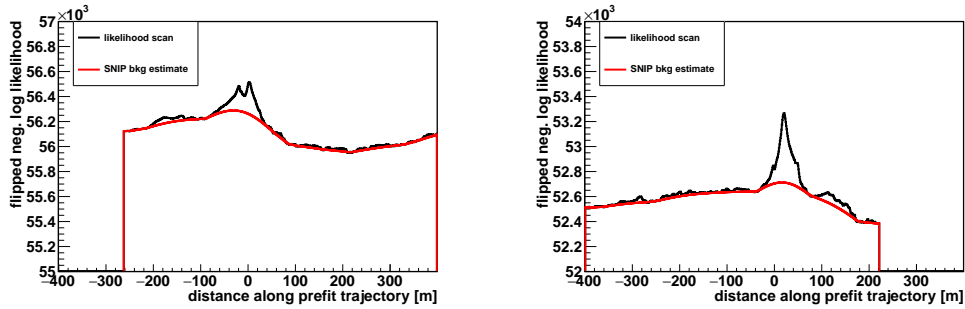


Figure 68: Flipped likelihood scans and the constant background estimation as a function of the position of the prefit trajectory as obtained by the SNIP algorithm.

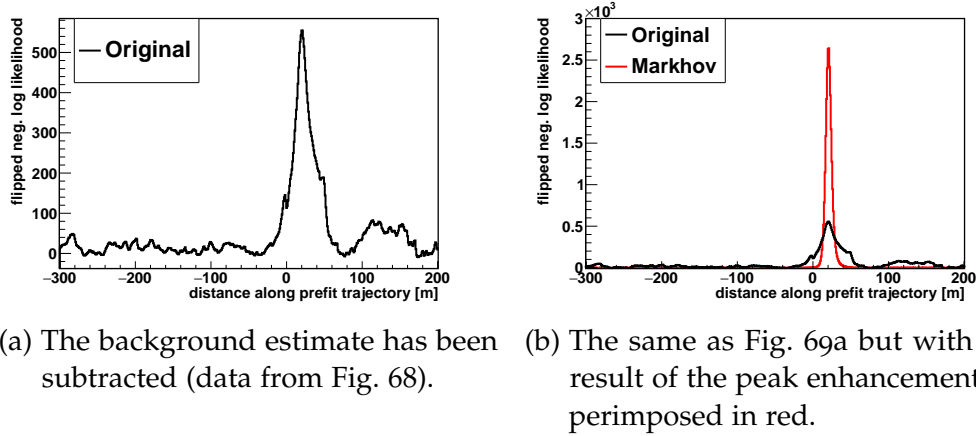
5.5.2 *TSpectrum peak identification*

The basic concept of most peak finding algorithm is evaluating the derivative of a given function or histogram. A change in the sign of the derivative from positive to negative identifies a maximum in the function or histogram. In addition, also the second derivative can be considered. Both of these methods suffer from random fluctuations due to low statistics. In order to overcome such problems, *TSpectrum* preprocesses the scan histograms with a peak enhancer [118]. The peak enhancer increases the peak to background ratio of all peaks present in the histogram.

The peaks are enhanced using an algorithm based on an analogy to the tunneling effect in quantum mechanics. Suppose a ball is lying in a given bin on the left flank of a peak. In a classical scenario, the ball will roll down the slope. If one gives the ball a non-zero chance to “tunnel” up the slope, it can move in the opposite direction. In order to utilize this idea to find peaks, one has to set the probabilities such that tunneling to the neighboring bin with higher $y(x)$ value is more likely than “rolling down” the slope to the bin with lower $y(x)$ value. When this procedure is iterated often enough and the position of each step is recorded, it results in a histogram with enhanced peaks. Examples of how the preprocessing enhances the peaks can be seen in Fig. 69. The algorithm is implemented as a finite Markov-Chain [119] for optimal effectiveness. The processed histograms are then analyzed with a first derivative peak finder algorithm as discussed in [120].

5.5.3 *TSpectrum for likelihood scans*

Applying *TSpectrum* to a likelihood scan histogram is a combination of the background estimation and peak finding method discussed in Sec. 5.5.1 and Sec. 5.5.2 respectively. The different steps combined have three input parameters: the assumed peak width σ for the background estimation, the maximum number of peaks to recorded (in descending peak height) and a threshold value



(a) The background estimate has been subtracted (data from Fig. 68). (b) The same as Fig. 69a but with the result of the peak enhancement superimposed in red.

Figure 69: Results of the Markhov-Chain peak enhancement procedure for one likelihood scan; the negative logarithm of the likelihood is shown as a function of distance to the prefit position on the prefit trajectory.

for peak rejection. The peaks are rejected based on their height h in comparison to the height of the highest found peak h_{\max} as given by:

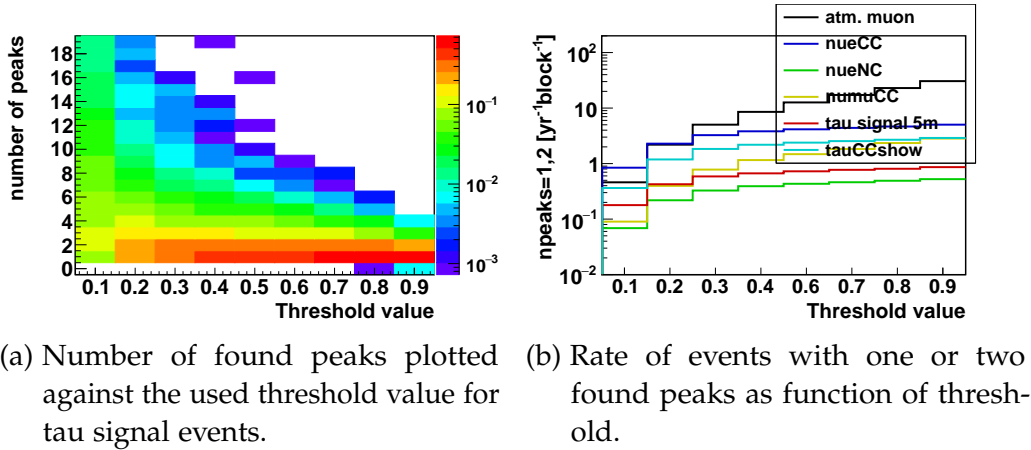
$$h \leq h_{\max} * T \quad , \quad (33)$$

where T is the threshold value. Discarded peaks do not count towards the maximum number of found peaks. The choice of peak width σ and threshold values can be optimized to match the tau “Double Bang” event signature while suppressing background signatures. Successfully reconstructed “Double Bang” events are expected to have one or two peaks, while background signatures can have any number of peaks. In the following the influence of different threshold and σ values on the results of the peak finder are discussed.

In order to study the influence of different threshold and sigma values, events are processed with the peak finder algorithm multiple times. While varying the threshold value a sigma value of 4 m is used, while varying the sigma value a threshold of 0.3 is used. Furthermore, only events with a reconstructed energy of $\log_{10}(\text{rec.E [GeV]}) \geq 4.5$ and the first reconstructed vertex contained in the detector volume are considered (see Chap. 6).

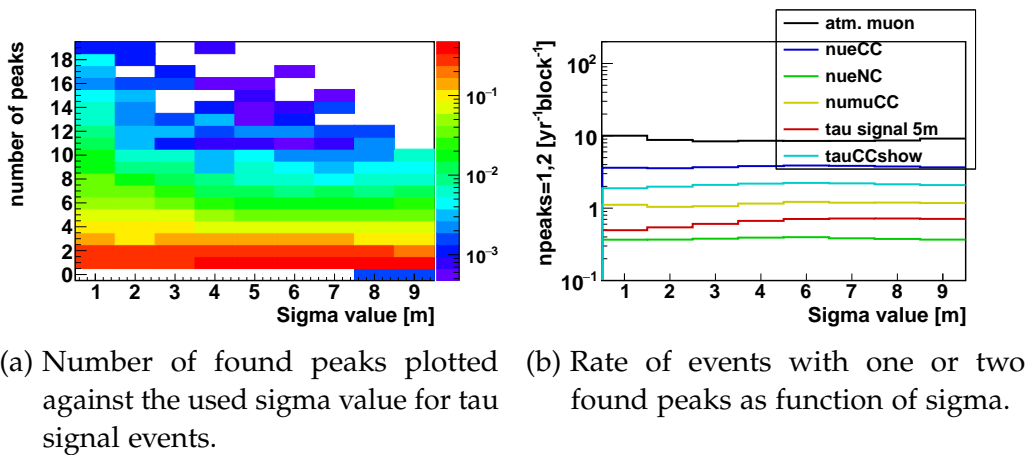
The results for varying the threshold value are shown in Fig. 70. Figure 70a shows the number of found peaks for a given threshold value for tau signal events. Figure 70b shows the number of events with only one or two peaks for a given threshold for all channels. As can be seen from Fig. 70a, the number of peaks in an event decreases with an increase in threshold, causing most events to have only one or two peaks at the highest threshold. This causes the increase in events with only one or two peaks as shown in Fig. 70b for all channels. The decrease with threshold value is caused by the definition of the threshold as given in Eq. 33.

The results for varying the sigma value are shown in Fig. 71. Figure 71a and Fig. 71b are in analogy with the threshold variation. As shown in Fig. 71a, the number of events with more than eight found peaks decreases with an increase in sigma, while the number of events with only one or two peaks is almost



(a) Number of found peaks plotted against the used threshold value for tau signal events. (b) Rate of events with one or two found peaks as function of threshold.

Figure 70: Threshold studies for a sigma value of 4 m; all events the first reconstructed vertex contained in the detector volume and $\log_{10}(\text{rec.E} [\text{GeV}]) \geq 4.5$; atmospheric muons scaled by 10^{-3} .



(a) Number of found peaks plotted against the used sigma value for tau signal events. (b) Rate of events with one or two found peaks as function of sigma.

Figure 71: Sigma studies for a used threshold value of 0.3; all events the first reconstructed vertex contained in the detector volume and $\log_{10}(\text{rec.E} [\text{GeV}]) \geq 4.5$; atmospheric muons scaled by 10^{-3} .

constant. This is caused by the fact, that for a small sigma value, the background fluctuates more. As can be seen from Fig. 71b, the number of events with only one or two peaks is approximately constant for all channels.

The final values for the threshold and sigma are fixed such that the number of events where one or two peaks have been found is maximal for tau signal events. As can be seen from Fig. 70b the tau signal drops for threshold values smaller than 0.3 and remains constant at larger values. Hence, a threshold value of 0.3 has been chosen. As can be seen from Fig. 71b the tau signal rate is approximately flat for sigma larger than 4 m whereas the rate of all background channels increases slightly. Since for sigma values smaller than 4 m the signal rate drops off, a sigma value of 4 m is chosen.

After determining the sigma and threshold values, the resulting peaks are evaluated for their significance. This is done in order to avoid statistical variations from the peak enhancement step being identified as a peak. Therefore, a

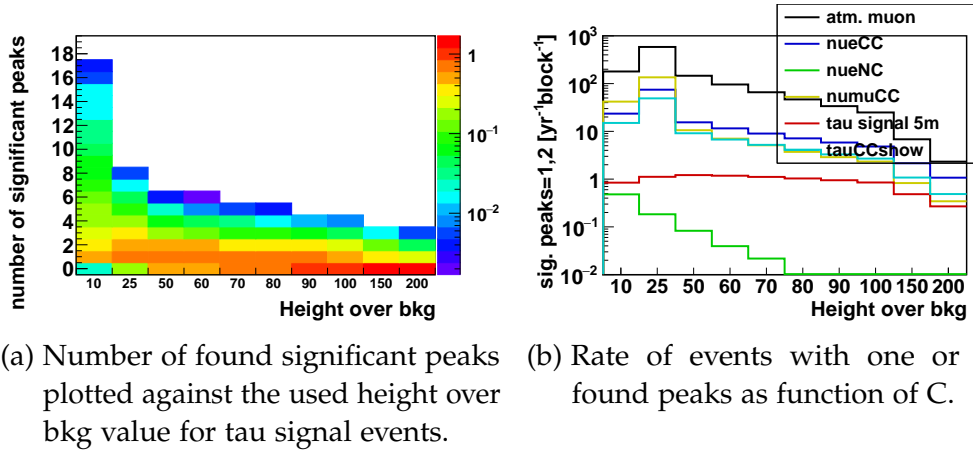


Figure 72: Peak height over bkg scan studies for a used threshold value of 0.3 and sigma value of 4; all selected events have vertices contained in the detector volume; atmospheric muons scaled by 10^{-3} .

value which determines the significance of peaks compared to the estimated background is used. Such a discriminator could be the difference, C , in height between the peak and the background. The influence of such a cut C on the different channels for different values of C is shown in Fig. 72. The Figure shows for values $C \leq 90$, the number of events with one or two significant peaks increases with increasing C . The reason is that at very low C the likelihood scans are more likely to have more than two significant peaks. For $C \geq 90$ the number of events with one or two significant peaks drops. In this case, even significant peaks are rejected since they no longer yield a sufficiently large value.

Figure 72b shows the rate of events with one or two significant peaks as a function of C for all channels. The rate of the background channels is rapidly decreasing with increasing C while the signal channel only shows small variations up to $C = 90$. Therefore, the value of $C = 90$ was chosen. This value provides for a large yield of signal events while keeping the backgrounds rates low.

Examples for the resulting significant peak positions of the likelihood scans are shown in Fig. 73.

5.5.4 Improvement of reconstructed positions

So far, the reconstructed shower positions are set to the position from the Prefit and that of the global minimum of the likelihood scan. For likelihood scans with two significant peaks, the position of these peaks is a better estimate for the vertex positions. Therefore, the two reconstructed vertex positions are set to the two peak positions in such cases. The effect of readjusting the peak position on the length resolution is shown in Fig. 74. As can be seen, after this readjusting the distribution is more sharply peaked and the tail of badly reconstructed lengths is suppressed. The distribution after adjusting shows two peaks. The

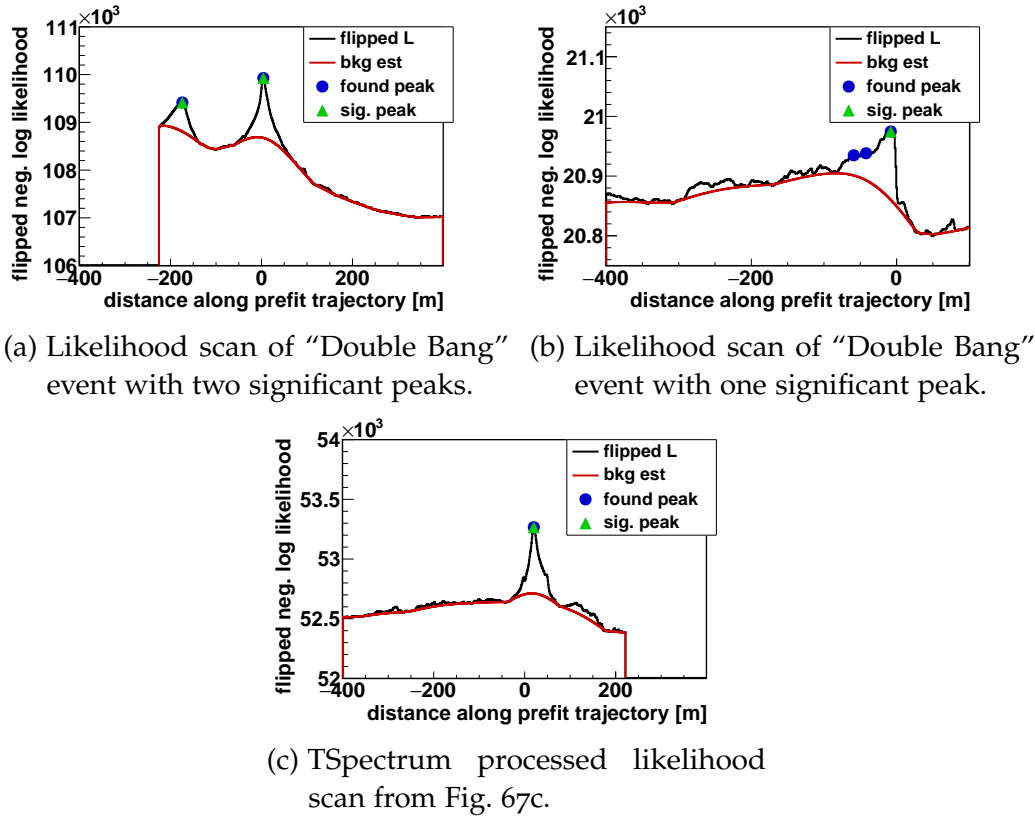


Figure 73: Likelihood scan histogram as processed by TSpectrum with parameters $\sigma = 4$ m, threshold = 0.3 and $C = 90$.

larger peak is offset from zero by around -7 m. This offset is introduced by the Prefit time offset. Events with two peaks typically do not show the time offset that is corrected for after the Prefit. The time of the positions in the scan are therefore off 5 ns. This offset is later compensated in the last step of the Belle Starr reconstruction.

5.5.5 Vertex position reconstruction performance

Once the vertex positions are determined the position reconstruction performance can be validated. As mentioned before, the reconstructed position is not exactly at the interaction or decay vertex, but closer to the position of the shower maximum. Because most photons are –by definition– emitted at the shower maximum. Therefore, the reconstruction performance is evaluated by comparing the reconstructed positions with the calculated shower maximum position which is computed using MC information. The distance between shower maximum and vertex position is $\mathcal{O}(\text{meter})$ and depends on the energy and type of the shower as shown in Fig. 75.

Since for "Double Bang" events two shower vertices are present, the reconstructed positions have to be compared to the correct vertex to obtain the position reconstruction performance. In the following, the vertex reconstructed earlier in time is compared with the simulated neutrino shower maximum and

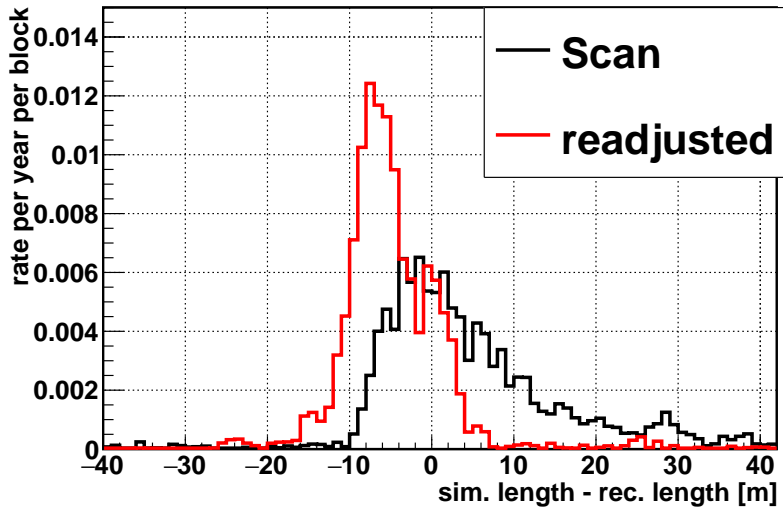


Figure 74: Distribution of the reconstructed tau flight length before and after the readjustment for tau signal events with two peaks.

the one later in time is compared with the simulated tau decay shower maximum. The resulting distributions between the distances of the reconstructed position to the neutrino shower maximum and tau decay shower maximum are shown in Fig. 76. The distribution of distances shown in Fig. 76a has a single peak with a median position resolution of 2.5 m. The distribution of distances shown in Fig. 76b shows two distinct peaks of comparable height separated by around 4 m. These peaks are only present for hadronic decay modes of the tau lepton.

Looking in detail at the differences in the tau hadronic decay modes, the cause for the two peaks in the position resolution can be found in the treatment of the pions in the simulation: While showers from neutral pions are like those of electrons, the showers of charged pions have their maxima offset by several meters from the initial vertex as shown in Fig. 22. This offset is caused by the difference in flight lengths of charged and neutral pions. Since this effect is not taken into account in the shower maximum calculation the shower maximum position of charged pions is underestimated by about 3.5 m. The tau decays into pions in more than 60% of the hadronic decay modes, therefore the two peaks are of comparable height.

The correlation between the two peak structure and the pion decays becomes clear when the vertex resolution is studied as function of the charged pion energy fraction of the visible energy in the tau decay as shown in Fig. 75. As can be seen, the second peak of the vertex resolution only shows up in a regime where charged pions carry over 80% of the energy.

The different tau decay modes therefore have an influence on the reconstruction. One could think this effect allows to probe the tau decay mode of an event but without knowledge of the tau flight length this effect is indistinguishable from a tau with a larger flight length. Because of this enhancement of the tau flight length, tau decay showers which are dominated by charged pions have

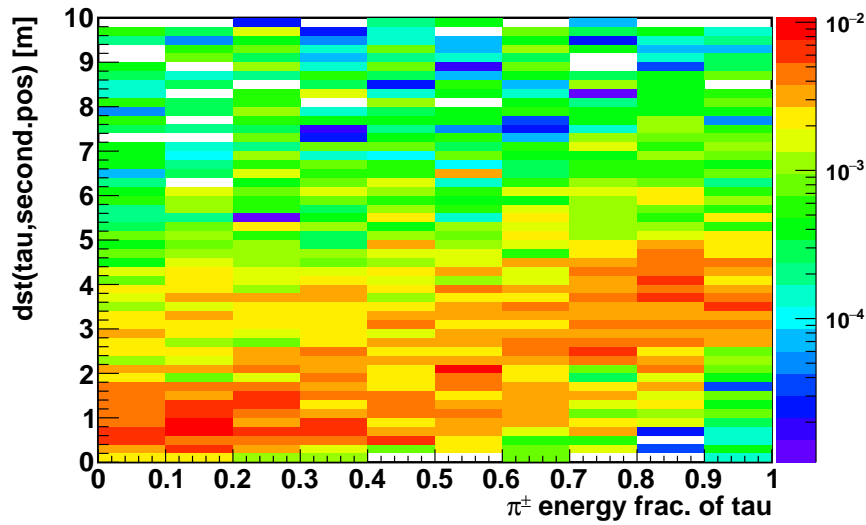
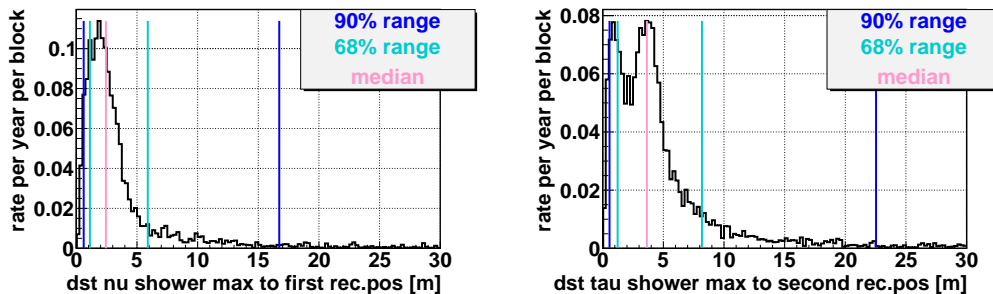


Figure 75: Distance between tau shower maximum and second reconstructed vertex vs charged pion energy fraction of tau decay; Z-axis: rate per year per block.

their distance between the shower maxima significantly enhanced compared to the actual tau flight length, making them easier to distinguish from single shower events.



(a) Distance between neutrino shower maximum and first rec. vertex.

(b) Distance between tau shower maximum and second rec. vertex.

Figure 76: Vertex resolution studies; the resolution is determined as the distances between reconstructed position and the shower maximum position; shown are tau signal events.

5.6 BELLE STARR REFIT

The optimal reconstruction method is a scan of the two shower likelihood over the full detector volume. The drawback of such a scan is the high demand on computational resources. Therefore, a minimization of the two shower likelihood is performed (full fit). The performance of such a minimization depends on the starting values. The reason being, that the likelihood landscape features many local minima and some of these cannot be overcome by the minimizer. Consequently, starting values close to the true values are needed in order to avoid the minimizer selecting one of the local minima. By performing the full fit after the previous steps, the results from the previous steps can be improved.

The vertex position resolution obtainable by the scan procedure is affected by the Prefit direction resolution of about 2° median. For instance, a deviation of 3° from the true direction translates to a position deviation of around 2.5 m assuming a tau flight length of 50 m. This is to be compared to the position resolution of a single shower position fit of around 1 m as shown in Sec. 5.3. Therefore, the full fit is expected to improve the position resolution in particular of the tau decay vertex.

An improved position reconstruction could yield an improvement of the reconstructed direction, depending on the final position resolution performance. A position resolution of around 1 m translates into a direction reconstruction of around 1.5° at 50 m distance. This would be a significant improvement of the angular resolution of the Prefit which is around 2° median.

The full fit minimizes the same negative log likelihood as used by the Scan given in Eq. 29 and uses the same hit selection. The used minimizer is the implementation of MINUIT2 in the ROOT framework [101]. The minimization is performed for two positions and one time (the time of the second vertex is fixed by the tau flight time between the two positions) which yields seven parameters. As start values, the results from the Peak step are used.

Since the fit is still computing intensive, it is only applied on preselected events. The selection is based on quantities such as the reconstructed energy and position, which are discussed in more detail in Chap. 6. The criteria are optimized such that “Double Bang” events are accepted while rejecting single shower and track events. The applied criteria are:

- reconstructed energy: $E_{\text{rec}} \geq 10^{4.5} \text{ GeV}$
- reconstructed shower positions: $|Z| \leq 300 \text{ m}$ and $\sqrt{X^2 + Y^2} \leq 500 \text{ m}$
- reconstructed length: $L \geq 5 \text{ m}$

5.6.1 Full fit performance

The performance of the full fit position resolution is shown in Fig. 77. As can be seen, both the tau and neutrino vertex resolution are only slightly improved compared to the performance after the peak algorithm shown in Fig. 76. These

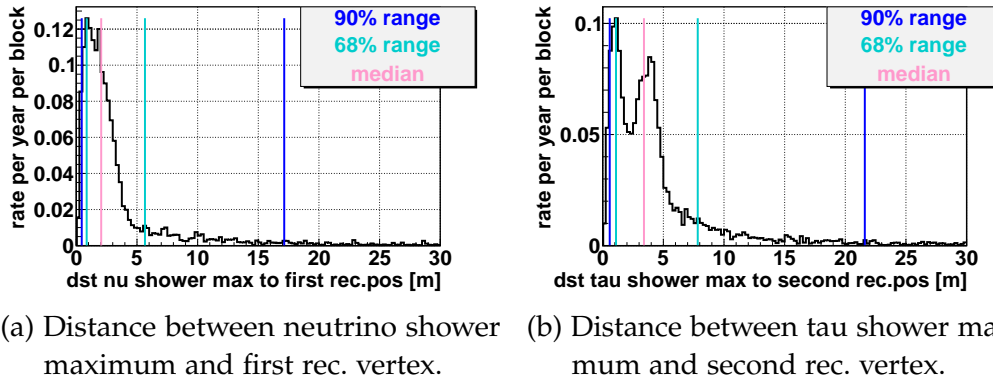


Figure 77: Position reconstruction performance for the full fit routine for tau signal events.

small improvements indicate that the trajectory reconstructed by the Prefit is close to the simulated trajectory for most events.

The reconstructed positions of the two showers translate directly to a direction. The achieved position resolution of 2 m median allows to improve on the Prefit direction reconstruction for showers which are a minimal distance apart. This relation is shown in Fig. 78a and Fig. 78b. The achieved angular resolution from the full fit positions and the Prefit is shown as a function of simulated tau flight length. The direction resolution from the full fit is better if the reconstructed tau flight length exceeds around 25 m. At large reconstructed distances, the limited statistics introduce some fluctuations.

Consequently, the direction reconstructed by the Prefit is used for events with reconstructed distance shorter than 25 m and the direction reconstructed by the full fit is used for events with a distance longer than 25 m. This results in a final direction resolution as shown in Fig. 79. As can be seen, the improvement of the direction resolution is small, since most “Double Bang” events have little energy and therefore a reconstructed distance smaller than 25 m.

The final performance is close to that achieved for the single showers as discussed before. The larger tails are caused by events with unfavorable topologies. Such events are rejected by the selection discussed in Chap. 6 yielding an improved angle and position reconstruction for the selected events.

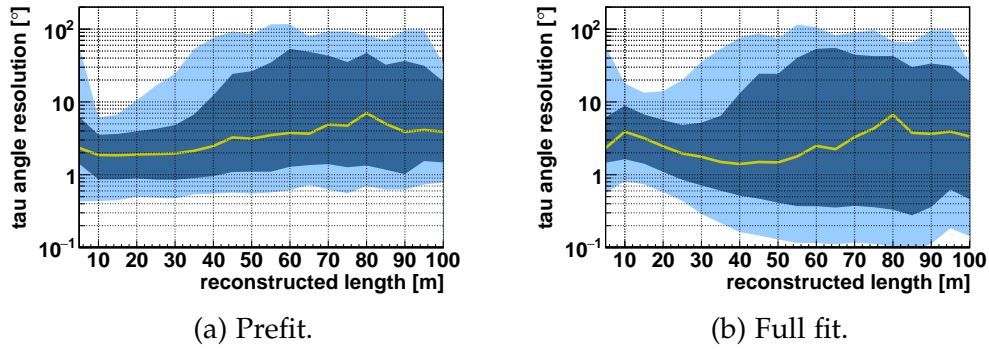


Figure 78: Tau direction reconstruction performance for the full fit and Prefit as function of reconstructed distance between the two vertices for tau signal events; Yellow line shows median; dark blue 68 % quantile and light blue 90 % quantile.

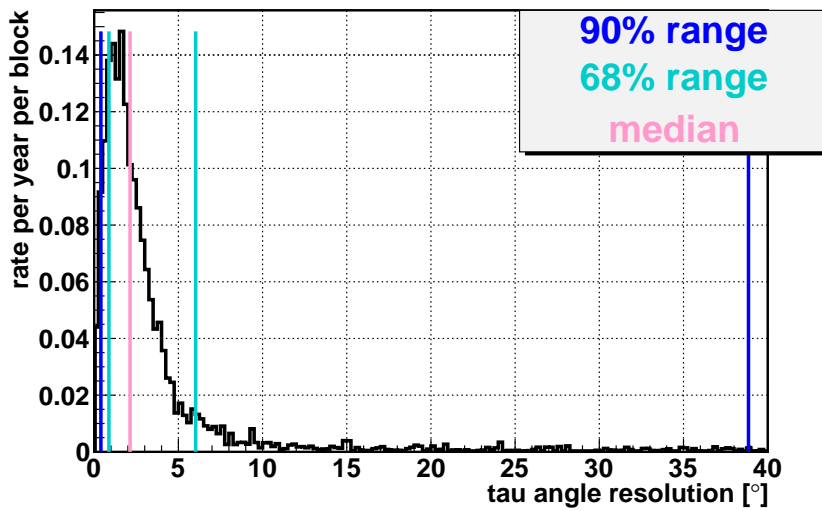


Figure 79: Tau direction reconstruction performance for the unconstrained fit routine for tau signal events for combining the Prefit and full fit.

TAU “DOUBLE BANG” SELECTION

And I heard, as it were, the noise
of thunder
One of the four beasts saying,
'Come and see.' and I saw, and
behold a white horse

Johnny Cash, The Man Comes
Around

In this chapter the selection criteria to identify “Double Bang” events using the Belle Starr reconstruction are presented. The assumed neutrino flux corresponds to the measured flux of high energy neutrinos by IceCube (see Sec. 1.2.5). The optimization of the selection criteria is performed using an energy spectrum of $E^{2.46}$ (see Chap. 5) with a 3 PeV cut-off. This spectrum is in accordance with the best fit to the IceCube data of $\Gamma = 2.5 \pm 0.9$ [121]. The reason for choosing $\Gamma = 2.46$ instead of $\Gamma = 2.5$ is the compatibility with the considered spectra in the KM3NeT LoI [67]. The spectral index has a large impact on the amount of reconstructable “Double Bang” events, since the tau travel length and therefore the separation between the two showers, depends on the tau energy.

In this chapter, the considered background channels are the neutrino interactions numuCC, nueCC, NC and atmospheric muons. In the last section, the influence of atmospheric neutrinos on the final results is presented.

For the atmospheric muons the MC simulation with a minimum leading muon energy of 50 TeV (threshold at the can) is used. The reason being, that high energy muons are more likely to mimic “Double Bang” events and lower threshold simulations do not offer sufficient statistics at high energies. Only neutrino events are considered, since at energies exceeding 10 TeV no significant differences between neutrinos and anti-neutrinos is expected.

6.1 SELECTION CRITERIA

So far, a first basic set of selection criteria was developed without performing a full optimization. The selection criteria are chosen to achieve a large signal yield and little remaining background with special attention to reducing the atmospheric muons background as much as possible.

With regard to these goals, five selection variables have been identified which show good discriminating power between signal and background signatures, namely: the logarithm of the reconstructed energy (energy cut), the position of the reconstructed vertices relative to the detector (position cut), the number of peaks in the likelihood scan (peak cut), the probability of hits to be optical

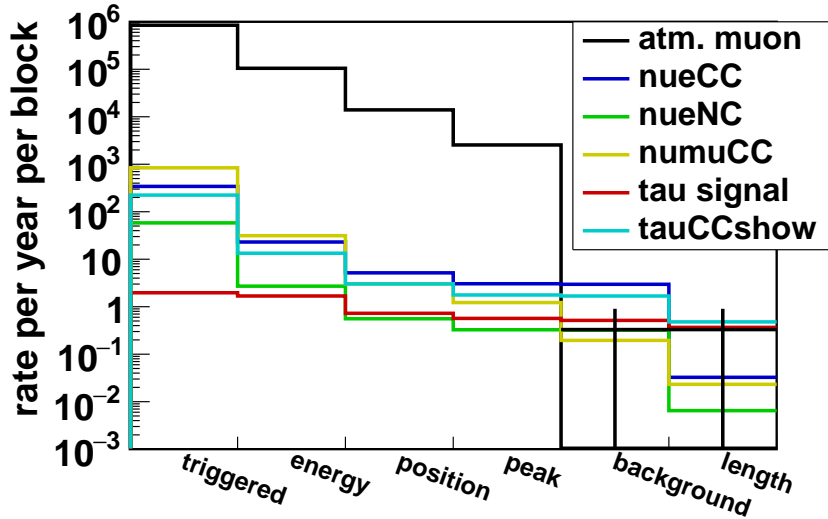


Figure 80: Inclusive event rates per block and year for different channels after applying the selection criteria.

background (background cut) and the reconstructed tau flight length (length cut). The values for the different cuts are chosen as follows:

- energy cut: $E_{\text{rec}} \geq 10^{4.5} \text{ GeV}$
- position cut:
 - Prefit position $Z \leq 250 \text{ m}$ and exclusion of outer part of detector
 - Refit positions $-300 \text{ m} \leq Z \leq 250 \text{ m}$ and $R_{xy} \leq 390 \text{ m}$
- peak cut: $n_{\text{peaks}} = 1, 2$
- background cut: $P(\text{bkg}) \geq 10^{-6}$
- length cut: reconstructed length $\geq 5 \text{ m}$

Applying these selection cuts to the MC simulations results in the distribution shown in Fig. 80. The X-axis shows the applied cuts from left to right and the Y-axis shows the inclusive rate for the different channels. Since the background cut rejects all simulated atmospheric muons the last two bins of the muon distribution show an estimation of the rejection performance based on the lifetime of the simulation. The lifetime, for the used atmospheric muon simulation, is 0.33 events per year per block for a single event. Therefore, the bin values after previous cuts are applied is set to the weight of a single event and the errors are set to the corresponding Poisson probability.

The order in which the cuts are applied to the events was chosen such that variables which reject the same background signatures are grouped together, resulting in the trend shown in Fig. 80: The energy cut rejects all background channels equally, the position, peaks and background cuts reject mainly track like channels and the length cut rejects mainly single shower like channels.

In the following, the different selection variables will be explained and their efficiencies discussed in detail. For all but the position cut, their distribution is shown three times for different selections: the distribution of all triggered events, the distribution after application of the previous steps and the distribution after all other cuts have been applied. The first distribution allows for a general characterization of the variable under investigation, the second shows the distribution of events that are subject to the current selection and the third indicates the effectiveness of the current selection. For the third histogram also a cumulative distribution is shown. Since the position cut involves two dimensions, the distributions will be separately shown.

6.1.1 Energy cut

“Double Bang” events can effectively be distinguished from single shower events if the tau lepton travels visible distances before its decay. As discussed in more detail in Sec. 5.1, the tau travels visible distances at energies around $\mathcal{O}(100 \text{ TeV})$ and higher (or $\log(E [\text{GeV}]) = 5$). Therefore, a selection based on the reconstructed energy is a natural choice given the “Double Bang” kinematics and the large population of background events at lower energies.

The distribution of the reconstructed energy of all channels is shown in Fig. 81a. The dependence of the tau flight length on the energy is visible for the tau signal channel. The rate of tau signal events decreases for reconstructed energies below $\log(E_{\text{rec}} [\text{GeV}]) = 5$. Above this energy, the tau signal events follow the tauCCshow curve up to $\log(E_{\text{rec}} [\text{GeV}]) = 6$. The latter deviation is caused by the tau flight length becoming so large, that the containment criterion for tau signal events rejects these events. The three neutrino channels show the expected behavior assuming an energy spectrum following a power law with $\gamma = -2.46$. The structure in the distribution of the reconstructed energy of the atmospheric muons is a feature of the simulation in which an energy threshold of 50 TeV (which corresponds to $\log(E [\text{GeV}]) = 4.7$) is applied. Most of these muons deposit significantly less energy in the detector.

The distribution of the reconstructed energies after all the other selection criteria is shown in Fig. 81c. Here, a cut-off is present in both tau signal and tauCCshow channels at reconstructed energies of $\log(E_{\text{rec}} [\text{GeV}]) = 4.5$. The reason for the cut-off edge to be so pronounced is the Bjorken y distribution. Whilst there are events with tau flight lengths longer than 5 m at energies below the cut-off, the Bjorken y values must then be very close to one. This makes a successful reconstruction of these events very unlikely. The populations of atmospheric muons at low energies are typically caused by events with a very asymmetric distributions of hits in the detector.

As can be seen from Fig. 81d, the final selection on the reconstructed energy of $\log(E_{\text{rec}}[\text{GeV}]) \geq 4.5$ rejects all atmospheric muons and about 50% of the neutrino background channels while keeping almost all signal events.

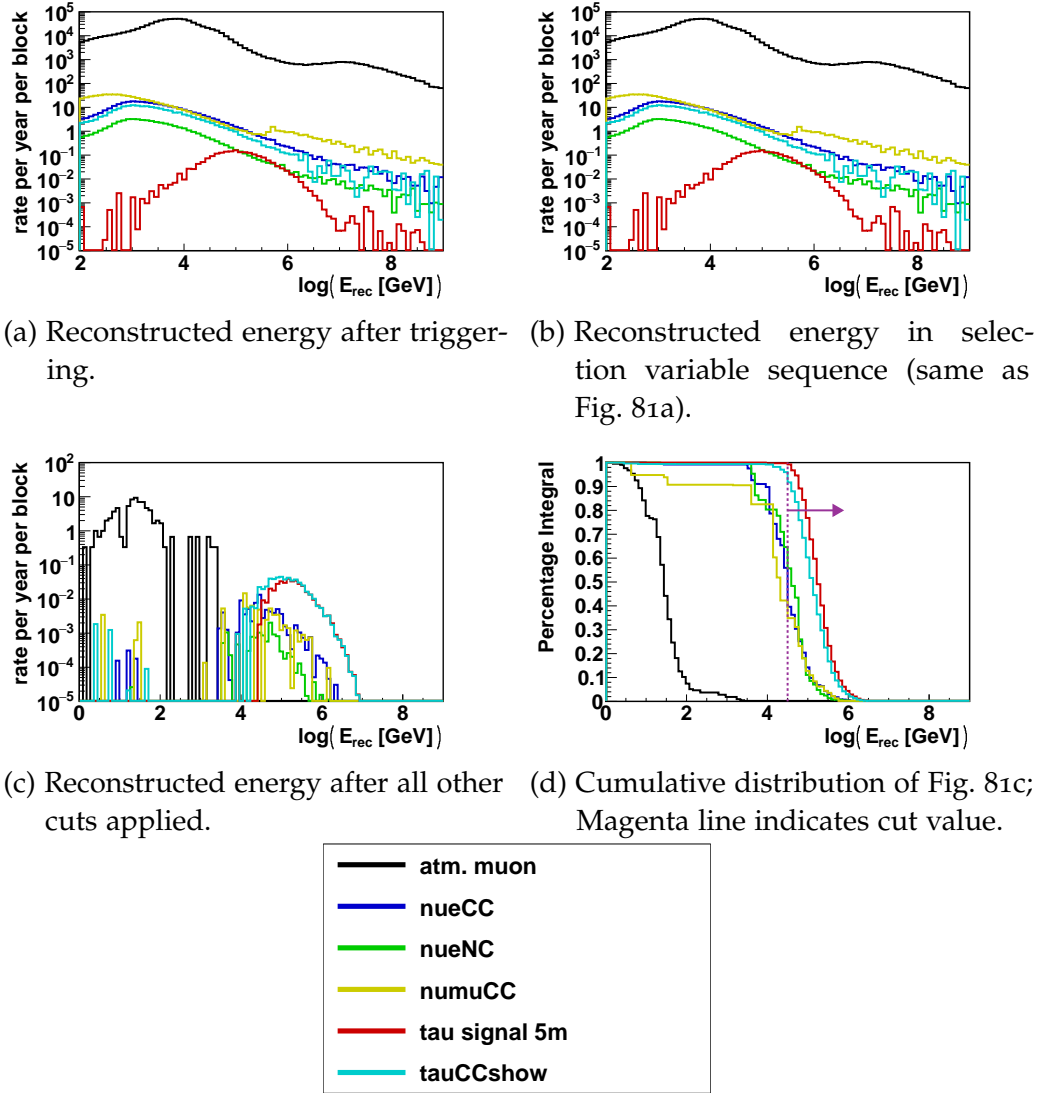


Figure 81: Distribution of the reconstructed energies for the different channels.

6.1.2 Position cut

The containment of the reconstructed vertices is crucial to support a good reconstruction performance. Additionally, the Position cut will help to suppress the atmospheric muon background. Reason being, that the characteristic zenith angle distribution of atmospheric muons yields reconstructed vertices at the sides and top of the detector. Whereas neutrinos arrive at the detector from all directions apart from a small bias for downward directions due to the possible absorption in the Earth.

For an early rejection of atmospheric muons, the position cut is applied to the reconstructed Prefit position. Note that for the Prefit early hits are selected, thereby biasing the Prefit vertex towards positions at the start of a track. Thereby causing the vertex for atmospheric muons to be pushed upstream the muon trajectory towards the outside of the detector volume, while for neutrinos the vertex is pushed towards their interaction points.

The reconstructed Prefit positions for atmospheric muons and tauCCshow events are shown in Fig. 82a and Fig. 82b, respectively. The atmospheric muons are indeed biased towards the top and outer edge of the detector while the tauCCshow events show no such bias. The visible pattern is caused by the regular DOM positions. The Prefit is known to prefer positions close to a set of DOMs.

The same position bias is observed for both channels after the other selection criteria are applied as shown in Fig. 82c and Fig. 82d. As can be seen, most of the remaining atmospheric muons events have a reconstructed vertex position within the top 50 m of the detector volume. A top view of these events is shown in Fig. 82e. Comparing the positions to the detector top view in Fig. 82f, it is clear that most of the events are located between the two outer layers of the detector. Applying a selection which rejects that volume as indicated by the red line in Fig. 82f therefore rejects most of the atmospheric muon events.

The remaining atmospheric muons are rejected by requiring the positions of the two reconstructed vertices after the Refit to be contained within the detector. This selection also works well for “Double Bang” events, as edge effects are avoided and reconstructed positions outside the detector volume most likely yield bad reconstruction performances.

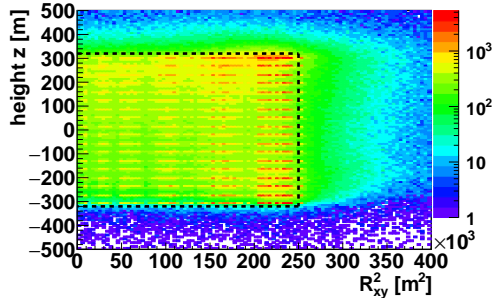
In summary, two different positions are utilized for the position cut: the Prefit and the final vertex positions. For the Prefit position, the height is required to be lower than 250 m and the radial distance from the detector center is required to be within the inner part shown in Fig. 82f. For the Refit positions the height is also required to be less than 250 m and the radius to be less than 400 m.

6.1.3 Peak cut

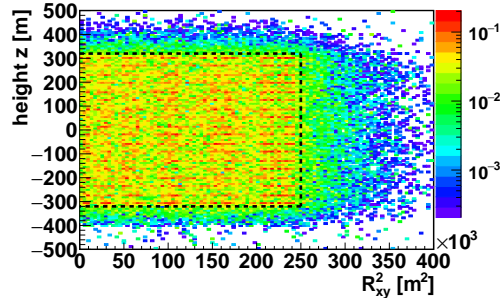
The number of significant peaks found in the likelihood scan by Belle Starr Peak constitutes a selection variable which is ideally suited for suppressing track signatures. The reason being, that every Bremsstrahlungs shower along the track with a sufficient number of hits will produce a peak. Therefore, the likelihood scan is expected to have a varying number of significant peaks for track events, one significant peak for contained single shower events and one or two significant peaks for contained “Double Bang” events. This feature can be seen in Fig. 83a. While the tau signal channel shows similar number of events with zero, one or two significant peaks, the other channels show a large contribution of events with zero or more than two significant peaks. Especially the track channels show tails towards large numbers of significant peaks.

The same distribution after the energy and position cuts have been applied is shown in Fig. 83b. While the distribution of events did not change much, the nueCC and tauCCshow distribution now show a maximum at one significant peak and the tau signal distribution shows mainly one or two significant peaks.

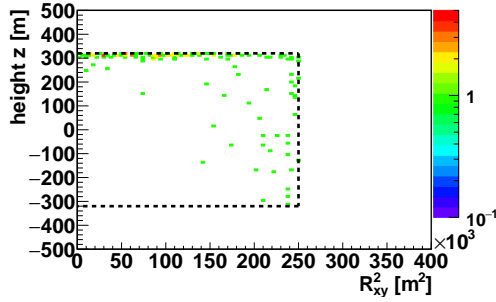
With all other cuts applied, the remaining atmospheric muon events have zero significant peaks and the numuCC events have a small tail with more than two significant peaks as can be seen from Fig. 83c. Therefore, the accepted



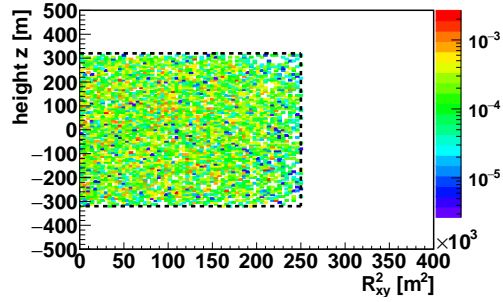
(a) Positions of atmospheric muon triggered events.



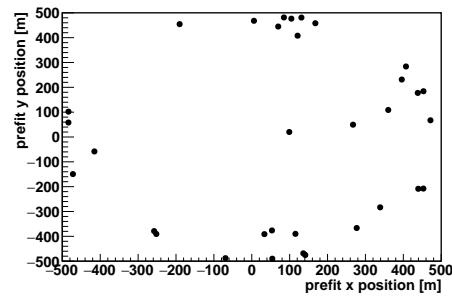
(b) Positions of tauCCshow triggered events.



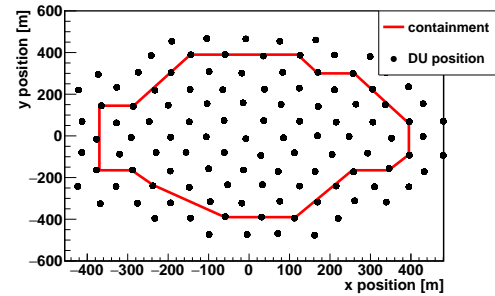
(c) Positions of atmospheric muons events after other selection criteria.



(d) Positions of tauCCshow events after other selection criteria.



(e) Top view of the detector for atmospheric muons with $z \leq 250$ m.



(f) DU position in top view; red line marks inner part.

Figure 82: Distributions of reconstructed Prefit vertex positions in the instrumented volume for atmospheric muon and “Double Bang” events; in the top 4 plots the black dotted line indicates the detector volume.

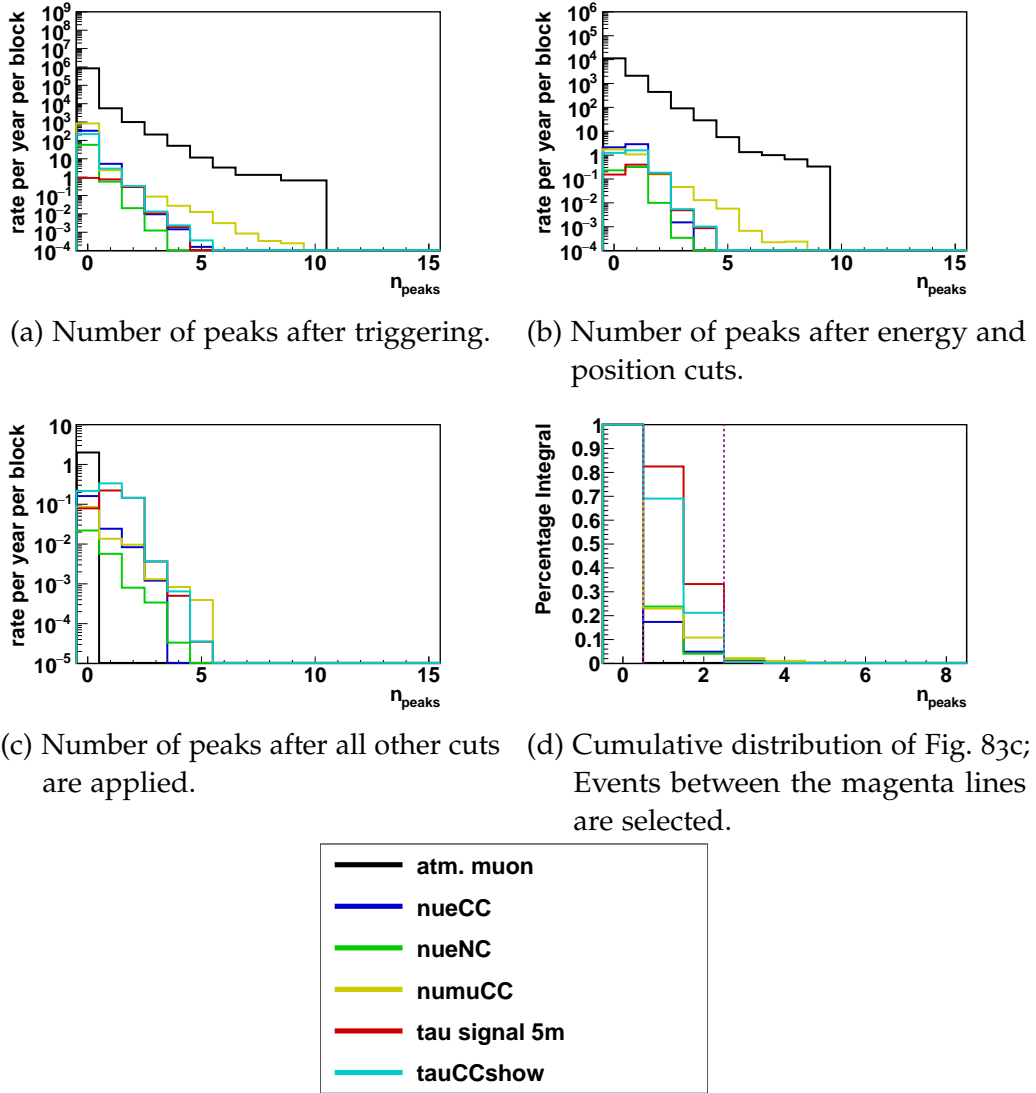


Figure 83: Distributions of the number of peaks for different channels.

number of significant peaks is set to be one or two. As can be seen from Fig. 83d, this cut rejects all remaining atmospheric muon events while keeping 82 % of the signal events.

6.1.4 Background cut

The background cut is a criterion to distinguish track events from “Double Bang” events. It uses the fact that track events contain a substantial number of photons which do not originate from either of the reconstructed shower positions. This is not the case for “Double Bang” events, because the tau lepton is minimal ionizing and the tau flight length is much shorter than that of muons at energies of interest. Therefore, the hits which cannot originate from either reconstructed vertex are caused by a signature different from “Double Bangs” or are optical background.

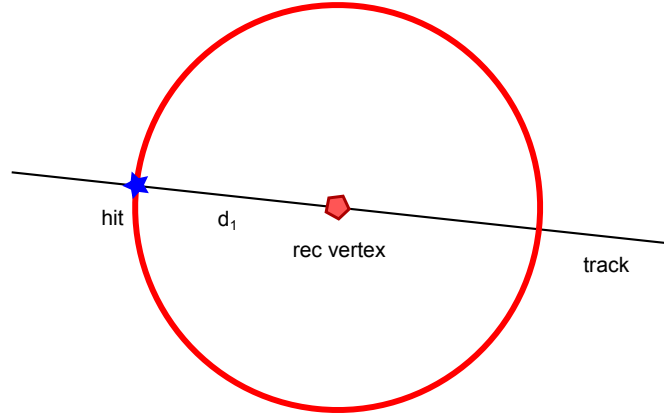


Figure 84: Estimated earliest hit time residual for chosen radius d_1 with respect to the reconstructed vertex.

In order to select the hits which cannot originate from either shower, the hit time residuals as defined in Eq. 24 are used. As can be seen from Fig. 66, the hit time residual distribution for showers at different energies has a long tail towards positive residuals and a sharp edge for negative residuals, with almost no hit time residuals below -20 ns. Because of this strict cut-off, selecting hits with hit time residuals $\Delta T \leq -20$ ns with respect to both reconstructed vertices will select hits not originating from either reconstructed vertex. Only hits within a certain radius around both the reconstructed vertex positions are considered. By limiting the radius, the total number of hits is dramatically reduced while only a small fraction of hits from any signature are lost in the process.

A suitable radius around the reconstructed vertices was found to be $d_1 = 200$ m. The choice of the considered radius translates to a lower limit for the hit time residuals. The lowest possible hit time residual is that of a track event if a hit is emitted from the track at exactly $d_1 = 200$ m distance to one of the reconstructed vertices. The reason being, that the muon travels faster than the light in the actual medium. The hit time residual of a hit which is emitted and detected at exactly d_1 distance to a reconstructed vertex is given by the travel time of the muon to the reconstructed vertex and the light travel time back to the hit position as shown in Fig. 84. This causes a minimal negative time residual as given by Eq. 34 of $\Delta T_{\min} = -1588$ ns for $d_1 = 200$ m. In order to avoid edge effects the value is increased to $\Delta T_{\min} = -1600$ ns.

$$\Delta T_{\min} = -1 \times (d_1/c + d_1/c_{\text{water}}) \quad . \quad (34)$$

To summarize, the selection is composed of a cut on the distance of the hits to either reconstructed vertex to be smaller than 200 m and a cut on the hit time residuals towards both reconstructed shower vertices to be $\Delta T_{\min} = -1600$ ns $\leq \Delta T \leq \Delta T_{\max} = -20$ ns.

For this hit selection, the expected number of optical background hits is given by:

$$N_{\text{bkg}} = N_{\text{PMT}} \times (\Delta T_{\text{min}} - \Delta T_{\text{max}}) \times R_{\text{bkg}} \quad , \quad (35)$$

where N^{PMT} is the number of PMTs present in the considered volume and R_{bkg} is the expected optical background rate. For the background rate a value of 5 kHz is used which corresponds to the background rate observed with the string prototype (see Chap. 4). For this single rate and an average of 2100 PMTs for the considered volume, the expected number of optical background hits is $N_{\text{bkg}} = 16.6$. This number will vary from event to event as the PMTs are not distributed evenly in the detector.

For an event the number of selected hits is then compared to the number of expected background hits. This is done using the Poisson probability of the selected hits being background, $P(\text{bkg})$, the distribution of the logarithm of $P(\text{bkg})$ can be seen from Fig. 85. As shown in Fig. 85a for all triggered events and channels the distribution is peaked around -3.5 with a tail towards smaller values. The peak at -3.5 is caused by low energy events which produce a small number of hits in the detector which is not significant compared to the random background hypothesis.

As can be seen from Fig. 85b, the distributions change after the previous selections. The distribution of the shower channels are peaked at $\log P(\text{bkg}) = -2$ while the numuCC channel has large tails with an offset of -10 from zero. After all other cuts are applied the numuCC channel is essentially flat, while the distribution of the muon channel remains unchanged as can be seen from Fig. 85c. The cumulative distribution of $\log P(\text{bkg})$ after other selection variables is shown in Fig. 85d. A cut of $P(\text{bkg}) \geq 10^{-6}$ is defined which selects more than 95 % of the ‘‘Double Bang’’ signal while rejecting the remaining atmospheric muon events and 90 % of the remaining numuCC events.

6.1.5 Length cut

The length cut is a criterion to distinguish single shower events from ‘‘Double Bang’’ events, since for well reconstructed single shower events both reconstructed vertices are expected to be at the same position. Therefore, selecting a minimum reconstructed length between the two vertices rejects single shower events.

The distributions of the reconstructed lengths can be seen in Fig. 86. Since the Belle Starr Refit algorithm is only run for a sub sample of events, the reconstructed length for all triggered events is combination of results from either the Scan, Peak or Refit module. This causes the plateau at lengths greater than 200 m.

This behavior changes when the other selection variables are applied as can be seen from Fig. 86b and Fig. 86c which are identical since the length cut is the last cut to be applied. The distributions of single shower and track events peak at reconstructed lengths smaller than 5 m with the track events having some

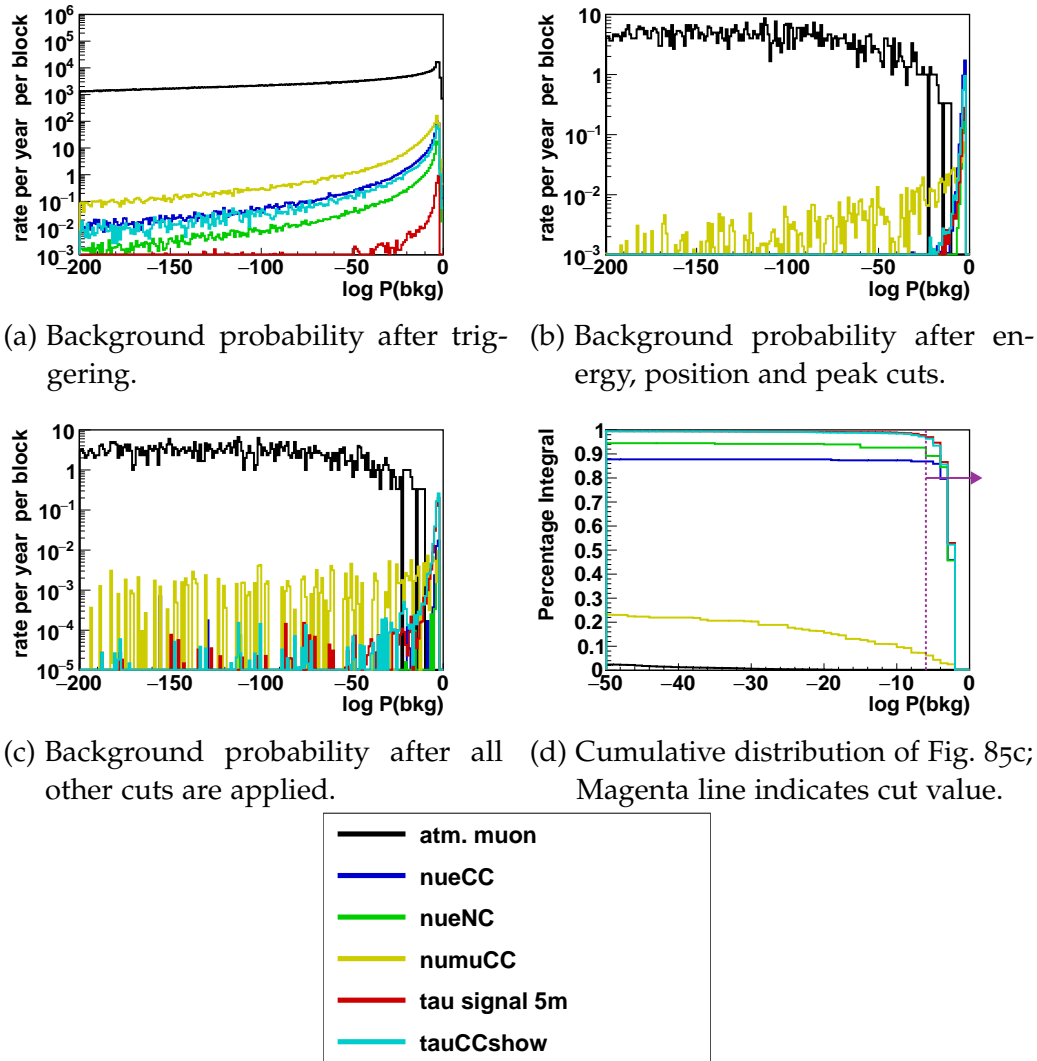


Figure 85: Distributions of the background probabilities for the different channels.

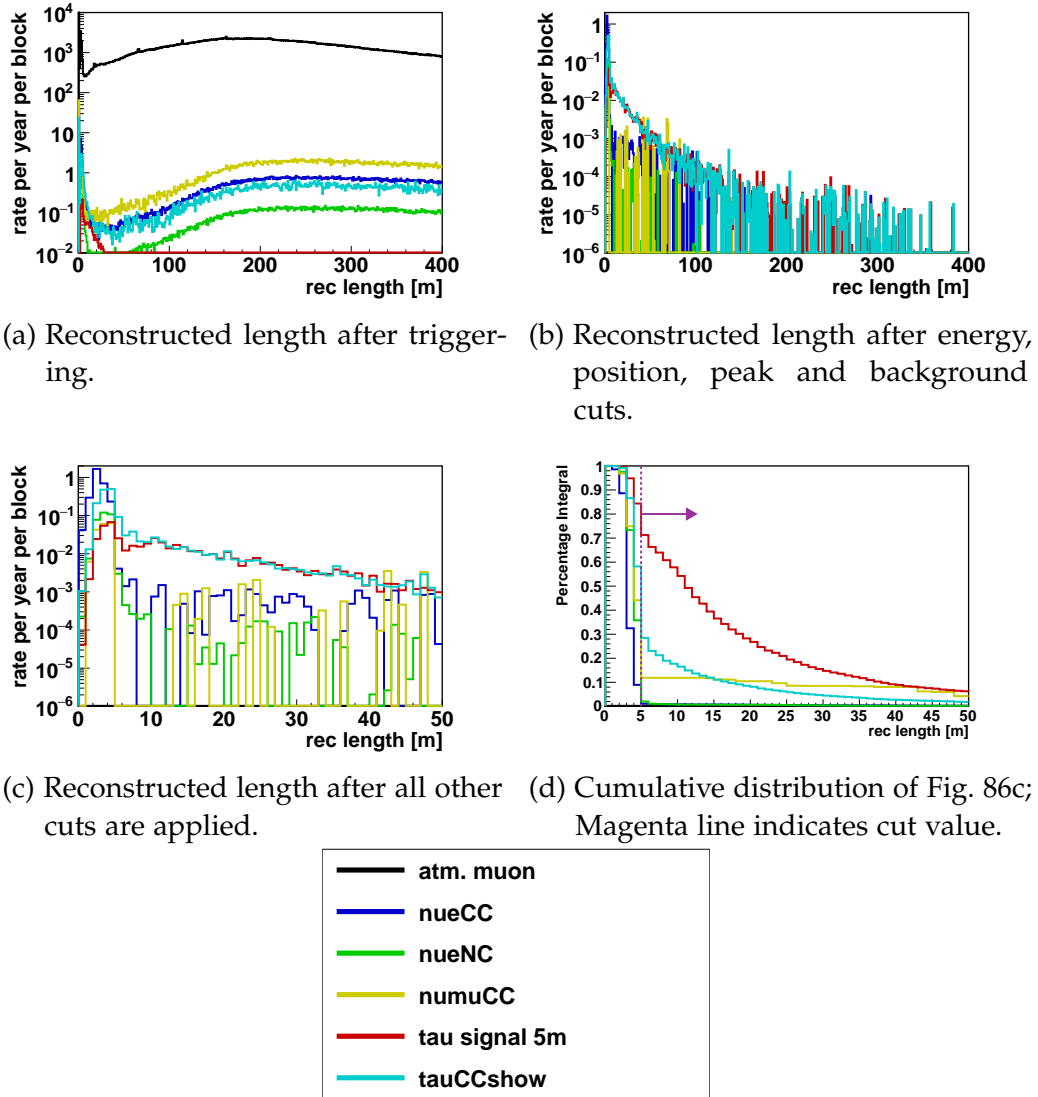


Figure 86: Distributions of the reconstructed lengths for the different channels.

events at longer lengths. For the tau signal events the distribution is peaked at zero with an exponential tail towards longer lengths. The dip at lengths between 5 m and 7 m is caused by the minimal flight length requirement of 5 m. The events which are wrongly reconstructed typically yield a shorter flight length than the simulated flight length. Therefore, the dip is only present in the tau signal and not the tauCCshow distribution.

By selecting events with a reconstructed length larger than 5 m the single shower and track events are highly suppressed.

6.2 SELECTION CRITERIA EFFICIENCY

The individual efficiencies of the selection criteria give a good indication of their performance. In order to quantify the performance, two different efficiencies are calculated for each criterion: the percentage of selected events of all triggered events (ϵ^{trig}) and the percentage of selected events after applying all other

selection criteria (ϵ^{selec}). The resulting efficiencies are shown in Tab. 2. In the case of ϵ^{selec} , if the other selection criteria rejected all simulated events the efficiency is denoted with “nan”. The error estimates for the efficiencies are given in Tab. 8 in the Appendix.

As can be seen from Tab.8, the energy cut applies equally well to all background channels, the background and peak cut mainly reject track like background events, the containment cut rejects atmospheric muons and the length cut rejects single shower events. The efficiencies for the “Double Bang” channels (tau signal and tauCCshow) show some differences for ϵ^{trig} while ϵ^{selec} are comparable. The differences for the ϵ^{trig} are caused by the preselection applied to the tau signal events resulting in a sample of reconstructable “Double Bang” events, whereas the tauCCshow events are dominated by events which are indistinguishable from single shower events. Therefore ϵ^{trig} is significantly lower for all cuts for the tauCCshow events. In the following, the ϵ^{selec} for the tau signal channel is discussed.

The ϵ^{selec} for the tau signal channel shows that the energy cut accepts almost all signal events. This is expected for a successful energy reconstruction, as the requirement for a minimal flight length of 5 m roughly translates to a minimal energy of 100 TeV. The position cut –by construction– reduces the detector volume by around 40 % and therefore rejects the same fraction of the tau signal events. The peak cut rejects around 18 % of the tau signal events. Most of these events have no significant peaks at all. The background cut accepts almost all tau signal events as expected in the case of a successful reconstruction. The length cut rejects around 30 %, these events typically have a large energy imbalance between the two showers (see e.g. in Fig. 55).

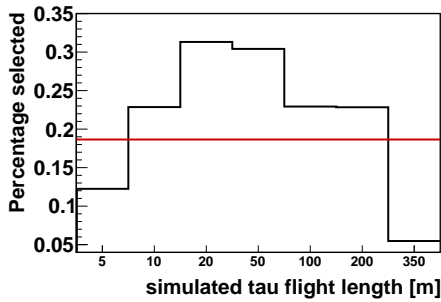
The dependence of the efficiencies are evaluated for different Bjorken y and tau flight length values for “Double Bang” events since these are important characteristics (for more details see Chap. 5.1). The selection efficiency given different simulated values for Bjorken y and tau flight length are shown in Fig. 87.

The flight length has a significant impact on the efficiency as shown in Fig. 87a. For flight lengths between 5 m to 10 m the low efficiency of around 0.1 is caused by the reconstruction performance. The efficiency increases and is maximal between 25 m to 50 m. The decrease towards longer lengths is caused by the background cut. At these lengths the finite Prefit direction resolution has a significant impact on the overall performance, causing the background cut to reject signal events. The average efficiency is dominated by small lengths as a result of the steep energy spectrum of the signal.

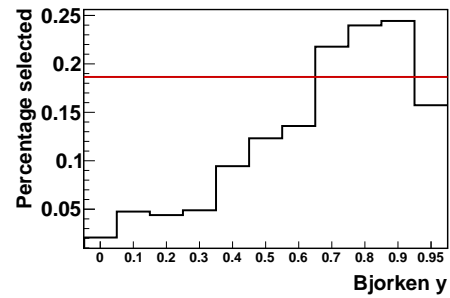
In principal, it could be assumed that the dependence on Bjorken y is symmetric, as Bjorken $y = 0.1$ and Bjorken $y = 0.9$ are two sides of the same coin. This is not the case for two reasons, namely: the vertices always have a fixed relative time ordering, with the neutrino vertex first and the tau decay vertex later, and the tau decay shower on average produces less visible energy than the neutrino interaction. As a result, the efficiency is highest at Bjorken y approaching one and lowest at Bjorken y approaching zero.

Table 2: Selection efficiencies using the selection criteria for the different MC channels; errors are given in Tab. 8.

	energy	position	peak	background	length
	ϵ^{trig}				
atm muon	0.041	0.053	0.003	0.023	0.290
nueCC	0.067	0.183	0.017	0.706	0.849
nueNC	0.047	0.179	0.010	0.705	0.872
numuCC	0.037	0.161	0.003	0.467	0.918
tau signal	0.855	0.417	0.533	0.827	0.698
tauCCshow	0.060	0.183	0.014	0.703	0.864
	ϵ^{selec}				
atm muon	0	0	0	0	nan
nueCC	0.396	0.188	0.168	0.869	0.011
nueNC	0.557	0.222	0.225	0.892	0.020
numuCC	0.349	0.276	0.207	0.061	0.119
tau signal	0.993	0.551	0.816	0.970	0.712
tauCCshow	0.917	0.512	0.684	0.963	0.285



(a) Length.



(b) Bjorken y.

Figure 87: Selection efficiency ϵ^{selec} for tauCCshow events for different simulated length and Bjorken y values; red line indicates the average selection efficiency.

6.3 BELLE STARR RESOLUTION FOR SELECTED EVENTS

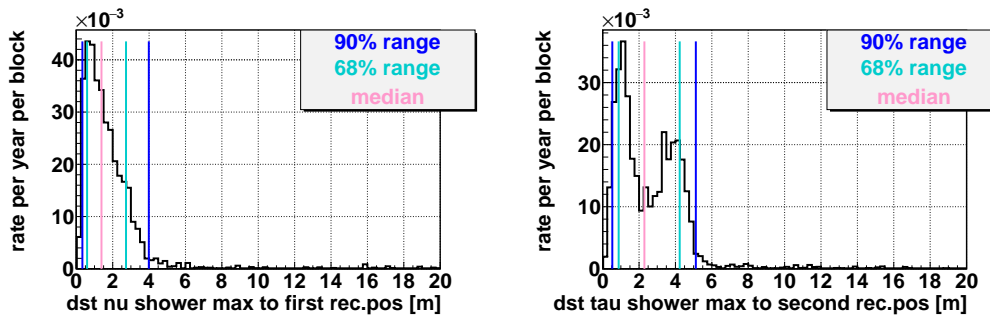
In this section the resolutions of the Belle Starr reconstruction chain for “Double Bang” events selected by the final criteria presented. The main focus is on the direction and position reconstruction.

For the position reconstruction the distance between the vertices and the corresponding simulated shower maxima are shown in Fig. 88a and Fig. 88b respectively. Again, the tau decay shower maximum resolution shows the double peak structure due to the difference in shower simulations for charged and neutral pions as discussed in Sec. 5.5.5. Hence, the position resolution is evaluated using the neutrino shower maximum.

A position resolution of 1.5 m median is achieved for the selected events. Compared to the position resolution of 2 m median for all tau signal events as shown in Fig. 77a the position resolution is significantly better. Especially the events in the tail of the distribution are rejected as is indicated by the significant improvement of the 90 % quantiles from 17 m to 4 m. This improvement further supports the selection criteria.

The position resolution results in a tau flight length resolution as shown in Fig. 89. The double peak of the tau shower maximum resolution is smeared by the neutrino shower maximum resolution and is therefore no longer visible. The peak is offset from zero by the difference between simulated flight length and the actual distance between the reconstructed shower maxima (on average 1.5 m). The shower maxima are almost always farther apart due to the energy distribution between the showers and the tau decay shower simulation. In order to give a better impression of the achieved length resolution the reconstructed length for MC events with different simulated length is shown in Fig. 90. As can be seen, for these events the same offset is visible, as they are simulated to have a Bjorken y of 0.9. The achieved length resolution in such a “clean” case is around 1 m FWHM.

The angular resolution is also improved as can be seen from Fig. 91 a median angular resolution of 1.3° is achieved compared to the 2° for all tau signal



(a) Distance between neutrino shower maximum and first vertex.

(b) Distance between tau shower maximum and second vertex.

Figure 88: Position resolution of the Belle Starr reconstruction chain for tau signal events selected by the final criteria.

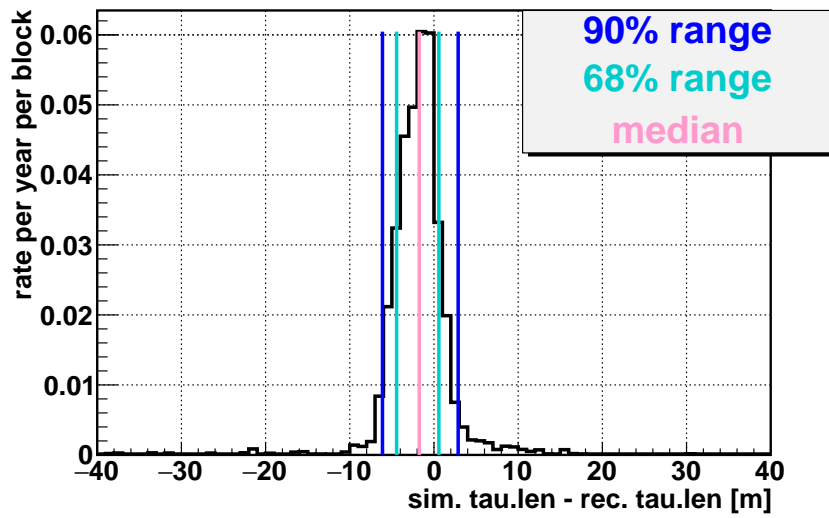


Figure 89: Tau flight length resolution for tau signal events selected by the final criteria.

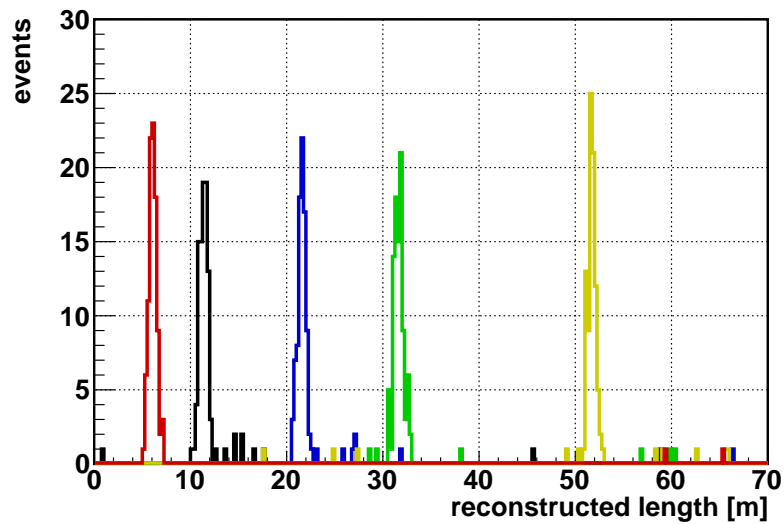


Figure 90: Reconstructed length for Toy MC events with different simulated flight length: 5 m, 10 m, 20 m, 30 m and 50 m from left to right; neutrino energy is 1 PeV and Bjorken y is 0.9 for all events.

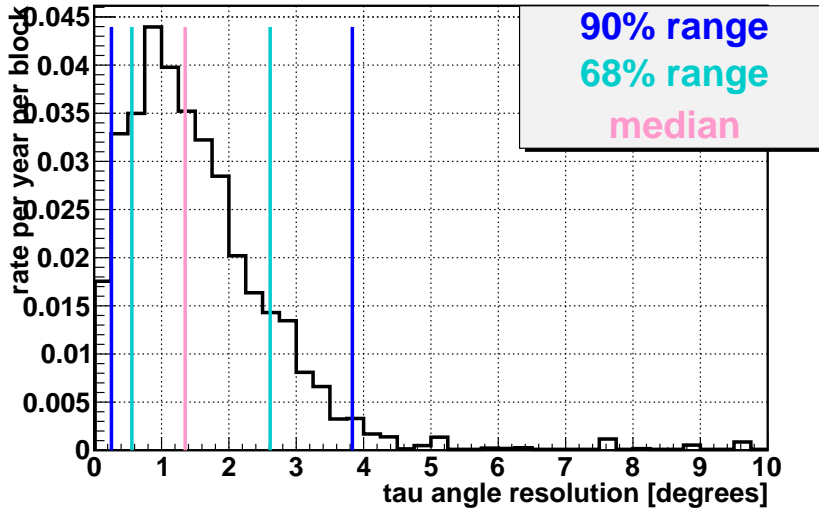


Figure 91: Tau angle resolution for tau signal events selected by the criteria described in Chap. 6.1.

events shown in Fig. 65a. As for the position resolution, the main improvement is achieved by reducing the tails of the distribution as the selection rejects badly reconstructed events and thereby significantly reduces the tails.

The length and direction resolution achieved for the selected events is directly comparable to the performance of AAShowerfit for single shower events as discussed in Chap. 5.3.

6.4 RESULTS OF THE TAU “DOUBLE BANG” SELECTION

The selection of “Double Bang” events presented in this chapter is successful at rejecting other neutrino interaction signatures and atmospheric muon signatures while accepting a significant amount of signal. With all selection cuts applied, the expected rates per year and block are summarized in Tab. 3. The number quoted for the atmospheric muons is an upper limit, as all simulated atmospheric muon events are rejected. The total statistics for atmospheric muons result in a rate per year per block of 0.33. Therefore, this value is quoted. The rates of background neutrino channels are all suppressed to at least one order of magnitude lower than the expected signal rate. The ν_{eNC} channel is the only flavor considered for the NC interaction. Since the NC interactions are identical for the three flavors assuming a (1:1:1) flavor ratio the expected total number of NC interactions is three times that of ν_{eNC} , i.e. 0.02 per year per block.

The rate of reconstructed “Double Bang” events is sensitive to the assumed neutrino flux. Due to the energy dependence of the tau flight length, the chosen soft spectrum with $\Gamma = 2.46$ and a 3 PeV cut-off is a conservative scenario. A more optimistic scenario is based on a harder spectrum without a cut-off. For example, a harder spectrum of $E^2\Phi_\nu = 1 \times 10^{-8} (E/\text{GeV}) \text{ GeV cm}^{-2} \text{ s}^{-1} \text{ sr}^{-1}$ per

Table 3: Results of the tau selection for a diffuse neutrino flux with spectral index $\gamma = 2.46$ and a 3 PeV cut-off for one ARCA building block.

channel	rate [per year per block]
atm. muon	0.33
nueCC	0.03
nueNC $\times 3$	0.02
numuCC	0.02
tauCCshow	0.48

flavor without a 3 PeV cut-off would result in a signal rate per year per block of 0.55 while keeping the signal to background ratio approximately unchanged.

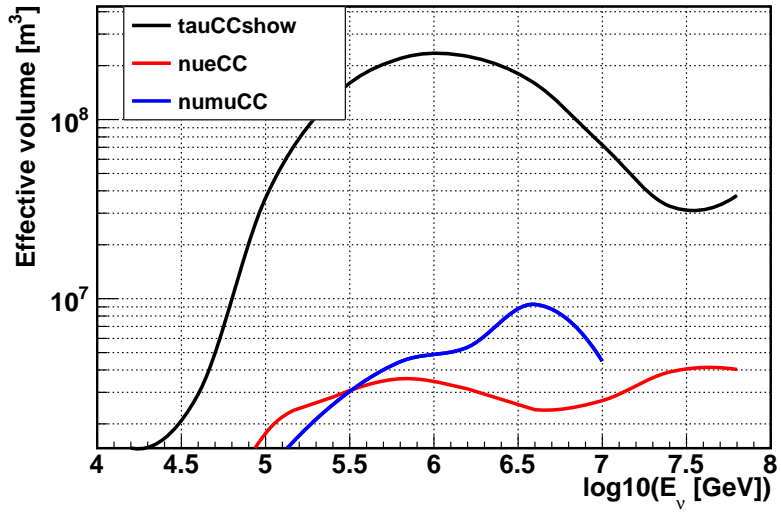
Since the results depend on the energy, they are expressed as the effective volume and effective area of one building block as a function of the neutrino energy. The effective volume is defined by

$$V_{\text{eff}}(E) = V_{\text{gen}} \times \frac{N_{\text{selec}}(E)}{N_{\text{gen}}(E)} \quad , \quad (36)$$

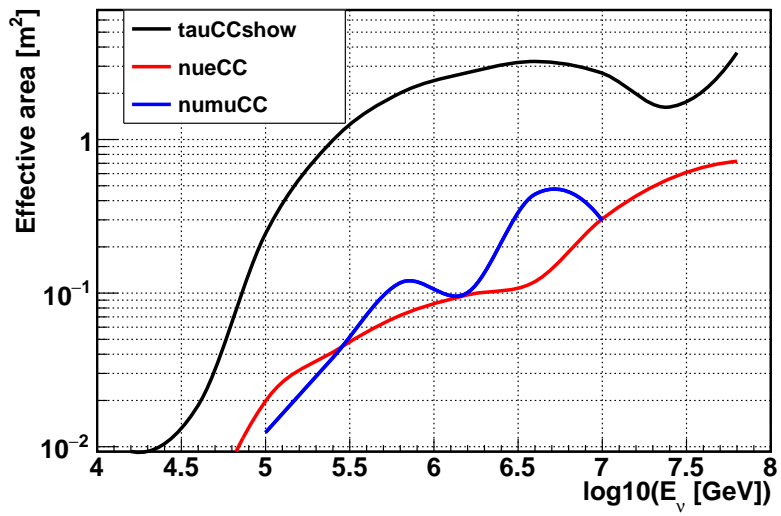
where V_{gen} is the generation volume, $N_{\text{selec}}(E)$ is the number of selected events in a given energy range and $N_{\text{gen}}(E)$ is the number of generated events in the same energy range. Therefore, the effective volume is the factual volume of the detector in which neutrinos are detected. By dividing the effective volume with the neutrino cross-section the effective area is obtained. The effective area represents the size of a virtual detector which has a 100 % detection efficiency.

The effective volume for a simulated neutrino energy is shown in Fig. 92a. For the numuCC and nueCC channels a spline interpolation is used due to the lack of statistics at high energies. Since the tauCCshow channel is simulated with a smaller spectral index it has sufficient statistics at high energies. For the signal channel, the effective volume is maximal around $\log(E_{\nu}[\text{GeV}]) = 6$. The high energy drop-off corresponds to the lower selection efficiencies at tau flight lengths above 50 m. The drop-off towards lower energies is caused by the energy cut. The numuCC and nueCC channels are approximately flat within the statistical variations. The effective volume for numuCC events has a higher energy threshold since these events deposit only a fraction of the neutrino energy in the detector.

The corresponding effective area are shown in Fig. 92b. It is maximal for the signal towards energies around $\log(E_{\nu}[\text{GeV}]) = 6.5$. This difference between effective volume and area is caused by the neutrino cross-section which monotonously increases with energy. Therefore, events at the highest energies corresponds to a large effective area.



(a) Effective volume after selection cuts.



(b) Effective area after selection cuts.

Figure 92: Studies of the effective area and volume for one ARCA building block for a spectral index of $\Gamma = 2.46$ and a 3 PeV cut-off.

6.5 DISCUSSION

The direct detection of “Double Bang” events using the KM₃NeT/ARCA detector touches on multiple topics of current scientific research. On the one hand, observed tau events can contribute significantly to the identification and characterization of an astrophysical neutrino flux. On the other hand, direct observations of tau neutrino interactions have only been performed by two experiments so far and in a completely different energy regime.

The tau neutrino events relate more directly to an astrophysical signal than electron or muon neutrinos for two reasons. Firstly, the background from atmospheric tau neutrinos is expected to be negligible so that tau events in principle yield a larger significance than electron or muon events. Secondly, the tau identification greatly benefits a flavor composition analysis since without tau identification a degeneracy in the flavor composition remains.

In order to evaluate the performance of Belle Starr, the results are compared to the results of the IceCube collaboration for a tau identification algorithm [122]. The IceCube algorithm identifies tau events by looking for a double pulse structure in the signal recorded by the PMTs. Therefore, only a “Double Bang” identification and no reconstruction of the two vertices is performed. This so-called “Double Pulse” algorithm achieves a tau identification of 0.22 events per year at a total expected background rate of 0.1 for all cosmic neutrino background channels for an assumed neutrino flux of $E^2\Phi_\nu = 1 \times 10^{-8} (E/\text{GeV}) \text{ GeV cm}^{-2} \text{ s}^{-1} \text{ sr}^{-1}$ per flavor.

In comparison, the Belle Starr algorithm identifies 0.55 tau events per year per ARCA block at a total expected background rate of 0.09 for all cosmic neutrino background channels. Additionally, the Belle Starr algorithm reconstructs the position of the two showers while the Double Pulse algorithm only identifies tau events. Considering, that a single ARCA block is around $2/3$ the instrumented volume of the IceCube detector, the Belle Starr algorithm clearly performs better than the Double Pulse algorithm.

This better performance is due to three main factors: the multi-PMT design of KM₃NeT, the detection medium and the two shower position reconstruction. The multi-PMT design offers excellent atmospheric muon rejection. The detection medium of KM₃NeT is liquid water and that of IceCube is ice. In water, light suffers less from scattering and therefore a better timing resolution is achieved. In ice, optical backgrounds are greatly reduced, but due to the KM₃NeT multi-PMT design the influence of these backgrounds are small. Last but not least, the two shower position reconstruction significantly improves the background rejection by allowing for powerful selection criteria.

The direct detection of tau neutrinos has been achieved by two experiments so far, namely: DONUT and OPERA. Both experiment observed tau neutrinos using a nuclear emulsion technique. In order to achieve the required tau tagging these detectors are designed to detect tau neutrino interactions at tau flight lengths in the $\mathcal{O}(\text{mm})$ range. The final analysis of the DONUT experiment [123] yielded 9 tau candidates in 5 months of data taking. The OPERA experiment

found a total of 5 tau events in 4 years of observation. Resulting in a 5σ discovery on $\nu_\mu \rightarrow \nu_\tau$ appearance [124].

Compared to these precision experiments, the Belle Starr reconstruction for KM₃NeT/ARCA adds a possibility to observe tau neutrinos from the cosmos at unprecedented energies. With the full realization of KM₃NeT consisting of 6 ARCA blocks, the largest sample of tau neutrino interactions in the world could be recorded.

APPENDIX

Table 4: PMT numbering scheme for a DOM

DAQ ID	PMT ID	Theta [rad]	Phi [rad]
22	A1	3.142	0
14	B1	2.582	0
19	B2	2.582	1.047
25	B3	2.582	2.094
24	B4	2.582	3.142
26	B5	2.582	4.189
18	B6	2.582	5.236
13	C1	2.162	0.524
21	C2	2.162	1.571
29	C3	2.162	2.618
28	C4	2.162	3.665
20	C5	2.162	4.712
17	C6	2.162	5.76
12	D1	1.872	0
15	D2	1.872	1.047
23	D3	1.872	2.094
30	D4	1.872	3.142
27	D5	1.872	4.189
16	D6	1.872	5.236
10	E1	1.27	0.524
6	E2	1.27	1.571
3	E3	1.27	2.618
2	E4	1.27	3.665
1	E5	1.27	4.712
11	E6	1.27	5.76
9	F1	0.98	0
8	F2	0.98	1.047
4	F3	0.98	2.094
0	F4	0.98	3.142
5	F5	0.98	4.189
7	F6	0.98	5.236

Table 5: ^{40}K parameters.

run	time offset [ns]
p1	-1.0383
p2	2.4347
p3	-0.68884
p4	1.3911

Table 6: DOM 3 time offsets using beacon 1 or 2 for calibration.

run	beacon 1 time offset [ns]	beacon 2 time offset [ns]
127	396.7	407.7
130	394.7	403.5
196	395.2	407.6
203	395	404.4

Table 7: Time offsets as determined with the muon calibration for the different periods in the data taking phase 2.

Time period	Run number	ended by	Hours	Time offset DOM 2 [ns]	Time offset DOM 3 [ns]
2014-09-16 to 2014-10-06	475 < run < 963	repower DOM 1	158.7	13.3±0.4	-21.1±0.4
2014-10-07 to 2014-10-13	964 < run < 1107	repower DOM 2	68.8	12.9±0.6	-20.5±0.6
2014-10-15 to 2014-10-17	1108 < run < 1158	repower DOM 2	25.3	12.8±0.9	-24.2±0.9
2014-10-20 to 2014-10-20	1159 < run < 1177	repower DOM 2	9.3	11.0±1.6	-25.7±1.6
2014-10-21 to 2014-10-27	1178 < run < 1339	power cut shore	77.8	10.4±0.6	-24.6±0.6
2014-12-01 to 2014-12-01	1440 < run < 1466	repower DOM 2	6.6	-1.4±2.3	-13.9±2.3
2014-12-03 to 2014-12-06	1467 < run < 1566	repower all DOMs	48.9	2.9±0.7	-12.0±0.7
2014-12-11 to 2014-12-13	1567 < run < 1664	repower all DOMs	45.0	2.4±0.7	-13.3±0.7
2014-12-14 to 2014-12-15	1665 < run < 1685	repower all DOMs	10.8	1.7±1.7	-8.1±1.7
2014-12-15 to 2014-12-15	1686 < run < 1695	repower all DOMs	6.0	1.6±2.9	-13.7±2.9

Table 8: Selection efficiencies error estimates.

	energy	position	npeaks	P(bkg)	length
	$\Delta\epsilon^{\text{trig}}$				
atm muon	0.0002	0.0002	0.0001	0.0002	0.0002
nueCC	0.0004	0.001	0.0002	0.001	0.001
nueNC	0.0004	0.001	0.0002	0.001	0.001
numuCC	0.001	0.001	0.0001	0.002	0.001
tau signal	0.007	0.007	0.007	0.005	0.006
tauCCshow	0.001	0.002	0.000	0.003	0.002
	$\Delta\epsilon^{\text{selec}}$				
atm muon	0.003	0.007	0.151	0.0002	0.0000
nueCC	0.044	0.020	0.019	0.039	0.001
nueNC	0.069	0.029	0.031	0.042	0.003
numuCC	0.096	0.073	0.059	0.016	0.035
tau signal 5m	0.004	0.010	0.013	0.004	0.011
tauCCshow	0.014	0.009	0.014	0.004	0.007

BIBLIOGRAPHY

- [1] V. F. Hess. Über Beobachtungen der durchdringenden Strahlung bei sieben Freiballonfahrten. *Physikalische Zeitschrift*, 13:1084–1091, November 1912.
- [2] W. Kolhörster. Measurements of the penetrating radiation in the free balloon at high altitudes. *Physikalische Zeitschrift*, 14:1153, 1913.
- [3] Carl D. Anderson. The Positive Electron. *Physical Review*, 43:491, 1933.
- [4] G. P. S. Occhialini and C. F. Powell. Nuclear Disintegrations Produced by Slow Charged Particles of Small Mass. *Physical Review*, 159:186–190, 1947.
- [5] Johannes Blumer, Ralph Engel, and Jörg R. Hörandel. Cosmic Rays from the Knee to the Highest Energies. *Prog. Part. Nucl. Phys.*, 63:293–338, 2009.
- [6] Katia M. Ferrière. The Interstellar Environment of our Galaxy. *Rev.Mod.Phys.*73:1031-1066, 2001.
- [7] Andreas Haungs. Cosmic Rays from the Knee to the Ankle. *Phys. Procedia*, 61:425–434, 2015.
- [8] K. A. Olive et al. Review of Particle Physics. *Chin. Phys.*, C38:090001, 2014.
- [9] Anthony M. Hillas. Cosmic Rays: Recent Progress and some Current Questions. In *Conference on Cosmology, Galaxy Formation and Astro-Particle Physics on the Pathway to the SKA Oxford, England*, 2006.
- [10] Ronnie Jansson and Glennys R. Farrar. A New Model of the Galactic Magnetic Field. *ApJ*, Volume 757, Issue 1, article id. 14, 13 pp., 2012.
- [11] Ronnie Jansson and Glennys R. Farrar. The Galactic Magnetic Field. *ApJ* 761 L11, 2012.
- [12] G. T. Zatsepin Greisen, Kenneth and V. A. Kuz'min. End to the cosmic ray spectrum? *Phys. Rev. Lett.*, 16:748–750, 1966.
- [13] C. Grupen. *Astroparticle Physics*. Springer, 2005.
- [14] The Fermi-LAT collaboration. Detection of the Characteristic Pion-Decay Signature in Supernova Remnants. *Science Magazine* 2013, volume 339, page 807, 2013.
- [15] Alexander Aab et al. Searches for Anisotropies in the Arrival Directions of the Highest Energy Cosmic Rays Detected by the Pierre Auger Observatory. *Astrophys. J.*, 804(1):15, 2015.

- [16] The Pierre Auger Collaboration. Update on the correlation of the highest energy cosmic rays with nearby extragalactic matter. *Astropart.Phys.*34:314-326, 2010.
- [17] M. P. Veron-Cetty and P. Veron. A catalogue of quasars and active nuclei: 12th edition. *Astron. Astrophys.*, 455:773-777, 2006.
- [18] The Pierre Auger Collaboration. Search for patterns by combining cosmic-ray energy and arrival directions at the Pierre Auger Observatory. *Eur. Phys. J. C* (2015) 75:269, 2014.
- [19] Enrico Fermi. On the origin of the cosmic radiation. *Phys. Rev.*, 75:1169-1174, Apr 1949.
- [20] Matthew G. Baring. Diffusive shock acceleration: The Fermi mechanism. In *Very high-energy phenomena in the universe. Proceedings, 32nd Rencontres de Moriond, Les Arcs, France, January 18-25, 1997*, pages 97-106, 1997.
- [21] R. D. Blandford and J. P. Ostriker. Particle Acceleration by Astrophysical Shocks. *Astrophys. J.*, 221:L29-L32, 1978.
- [22] G. F. Krymskii. A regular mechanism for the acceleration of charged particles on the front of a shock wave. *Akademiia Nauk SSSR Doklady*, 234:1306-1308, June 1977.
- [23] David R. Ballantyne, Fulvio Melia, Siming Liu, and Roland M. Crocker. A Possible Link Between the Galactic Center HESS Source and Sgr A*. *Astrophys. J.*, 657:L13-L16, 2007.
- [24] F. Fraschetti and F. Melia. Ultra-High-Energy Cosmic Rays from the Radio Lobes of AGNs. *Mon. Not. Roy. Astron. Soc.*, 391:1100-1106, 2008.
- [25] W. Pauli. Offener Brief an die Gruppe der Radioaktiven bei der Gauvereine-Tagung zu Tübingen. December 1930.
- [26] W. Ganchang. A Suggestion on the Detection of the Neutrino. *Phys.Rev.*, 61:97, 1942.
- [27] C. L. Cowan, F. Reines, F. B. Harrison, H. W. Kruse, and A. D. McGuire. Detection of the free neutrino: A Confirmation. *Science*, 124:103-104, 1956.
- [28] G. Danby, J. M. Gaillard, Konstantin A. Goulianos, L. M. Lederman, Nari B. Mistry, M. Schwartz, and J. Steinberger. Observation of High-Energy Neutrino Reactions and the Existence of Two Kinds of Neutrinos. *Phys. Rev. Lett.*, 9:36-44, 1962.
- [29] K. Kodama et al. Observation of tau neutrino interactions. *Phys. Lett.*, B504:218-224, 2001.
- [30] Ivan V. Anicin. The Neutrino - Its Past, Present and Future. SFIN (Institute of Physics, Belgrade) year XV, Series A: Conferences, No. A2 3-59, 2002.

- [31] Raymond Davis, Jr., Don S. Harmer, and Kenneth C. Hoffman. Search for neutrinos from the sun. *Phys. Rev. Lett.*, 20:1205–1209, 1968.
- [32] I. Esteban et al. ν -fit. www.nu-fit.org.
- [33] B. Povh. *Teilchen und Kerne*. Springer, 7. Aufl. Springer Berlin Heidelberg New York edition, 2006.
- [34] SNO Collaboration. Measurement of the rate of $\nu_e + d \rightarrow p + p + e^-$ interactions produced by 8B solar neutrinos at the Sudbury Neutrino Observatory. *Phys.Rev.Lett.*87:071301, 2001.
- [35] Y. Fukuda et al. Evidence for oscillation of atmospheric neutrinos. *Phys. Rev. Lett.*, 81:1562–1567, 1998.
- [36] V. Gribov and B. Pontecorvo. Neutrino astronomy and lepton charge. *Physics Letters B*, 28:493–496, January 1969.
- [37] B. Povh. *Teilchen und Kerne*. 2006.
- [38] Sheldon Stone. New physics from flavor. *PoS, ICHEP2012:033*, 2013.
- [39] Jorge G. Morfin, Juan Nieves, and Jan T. Sobczyk. Recent Developments in Neutrino/Antineutrino - Nucleus Interactions. *Adv. High Energy Phys.*, 2012:934597, 2012.
- [40] Kalpana Bora and Neelakshi Sarma. Neutrino-Nucleon Cross section in Ultra High Energy Regime. *Springer Proc. Phys.*, 174:345–351, 2016.
- [41] Raj Gandhi, Chris Quigg, Mary Hall Reno, and Ina Sarcevic. Ultrahigh-Energy Neutrino Interactions. *Astropart.Phys.*5:81-110, 1996.
- [42] Sheldon L. Glashow. Resonant Scattering of Antineutrinos. *Phys. Rev.*, 118:316–317, 1960.
- [43] V. Barger, Lingjun Fu, J. G. Learned, D. Marfatia, S. Pakvasa, and T. J. Weiler. Glashow resonance as a window into cosmic neutrino sources. *Phys. Rev.*, D90:121301, 2014.
- [44] L. Wolfenstein. Neutrino Oscillations in Matter. *Phys. Rev.*, D17:2369–2374, 1978.
- [45] S. P. Mikheev and A. Yu. Smirnov. Resonance Amplification of Oscillations in Matter and Spectroscopy of Solar Neutrinos. *Sov. J. Nucl. Phys.*, 42:913–917, 1985. [*Yad. Fiz.*42,1441(1985)].
- [46] S Ricciardi. Lecture Notes on Neutrino oscillations in Matter. 2013.
- [47] Petr Vogel, Liangjian Wen, and Chao Zhang. Neutrino Oscillation Studies with Reactors. *Nature Commun.*, 6:6935, 2015.
- [48] Tomasz Palczewski.

- [49] Rikard Enberg, Mary Hall Reno, and Ina Sarcevic. Prompt neutrino fluxes from atmospheric charm. *Phys. Rev.*, D78:043005, 2008.
- [50] S. Adrian-Martinez et al. Measurement of the atmospheric ν_μ energy spectrum from 100 GeV to 200 TeV with the ANTARES telescope. *Eur. Phys. J.*, C73(10):2606, 2013. [Eur. Phys. J.C73,2606(2013)].
- [51] M. G. Aartsen et al. Measurement of the Atmospheric ν_e Spectrum with IceCube. *Phys. Rev.*, D91:122004, 2015.
- [52] M. G. Aartsen et al. Development of a General Analysis and Unfolding Scheme and its Application to Measure the Energy Spectrum of Atmospheric Neutrinos with IceCube. *Eur. Phys. J.*, C75(3):116, 2015.
- [53] John N. Bahcall. Solar models: An Historical overview. *AAPPS Bull.*, 12(4):12–19, 2002. [Int. J. Mod. Phys.A18,3761(2003)].
- [54] John N. Bahcall. Solar models and solar neutrinos: Current status. *Phys. Scripta*, T121:46–50, 2005.
- [55] Amand Faessler, Rastislav Hodak, Sergey Kovalenko, and Fedor Simkovic. Can one measure the Cosmic Neutrino Background? 2016.
- [56] N. Sahakyan. Galactic sources of high energy neutrinos: Expectation from gamma-ray data. *EPJ Web Conf.*, 121:05005, 2016.
- [57] Paolo Lipari, Maurizio Lusignoli, and Davide Meloni. Flavor composition and energy spectrum of astrophysical neutrinos. *Phys. Rev. D*, 75:123005, Jun 2007.
- [58] M. C. Gonzalez-Garcia, Michele Maltoni, and Thomas Schwetz. Updated fit to three neutrino mixing: status of leptonic CP violation. *JHEP*, 11:052, 2014.
- [59] M. G. Aartsen et al. A combined maximum-likelihood analysis of the high-energy astrophysical neutrino flux measured with IceCube. *Astrophys. J.*, 809(1):98, 2015.
- [60] Aaron C. Vincent, Sergio Palomares-Ruiz, and Olga Mena. Analysis of the 4-year IceCube high-energy starting events. *Phys. Rev.*, D94(2):023009, 2016.
- [61] M. A. Markov. On high energy neutrino physics. In *Proceedings, 10th International Conference on High-Energy Physics (ICHEP 60)*, pages 578–581, 1960.
- [62] P. W. Groham et al. Mechanical and Acoustic Studies of Deep Ocean Glass Sphere Implosions. *Unfinished*.
- [63] Francis Halzen and Spencer R. Klein. IceCube: An Instrument for Neutrino Astronomy. *Rev. Sci. Instrum.*, 81:081101, 2010.

- [64] V. Aynutdinov et al. The Baikal neutrino experiment: From NT200 to NT200+. *Nucl. Instrum. Meth.*, A567:433–437, 2006.
- [65] A. V. Avrorin et al. Data acquisition system of the NT1000 Baikal neutrino telescope. *Instrum. Exp. Tech.*, 57(3):262–273, 2014.
- [66] M. Ageron et al. ANTARES: the first undersea neutrino telescope. *Nucl. Instrum. Meth.*, A656:11–38, 2011.
- [67] Adrián-Martínez et al. Letter of intent for KM₃NeT 2.0. *Journal of Physics G: Nuclear and Particle Physics*, 43(8):084001, 2016.
- [68] C. Spiering. The Global Neutrino Network. <http://www.globalneutrino.org>.
- [69] Pavel A. Cherenkov. Visible emission of clean liquids by action of γ radiation. *Doklady Akademii Nauk SSSR* 2, 1934.
- [70] A. A. Watson. The Discovery of Cherenkov Radiation and its use in the detection of extensive air showers. 2011.
- [71] C. A. Mead. Quantum Theory of the Refractive Index. *Physical Review*, 110:359–369, April 1958.
- [72] M. de Jong. The probability density function of the arrival time of light. KM₃NeT internal note, 2012.
- [73] M. Jongen. Single photon tracking using Markov Chain MC simulations. Private correspondence, 2017.
- [74] C. Kopper. *Performance Studies for the KM₃NeT Neutrino Telescope*. PhD thesis, Friedrich-Alexander-Universität Erlangen-Nürnberg, Germany, 2010.
- [75] R. Mirani. *Parametrisation of EM-showers in the ANTARES detector-volume*. PhD thesis, Universiteit van Amsterdam, Netherlands, 2002.
- [76] K. S. Hirata et al. Observation in the Kamiokande-II Detector of the Neutrino Burst from Supernova SN 1987a. *Phys. Rev.*, D38:448–458, 1988.
- [77] R. M. Bionta et al. Observation of a Neutrino Burst in Coincidence with Supernova SN 1987a in the Large Magellanic Cloud. *Phys. Rev. Lett.*, 58:1494, 1987.
- [78] Alessandro Mirizzi, Irene Tamborra, Hans-Thomas Janka, Ninetta Saviano, Kate Scholberg, Robert Bollig, Lorenz Hudepohl, and Sovan Chakraborty. Supernova Neutrinos: Production, Oscillations and Detection. *Riv. Nuovo Cim.*, 39(1-2):1–112, 2016.
- [79] M. G. Aartsen et al. First observation of PeV-energy neutrinos with IceCube. *Phys. Rev. Lett.*, 111:021103, 2013.

- [80] M. G. Aartsen et al. Evidence for High-Energy Extraterrestrial Neutrinos at the IceCube Detector. *Science*, 342:1242856, 2013.
- [81] M. G. Aartsen et al. Observation and Characterization of a Cosmic Muon Neutrino Flux from the Northern Hemisphere using six years of IceCube data. *Astrophys. J.*, 833(1):3, 2016.
- [82] The KM₃NeT collaboration. Expansion cone for the 3-inch PMTs of the KM₃NeT optical modules. *Journal of Instrumentation*, 8(03):T03006, 2013.
- [83] S. Aiello, L. Classen, V. Giordano, Oleg Kalekin, E. Leonora, H. Peek, J. Reubelt, D. Samtleben, and E. Visser. Characterization of the 80-mm diameter Hamamatsu PMTs for the KM₃NeT project. *AIP Conf. Proc.*, 1630:118–121, 2014.
- [84] P. Timmer, E. Heine, and H. Peek. Very low power, high voltage base for a photo multiplier tube for the KM₃NeT deep sea neutrino telescope. *JINST*, 5:C12049, 2010.
- [85] Alexander Enzenhöfer. Integration of acoustical sensors into the KM₃NeT Optical Modules. *AIP Conf. Proc.*, 1630:189–192, 2014.
- [86] David Calvo. Nanobeacon: A low cost time calibration instrument for the KM₃NeT neutrino telescope. *AIP Conf. Proc.*, 1630:138–141, 2014.
- [87] Gerard Kieft and Marinus van der Hoek. Aspects of the optical system relevant for the KM₃NeT timing calibration. In *Proceedings, 7th Very Large Volume Neutrino Telescope Workshop (VLVnT15)*, 2015.
- [88] Prashant Shukla. Energy and angular distributions of atmospheric muons at the Earth. 2016.
- [89] C. W. James. GENHEN release v7r6. KM₃NeT Internal Note, 2016.
- [90] P. Antonioli, C. Ghetti, E. V. Korolkova, V. A. Kudryavtsev, and G. Sartorelli. A Three-dimensional code for muon propagation through the rock: Music. *Astropart. Phys.*, 7:357–368, 1997.
- [91] Stanislaw Jadach, Johann H. Kuhn, and Zbigniew Was. TAUOLA: A Library of Monte Carlo programs to simulate decays of polarized tau leptons. *Comput. Phys. Commun.*, 64:275–299, 1990.
- [92] G. Carminati, A. Margiotta, and M. Spurio. Atmospheric MUons from PArametric formulas: A Fast GEnerator for neutrino telescopes (MUPAGE). *Comput. Phys. Commun.*, 179:915–923, 2008.
- [93] D. Heck et al. CORSIKA web page. <http://www.ikp.kit.edu/corsika/>, 2017.

- [94] Edgar Bugaev, Teresa Montaruli, Yuri Shlepin, and Igor A. Sokalski. Propagation of tau neutrinos and tau leptons through the earth and their detection in underwater / ice neutrino telescopes. *Astropart. Phys.*, 21:491–509, 2004.
- [95] D. Bailey. ANTARES-SOFT-2002-006. Antares Internal Note, 2002.
- [96] M. de Jong et al. The JPP software package. www.km3net.org.
- [97] E. De Wolf, R. Bakker, H. Boer Rookhuizen, L. Gostiaux, R. Groenewegen, H. Van Haren, J. Van Heerwaarden, Th. Hillebrand, M. Laan, and A. Smit. A launching vehicle for optical modules of a deep-sea neutrino telescope. *Nucl. Instrum. Meth.*, A725:241–244, 2013.
- [98] S. Adrián-Martínez, M. Ageron, F. Aharonian, S. Aiello, A. Albert, F. Ameli, E. G. Anassontzis, M. Anghinolfi, G. Anton, S. Anvar, and et al. Deep sea tests of a prototype of the KM₃NeT digital optical module. *European Physical Journal C*, 74:3056, September 2014.
- [99] R. Bormuth et al (KM₃NeT collaboration). Characterization of the ETEL and HZC 3-inch PMTs for the KM₃NeT project. *Proceedings, Topical Workshop on Electronics for Particle Physics (TWEPP14)*, 1630:114, 2014.
- [100] *Proceedings, 34th International Cosmic Ray Conference (ICRC 2015)*, volume ICRC2015, 2015.
- [101] Rene Brun and Fons Rademakers. Root - An Object Oriented Data Analysis Framework. In *Proceedings AIHENP'96 Workshop, Lausanne, Sep. 1996, Nucl. Inst. & Meth. in Phys. Res. A 389 (1997) 81-86*. See also <http://root.cern.ch/>.
- [102] M. Bazzotti, G. Carminati, A. Margiotta, and M. Spurio. An update of the generator of atmospheric muons from parametric formulas (MUPAGE). *Computer Physics Communications*, 181:835–836, April 2010.
- [103] J. Brunner. Antares simulation tools. In *Technical aspects of a Very Large Volume Neutrino Telescope in the Mediterranean Sea. Proceedings, Workshop, VLVnT Workshop, Amsterdam, Netherlands, October 5-8, 2003*, pages 109–113, 2003.
- [104] A. Margiotta. Common simulation tools for large volume neutrino detectors. *Nucl. Instrum. Meth.*, A725:98–101, 2013.
- [105] The KM₃NeT collaboration. KM₃NeT: Technical Design Report for a Deep-Sea Research Infrastructure in the Mediterranean Sea Incorporating a Very Large Volume Neutrino Telescope. 2009. ISBN 978-90-6488-033-9.
- [106] R. Bormuth and D.F.E. Samtleben. PPM-DU Time Calibration Note. 2015-CALIB-009. www.km3net.org.

- [107] A. G. Tsirigotis, A. Leisos, S. E. Tzamarias, and for the KM₃NeT Consortium. Reconstruction efficiency and discovery potential of a Mediterranean neutrino telescope: A simulation study using the Hellenic Open University Reconstruction & Simulation (HOURS) package, 2012.
- [108] R. Bormuth and N. Kitzmann. PPM-DU Intra-DOM Calibration Studies. 2015. www.km3net.org.
- [109] Alexander Kappes, Jim Hinton, Christian Stegmann, and Felix A. Aharonian. Potential Neutrino Signals from Galactic Gamma-Ray Sources. *Astrophys. J.*, 656:870–896, 2007. [Erratum: *Astrophys. J.*661,1348(2007)].
- [110] Karel Melis. Reconstruction of High-energy Neutrino-induced Particle Showers in KM₃NeT. Master’s thesis, Universiteit van Amsterdam, the Netherlands, 2014.
- [111] M. Ageron. Performance of the First ANTARES Detector Line. *Astropart. Phys.*, 31:277–283, 2009.
- [112] A. Heijboer. Shower Direction Reconstruction: aashowerfit. *KM₃NeT internal*, 2014.
- [113] William H. Press, Saul A. Teukolsky, William T. Vetterling, and Brian P. Flannery. *Numerical Recipes 3rd Edition: The Art of Scientific Computing*. Cambridge University Press, New York, NY, USA, 3 edition, 2007.
- [114] R. L. Launer and G. N. Wilkinson. *Robustness in Statistics*. 1983.
- [115] M. et al. Morhac. Background elimination methods for multidimensional coincidence gamma-ray spectra. *Nucl. Instrum. Meth.*, A401:113–132, 1997.
- [116] M. et al. Morhac. Identification of peaks in multidimensional coincidence gamma-ray spectra. *Nucl. Instrum. Meth.*, A443:108–125, 2000.
- [117] C. G. Ryan, E. Clayton, W. L. Griffin, S. H. Sie, and D. R. Cousens. SNIP, a statistics-sensitive background treatment for the quantitative analysis of PIXE spectra in geoscience applications. *Nuclear Instruments and Methods in Physics Research B*, 34:396–402, September 1988.
- [118] Z. K. Silagadze. A New algorithm for automatic photopeak searches. *Nucl. Instrum. Meth.*, A376:451–454, 1996.
- [119] W. Feller. An introduction in probability theory and its applications. v1, 1966.
- [120] M.A. Mariscotti. A method for automatic identification of peaks in the presence of background and its application to spectrum analysis. *Nucl. Instrum. Meth.*, 50:309, 1967.
- [121] IceCube Collaboration. A combined maximum-likelihood analysis of the high-energy astrophysical neutrino flux measured with icecube. *Astrophysical Journal* 809, 98, 2015.

- [122] M. G. Aartsen et al. Search for Astrophysical Tau Neutrinos in Three Years of IceCube Data. *Phys. Rev.*, D93(2):022001, 2016.
- [123] K. Kodama et al. Final tau-neutrino results from the DONuT experiment. *Phys. Rev.*, D78:052002, 2008.
- [124] N. Agafonova et al. Discovery of τ Neutrino Appearance in the CNGS Neutrino Beam with the OPERA Experiment. *Phys. Rev. Lett.*, 115(12):121802, 2015.

SUMMARY

Human societies share a fascination for the night sky. This led to independent development of astronomy in various ancient civilizations such as the Babylonians or the Chinese. Today, astronomy is a major field of scientific research with the aim to probe the Universe in time and space. Throughout its long history astronomy has primarily relied on light-based observations, known as optical astronomy. During the past decades, optical astronomy has expanded from observations of light in the visual spectrum to observations extending over 12 orders of magnitude in wavelength. Despite its many successes, optical astronomy has so far not been able to answer several fundamental questions and may never be.

Among these questions is the topic of Cosmic Rays. Cosmic Rays are charged particles (mainly nuclei) traversing the Universe. Their energy spectrum extends up to the highest energies ever observed. Since their discovery more than 100 years ago, one has not been able to identify their sources nor explain how they obtain their energies. The lack of conclusive observations is caused by the interactions between Cosmic Rays and the magnetic fields present in the Universe. When a Cosmic Ray traverses a magnetic field it is forced onto a curved trajectory, which makes location of the sources fade away.

This inherent problem can be overcome by observing neutrinos. Neutrinos are almost massless elementary particles with two properties that make them suitable candidates for observing the Universe: they have a very low interaction probability with matter and they have no charge. The former allows them to travel quasi infinite distances through the Universe and the latter keeps their trajectories straight. Neutrinos are well-suited to investigate the sources of Cosmic Rays as they are produced by interactions of Cosmic Rays with matter or light surrounding their sources. The different behavior of neutrinos compared to other particles traversing the Universe is illustrated in Fig. 1.

Although the low interaction probability makes neutrinos ideal for investigating the origin of Cosmic Rays, it also makes their detection challenging. A large detection volume is necessary in order to record sufficient statistics. Once a neutrino interacts in the detection volume, the subsequently produced particles generate light along their trajectories (so-called Cherenkov light). The light is emitted at a fixed angle relative to the particle trajectory, which is related to the known refractive index of the medium. By detecting the Cherenkov light, the direction of the particles and therefore the direction of the initial neutrino can be reconstructed. In order to detect the light, the detection volume has to be instrumented with sensors and the instrumented medium has to be transparent. This makes natural ice and water good candidates. In the detector volume, the sensors are arranged in a three dimensional array. To ensure that the detected light is produced by neutrino interactions, neutrino telescopes are located at large depths to provide shielding. For these reasons, neutrino telescopes typi-

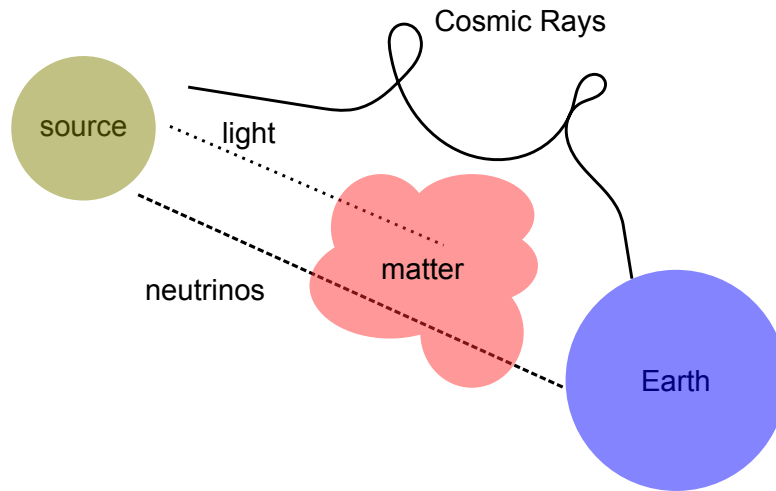


Figure 1: An illustration of the trajectories of different cosmic particles from a source to the Earth. The magnetic fields are not drawn but are omnipresent. As a consequence of the different interactions particles can undergo during their propagation through the Universe, neutrinos are ideal particles to find the origin of Cosmic Rays.

cally instrument around a cubic-kilometer of ice or water at depths between 2 to 4 kilometers.

The first and currently only neutrino telescope that observed cosmic neutrinos is the IceCube detector. The first evidence for a cosmic neutrino signal was reported in 2013. Since then, the IceCube telescope has proven the signal to be of cosmic origin. However, other properties such as the neutrino sources and the energy spectrum need further investigation due to the low number of events and the limited angular resolution.

In order to improve our understanding of this cosmic neutrino signal, more neutrino telescopes of a comparable volume with enhanced performance are needed. One such telescope will be the KM₃NeT detector located in the abyss of the Mediterranean Sea, which is currently under construction. For KM₃NeT, the sensors are mounted inside glass spheres as shown in Fig. 2. Of these spheres 18 are in turn attached to a string, resembling a pearl necklace. The strings are anchored to the sea floor and held upright by the intrinsic buoyancy of the glass spheres. A set of 115 strings makes up one KM₃NeT block.

The KM₃NeT telescope is expected to yield a more accurate measurement of the cosmic neutrino signal compared to the IceCube telescope. The improvement is mainly due to two factors: the optical properties of water compared to ice and the detection technology employed by KM₃NeT. The latter can largely be attributed to the transition from a single large light sensor to 31 small light sensors. This allows to point sensors in one sphere in almost all directions and to separately count the photons of the detected light signal. A comparison between the IceCube and the KM₃NeT spheres is shown in Fig. 2. The new technology of KM₃NeT required thorough planning and prototyping. In this

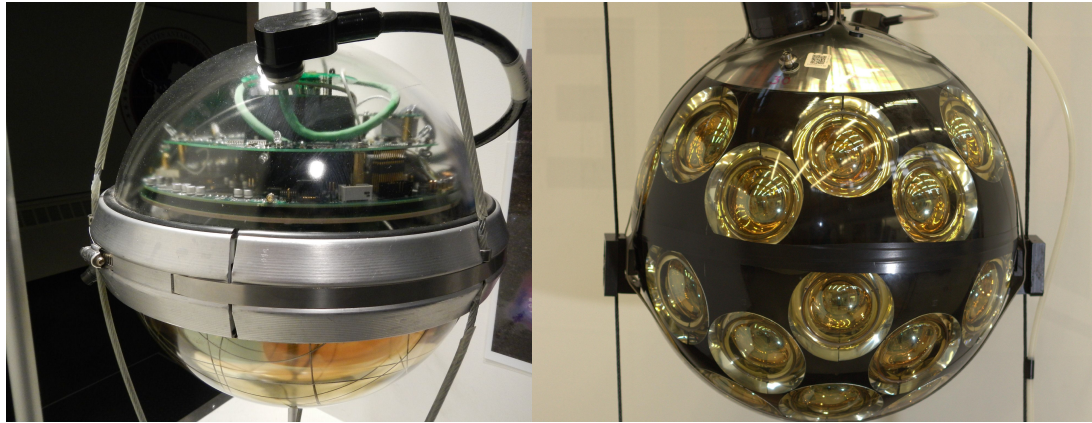


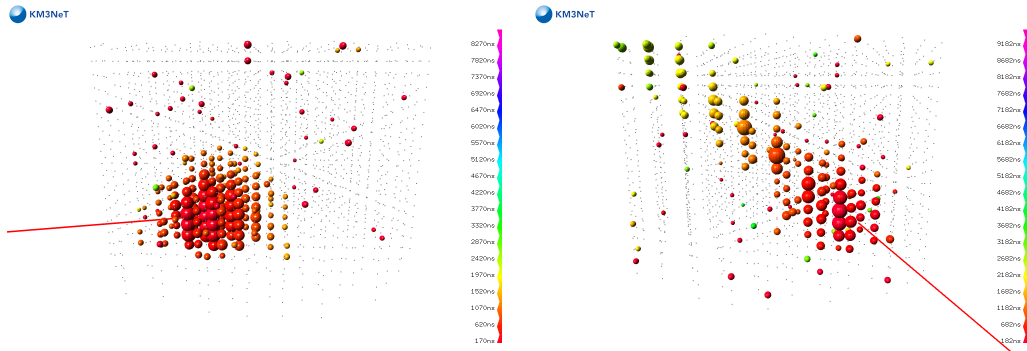
Figure 2: A picture of an IceCube module (left) and a KM₃NeT module (right), showing the difference in light sensors.

work results of the string prototype are shown. The prototype, installed in 2014 at the KM₃NeT Italy site, allowed to test important parts of the KM₃NeT hardware and helped to establish protocols for future detector construction and operation. The results include the time calibration procedure and the identification and reconstruction of atmospheric muons.

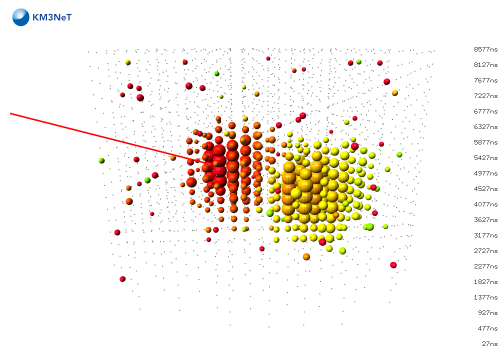
The performance improvements enable the KM₃NeT telescope to identify the type of the interacting neutrino with unprecedented accuracy. There are three neutrino types (distinguished by *flavor*), one for each charged lepton: electron, muon and tau. Neutrinos can change from one type to another during propagation depending on the path length and energy. This phenomenon is referred to as *neutrino oscillations* and as a result an approximately equal share of neutrino flavors is expected to arrive on Earth from a cosmic neutrino signal. Nevertheless, the exact flavor composition of a cosmic neutrino signal can in principle be reconstructed with a neutrino telescope. This allows to scrutinize theoretical models for neutrino sources and helps to reduce backgrounds from non-cosmic neutrinos.

The three different neutrino types can be distinguished from another by the different signatures of light they leave in the detector after an interaction. The different signatures are caused by the different neutrino flavors producing different particles. The signatures are combinations of the so-called *shower* and/or *track* signatures. Shower signatures are caused by multiple particles with short trajectories resulting in light emitted from an approximately point-like source, akin to a firework explosion. Track signatures are caused by muons which can travel kilometers before they decay and emit light along the way, akin to a shooting star. Examples of a shower, track and two shower signatures are shown in Fig. 3 for the KM₃NeT detector. Shower signatures can be caused by electron neutrinos, track signatures by muon neutrinos and two shower signatures by tau neutrinos (“Double Bangs”). However, depending on energies and processes involved, these associations can be hampered.

In this work, an algorithm for identifying and reconstructing “Double Bang” events using the KM₃NeT detector is presented. While single shower and track



(a) A shower signature induced by an electron neutrino. (b) A track signature induced by a muon neutrino.



(c) A two shower signature induced by a tau neutrino.

Figure 3: Simulations of the detector response for the different signatures in one KM₃NeT block; shown are the positions of glass spheres housing the light detectors. The size indicates the number of detected photons and the color the time (red=early to purple=late). The red line shows the simulated neutrino trajectory.

reconstruction algorithms are well established, a reconstruction algorithm for “Double Bang” signatures was missing. With the “Double Bang” reconstruction, the tau neutrino interactions can be distinguished from the electron and the muon neutrino interactions. This is desirable for two reasons. First, it makes it possible to reconstruct the flavor composition of a cosmic neutrino signal. Second, the neutrino background for the tau flavor is expected to be much smaller compared to that of cosmic electron and muon neutrinos. Thus, the observation of a single “Double Bang” event represents a “smoking gun” for a cosmic neutrino signal.

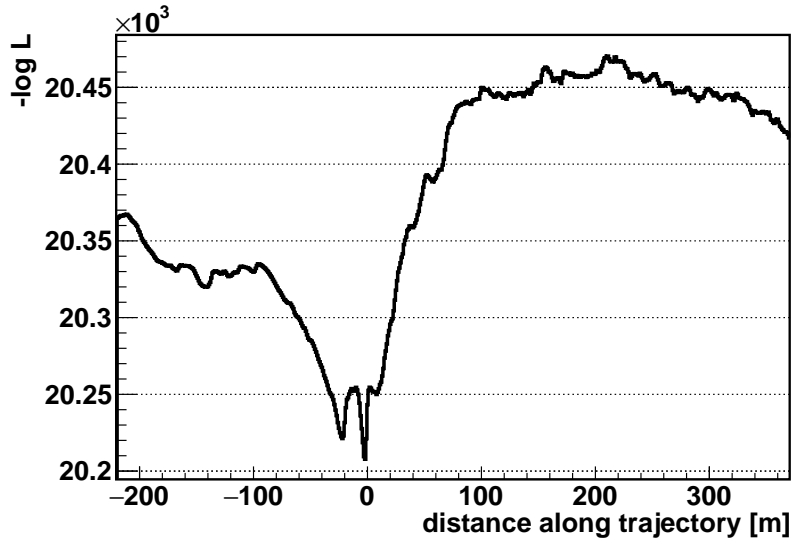
The tau “Double Bang” reconstruction algorithm is called “Belle Starr”. Its implementation proceeds in four steps. The steps build upon each other, gradually becoming more intricate and tailored to identify “Double Bang” signatures.

In the first step, a robust method is provided to establish starting parameters for the following steps. For this purpose a single shower position fit combined with a single shower direction and energy fit are performed. The position fit minimizes a modified χ^2 based on the expected time of the hits given a single shower hypothesis. For two shower signatures, a fit typically yields the position of the shower that produces more light, the direction of the original neutrino and the total energy deposited in the detector.

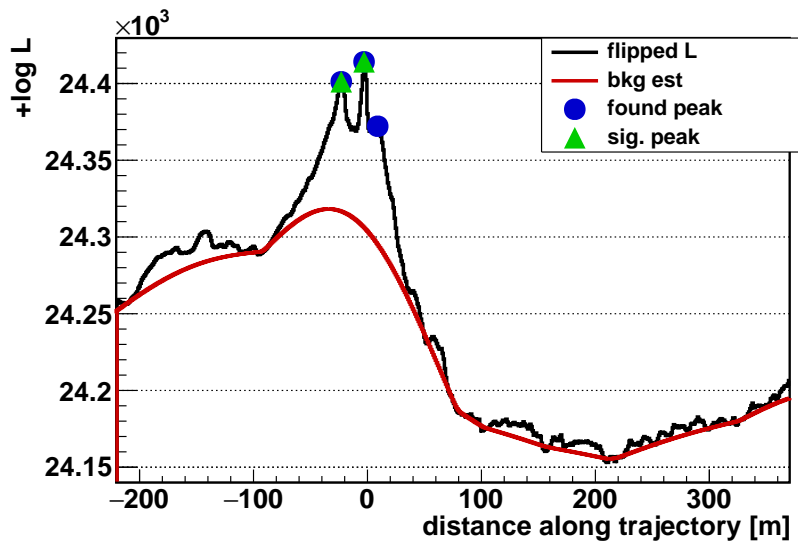
In the second step, the reconstructed position and direction from the previous step are used as starting values. The reason being, that the second shower vertex is expected to be on the trajectory found in the previous step due to the kinematics of the interaction. Therefore, a two shower likelihood is evaluated along the defined trajectory. The two shower likelihood is defined by a combination of the hit time distributions for two single shower hypotheses. The best fit of the two shower positions corresponds to minima in the negative logarithm of this likelihood. In Fig. 4a an example of the likelihood as a function of the position of the second shower along the trajectory of the first shower is shown. The two minima correspond to the simulated shower positions.

In the third step, the likelihood scans obtained in step 2 are analyzed by applying a peak finder algorithm to the inverted likelihood distribution. In the case of finding two significant peaks, the corresponding positions are used as a result. In the case of finding one or more than two significant peaks, the position of the highest peak and the position from step 1 are used. An example of evaluating the likelihood scan from step 2 is shown in Fig. 4b.

In the fourth step, the two shower likelihood is minimized for the whole detector rather than just along the trajectory defined in step 1. For this purpose the positions established in step 3 are used as starting values. This is not done immediately after step 1, since the performance of such a general minimization is strongly dependent on good starting values. Performing the general fit after step 3 allows to account for errors in the reconstruction of the position and the direction from step 1. With the general fit, a position resolution for both shower vertices of around 2 m median and a tau direction resolution of around 2° median is achieved.



(a) Scan from step 2.



(b) Analyzed scan from step 3.

Figure 4: Scans of the logarithm of the two shower likelihood along the trajectory defined in step 1; "0" on the X-axis corresponds to the position obtained in step 1.

This resolution allows to identify “Double Bang” signatures if their showers are separated by 5 m or more. By applying selection criteria based on the reconstructed parameter values and assuming an isotropic cosmic neutrino flux as observed by IceCube, a rate of 0.5 “Double Bang” events per KM₃NeT block per year are expected. The background is estimated to be 0.06 events per block per year. Comparing this to IceCube, an approximately three times better performance is achieved.

The presented method will yield sufficient statistics to reconstruct the flavor composition of the cosmic neutrino signal and the detection of two or more tau neutrinos would prove the cosmic origin of the neutrino signal.

SAMENVATTING

Samenlevingen koesteren sinds oudsher een gemeenschappelijke fascinatie voor de nachtelijke hemel. Dit heeft geleid tot de ontwikkeling van astronomie in verschillende oude beschavingen zoals die van de Babylonische tot de Chinese. Tegenwoordig is de astronomie een belangrijk wetenschappelijk onderzoeksveld met als doel het heelal te bestuderen in tijd en ruimte. Gedurende haar lange geschiedenis is de astronomie met name gebaseerd geweest op observaties van licht. Deze wordt daarom ook wel optische astronomie genoemd. In de laatste decennia is de optische astronomie uitgebreid van zichtbaar licht tot observaties die 12 orde groottes in golflengte bestrijken. Ondanks de talrijke successen heeft de optische astronomie niet geleid tot antwoorden op bepaalde fundamentele vragen en zal dat misschien ook wel nooit doen.

Een van deze vragen betreft Kosmische Straling. Kosmische Straling bestaat uit geladen deeltjes (voornamelijk atoomkernen) die het heelal doorkruisen. Hun energiespectrum reikt tot aan de hoogste energieën die ooit zijn waargenomen. Sinds hun ontdekking meer dan 100 jaar geleden heeft men uit directe waarnemingen niet kunnen opmaken waar ze vandaan komen en hoe ze zulke hoge energieën kunnen bereiken. Dit is te wijten aan de wisselwerking tussen Kosmische Straling en de magneetvelden die aanwezig zijn in het heelal. Wanneer een Kosmisch Stralingsdeeltje door een magneetveld beweegt wordt het afgebogen waardoor de bron vervaagt.

Dit probleem kan omzeild worden door neutrino's te observeren. Neutrino's zijn vrijwel massaloze elementaire deeltjes met twee nuttige eigenschappen voor het bestuderen van het heelal: ze hebben een extreem lage interactie waarschijnlijkheid met materie en ze hebben geen elektrische lading. Dankzij de eerste eigenschap kunnen ze schier oneindige afstanden overbruggen in het heelal terwijl de tweede eigenschap ervoor zorgt dat hun pad recht blijft. Neutrino's zijn inzetbaar om de bronnen van Kosmische Straling te onderzoeken omdat ze gecreëerd worden door interacties van Kosmische Straling met materie of licht in de nabijheid van de bronnen. Het verschillende gedrag van neutrino's ten opzichte van andere deeltjes die zich door het heelal voortbewegen is schematisch weergegeven in Fig. 1.

Hoewel de lage interactie waarschijnlijkheid neutrino's zeer geschikt maakt om de oorsprong van Kosmische Straling te bestuderen, wordt de waarneming daarmee ook bijzonder uitdagend. Een zeer groot detectievolume is noodzakelijk om voldoende statistiek te verzamelen. Wanneer een neutrino botst met een atoom in het detectievolume genereren de daarbij vrijkomende deeltjes Cherenkov licht. Dit licht wordt onder een vaste hoek uitgezonden die afhangt van de brekingsindex van het detectiemedium. Dankzij deze vaste hoek kan de richting van de deeltjes - en daarmee de richting van het inkomende neutrino - gereconstrueerd worden. Om het licht te kunnen detecteren moeten er sensoren in het detectiemedium geplaatst worden en dient het medium transparant te

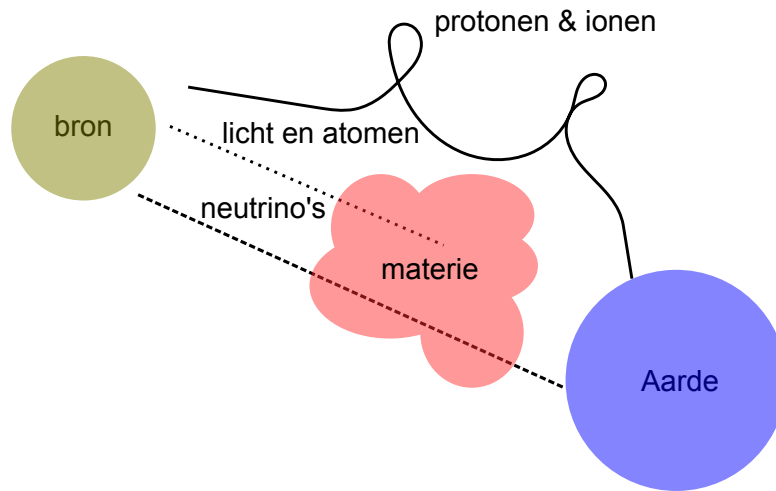


Figure 1: Een schematische weergave van de weg die verschillende kosmische deeltjes afleggen van een bron naar de Aarde. De magneetvelden zijn niet expliciet getekend. Als gevolg van de verschillende interacties die de deeltjes kunnen ondergaan tijdens hun weg door de ruimte zijn neutrino's de enige deeltjes die noch vastlopen op hun weg naar de Aarde noch van richting veranderen.

zijn. Dat maakt ijs en water tot geschikte media. Het detectievolume wordt bestreken door een driedimensionale matrix van lichtsensoren. Om er zeker van te zijn dat het gedetecteerde licht afkomstig is van neutrinobotsingen worden neutrino telescopen ter afscherming op grote dieptes geplaatst. Kort gezegd, neutrino telescopen omvatten een volume van ruwweg een kubieke kilometer ijs of water op een diepte van twee tot vier kilometer.

De eerste neutrino telescoop waarmee kosmische neutrino's zijn waargenomen is IceCube. De eerste aanwijzingen voor een kosmisch neutrinosignaal werden in 2013 gepubliceerd. Echter, de bron van deze neutrino's is nog niet gevonden en het energiespectrum niet nauwkeurig gemeten vanwege het lage aantal geregistreerde gebeurtenissen en de beperkte resolutie van de detector.

Om beter inzicht te krijgen in dit kosmische neutrinosignaal zijn nieuwe neutrino telescopen nodig met een vergelijkbaar volume en beter oplossend vermogen. Eén zo'n telescoop is KM₃NeT, momenteel in aanbouw op de bodem van de Middellandse Zee. De lichtsensoren van KM₃NeT bevinden zich in glazen ballen zoals getoond in Fig. 2.

Met twee touwen worden 18 glazen ballen verbonden, vergelijkbaar met een parelsnoer. De snoeren worden verankerd op de zeebodem en blijven vervolgens rechtop staan door het drijfvermogen van de glazen ballen. Een verzameling van 115 snoeren vormt één KM₃NeT blok.

De KM₃NeT telescoop zal naar verwachting een veel nauwkeurigere meting opleveren dan de IceCube telescoop. Dit is te danken aan twee factoren: de optische eigenschappen van water vergeleken met ijs en de sensortechnologie van KM₃NeT. De sensortechnologie is aanzienlijk verbeterd door gebruik te

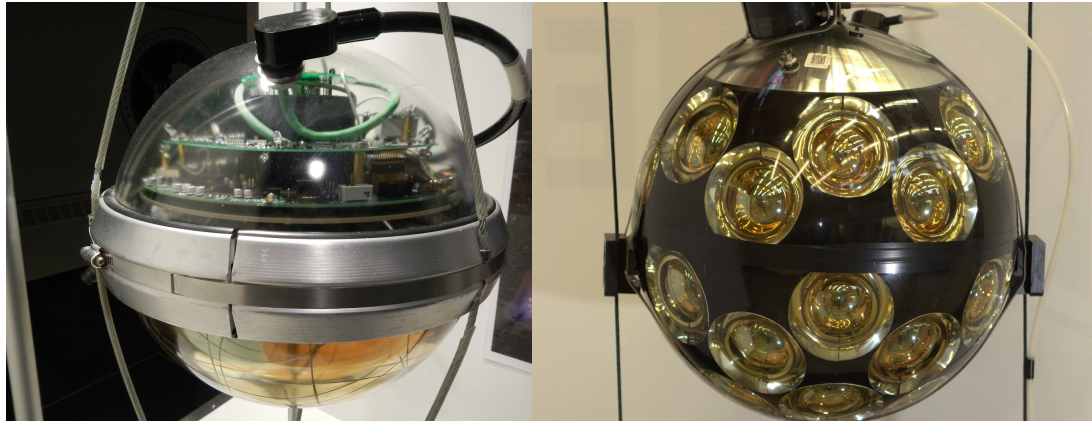


Figure 2: Een foto van een IceCube glazen bol (links) en een KM₃NeT glazen bol (rechts); het verschil tussen de lichtsensoren is duidelijk te zien.

maken van 31 kleinere lichtsensoren in plaats van één enkele grote lichtsensor. Dit maakt het mogelijk om de sensoren binnen één bol in vrijwel alle richtingen te laten wijzen en om lichtdeeltjes apart te registreren. Ter vergelijking worden een glazen bol van IceCube en van KM₃NeT getoond in Fig. 2. De nieuwe technologie van KM₃NeT vereiste een grondige voorbereiding. In dit werk worden de resultaten van het prototype getoond. Dit prototype, dat in 2014 werd geïnstalleerd op de Italiaanse KM₃NeT locatie, maakte het mogelijk om belangrijke onderdelen van de KM₃NeT hardware nauwkeurig te testen en heeft bijgedragen aan het opstellen van protocollen voor de bouw en het gebruik van de detector. De resultaten omvatten een tijdkalibratie procedure en een eerste identificatie en reconstructie van deeltjessporen.

Een belangrijke verbetering is het vaststellen van het type neutrino. Er komen drie types neutrino's in de natuur voor. Er hoort één neutrino bij elk geladen lepton: elektron, muon en tau. Neutrino's veranderen spontaan tijdens hun reis door de ruimte van het ene type in het andere type al naar gelang de afgelegde weg en de energie. Dit fenomeen wordt neutrino-oscillatie genoemd en heeft tot gevolg dat van ieder kosmisch neutrinosignaal ongeveer gelijke aantallen van elk neutrino type de Aarde bereiken. Toch kan de samenstelling van een kosmisch neutrinosignaal bepaald worden met de neutrinotelescoop. Dit maakt het mogelijk om theoretische modellen van neutrino bronnen te testen en helpt de achtergrond van niet-kosmische neutrino's te verminderen.

De drie verschillende neutrino types kunnen van elkaar onderscheiden worden op basis van het karakteristieke patroon van het lichtsignaal dat ze in de detector achterlaten wanneer ze een botsing hebben gemaakt in het zeewater. De verschillende karakteristieke patronen worden veroorzaakt door de verschillende deeltjes die vrijkomen bij zo'n botsing. De basispatronen zijn te herkennen aan een *deeltjesregen* en/of een *spoor*. De regens worden veroorzaakt door een hoeveelheid deeltjes die slechts een korte afstand afleggen waardoor het licht uit één punt lijkt te komen, zoals bij een vuurwerkexplosie. Sporen worden veroorzaakt door muonen, die kilometers af kunnen leggen in water voordat ze vervallen en onderweg licht uitzenden zoals een vallende ster. Voorbeelden

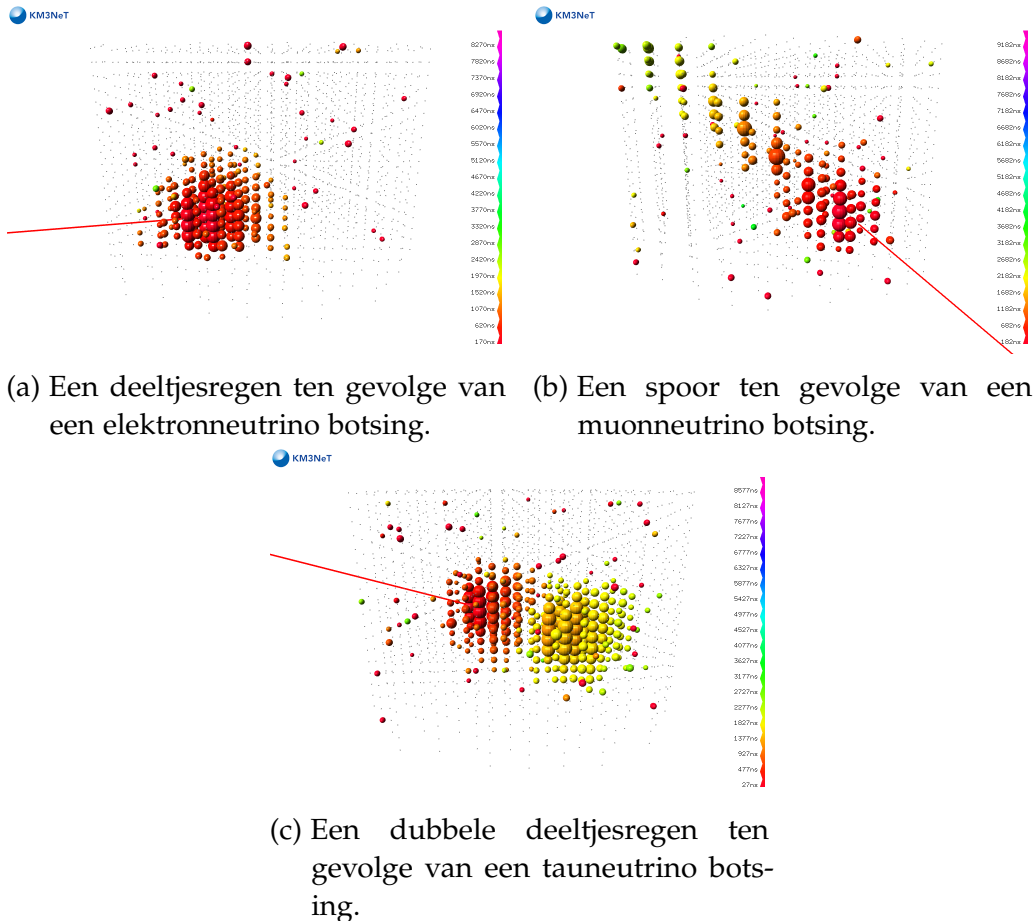


Figure 3: Simulaties van de gedetecteerde signalen voor de verschillende karakteristieke patronen in één KM₃NeT blok; de posities van de glazen bollen worden hier weergegeven. De grootte geeft het gemeten aantal lichtdeeltjes aan en de kleur de tijd (rood=vroeg en paars=laat). De rode lijn toont het pad dat het gesimuleerde neutrino aflegt.

voor de KM₃NeT detector van een regen, een spoor, en een dubbele regen zijn te zien in Fig. 3. Meestal worden regens veroorzaakt door elektronneutrino's, sporen door muonneutrino's en dubbele regens (ook wel "Dubbele Knal") door tauneutrino's. Echter, afhankelijk van de energieën en de optredende processen kan deze associatie vertroebeld raken.

In dit werk wordt een algoritme gepresenteerd om een "Dubbele Knal" te identificeren en te reconstrueren met de KM₃NeT detector. Hoewel reconstructie-algoritmes voor een enkele deeltjesregen en een enkel spoor al beschikbaar waren, ontbrak het nog aan een reconstructie-algoritme voor "Dubbele Knallen". Met de "Dubbele Knal" reconstructie kunnen de tauneutrino interacties onderscheiden worden van de elektron- en muonneutrino interacties. Dat is belangrijk om twee redenen. Ten eerste maakt dit het mogelijk om de samenstelling van een kosmisch neutrinosignaal te reconstrueren. Ten tweede verwacht men dat de neutrino achtergrond voor kosmische tauneutrino's veel kleiner is dan die voor kosmische elektron- en muonneutrino's. Bij de detectie van een "Dubbele Knal" is de verwachting dus direct dat het een neutrinosignaal uit het heelal is.

Het tau “Dubbele Knal” reconstructie-algoritme heet “Belle Starr” en verloopt in vier stappen. Iedere stap is steeds gedetailleerder en specifiek gericht op het herkennen van de “Dubbele Knal” signalen.

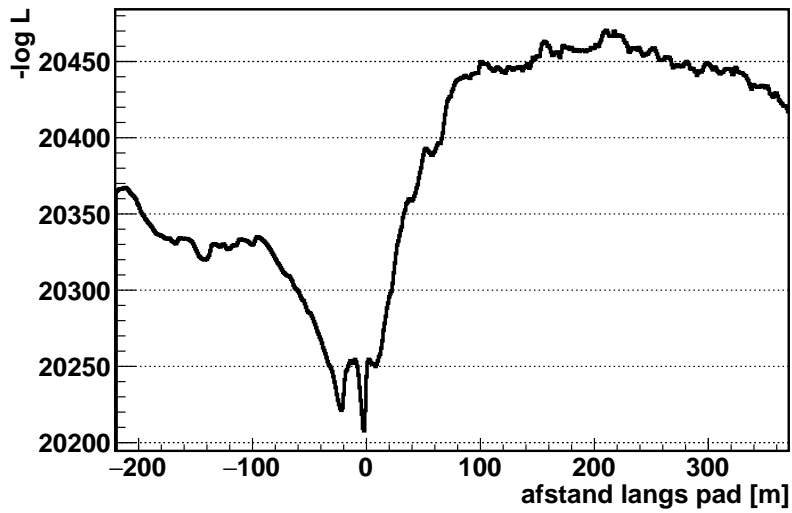
In de eerste stap wordt een robuuste methode ingezet om de startwaarden te bepalen voor de daarop volgende stappen. Hiertoe wordt er een fit van de positie van een enkele deeltjesregen uitgevoerd, gecombineerd met een fit van de richting en de energie van een enkele deeltjesregen. Voor de fit van de positie wordt een aangepaste χ^2 geminimaliseerd die gebaseerd is op de verwachte aankomsttijden van het licht uitgaande van de hypothese van één enkele deeltjesregen. Voor dubbele regens zal de fit de positie van de regen opleveren die het meeste licht produceert, de richting van het oorspronkelijke neutrino en de totale energie die in de detector afgegeven wordt.

In de tweede stap worden de gereconstrueerde positie en richting uit de vorige stap gebruikt als startwaarden. Als gevolg van de dynamiek van de neutrinobotsing bevindt de tweede regen zich op het eerder bepaalde pad. Daarom kan er een waarschijnlijkheid voor twee regens bepaald worden langs dit pad. De waarschijnlijkheid voor twee regens bestaat uit een combinatie van verdelingen van aankomsttijden van licht gebaseerd op twee losstaande hypothesen, ieder voor één enkele deeltjesregen. De beste fit voor de posities van de twee regens komt dan overeen met de minima in het negatieve logaritme van de waarschijnlijkheid voor de twee deeltjesregens. In Fig. 4a is een voorbeeld te zien van de waarschijnlijkheden langs het pad verkregen uit de eerste stap. De twee minima komen overeen met de gesimuleerde posities van de regens.

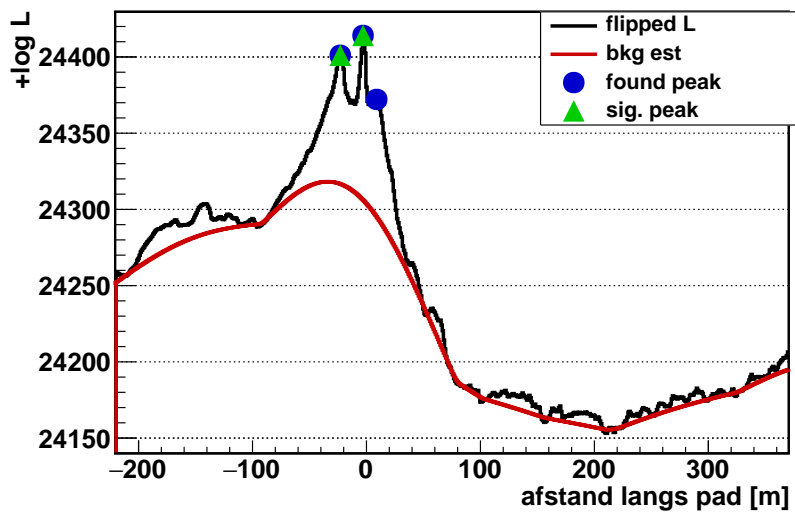
In de derde stap worden de waarschijnlijkheidsverdelingen uit stap twee geanalyseerd door een algoritme voor het vinden van pieken toe te passen op de omgekeerde uitkomst van stap twee. Als dit algoritme twee significante pieken oplevert, worden deze posities overgenomen. Als er één of meer dan twee pieken gevonden worden, worden de posities gezet op die van de hoogste piek en de positie verkregen in stap een. Een voorbeeld van de evaluatie van de scan van waarschijnlijkheden van stap twee is te zien in Fig. 4b.

In de vierde stap wordt de waarschijnlijkheid voor twee deeltjesregens geminimaliseerd in algemene zin in plaats van alleen langs het pad verkregen uit de eerste stap. De posities bepaald in stap drie worden als startwaarden gebruikt. Dit wordt niet direct na stap een gedaan omdat de uitkomst van zo’n algemene minimalisatie sterk afhankelijk is van de beginwaarden. Het uitvoeren van de algemene fit na stap drie zorgt ervoor dat eventuele fouten in de reconstructie van de positie en de richting in stap een gecompenseerd kunnen worden. Met de algemene fit wordt een positieresolutie voor beide deeltjesregens van ongeveer 2 m (mediaan) bereikt en een resolutie op de richting van het tau lepton van rond de 2° (mediaan).

De verkregen positiereconstructie maakt het mogelijk “Dubbele Knallen” te herkennen wanneer de twee regens 5 m of meer uit elkaar liggen. Door selectiecriteria toe te passen op basis van gereconstrueerde parameters en uitgaande van een isotrope flux van kosmische neutrino’s zoals gemeten door IceCube, worden er 0.5 “Dubbele Knallen” per KM₃NeT blok per jaar verwacht.



(a) Scan van stap twee.



(b) Geanalyseerde scan van stap drie.

Figure 4: Scan van de logaritme van de waarschijnlijkheden voor twee deeltjesregens langs het pad verkregen in stap één; "0" op de X-as komt overeen met de gereconstrueerde positie uit stap één.

Het aantal achtergrondgebeurtenissen is naar verwachting 0.06 per blok per jaar. Dat is driemaal zo goed als verkregen wordt met de IceCube neutrino telescoop.

De gepresenteerde methode levert voldoende statistiek op om de neutrino-types van het neutrinosignaal uit de kosmos te bepalen, terwijl de detectie van twee of meer tauneutrino's de kosmologische oorsprong van het signaal bevestigt.

ABOUT THE AUTHOR

Robert Bormuth was born in the town of Heppenheim at the 29th of December 1986. After finishing the first class of elementary school in the town of Bickenbach, a move of the family to the town of Kelsterbach saw him finishing elementary school at the Bürgermeister Hardt Schule in 1997.

After elementary school he transferred to the Schloss Gymnasium in Mainz where he graduated with his Abitur in 2006. Before continuing on to study at university, he performed an almost year long civil service at the children hospital of the Universitäts Klinik Mainz.

Robert then decided to study physics at the Johannes Gutenberg Universität Mainz. During his studies he was involved with the student council for three years. He finished his physics studies with a Diploma on the topic of $\gamma\gamma \rightarrow \pi^+\pi^-\pi^0$ at the BES-III detector with Professor A. Denig in 2012.

The desire to stay in science and to experience a foreign culture triggered a search for a PhD position abroad, which resulted in the PhD position in the KM3NeT group of the Nikhef. During the PhD not only did he work on the string prototype and the tau neutrino reconstruction, but was also involved in PMT and DOM testing as well as some work on a reconstruction code for ORCA. In addition to supervising bachelor and master students, he attracted and supervised two German students for an internship organized via the DAAD.

ACKNOWLEDGMENTS

First and foremost I want to thank my supervisor Dorothea F. E. Samtleben for her involvement during my promotion and in the making of this thesis. Her willingness to improve on our communication and working habits to make them as positive and effective as they can be never ceased throughout my PhD. In addition, her almost permanent availability and scientific knowledge have been much needed support.

Secondly, I want to thank my promotor Maarten de Jong. His door was always open for any questions I had during my promotion and the depth and directness of any discussion we had always set me on the right track.

In addition to these two, the support I received from the KM₃NeT and Antares group at Nikhef has been substantial to this thesis, thank you to all past and present members of the group: Aart, Arjen, Bas, Bram, Bruno, Claudio, Daan, Erwin, Eline, Els, Ernst-Jan, Freek, Jacqueline, Jorinde, Karel, Lodewijk, Martijn, Mieke, Niklas, Paul, Rasa, Ronald, Stephan, Thomas, Tino and Tri. You helped to make this thesis reality.

I also want to thank the whole KM₃NeT collaboration. Many a member worked hard to lay the ground work this thesis is based upon, from hardware to software. Also, thank you all for making our meetings so fruitful and greatly enjoyable. Special thanks go to Clancy and Rodrigo for working so hard to get the tau simulations working.

My parents and family deserve a special thank you, as their constant support made me go into science and never made me falter during my dissertation.

Last but not least I want to thank my partner Ulrike for her support and open ear during my research and especially her support during the writing of the thesis itself. You always kept me optimistic and listened to my problems.

Robert Bormuth